APPLICATION OF SYNTHETIC APERTURE RADAR INTERFEROMETRY FOR MINE SUBSIDENCE MONITORING IN THE WESTERN UNITED STATES

by

Jessica Michelle Wempen

A dissertation submitted to the faculty of
The University of Utah
in partial fulfillment of the requirements for the degree of

Doctor of Philosophy

Department of Mining Engineering

The University of Utah

August 2016

The University of Utah Graduate School

STATEMENT OF DISSERTATION APPROVAL

The dissertation of **Jessica Michelle Wempen**

has been approved by the following supervisory committee members:

Michael K. McCarter	, Chair	**4/15/2016** Date Approved
Richard R. Forster	, Member	**4/15/2016** Date Approved
Michael G. Nelson	, Member	**4/15/2016** Date Approved
Kristine L. Pankow	, Member	**4/15/2016** Date Approved
Jeffrey K. Whyatt	, Member	**4/21/2016** Date Approved

and by **Michael G. Nelson** , Chair/Dean of

the Department/College/School of **Mining Engineering**

and by David B. Kieda, Dean of The Graduate School.

ABSTRACT

Differential Interferometric Synthetic Aperture Radar (DInSAR), a satellite-based remote sensing technique, is a practical method for measuring deformation of the earth's surface. In this investigation, the application of DInSAR for monitoring mine subsidence was evaluated for active underground mining regions in the Green River Basin in southwest Wyoming and the Wasatch Plateau in central Utah. Interferograms were generated using X-band (3-cm wavelength) Synthetic Aperture Radar data from the TerraSAR-X mission and L-band (24-cm wavelength) Synthetic Aperture Radar data from the Advanced Land Observing Satellite.

In general, the DInSAR data have high spatial and temporal resolutions and show gradual, progressive subsidence. In the Green River Basin, displacements were estimated using both L-band and X-band data. In the Wasatch Plateau, displacements were only estimated using L-band data; areas affected by subsidence are identifiable in the X-band data, but precisely quantifying subsidence magnitudes is difficult as a result of significant phase noise. In the Green River Basin, the maximum subsidence magnitude was 150 cm over 690 days, estimated using L-band DInSAR. In the Wasatch Plateau, the maximum subsidence magnitude was 180 cm over 414 days. In both regions, as a result of low coherence in the areas with large displacements, the maximum displacements may be underestimated by tens of centimeters.

Additionally, relationships between surface deformations measured by DInSAR and mining-induced seismicity (MIS) in the Green River Basin and the Wasatch Plateau were explored. Both regions exhibit large magnitude, relatively rapid subsidence, but the characteristics (rates and magnitudes) of MIS in the Wasatch Plateau study region and the Green River Basin are significantly different. In the Wasatch Plateau study region, surface displacements tend to precede seismicity, event rates tend to be high, and event magnitudes tend to be relatively low. In the Green River Basin, seismicity spatially correlates with surface displacements, but only over long periods. Seismic events tend to be relatively large in magnitude and the event rate tends to be low. Further investigations of differences in the seismic characteristics in the Wasatch Plateau and the Green River Basin and of the dependence of MIS and subsidence on regional geologic and mining parameters are warranted.

CONTENTS

LIST OF TABLES

LIST OF FIGURES

ACKNOWLEDGMENTS

For their interest and guidance, I extend sincere thanks to my committee: Kim McCarter, Rick Forster, Mike Nelson, Kris Pankow, and Jeff Whyatt. I am also grateful to Keith Koper, Bill Pariseau, Derrick Chambers, Katherine Whidden, Jared Stein, Shawn Boltz, Tex Kubacki, and Fitra Ismaya.

Primary financial support for this research was provided by the National Institute for Safety and Health (NIOSH) through contract number 200-2011-3961. Additional financial support was provided by the R. D. Call Memorial Scholarship and the University of Utah Department of Mining Engineering. Data for this research were provided by the Alaska Satellite Facility, the Japan Aerospace Exploration Agency, the German Space Agency, the EarthScope Array Network Facility, and the University of Utah Seismograph Stations. Though the conclusions expressed in this research do not represent the opinions or policies of NIOSH or any of these organizations, they all contributed significantly and are gratefully acknowledged.

I extend my deepest thanks to my family: my parents, Kris and Stan, for their unbreakable love; my brother, Jake, for naming me; and my husband, Corey, for his love and friendship. Final thanks to Homer for teaching me to read.

CHAPTER 1

INTRODUCTION

1.1 Background

Land subsidence can be a significant consequence of underground mining. It has potential to damage surface and underground structures, and to affect future land use and local hydrology. A 1991 study by the National Research Council estimated that over 44,000 km^2 of land in the United States has subsided, with close to 20% of this subsidence due to underground coal mining. Land subsidence has a variety of anthropogenic and natural sources including underground fluid withdrawal, sinkholes, hydrocompaction, and drainage of organic soils, but mining is one of the most significant causes of subsidence in the Mountain West of the United States.

In the western United States, most mine subsidence occurs gradually and progressively with mine development (Dunrud 1984). However, rapid, large displacement, and large extent subsidence does occur, and has been measured coincident to several significant mine collapses, including the 2007 Crandall Canyon mine collapse in central Utah and the 1995 and 2000 Solvay mine collapses in southwest Wyoming (Arabasz and Pechmann 2001; Foxall et al. 1998; Lu and Wicks 2010; Plattner et al. 2010; Whyatt and Varley 2008). In addition, these collapses exhibited significant

seismicity (Pechmann et al. 1995; 2008).

Subsidence and mining-induced seismicity (MIS) may both be indicative of how potential energy generated by underground mine advance is relieved. Whyatt and Varley (2008) reviewed a number of collapse case histories and proposed that there is correlation between the change in potential energy due to subsidence and the energy released by MIS for some collapse events, and that the presence of strong, brittle strata is an important risk factor for collapse potential. Additionally, research by Boltz et al. (2014) indicates that for the Trail Mountain mine, an underground longwall mine in central Utah, MIS is associated with mine advance and occurs predominantly in the mine roof, leading to the assumption that MIS and subsidence are likely correlated.

Regularly monitoring subsidence and MIS may help define whether caving is progressing normally or if potentially hazardous conditions are developing, and has potential to improve ground control safety by better quantifying potential risks to mine stability. However, this type of assessment depends on complete and accurate subsidence data, and though conventional subsidence surveys are accurate, the data are generally too spatially and temporally sparse for regular evaluation of mine stability. In contrast, Differential Interferometric Synthetic Aperture Radar (DInSAR), a satellite-based remote sensing technique, has the potential to quantify subsidence accurately, with high spatial and temporal resolutions. Using DInSAR to monitor subsidence consistently, with high spatial resolution, could help build a more comprehensive understanding of subsidence dynamics, provide insight into strata behavior during caving, and better define relationships among, subsidence, MIS, and mine stability.

1.2 Objectives

This research investigates the application of DInSAR for monitoring mine subsidence in the Green River Basin in southwest Wyoming and in the Wasatch Plateau in central Utah. There are three primary objectives. The first objective is to evaluate the application of L-band (24-cm wavelength) and X-band (3-cm wavelength) DInSAR for measuring mine subsidence in mining regions in the western United States with different topographic and vegetative characteristics. The second objective is to utilize multiple interferograms spanning consecutive time periods to map accumulated mine subsidence, and to better define the spatial and temporal progression of subsidence in these mining regions. The third and final objective is to explore possible relationships between surface deformations measured using DInSAR and MIS.

CHAPTER 2

UNDERGROUND MINING METHODS AND CHARACTERISTICS

2.1 Introduction

Longwall, room and pillar, and solution mining are important and productive methods for mineral resource extraction. Because these underground mining methods remove subsurface support, they have the potential to generate subsidence and induce seismicity. In this chapter, production characteristics of underground mining in coal and in trona are presented. Typical longwall, room and pillar, and solution mining parameters are summarized. Next, characteristics of subsidence are discussed. Subsidence regulations and conventional methods for subsidence monitoring are presented, and DInSAR is introduced as a method for subsidence monitoring.

2.2 Coal and Trona Production Characteristics

Room and pillar mining using continuous miners and longwall mining are important methods of coal production in the United States. In 2012, underground mines produced 310,608,000 tons of coal, one third of the total U.S. coal production. Approximately half of the underground coal production was generated by longwall mines and, in terms of reserve recovery, longwall mines are more efficient than room and

pillar mines. In 2012, longwall mines had an average recovery of about 60%, 7% higher than the average recovery of room and pillar mines (U.S. Energy Information Administration 2013).

In the western United States, longwall mining is a particularly important method for coal production because mineable reserves are deep, often more than 600 m below the surface topography. Deep reserves often prohibit the use of room and pillar mining because pillars must be excessively large to maintain mine stability, making resource recovery low (Barron et al. 1994; Foy 2008; Nieto 2011). As a caving method, longwall mining can be applied in deep mines with a high reserve recovery. In 2013, 11 of 40 longwall coal mines operating in the United States were located in western states (Fiscor 2014), and in 2012, longwall mines west of the Mississippi River generated over 95% of the total underground coal production in the western United States (U.S. Energy Information Administration 2013).

Trona, an evaporite mineral used to produce soda ash, is also an important resource in the western United States; about 80% of the known global resource of natural soda ash occurs in the Green River Basin (Gandhi 2013). The trona deposits are extensive and shallowly dipping, and mining has historically been carried out using longwall and room and pillar methods at depths from 245 to 520 m (Brown 1995; Mannion 1975; Santini et al. 2006). In 2013, two longwall mines and two room and pillar mines produced a total of 14,854,000 tons of trona from the Green River Basin (Adcock 2013). Forty-six percent of the trona was produced by the longwall mines with an average recovery of 75%, and 54% of the trona was produced by the room and pillar mines with an average recovery of 45%. In addition to conventional mining methods, trona can be

produced by dissolution with an estimated recovery near 30% (Santini et al. 2006). In 2012, 1,125,000 tons of trona were produced in the Green River Basin by solution mining (FMC Granger 2013).

2.3 Mine Parameters

Generally, longwall mining can be applied to laterally extensive, continuous, and horizontal to shallow dipping mineral deposits, and is used most productively in deposits with seam thicknesses ranging from 1.75 to 3.75 m (Bessinger 2011). In longwall mining, the mined stratum should be relatively weak so it can be efficiently broken by mechanical cutting. The overlying strata should also be relatively weak so the strata cave regularly with longwall advance (Nieto 2011; Peng 2006).

During longwall mine development, continuous miners advance headgate, tailgate, and bleeder entries around large, rectangular longwall panels, typically between 274 to 305 m wide and 2,500 to 4,000 m long. An example of a three-entry longwall mine layout is shown in Figure 2.1. Once the entries surrounding a longwall panel have been developed, a longwall, including a shearer, an armored face conveyor, and hydraulic shields, is installed across the width of the panel near the bleeder entries. During production, material is broken by the shearer, which is driven back and forth across the width of the panel as the shields advanced toward the main entries. Broken material is loaded onto the armored face conveyor and carried away from the production face. In addition to advancing the armored face conveyor and the shearer, the shields temporarily support the strata immediately near the production face. As the longwall advances and the strata behind the shields are left unsupported, these strata cave, filling the void behind the

hydraulic shields and forming the longwall gob and eventually producing subsidence.

Typically, room and pillar mining using continuous miners is applied to deposits with characteristics similar to those required for longwall mining. The deposits are most often weak, laterally extensive, and fairly flat lying. However, room and pillar mining is more flexible than longwall mining and can be applied more readily to mineral deposits that are not uniform (Nieto 2011). In room and pillar mining, development entries and crosscuts, typically 6 m wide, are mined systematically in a gridded pattern, forming rooms. Pillars, ranging from 12 to 24 m wide, are left for structural support (Bullock 2011; Tien 2011). Layout of room and pillar mines is similar to layout of longwall mines, with section entries developed perpendicular to main entries, and is illustrated in Figure 2.2.

In solution mining, minerals are extracted by dissolution. A lixiviant is pumped into a deposit through an injection borehole to dissolve a target mineral, and after dissolution, the solution is pumped out of the deposit through a production borehole. For soluble minerals, solution mining can be applied as a secondary mining method after conventional underground mining has reached a feasible limit. During secondary mining, abandoned regions of the conventional mine are sealed and flooded, and the mineral remaining in the pillars is dissolved (Kyle et al. 2011).

2.4 Subsidence

As subsurface structural support is removed by longwall, room and pillar, or solution mining, the potential for subsidence develops. The mining method, the width of the mined area, the reserve recovery, the rate of mine development, the topography, and

the strata thickness, depth, and dip are significant parameters that affect the magnitude, extent, and duration of subsidence (Dunrud 1984; Jeran and Trevits 1995; Kratzsch 1983; Singh 1992). Regional hydrology, geologic structures, and the geotechnical properties of the strata also affect subsidence. Though all of these parameters affect subsidence, the characteristics of subsidence vary significantly, and the effects are difficult to explicitly quantify.

Subsidence most often develops gradually forming troughs, with smooth margins and a slow transition between subsided regions and regions with no significant subsidence. Subsidence can develop rapidly forming sinkholes, with sharp transitions from regions with minor subsidence to regions with significant subsidence (Dunrud 1984; Singh 1984). Generally, the vertical displacement associated with subsidence is less than the mining extraction height because the strata volume tends to increase with failure (Bauer 2006; Dunrud 1976; Whittaker and Reddish 1989). Modern longwall and solution mines tend to form trough subsidence with large areal extents and magnitudes. Usually, subsidence formed by longwall mining is a result of caving and occurs concurrently with mine development. Subsidence generated by room and pillar or solution mining tends to occur less predictably and is most often a result of pillar failure (Kyle et al. 2011).

Historically in the western United States, subsidence has been a significant safety and environmental issue. In this region, old room and pillar mines with less than 90 m of weak overburden have formed dramatic sinkholes. Figure 2.3 shows a historic mining area near Sheridan, Wyoming significantly affected by sinkhole subsidence. Sinkhole subsidence tends to develop rapidly and unpredictably and can occur years after mining has ceased (Bauer 2006; Bauer 2008; Dunrud 1984; Dunrud and Osterwald 1980).

In the United States, subsidence due to active underground coal mining is federally regulated by the Surface Mining Control and Reclamation Act (SMCRA), originally enacted in 1977. These regulations require that underground coal mines are permitted and that mine operators either prevent subsidence, maximize mine stability, and maintain the land value and use, or that subsidence is planned and occurs in a predictable and controlled manner (30 U.S. Code Chapter 25 1992).

2.4.1 Subsidence Prediction and Characterization

Subsidence that results from caving is usually more predictable than subsidence that results from structural failure related to either solution mining or room and pillar mining. Since relatively early in the application of mechanized longwall mining, significant engineering effort has been directed toward predicting the characteristics of longwall mine subsidence. The 1975 *Subsidence Engineers' Handbook* is one early comprehensive study of subsidence and presents substantial empirical data from U.K. coal basins (National Coal Board 1975). Other empirical methods for subsidence prediction include profile functions that predict subsidence profiles using mathematical functions and influence functions that predict subsidence using areas of influence and superposition (Whittaker and Reddish 1989). Numerical methods that use physical and mechanical laws to derive displacements are also used for subsidence prediction (Bahuguna et al. 1991). Both empirical and numerical subsidence models are mine specific and must be calibrated to accurately predict subsidence.

Longwall mine subsidence is often characterized by the width to depth ratio, angle of draw, vertical displacement, horizontal displacement, horizontal strain, slope,

and curvature (Gray and Bruhn 1984; Singh 1984). The width to depth ratio, which is the width of the extraction area to the mining depth, affects the extent and magnitude of subsidence. As the depth increases, the subsidence extent increases and the subsidence magnitude decreases. Increasing the panel width tends to increase the magnitude or extent of subsidence and the panel width is often classified as subcritical, critical, or super critical (National Coal Board 1975). When the width is subcritical, the width to depth ratio is small and the maximum subsidence that develops is less than the maximum possible subsidence; when the panel width is critical, the maximum possible subsidence develops at the center of the panel; and when the panel width is super critical, the width to depth ratio is large and the maximum possible subsidence occurs over a large area, forming a relatively flat subsidence trough (Gray and Bruhn 1984).

The angle of draw, illustrated in Figures 2.4 and 2.5, is the angle of inclination from vertical of the line connecting the edge of the longwall panel to the edge of the subsidence area. The angle of draw strongly depends on the geologic character of the overburden strata and affects the subsidence extent. In general, larger angles of draw are associated with weaker strata and unconsolidated materials (National Coal Board 1975). Angles of draw ranging from 10° to 35° have been reported in the United States (Gray and Bruhn 1984).

Vertical displacement, horizontal displacement and strain, slope, and curvature, illustrated in Figures 2.4 and 2.5, are all displacement characteristics of subsidence. Vertical displacements tend to be of the largest magnitude and occur over the entire subsidence profile, increasing from zero at the edge of the trough to a maximum at the center of the extracted region. Subsidence also causes small horizontal displacements.

Horizontal displacements are typically at a maximum near the mining boundary and decrease away from the boundary, with close to zero horizontal displacements near the center and edges of the subsidence trough (Harrison 2011). Relationships between vertical and horizontal displacements are defined by slope, the derivative of the vertical displacement with respect to horizontal displacement, and curvature, the derivative of the slope.

2.4.2 Subsidence Monitoring

Subsidence monitoring is important for assessing surface damage and for model calibration and validation. Traditionally, subsidence has been monitored using leveling, GPS, or photogrammetric surveys. Leveling and GPS both use differential surveying to measure relative changes in the position of the land surface. In differential surveys, geodetic markers are anchored into the ground and, using repeat surveys, vertical and horizontal changes in the locations of the markers are measured relative to stable benchmarks (Galloway et al. 1999). In leveling surveys, the elevation from a stable benchmark is carried to other geodetic markers using a precise optical or laser level and graduated vertical rods. Leveling has the benefit of being relatively simple and very accurate over small areas, with a vertical resolution from 0.1 to 1 mm. Using GPS, locations are trilaterated, based on the time required for a radio signal transmitted by satellites with known locations to reach a receiving antenna. In GPS subsidence surveys, the relative position between two markers is determined by locating each point simultaneously using two GPS receivers. GPS surveys typically have horizontal and vertical accuracies of 5 mm and 20 mm, respectively.

In addition to ground based surveys, aerial photogrammetric surveys are commonly used to measure mine subsidence (Fry 1986; LaScola 1988). Photogrammetric surveys use stereoscopic pairs of photographic images taken from known locations to form three-dimensional surface models. These surveys generally provide more data over a larger spatial extent than leveling or GPS surveys. Although photogrammetric surveys are performed remotely, ground control points are required to quantify the horizontal and vertical displacement. Additionally, the accuracy of photogrammetric surveys is lower than that of ground based surveys. Using survey grade drones to capture stereoscopic images under ideal conditions, surface models have accuracies of 3 cm horizontally and 5 cm vertically (Roze et al. 2015).

In contrast to traditional methods of subsidence monitoring, DInSAR can produce displacement measurements over large regions with high spatial resolution, and under good conditions, centimeter to subcentimeter accuracies in displacement measurements can be attained (Buckley 2000; Massonnet and Feigl 1998). Additionally, DInSAR typically has high temporal resolution and data are acquired regularly, often every 10 to 50 days (Rosenqvist et al. 2004; Roth 2004). DInSAR has potential to accurately measure subsidence, but unlike conventional surveys, it is strongly time dependent. Significant changes in the satellite orbits and the surface conditions over time and large deformation gradients can make the radar images incoherent and inhibit accurate measurements of displacement.

In the last two decades, the application of DInSAR for monitoring mine subsidence has been demonstrated in coal basins in Europe, Australia, China, and the United States (Carnec and Delacourt 2000; Ge et al. 2007; Ge et al. 2008; Ismaya and

Donovan 2012; Ng et al. 2010; Perski 2000; Perski and Jura 2003; Popiołek and Krawczyk 2006; Wegmuller et al. 2005; Wright and Stow 1999; Zhao et al. 2014; Xinglin et al. 2014). Overall, these studies demonstrate high data density, strong relationships among mine development and subsidence, and reasonable agreement between displacements measured by DInSAR and displacement measured by conventional surveys.

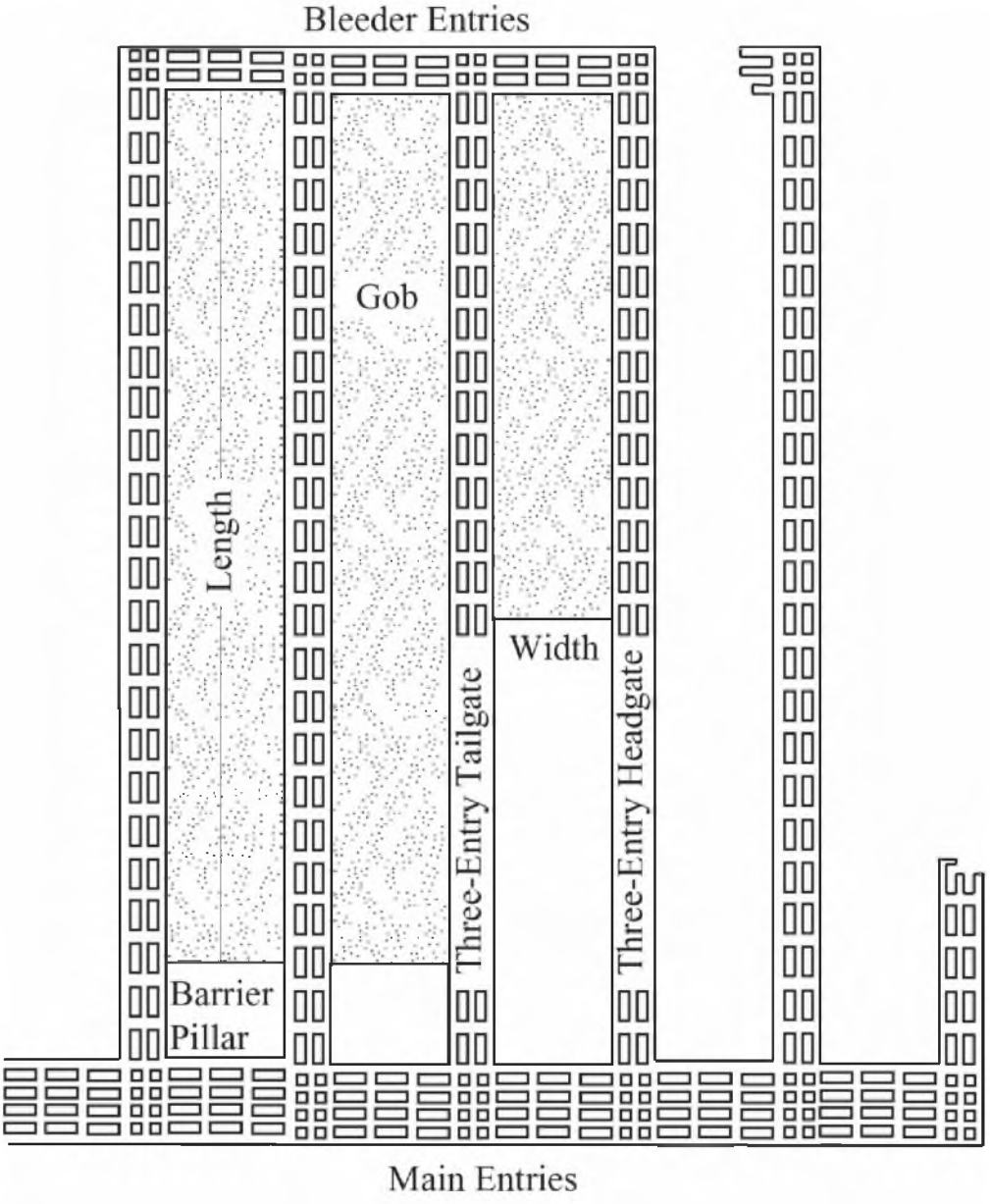

FIGURE 2.1 Illustrative three-entry longwall mine layout

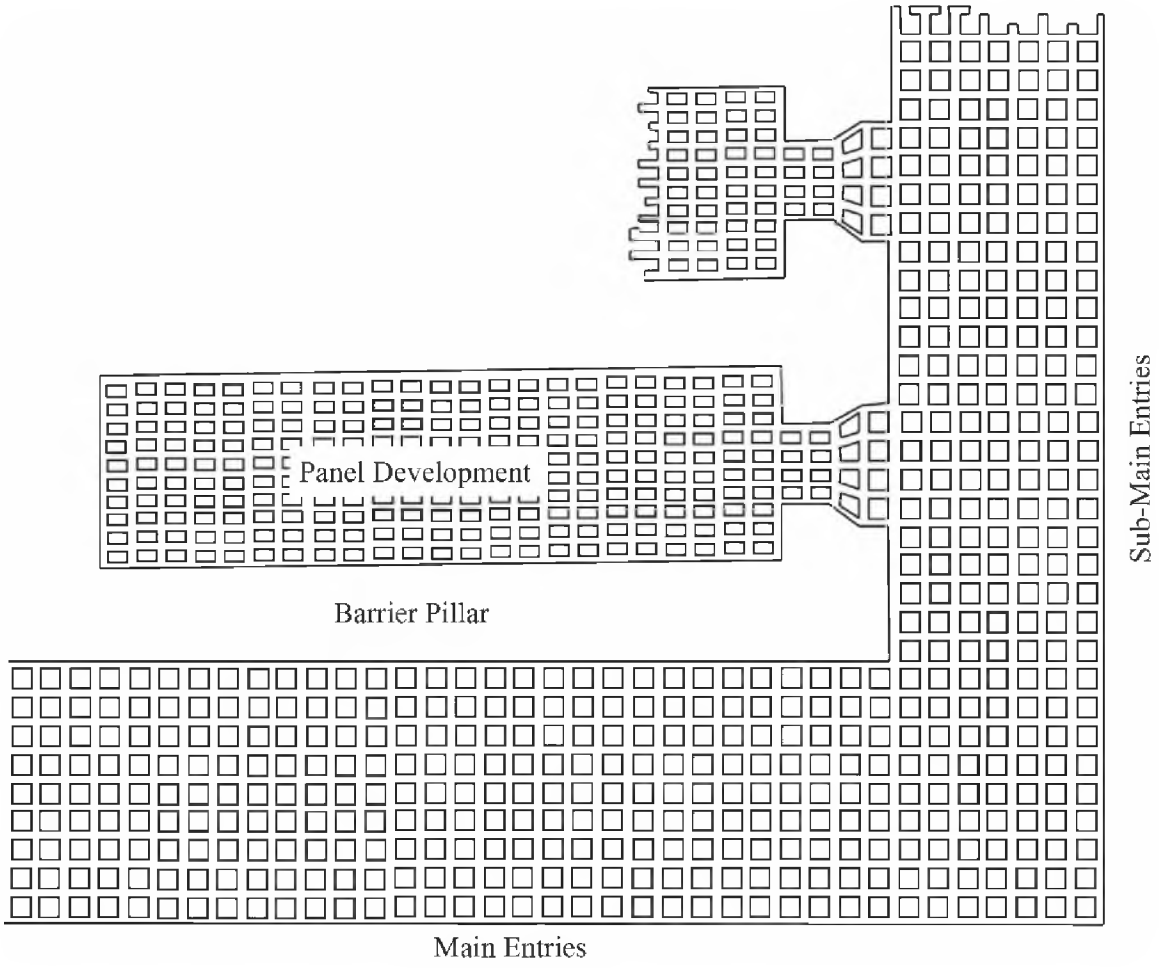

FIGURE 2.2 Illustrative room and pillar mine layout

Source: Adapted from Google 2015

FIGURE 2.3 Subsidence caused by historic room and pillar mining near Sheridan, Wyoming

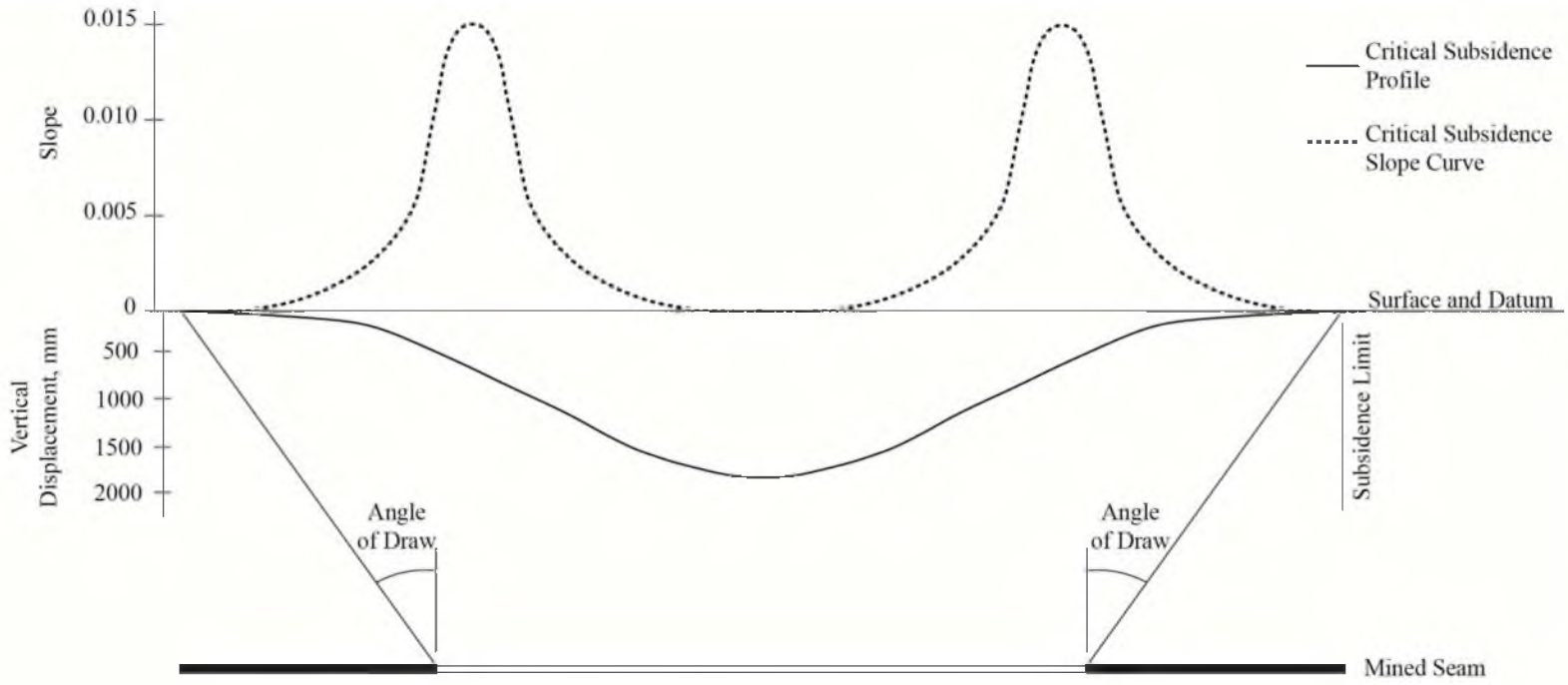

Source: Adapted from National Coal Board 1975

FIGURE 2.4 Section view illustrating longwall subsidence angle of draw, slope, and vertical displacement

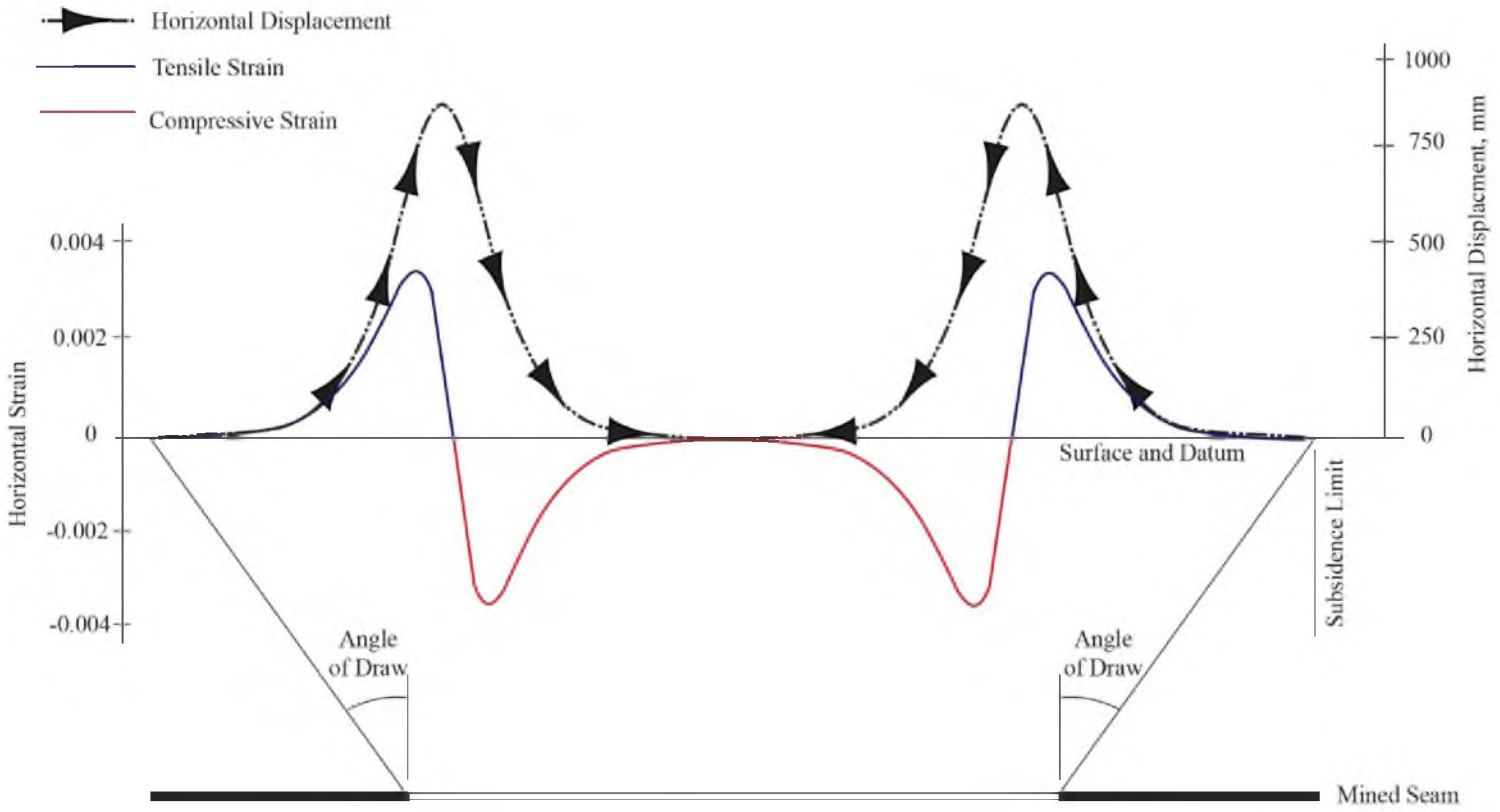

Source: Adapted from National Coal Board 1975

FIGURE 2.5 Section view illustrating longwall subsidence horizontal displacement and strain

CHAPTER 3

PRINCIPLES OF RADAR INTERFEROMETRY

3.1 Introduction

Radar interferometry is an established discipline with broad applications in earth science. This chapter begins with a review of early applications of satellite-based Synthetic Aperture Radar (SAR) Interferometry, and includes a summary of developing applications with emphasis on mine subsidence monitoring. Next, basic concepts of radar interferometry are outlined; interferometer geometry, interferometric phase, and complex interferogram are defined; applications of interferometry for topographic and displacement mapping are presented; correlation, a method for evaluating the quality of interferograms, is introduced; and finally, decorrelation and other error sources are summarized. This chapter is intended to review important concepts of SAR interferometry, but because it is an established discipline, quality references exist, including works by Bamler and Hartl (1998), Massonnet and Feigl (1998), Burgmann et al. (2000), Rosen et al. (2000), Hanssen (2001), Simons and Rosen (2007), Massonnet and Souyris (2008), and Richards (2009).

3.2 Literature Review

Civilian applications of Interferometric Synthetic Aperture Radar (InSAR) have been developing since early demonstrations of satellite-based radar interferometry. Using SAR data from the Seasat satellite, the earliest studies established the application of InSAR for topographic mapping (Goldstein et al. 1988) and DInSAR for displacement measurement (Gabriel et al. 1989). Both the studies by Goldstein et al. and Gabriel et al. demonstrated high resolution results and established the potential for broader applications of interferometry. With the launch of the ERS-1 satellite in 1991, significant applications of DInSAR developed: in one seminal application, co-seismic deformation resulting from the 1992 Landers earthquake was measured (Massonnet et al. 1993; Zebker et al. 1994) and in another groundbreaking study, DInSAR was used to quantify Antarctic glacial flow (Goldstein et al. 1993).

New satellites with SAR sensors and better SAR data availability have dramatically increased applications of radar imagining since the first influential studies. Figure 3.1 shows the operational periods and radar bands of satellites with SAR sensors launched after 1990. Over the last two decades, radar imaging has been applied in forestry and wetlands monitoring for land surface change detection, land use, and land cover classification. DInSAR has been used for quantifying seismic and aseismic slip on faults, measuring deformation associated with active volcanic systems, evaluating glacial mechanics, monitoring infrastructure, and identifying landslide hazards. Additionally, DInSAR has significant application quantifying surface deformation due to fluid injection, fluid withdrawal, and resource extraction. Radar imaging has broad relevance and SAR technology continues to progress. Table 3.1 lists the anticipated launch dates of

proposed satellite missions that include SAR sensors. With the development and launch of these satellites, the variety of available radar bands will increase, data availability will improve, and applications of radar imaging will continue to develop and mature.

Mine subsidence monitoring is one area where the application of DInSAR continues to progress. Foxall et al. (1998), Wright and Stow (1999), and Carnec and Delacourt (2000) first evaluated DInSAR for mine subsidence monitoring using ERS data. These studies all demonstrated the ability to identify mine subsidence using DInSAR; they also identified difficulty in accurately measuring subsidence over long periods due to data decorrelation. Since these initial studies, DInSAR has been evaluated as a method for monitoring mine subsidence in coal basins in Europe, Australia, China, and the United States.

In one of the studies most relevant to this research, Ismaya (2010) evaluated DInSAR for monitoring subsidence due to underground coal mining in Utah using C-band (6-cm wavelength) and L-band (24-cm wavelength) data. This study demonstrated that the accuracy of subsidence measured by DInSAR depends on the radar band, the spatial baseline, and the temporal resolution. Notably, there are no studies evaluating the application of DInSAR using X-band radar in mining districts in the western United States. Because the results of DInSAR are band dependent, evaluating the effectiveness of X-band DInSAR for measuring subsidence in mining regions in the Mountain West is significant and is one objective of this research. As additional objectives, this research aims to map subsidence using DInSAR to better define the progression of subsidence over time and to explore possible relationships between subsidence and MIS in the Wasatch Plateau and the Green River Basin. There have been studies investigating

relationships between mine subsidence and MIS, including studies evaluating deformation and MIS related to the 2007 Crandall Canyon mine collapse (Plattner et al. 2010; Lu and Wicks 2010), but relationships between subsidence and seismicity in both the Wasatch Plateau and the Green River Basin are relatively unexplored.

3.3 Fundamental Concepts of Synthetic Aperture Radar (SAR) Imaging

SAR systems operate in the microwave portion of the electromagnetic spectrum, typically with centimeter-level wavelengths. Though SAR sensors are most commonly described by a wavelength, they can equally be described by a frequency, which is related to the wavelength by the speed of light, approximately 300 Mm/s. The wavelengths and frequencies of the most common radar bands used for satellite-based SAR are listed in Table 3.2. Like all electromagnetic waves, in addition to wavelength and frequency, radar waves have amplitude, polarization, and phase characteristics (Rosen 2014).

As shown in Figure 3.2, in SAR imaging, a satellite carries a radar sensor along a curvilinear track. The direction of travel is defined as the along-track, or azimuth, direction of the radar system. A radar signal, generated by a side looking antenna, is transmitted toward the earth's surface at a regular interval, defined as the pulse repetition frequency. With each pulse, a narrow strip of ground is illuminated in the cross-track, or range, direction of the radar system. Because the distance from the sensor to the imaged terrain is variable—the sensor is closer to the terrain in the near swath and further from the terrain in the far swath—each radar pulse sweeps across the swath (Richards 2009; Simons and Rosen 2007).

As the radar signal sweeps across the swath, it interacts with structures on the

surface of the earth and is scattered back to the antenna with the amplitude, polarization, and phase of the signal changed (Rosen 2014). Amplitude and polarization changes primarily result from interactions between the radar signal and surface features. These features are often called scatterers because they scatter the radar signal. Phase changes depend both on a random component due to the interaction of the signal with scatterers and on the distance from the sensor to the surface (Buckley 2000; Simons and Rosen 2007).

In each region on the ground resolved by the radar system, known as a resolution element or pixel, scatterers are randomly distributed, and the length of the radar path to each scatterer is variable. This geometry is illustrated in Figure 3.3, where ρ represents the constant range from the sensor to the resolution element and $\delta\rho_k$ represents the variable path length to each scatterer. For each resolution element, the complex radar return, E_{rec}, the sum of the propagation phase delay and the coherent backscatter, can be expressed by:

$$E_{rec} = \sum_k E_k \, e^{i(\omega t + \Phi_0 + \phi_k)} = e^{i(\omega t + \Phi_0)} \sum_k E_k \, e^{i\phi_k} \tag{3.1}$$

where ω is the radian frequency, t is the time, and Φ_0 is the propagation phase. The term $e^{i(\omega t + \Phi_0)}$ is common to all of the radar ray paths. E_k and ϕ_k are the backscatter amplitude and phase for each of the k scatterers. Because of the random contribution to the amplitude and phase from the scatterers in each resolution element, radar images are speckled—there is significant amplitude and phase variation from pixel to pixel. Speckle appears like noise, but it is an inherent property of SAR images and results from the

coherent interaction of the radar signal with random scatterers (Richards 2009).

3.3.1 Range Resolution

In SAR imaging, it is often important that the radar systems have high resolution so that scatterers that are relatively close together, often on the order of a meter or less, can be distinguished. To resolve radar images in the range direction, radar pulses are chirped, meaning the frequency of the pulse is varied linearly in time. Matched filtering, where the returned signal is correlated with the transmitted signal, is used to compress the ranging pulses and resolve closely spaced scatterers. The magnitude of the range resolution is determined by the chirp bandwidth, the change in frequency of the radar pulse. The slant range resolution, the resolution along the look direction of the satellite, is defined by:

$$\Delta\rho = \frac{c}{2\mathcal{B}_c} \tag{3.2}$$

where $\Delta\rho$ is the slant range resolution in m, c is the speed of light in m/s, and $\mathcal{B}_c$ is the chirp bandwidth in Hz. Often, range resolution is more usefully expressed as the ground range resolution, given by:

$$\Delta g = \frac{\Delta\rho}{\sin\theta} \tag{3.3}$$

where Δg is the ground range resolution in m, $\Delta\rho$ is the slant range resolution in m, and

θ is the incidence angle, the angle between line of sight and the normal to surface, illustrated in Figure 3.4 (Richards 2009; Rosen 2014).

3.3.2 Azimuth Resolution

Radar images must also be resolved in the azimuth direction. The azimuth resolution depends on the beamwidth of the radar antenna, where beamwidth is inversely proportional to antenna length. In general, it is not practical for satellite-based SAR systems to have antennas long enough to achieve meter level azimuth resolution. To achieve high azimuth resolution, long antennas (apertures) are synthetized using the forward motion of the satellite, and the length of the synthetic aperture is defined by the time that a scatterer is illuminated. This concept is illustrated in Figure 3.4. The forward motion of the satellite causes a Doppler shift—a frequency change—in the returned signal as a target is repeatedly illuminated: the frequency of a return signal increases as satellite moves toward the target and decreases as the satellite moves away from the target. This variable frequency creates a Doppler-induced chirp and, like range compression, matched filtering can be applied to compress the returned signal and resolve closely spaced targets in the azimuth direction. Azimuth resolution, Δx, in m can be expressed by:

$$\Delta x = \frac{v}{\mathcal{B}_c} = \frac{l_a}{2} \tag{3.4}$$

where v is radar platform along-track velocity in m/s, $\mathcal{B}_c$ is the Doppler chirp bandwidth

in Hz, and l_a is the real antenna length in the azimuth direction in m (Richards 2009; Rosen 2014).

3.3.3 Scattering

Radar imaging is dependent on scattering, the reflection of incident energy by features on the surface of the earth, and how energy scatters depends strongly on the surface characteristics. There are typically three scattering mechanisms: surface scattering, volume scattering, and hard target scattering. Surface scattering occurs when energy is reflected from a well-defined interface. In volumetric scattering, energy is reflected from a large number of scatterers; the interaction with individual scatterers is multifaceted. Hard target scattering occurs when radiated energy interacts with a discrete, strong reflector and results in relatively strong backscattered signal (Richards 2009).

Overall, the strength of the backscattered signal depends on the type of scattering, which is affected by the surface characteristics, and on the wavelength, polarization, and the incidence angle of the radar signal. The dielectric properties of the surface materials are an important characteristic related to backscatter strength, and materials with larger dielectric constants generally have stronger backscatter. Water has a large dielectric constant, and the reflectively of soil strongly depends on the saturation level. Notably, calm bodies of water typically act as specular surfaces, scattering the signal away from the sensor (Richards 2009).

Surface roughness is another important characteristic for scattering, and rougher surfaces tend to generate stronger backscatter. However, surface roughness is dependent on the radar band: radar waves tend to interact more strongly with structures similar in

size to the radar wavelength. Surfaces typically look rougher at X-band, which has a shorter wavelength, than at L-band, which has a longer wavelength. Additionally, radar signals with longer wavelengths tend to have some penetration of vegetation, dry soils, and ice; phase measurements from longer wavelengths tend to be less sensitive to small changes in the surface conditions over time (Rosen 2014).

Because the surface characteristics can change the polarization of the radar signal, the polarization of the transmitted and received radar signals affect the measured backscatter. Radar signals that are co-polarized, where a horizontally (vertically) polarized signal is transmitted and a horizontally (vertically) polarized signal is received, typically have stronger responses than radar signals that are cross-polarized, where horizontally (vertically) polarized signal is transmitted and a vertically (horizontally) polarized signal is received. Though the strength of the backscattered signal depends on the type of scattering, the surface characteristics, and the properties of the transmitted radar signal, typically only a small percentage of the incident energy is backscattered (Richards 2009).

Finally, because the polarization, amplitude, and phase of the radar signal are changed by interaction with the surface, the properties of the backscattered signal are indicative of the surface characteristics. Directly interpreting the phase and amplitude of the backscattered signal from each pixel is difficult because the images are speckled. Even for pixels with similar surface composition, random phase and amplitude variation from pixel to pixel can mask the intrinsic backscatter. To reduce speckle, radar images are often multilooked, or spatially averaged. Multilooking the images reduces the resolution, but it helps define the natural backscatter characteristics (Rosen 2014).

3.3.4 Geometric Distortion

In radar imaging, the three-dimensional world is collapsed into two dimensions, and images have geometric and radiometric distortions. Figure 3.5 illustrates three types of geometric distortion, layover, foreshortening, and shadow, as well as the effects of the surface geometry on the magnitude, or brightness, of the radar response. Layover occurs along steep slopes, where the radar backscatter from the top of the slope arrives at the receiver before the backscatter from the base of the slope. As a result, in the image, the slope appears collapsed or laid over. The geometry of the surface also affects the radar response, and topography affected by layover appears bright—there is significant backscatter. Sloped topography is also affected by foreshortening, where the slopes facing the radar appear shortened and the slopes facing away from the radar appear lengthened, and in general, the slopes appear displaced toward the radar. If the height of the topography is known, displacement can be calculated and corrected. Again the geometry of the surface affects the radar response: slopes facing the radar appear brighter, where the signal is backscattered more strongly, and slopes facing away from the radar appear darker due to less radar backscatter. Shadowing, where the back face of a slope is not illuminated by the radar, is another source of image distortion. Shadowing cannot be corrected, but it is less severe at small angles of incidence (Richards 2009).

3.4 Interferometric Synthetic Aperture Radar (SAR)

The data in radar images are complex; they have both amplitude, which measures the strength of the backscatter, and phase, which indicates the state of vibration of the backscattered wave (Massonnet and Souyris 2008). In radar interferometry, the

differences in the phases of nearly coincident radar images are used to precisely measure relative distances (Rosen 2014). Figure 3.6 illustrates a single antenna, repeat-pass interferometer geometry, where the image acquisitions are separated spatially in the cross-track direction and temporally. In Figure 3.6, A_1 represents an antenna at height h imaging a target at height z. The antenna look angle is θ and the one-way range between the antenna, A_1, and the surface is ρ. A_2 represents the same antenna imaging the same point from a different cross-track location. The acquisitions are separated by the baseline B at the angle α, measured relative to horizontal. The one-way range between the antenna, A_2, and the surface is $\rho + \delta\rho$. The change in range, $\delta\rho$, from A_1 to A_2 is primarily dependent on the topography, but it can be affected by surface deformation and variation in the atmospheric composition (Buckley 2000).

In interferometry, the complex data from one image are multiplied by the complex conjugate of the data from a second, nearly coincident image, forming an interferogram. This multiplication eliminates the common backscatter phase in each pixel, leaving the phase proportional to the path difference, the interferometric phase (Simons and Rosen 2007). For each pixel, the total change in phase of the signal, from when it is transmitted to when it is received, depends on the two-way range between the antenna and the surface. This relationship can be expressed by:

$$\phi_t = \frac{2\pi}{\lambda} 2\rho \tag{3.5}$$

where ϕ_t is the total change in the phase in radians, ρ is the one-way range between the antenna and the imaged surface in m, and λ is the carrier wavelength in m (Richards

2009). Using the interferometer geometry from Figure 3.6, the phase change between two images, which results from the differential path, can be expressed by:

$$\Delta\phi = \frac{2\pi}{\lambda}[2(\rho + \delta\rho) - 2\rho] = \frac{4\pi}{\lambda}\delta\rho \tag{3.6}$$

where $\Delta\phi$ is interferometric phase in radians and $\delta\rho$ is the differential range in m (Buckley 2000).

3.4.1 Topographic Mapping (InSAR)

Using the phase difference between two images acquired from slightly different locations at different times, InSAR can be applied to determine the surface topography. However, it is important that there are no changes in the surface properties or atmospheric composition that could affect the scattering characteristics, and also that there are no changes in surface elevation in the time between the radar image acquisitions (Burgmann et al. 2000). When the backscatter is constant and the surface elevation is stable, the interferometric phase is directly proportional to the range difference between the imaging locations, which can be expressed in terms of the baseline *B,* the vector separating the two imaging locations, shown Figure 3.6. Assuming the baseline, *B*, is much smaller than the range, ρ, the length of the path difference can be approximated by:

$$\delta\rho \approx -B\sin(\theta - \alpha) \tag{3.7}$$

From Equation 3.6 and 3.7, the interferometric phase, $\Delta\phi$, is approximated by:

$$\Delta\phi \approx -\frac{4\pi}{\lambda} B \sin(\theta - \alpha) \tag{3.8}$$

where θ is the look angle and α is the angle of the baseline relative to horizontal.

Based on Equation 3.8, the interferometric phase depends on the baseline, which is constant, and the look angle, which varies across the swath and is affected by the topography (Buckley 2000; Simons and Rosen 2007). In interferograms, there is a large phase gradient across the swath caused by variation in the look angle. To evaluate the effect of topography on the interferometric phase, the phase gradient due to the variation in the look angle must be removed. This phase gradient is removed by flattening, subtracting the expected interferometric phase produced by a surface of constant elevation from the total interferometric phase.

Using the interferometer geometry illustrated in Figure 3.6, the look angle, θ, can be expressed by:

$$\theta = \theta_o + \delta\theta \tag{3.9}$$

where θ_o is the look angle to a reference surface at range ρ and $\delta\theta$ is the additional contribution to the look angle due to the topography (Simons and Rosen 2007). Assuming that $\delta\theta$ is small, the flattened interferometric phase, $\Delta\phi_{flat}$, can be expressed as:

$$\Delta\phi_{flat} = -\frac{4\pi}{\lambda} B[\sin(\theta - \alpha) - \sin(\theta_o - \alpha)] \approx -\frac{4\pi}{\lambda} B \cos(\theta - \alpha)\, \delta\theta \tag{3.10}$$

Approximating $\delta\theta$ by:

$$\delta\theta \approx \frac{z}{\rho \sin(\theta_o)} \tag{3.11}$$

where z represents the height of the topography above the reference surface in m, the flattened interferometric phase, $\Delta\phi_{flat}$, can be reduced to:

$$\Delta\phi_{flat} \approx -\frac{4\pi}{\lambda} B\cos(\theta - \alpha) \frac{z}{\rho \sin(\theta_o)} \approx -\frac{4\pi}{\lambda} B_{\perp} \frac{z}{\rho \sin(\theta_o)} \tag{3.12}$$

where $B\cos(\theta - \alpha)$ is the baseline component perpendicular to the look angle, commonly referred to as the perpendicular baseline, $B_{\perp}$(Buckley 2000; Burgmann et al. 2000; Rosen 2014; Simons and Rosen 2007).

From Equation 3.12, the flattened interferometric phase is directly proportional to the topographic height and this relationship can be used to generate topographic maps. The flattened phase is also directly proportional to the perpendicular baseline, so a larger perpendicular baseline will generate stronger phase variation for a given topographic change, which can make the phases easier to interpret topographically (Simons and Rosen 2007). If the perpendicular baseline is too large, the phases change too rapidly with variation in the topography and become ambiguous. The effect of the perpendicular baseline on the phase variation is quantified by the ambiguity height, the amount of topographic variation required to change the interferometric phase by a full 2π cycle (Burgmann et al. 2000). The ambiguity height, h_a, can be expressed as:

$$h_a = -\frac{\lambda}{2}\frac{\rho \sin(\theta_o)}{B_\perp} \tag{3.13}$$

3.4.2 Deformation Mapping (DInSAR)

When there are changes in surface topography in the time between the radar images, the displacement contributes to the interferometric phase and DInSAR can be applied to quantify the displacement. An interferometer geometry, with surface displacement, is illustrated in Figure 3.7, and in this case the flattened interferometric phase is described by:

$$\Delta\phi_{flat} = -\frac{4\pi}{\lambda}B_\perp \frac{z}{\rho \sin(\theta_o)} + \frac{4\pi}{\lambda}\Delta\rho_d \tag{3.14}$$

where $\Delta\rho_d$ is the change in the range due to displacement in m. Like Equation 3.12, the flattened interferometric phase in Equation 3.14 includes a topographic contribution, represented by the first term. In addition to the topographic term, Equation 3.14 includes a term that defines the interferometric phase resulting from surface displacement.
In DInSAR, the topographic contribution to the interferometric phase is synthesized, using an independent digital elevation model, and subtracted from the flattened interferometric phase. With the topographic contribution removed, the change in the range due to displacement is directly proportional to the flattened interferometric phase:

$$\Delta\phi_{flat} = \frac{4\pi}{\lambda}\Delta\rho_d \tag{3.15}$$

Based on Equation 3.14, because the perpendicular baseline, $B_{\perp}$, is much smaller than the range, ρ, the flattened interferometric phase is much more sensitive to displacement than to topography and the topographic contribution depends strongly on the baseline. If the baseline is zero—there is no spatial separation between the image acquisitions—the topography has no influence on the flattened interferometric phase. Usually, there is some baseline separation between image acquisitions, and the quality of the calculated displacements depends on the quality of the reference elevation model and on how well the topographic phase is synthesized (Buckley 2000; Burgmann et al. 2000; Simons and Rosen 2007).

3.4.3 Phase Unwrapping

In general the phase due to topography or deformation varies over a large range, but because of how the phases are expressed mathematically, measured interferometric phases are restricted to the range from zero to 2π. So, while the physical phases are fairly continuous, in interferograms the phases are wrapped—there are step changes for every full cycle of 2π. To evaluate the topography or deformation in absolute terms, the interferometric phases must be unwrapped. Phase unwrapping is critical for accurately quantifying elevation or deformation, but it is nontrivial and requires independent information, like ground control points, so the phases are correctly associated with elevations or deformations. Additionally, geometric distortions, including layover and shadowing, can lead to noncontinuous phases and can confound the phase unwrapping process (Richards 2009; Burgmann et al. 2000).

3.4.4 Interferometric Limitations

In interferometry, the phases strongly depend on topography and displacement. However, interferometric phases can be affected by other factors leading to measurement and interpretation errors. The concept of correlation is important for describing interferometric errors and limitations. When radar images are acquired with small baselines, the propagation phases of the pixels change, but the backscatter phases and amplitudes are nearly the same. Correlation is a measure of the sameness of the backscattered signals. As a statistic, the correlation coefficient, or coherence, ranges from zero to one, where one represents perfect correlation and zero indicates the signals are completely decorrelated (Richards 2009).

Any mechanism that significantly changes the random backscatter phase of a pixel can lead to some level of decorrelation. Thermal noise and baseline, rotational, and temporal decorrelation are some of the most significant sources of decorrelation in interferometry. Thermal noise decorrelation is a result of thermal noise generated by the radar receiver and contributes a random phase from pixel to pixel. Baseline decorrelation is a geometric effect; as the perpendicular baseline of the interferometer increases, changes in the backscatter characteristics become significant leading to decorrelation. Baseline decorrelation can be quantified by the critical baseline, $B_{critical}$, the perpendicular baseline where the images completely decorrelate. The critical baseline is often expressed as:

$$B_{critical} = \frac{\lambda \rho \tan \theta}{\Delta \rho} \tag{3.16}$$

From Equation 3.16, interferometers with finer range resolution, $\Delta\rho$, and longer wavelengths, λ, have larger critical baselines and are less affected by baseline decorrelation. Rotation decorrelation is also a geometric effect, where changes in the backscatter characteristics result from changes in the azimuth geometry. Finally, temporal decorrelation results from physical changes in the scatterers over time and is a significant source of decorrelation in repeat-pass interferometry (Burgmann et al. 2000; Rosen 2014).

In addition to decorrelation, significant phase errors in interferometry can be generated by changes in the atmospheric composition, primarily changes in the atmospheric water content. Changes in the atmospheric composition affect the radar propagation velocity and lead to significant interferometric phase shifts. In general, the atmospheric phase noise is not distinguishable from the interferometric phase due to surface displacements, and as a result, the atmospheric phase contribution can mask deformation. In repeat pass interferometry, where there are significant changes in the atmospheric composition between image acquisitions, atmospheric phase noise can be a limiting effect (Burgmann et al. 2000).

TABLE 3.1 Planned SAR satellites and radar bands

Satellite	Expected Launch	Band
CSG-1	2016	X
CSG-2	2017	X
HRWS SAR	2022	X
PAZ	2015	X
TSX-NG	2018	X
RADARSAT C-1	2018	C
RADARSAT C-2	2018	C
RADARSAT C-3	2018	C
Sentinel-1 B	2015	C
NISAR	2020	L, S
SAOCOM 1A	2015	L
SAOCOM 1B	2016	L
SAOCOM-2A	2019	L
SAOCOM-2B	2020	L

Source: Data from CEOS ESA 2015

TABLE 3.2 Common radar bands

Band	X	C	S	L	P
Wavelength, cm	3	6	12	24	75
Frequency, GHz	10	5	2.5	1.3	0.4

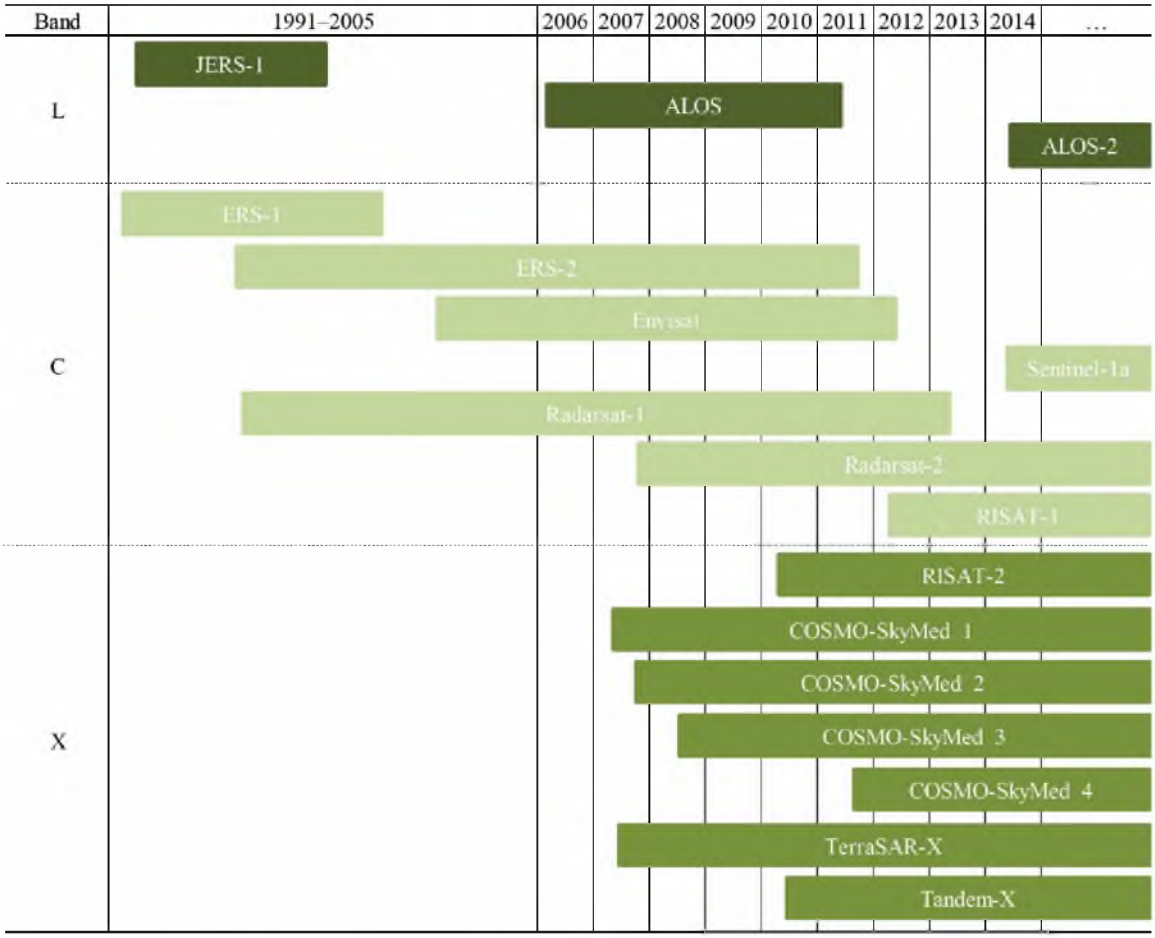

Source: Data from ALTAMiRA 2015 and CEOS ESA 2015

FIGURE 3.1 SAR satellites, approximate operational periods, and radar bands

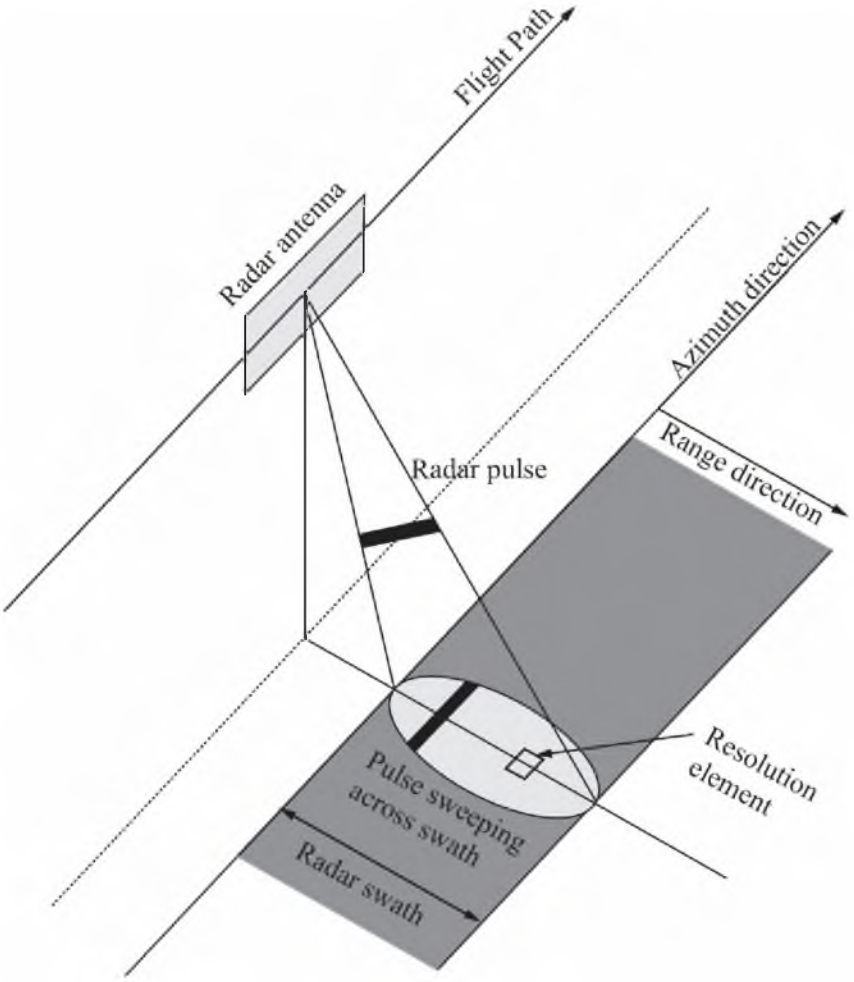

Source: Adapted from Richards 2009, Rosen et al. 2000, and Simons and Rosen 2007

FIGURE 3.2 Radar imaging

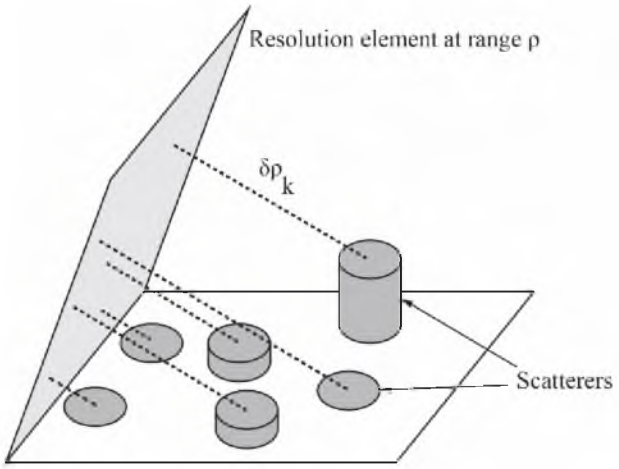

Source: Adapted from Buckley 2000 and Simons and Rosen 2007

FIGURE 3.3 Conceptual illustration of scattering

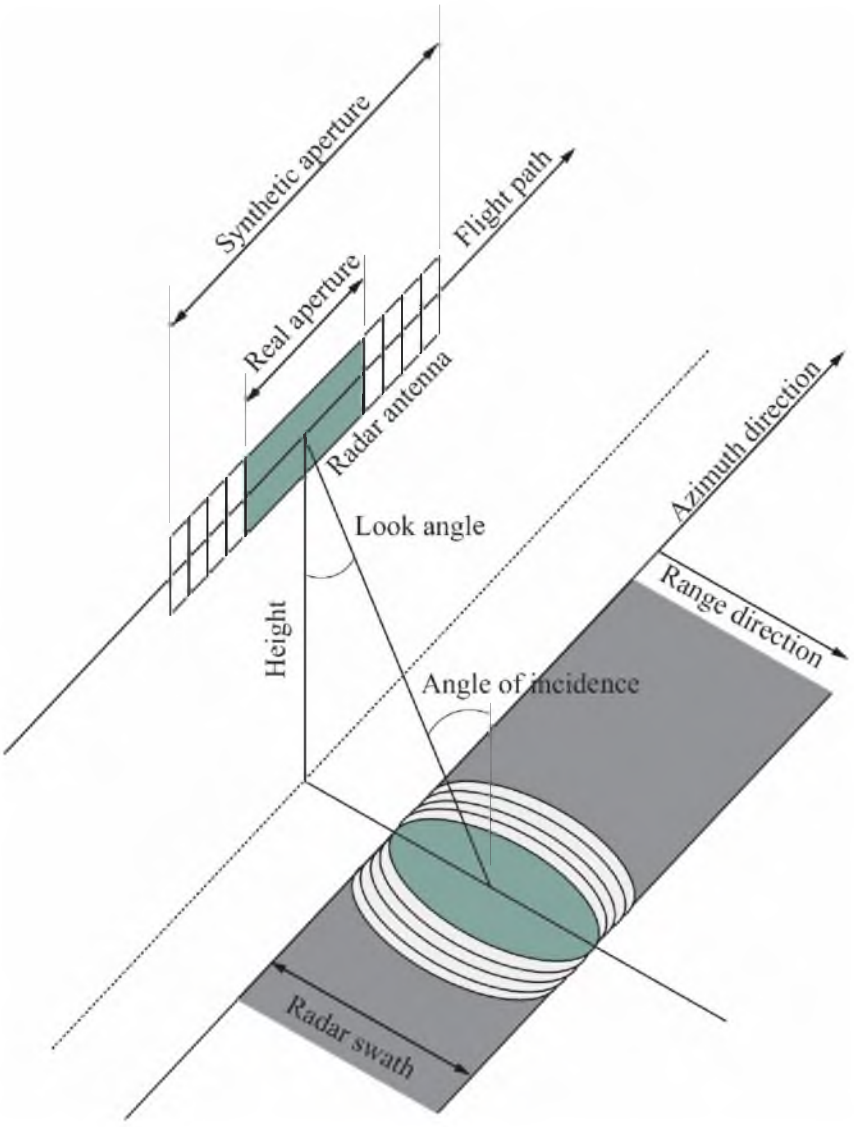

Source: Adapted from Richards 2009 and Rosen 2014

FIGURE 3.4 Synthetic aperture radar imaging

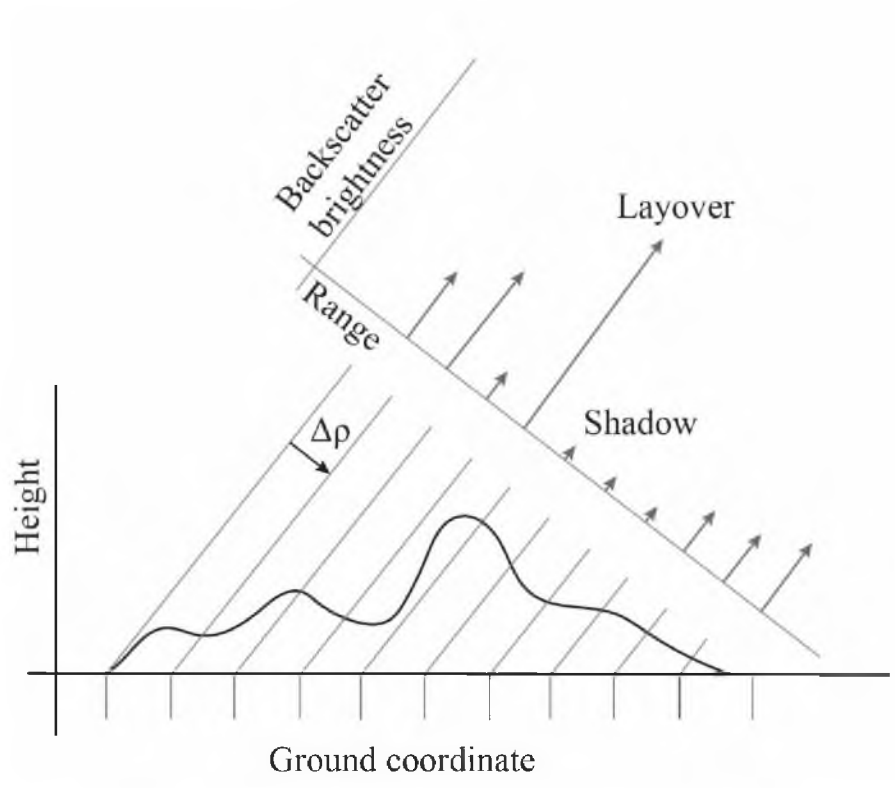

Source: Adapted from Rosen et al. 2000, Rosen 2014, and Simons and Rosen 2007

FIGURE 3.5 Illustration of radar image geometric and radiometric distortion ($\Delta\rho$ is the slant range resolution from Equation 3.2)

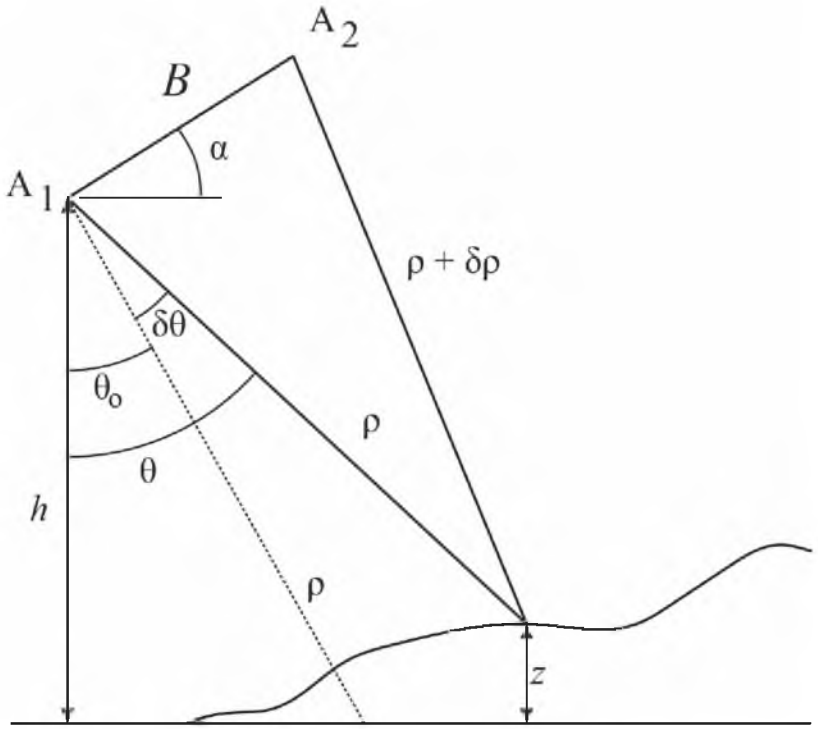

Source: Adapted from Buckley 2000, Richards 2009, Rosen et al. 2000, Rosen 2014, and Simons and Rosen 2007

FIGURE 3.6 Synthetic aperture radar interferometry imaging geometry

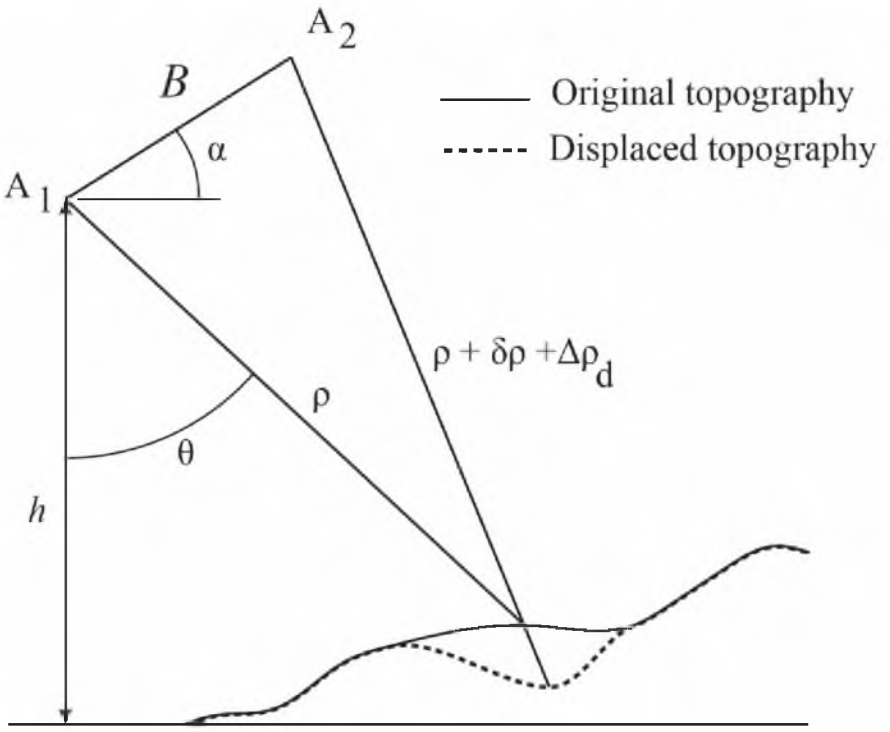

Source: Adapted from Buckley 2000, Richards 2009, Rosen et al. 2000, Rosen 2014, and Simons and Rosen 2007

FIGURE 3.7 Synthetic aperture radar interferometry imaging geometry with surface displacement

CHAPTER 4

INTERFEROMETRIC DATA CHARACTERISTICS AND PROCESSING

4.1 Introduction

Applying DInSAR for monitoring mine subsidence requires significant interferometric data processing. This chapter outlines the procedure for reducing SAR data from the Advanced Land Observing Satellite (ALOS) and TerraSAR-X mission using SARscape® and ENVI®. First, important characteristics of the satellites and of the data used in this study are presented. Next, significant processing steps are outlined. To generate a subsidence map, DInSAR processing steps include estimating the perpendicular and temporal baselines of paired images, coregistering the images and forming an interferogram, estimating the data coherence and filtering the interferogram, unwrapping the interferogram and determining the absolute interferometric phases, and calculating the vertical deformations and geocoding the data (SARscape® 2014).

4.2 Advanced Land Observing Satellite (ALOS) Characteristics

ALOS was operated by the Japanese Aerospace Exploration Agency (JAXA) from 2006 to 2011, and acquired data globally with a minimum recurrence cycle of 46 days. For radar imaging, ALOS used a fully polarimetric Phased Array type L-band

Synthetic Aperture Radar (PALSAR) with a 1.27-GHz carrier frequency (23.6-cm wavelength). The data used in this study were imaged in fine-beam mode with both single and dual polarization; only the co-polarized images were used in interferometric processing. These data have swath widths of 70 km, azimuth resolutions of 10 m, and ground range resolutions of 10 m and 20 m for single and dual polarizations, respectively (Rosenqvist et al. 2004).

The ALOS data were acquired from the Alaska Satellite Facility (ASF) as unprocessed images with the radar responses spread in azimuth and range (ASF 2015). Before interferometric processing, the data were imported into SARscape® and focused to form Single Look Complex (SLC) images with the radar responses compressed into complex valued pixels with a phase and a radiometrically uncalibrated amplitude (SARscape® 2014). Characteristics of the central Utah data are given in Table 4.1 and characteristics of the southwest Wyoming data are given in Table 4.2. These tables include the orbit path, frame, number, and pass direction, and the acquisition date, polarization, and look angle for each image.

4.3 TerraSAR-X Characteristics

The TerraSAR-X mission is operated by the German Aerospace Center (DLR) and uses two satellites: TerraSAR-X (TSX-1), launched in 2007, and TanDEM-X (TDX-1), launched in 2010. These satellites use fully polarimetric X-band sensors with 9.65-GHz carrier frequencies (3.1-cm wavelengths) and acquire data with minimum recurrence cycles of 11 days. For this study, data were imaged in stripmap mode with single horizontal polarization. The images have 30-km swath widths and maximum

ground resolutions of 3.3 m in azimuth and 1.7 m in range (DLR 2013). The data were acquired from DLR as Single Look Slant Range Complex (SSC) images, which are focused and radiometrically calibrated (DLR 2015), and these images only require import into SARscape® for interferometric processing. Characteristics of the central Utah data and the southwest Wyoming data, including the satellite, orbit number, orbit cycle, orbit pass direction, beam, acquisition date, and minimum and maximum incidence angles, are given in Tables 4.3 and 4.4, respectively.

4.4 Differential Interferometric Data Processing Using SARscape®

Fundamentally, SAR interferometry requires a pair of nearly coincident images. A master (reference) image, usually the earliest in time, is paired with a slave image to form an interferogram. Before generating interferograms, it is useful to estimate the perpendicular and temporal baselines of paired images because these parameters help to characterize the potential interferometric data quality. The critical baseline, the 2π ambiguity height, and the 2π ambiguity displacement are additional baseline parameters that are useful for defining the data quality. In SARscape®, all of the baseline parameters are calculated using *Baseline Estimation*. For this study, the baseline parameters for the ALOS data for the Utah and Wyoming regions are presented in Tables 4.5 and 4.6. The baseline parameters for the TerraSAR-X data for each region are presented in Tables 4.7 and 4.8.

For mine subsidence monitoring, interferograms with small perpendicular and short temporal baselines are often relatively good quality. These interferograms have limited topographic effects and tend to have relatively high coherence. DInSAR

processing can be performed on paired images with relatively large perpendicular baselines, but if the perpendicular baselines are too large, data coherence is lost. The critical baseline defines the maximum theoretical baseline where coherence is maintained and is a function of the incidence angle, which is strongly affected by topography and the radar wavelength. In this study, the perpendicular baselines of the interferometric data were at most 50% of the critical baselines. Additionally, image pairs with large baselines are more sensitive to topography, and this sensitivity is quantified by the 2π ambiguity height. Larger ambiguity heights indicate that more significant changes in elevation are necessary to cause 2π phase changes (fringes) in the interferograms. The 2π ambiguity displacement represents the sensitivity of an interferogram to displacement and is a direct function of the radar wavelength. At best, L-band SAR can measure deformation gradients of 0.118 m/pixel, or 0.006 m/m for 20-m pixels, and X-band SAR can measure deformation gradients of 0.016 m/pixel, or 0.009 m/m for 1.7-m pixels.

In SARscape®, once image pairs with suitable baseline characteristics are selected, multilooking parameters are specified and interferograms are formed using *Interferogram Generation.* Multilooking can reduce speckle, but it also reduces the spatial resolution of the interferograms. In this study, the TerraSAR-X images were not multilooked and were processed at full resolution. Short wavelength X-band data are very sensitive to surface deformation per pixel, and in areas of large deformation, the phases tend to saturate at lower spatial resolutions. Longer wavelength L-band data are less sensitive to deformation per pixel, and the ALOS images were multilooked to produce images with approximately 20 by 20-m pixels.

As part of the *Interferogram Generation* process, paired images are coregistered

to correct for relative translation shifts and rotational and scale differences, and an interferogram is formed by multiplying one image by the complex conjugate of the second image. An example of an interferogram is shown in Figure 4.1. This image was generated using TerraSAR-X data from Wyoming for the period from July 27 to August 7, 2015. It shows a region strongly affected by subsidence. The paired images used to generate this inteferogram have a spatial baseline of −10 m and the topographic effects are minimal. This interferogram is not flattened, and strong, regular phase fringes resulting from the acquisition geometry are apparent. Dense phase fringes due to surface displacement are also visible. Figures 4.2 through 4.6 show further processing stages and data for this region.

Once an interferogram is formed, it is flattened, creating a differential interferogram (Figure 4.2). In this process, phase shift due to the acquisition geometries and the phase shifts due to the topography are synthesized and removed. In this study, the topographic phases for all of the interferograms were synthesized using the National Elevation Dataset (NED) Digital Elevation Models (DEMs) with 10-m resolutions (National Map 2015). The DEMs were resampled to match the interferogram resolutions. In Figure 4.2, the topographic and geometric effects are removed and the phase fringes are due to subsidence. Each interferometric fringe, represented by a full color cycle, indicates 0.016 m displacement in the satellite look direction.

Coregistered master and slave intensity images, which quantify the strength of the backscatter signals, and differential interferograms are the primary results of *Interferogram Generation.* These images are used in the next stage of data processing: *Adaptive Filter and Coherence Generation.* In this step of image processing, a coherence

image is generated by calculating the similarity of the intensities and phases of the interferometric data. Like the baseline parameters, coherence is useful for quantifying the data quality, and for the data in this study, the average coherence values of each interferogram are given in Tables 4.5 through 4.8. Additionally, coherence is useful for data processing. Pixels below a coherence threshold where data are significantly decorrelated can be removed, or masked, from the images. Figure 4.3 shows an example of a coherence image. In this image, pixels with coherence near one are white and pixels with coherence near zero are black. Generally, because subsidence changes the phase of the signal, the coherence in areas affected by subsidence is reduced. In Figure 4.3, the area affected by subsidence has slightly lower coherence than the surrounding region, but the overall coherence in this entire image is relatively high.

Additionally, using *Adaptive Filter and Coherence Generation*, differential interferograms are spatially filtered to reduce the phase noise and enhance the structure of the interferometric fringes. In this study, two spatial filtering methods were used: boxcar filtering and adaptive filtering. Boxcar filtering is a low pass filtering method and applies a simple moving window to average the data. In adaptive filtering, a moving window is also used to average the data, but the dimension and shape of the filtering window are varied based on the coherence. In the TerraSAR-X data, the interferometric fringes due to subsidence tend to be high frequency and the spatial resolution of the data is high. For these data, boxcar filtering clarified the fringe structure, and an example of a boxcar filtered differential interferogram is shown in Figure 4.4. In the ALOS data, the interferometric fringes due to subsidence tend to be high frequency, but the spatial resolution of the data is low. For these data, boxcar filtering tended to distort the fringe

structure. So, to preserve the high frequency fringes and reduce the phase noise, these data were filtered adaptively.

To quantify the deformation represented by the fringes in differential interferograms, the 2π ambiguity of the fringes must be resolved by unwrapping the phases. In SARscape®, this process is carried out by *Phase Unwrapping* after the differential interferograms have been filtered. In general, phase unwrapping is nontrivial and the quality of phase unwrapping depends on the data coherence and the coherence continuity. All of the data in this study were unwrapped using a minimum cost flow algorithm (Costantini 1998), and an example of an unwrapped interferogram is presented in Figure 4.5.

Phase ambiguity is resolved by phase unwrapping, but because the unwrapping process is nontrivial, the unwrapped phases are generally offset from the absolute phases. In SARscape®, *Refinement and Re-flattening* is used to estimate the phase offset and to transform the relative phases into absolute phases. *Refinement and Re-flattening* also corrects potential orbital inaccuracies and removes phase ramps apparent in the unwrapped data. Importantly, ground control points with known positions and known displacements are required to determine the phase offset and correct the orbital inaccuracies. In SARscape® these points are defined using *Generate Ground Control Point File*. For this study, ground control points were defined for each interferogram at pixels with relatively high coherence that were far from residual topographic fringes and fringes caused by deformation. For each interferogram, at least seven ground control points, distributed over the images, were defined. These points were assumed to have no displacement.

In the final stage of interferometric data processing, *Phase to Displacement Conversion and Geocoding* converts the absolute unwrapped phases in radians to displacements in meters, and locates the data in cartographic space. For subsidence mapping, deformations measured in the satellite look directions are most often projected vertically. To accurately account for horizontal and vertical displacements using DInSAR, ground control points with known displacements are necessary, or coincident radar images must be acquired in ascending and descending orbits (Duro et al. 2013). However, because vertical displacements are usually the most significant component of subsidence, assuming that all of the displacements are vertical is practical. An example of a vertical deformation map is presented in Figure 4.6. This figure shows a maximum vertical subsidence of more than 0.16 m for the 11-day period from July 27 to August 7, 2015. The vertical displacement is contoured from 0 to −0.15 m with a 0.015-m increment.

Table 4.1 ALOS SAR data characteristics—Utah region

Orbit				Acquisition Date	Polarization	Look Angle, °
Path	Frame	Number	Pass Direction			
201	770	4,612	Ascending	December 6, 2006	Single	34.3
201	770	7,296	Ascending	June 8, 2007	Dual	34.3
201	770	8,638	Ascending	September 8, 2007	Dual	34.3
201	770	9,309	Ascending	October 24, 2007	Single	34.3
201	770	9,980	Ascending	December 9, 2007	Single	34.3
201	770	20,716	Ascending	December 14, 2009	Single	34.3
201	770	22,729	Ascending	May 1, 2010	Dual	34.3
201	770	23,400	Ascending	June 16, 2010	Dual	34.3
201	770	24,071	Ascending	August 1, 2010	Dual	34.3
201	770	24,742	Ascending	September 16, 2010	Dual	34.3
201	770	26,084	Ascending	December 17, 2010	Single	34.3
201	770	26,755	Ascending	February 1, 2011	Single	34.3

Table 4.2 ALOS SAR data characteristics—Wyoming region

Orbit				Acquisition Date	Polarization	Look Angle, °
Path	Frame	Number	Pass Direction			
198	820	5,210	Ascending	January 16, 2007	Single	34.3
198	820	9,907	Ascending	December 4, 2007	Dual	34.3
198	820	10,578	Ascending	January 19, 2008	Single	34.3
198	820	11,920	Ascending	April 20, 2008	Single	34.3
198	820	12,591	Ascending	June 5, 2008	Dual	34.3
198	820	13,262	Ascending	July 21, 2008	Dual	34.3
198	820	19,972	Ascending	October 24, 2009	Dual	34.3
198	820	22,656	Ascending	April 26, 2010	Single	34.3
198	820	23,327	Ascending	June 11, 2010	Dual	34.3
198	820	23,998	Ascending	July 27, 2010	Dual	34.3
198	820	24,669	Ascending	September 11, 2010	Dual	34.3
198	820	25,340	Ascending	October 27, 2010	Dual	34.3
198	820	26,682	Ascending	January 27, 2011	Single	34.3
198	820	27,353	Ascending	March 14, 2011	Single	34.3

Table 4.3 TerraSAR-X SAR data characteristics—Utah region

Satellite	Orbit			Beam	Acquisition Date	Incidence Angle, °	
	Number	Cycle	Pass Direction			Minimum	Maximum
TSX-1	159	265 / 44247	Descending	4R	June 7, 2015	22.4	25.5
TSX-1	159	266 / 44414	Descending	4R	June 18, 2015	22.4	25.5
TSX-1	159	268 / 44748	Ascending	4R	July 10, 2015	22.4	25.5
TSX-1	30	266 / 44285	Ascending	10R	June 10, 2015	36.1	38.5
TSX-1	30	267 / 44452	Ascending	10R	June 21, 2015	36.1	38.5
TSX-1	30	270 / 44953	Ascending	10R	July 24, 2015	36.1	38.5
TSX-1	30	271 / 45120	Ascending	10R	August 4, 2015	36.1	38.5
TSX-1	30	272 / 45287	Ascending	10R	August 15, 2015	36.1	38.5
TSX-1	30	273 / 45454	Ascending	10R	August 26, 2015	36.1	38.5
TSX-1	30	274 / 45621	Ascending	10R	September 6, 2015	36.1	38.5
TSX-1	30	275 / 45788	Ascending	10R	September 17, 2015	36.1	38.5
TSX-1	30	276 / 45955	Ascending	10R	September 28, 2015	36.1	38.5
TSX-1	30	277 / 46122	Ascending	10R	October 9, 2015	36.1	38.5
TDX-1	30	278 / 29559	Ascending	10R	October 20, 2015	36.1	38.5
TSX-1	30	279 / 46459	Ascending	10R	October 31, 2015	36.1	38.5
TSX-1	30	280 / 46623	Ascending	10R	November 11, 2015	36.1	38.5
TDX-1	30	281 / 30060	Ascending	10R	November 22, 2015	35.9	38.6

Table 4.4 TerraSAR-X SAR data characteristics—Wyoming region

Satellite	Orbit			Beam	Acquisition Date	Incidence Angle, °	
	Number	Cycle	Pass Direction			Minimum	Maximum
TSX-1	83	265 / 44171	Descending	8R	June 2, 2015	31.9	34.5
TSX-1	83	266 / 44338	Descending	8R	June 13, 2015	31.9	34.5
TSX-1	83	269 / 44839	Descending	8R	July 16, 2015	31.9	34.5
TSX-1	83	270 / 45006	Descending	8R	July 27, 2015	31.9	34.5
TSX-1	83	271 / 45173	Descending	8R	August 7, 2015	31.9	34.5
TSX-1	83	272 / 45340	Descending	8R	August 18, 2015	31.9	34.5
TSX-1	83	273 / 45507	Descending	8R	August 29, 2015	31.9	34.5
TSX-1	83	274 / 45674	Descending	8R	September 9, 2015	31.9	34.5
TSX-1	83	275 / 45841	Descending	8R	September 20, 2015	31.9	34.5
TSX-1	83	276 / 46008	Descending	8R	October 1, 2015	31.9	34.5
TSX-1	83	277 / 46175	Descending	8R	October 12, 2015	31.9	34.5
TSX-1	83	278 / 46342	Descending	8R	October 23, 2015	31.9	34.5
TSX-1	83	279 / 46509	Descending	8R	November 3, 2015	31.9	34.5

Table 4.5 ALOS interferometric data parameters—Utah region

Acquisition Dates			Elapsed Time, days	Baseline, m	Critical Baseline, m	2π Ambiguity Height, m	2π Ambiguity Displacement, m	Average Coherence
December 6, 2006	–	June 8, 2007	184	394	± 9,820	163	0.118	0.41
June 8, 2007	–	September 8, 2007	92	637	± 6,550	101	0.118	0.51
September 8, 2007	–	October 24, 2007	46	326	± 9,820	197	0.118	0.57
October 24, 2007	–	December 9, 2007	46	176	± 13,080	366	0.118	0.33
December 14, 2009	–	May 1, 2010	138	1,277	± 9,830	50	0.118	0.30
May 1, 2010	–	June 16, 2010	46	16	± 6,550	4,084	0.118	0.54
June 16, 2010	–	August 1, 2010	46	299	± 6,550	215	0.118	0.59
August 1, 2010	–	September 16, 2010	46	−43	± 6,540	1,480	0.118	0.63
September 16, 2010	–	December 17, 2010	92	575	± 9,830	112	0.118	0.36
December 17, 2010	–	February 1, 2011	46	596	± 13,100	108	0.118	0.43

Table 4.6 ALOS interferometric data parameters—Wyoming region

Acquisition Dates			Elapsed Time, days	Baseline, m	Critical Baseline, m	2π Ambiguity Height, m	2π Ambiguity Displacement, m	Average Coherence
December 4, 2007	–	January 19, 2008	46	526	± 9,830	122	0.118	0.39
January 19, 2008	–	April 20, 2008	92	1075	± 13,090	60	0.118	0.26
April 20, 2008	–	June 5, 2008	46	−67	± 9,830	964	0.118	0.44
June 5, 2008	–	July 21, 2008	46	−3273	± 6,550	20	0.118	0.46
July 21, 2008	–	October 24, 2009	460	493	± 6,540	130	0.118	0.43
October 24, 2009	–	April 26, 2010	184	1389	± 9,830	46	0.118	0.47
April 26, 2010	–	June 11, 2010	46	13	± 9,830	5082	0.118	0.51
June 11, 2010	–	July 27, 2010	46	377	± 6,550	171	0.118	0.54
July 27, 2010	–	September 11, 2010	46	158	± 6,550	407	0.118	0.60
September 11, 2010	–	October 27, 2010	46	423	± 6,550	152	0.118	0.53
October 27, 2010	–	January 27, 2011	92	743	± 9,830	87	0.118	0.29
January 27, 2011	–	March 14, 2011	46	756	± 13,110	85	0.118	0.28

Table 4.7 TerraSAR-X interferometric data parameters—Utah region

Orbit	Acquisition Dates			Elapsed Time, days	Baseline, m	Critical Baseline, m	2π Ambiguity Height, m	2π Ambiguity Displacement, m	Average Coherence
159	June 7, 2015	–	June 18, 2015	11	81	± 3,410	42	0.016	0.52
159	June 18, 2015	–	July 10, 2015	22	−178	± 3,410	19	0.016	0.50
30	June 10, 2015	–	June 21, 2015	11	−88	± 6,530	67	0.016	0.58
30	June 21, 2015	–	July 24, 2015	33	−37	± 6,530	157	0.016	0.54
30	July 24, 2015	–	August 4, 2015	11	14	± 6,530	405	0.016	0.58
30	August 4, 2015	–	August 15, 2015	11	−16	± 6,530	366	0.016	0.60
30	August 15, 2015	–	August 26, 2015	11	−44	± 6,530	135	0.016	0.66
30	August 26, 2015	–	September 6, 2015	11	−55	± 6,530	106	0.016	0.60
30	September 6, 2015	–	September 17, 2015	11	142	± 6,530	41	0.016	0.61
30	September 17, 2015	–	September 28, 2015	11	−25	± 6,530	237	0.016	0.61
30	September 28, 2015	–	October 9, 2015	11	−16	± 6,530	365	0.016	0.60
30	October 9, 2015	–	October 20, 2015	11	282	± 6,530	21	0.016	0.55
30	October 20, 2015	–	October 31, 2015	11	−360	± 6,530	16	0.016	0.54
30	October 31, 2015	–	November 11, 2015	11	82	± 6,530	72	0.016	0.60
30	November 11, 2015	–	November 22, 2015	11	90	± 6,530	65	0.016	0.56

Table 4.8 TerraSAR-X interferometric data parameters—Wyoming region

Orbit	Acquisition Dates			Elapsed Time, days	Baseline, m	Critical Baseline, m	2π Ambiguity Height, m	2π Ambiguity Displacement, m	Average Coherence
83	June 2, 2015	–	June 13, 2015	11	−155	± 5,430	33	0.016	0.68
83	June 13, 2015	–	July 16, 2015	33	4	± 5,430	1,170	0.016	0.55
83	July 16, 2015	–	July 27, 2015	11	−83	± 5,430	61	0.016	0.62
83	July 27, 2015	–	August 7, 2015	11	−10	± 5,430	520	0.016	0.75
83	August 7, 2015	–	August 18, 2015	11	−16	± 5,430	317	0.016	0.76
83	August 18, 2015	–	August 29, 2015	11	64	± 5,430	80	0.016	0.75
83	August 29, 2015	–	September 9, 2015	11	−60	± 5,430	85	0.016	0.73
83	September 9, 2015	–	September 20, 2015	11	−42	± 5,430	120	0.016	0.74
83	September 20, 2015	–	October 1, 2015	11	97	± 5,430	52	0.016	0.76
83	October 1, 2015	–	October 12, 2015	11	42	± 5,430	122	0.016	0.75
83	October 12, 2015	–	October 23, 2015	11	−191	± 5,430	27	0.016	0.76
83	October 23, 2015	–	November 3, 2015	11	111	± 5,430	46	0.016	0.78

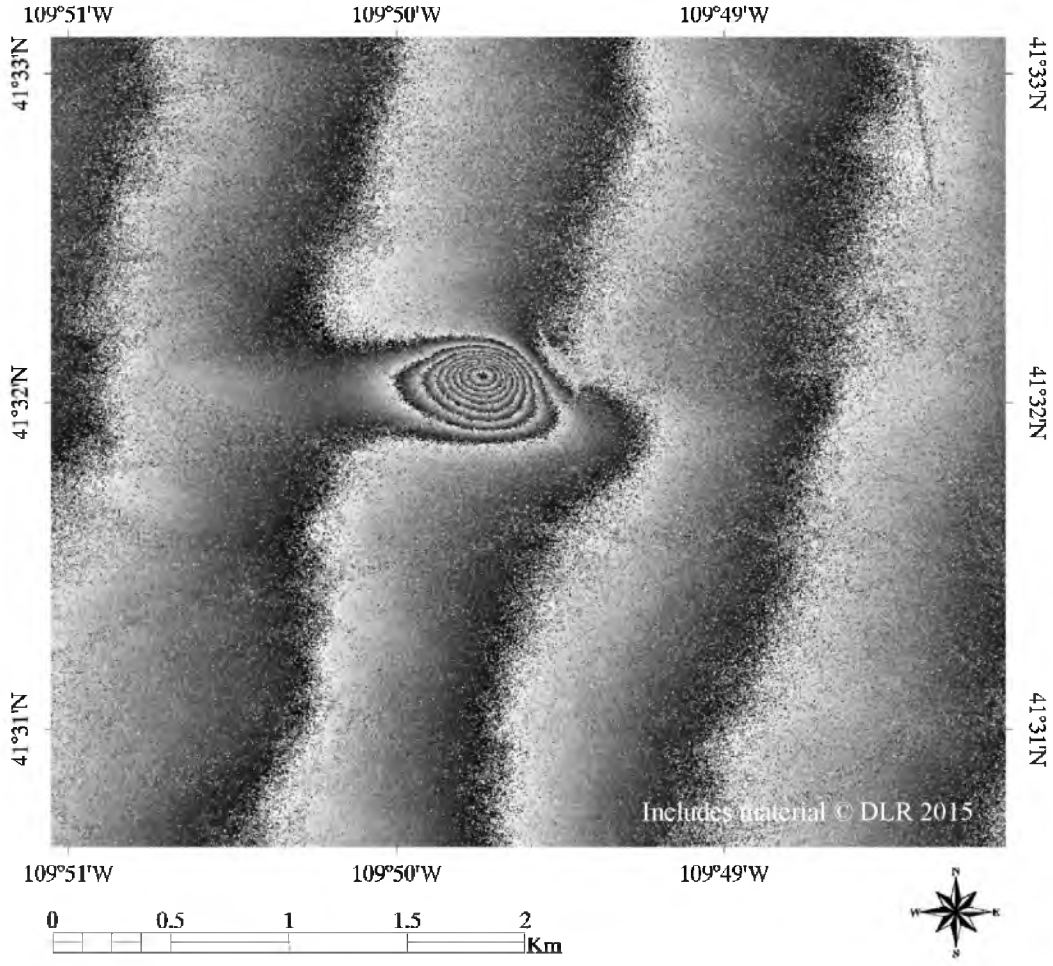

FIGURE 4.1 Interferogram (X-band) from the southwest Wyoming region: July 27, 2015 to August 7, 2015

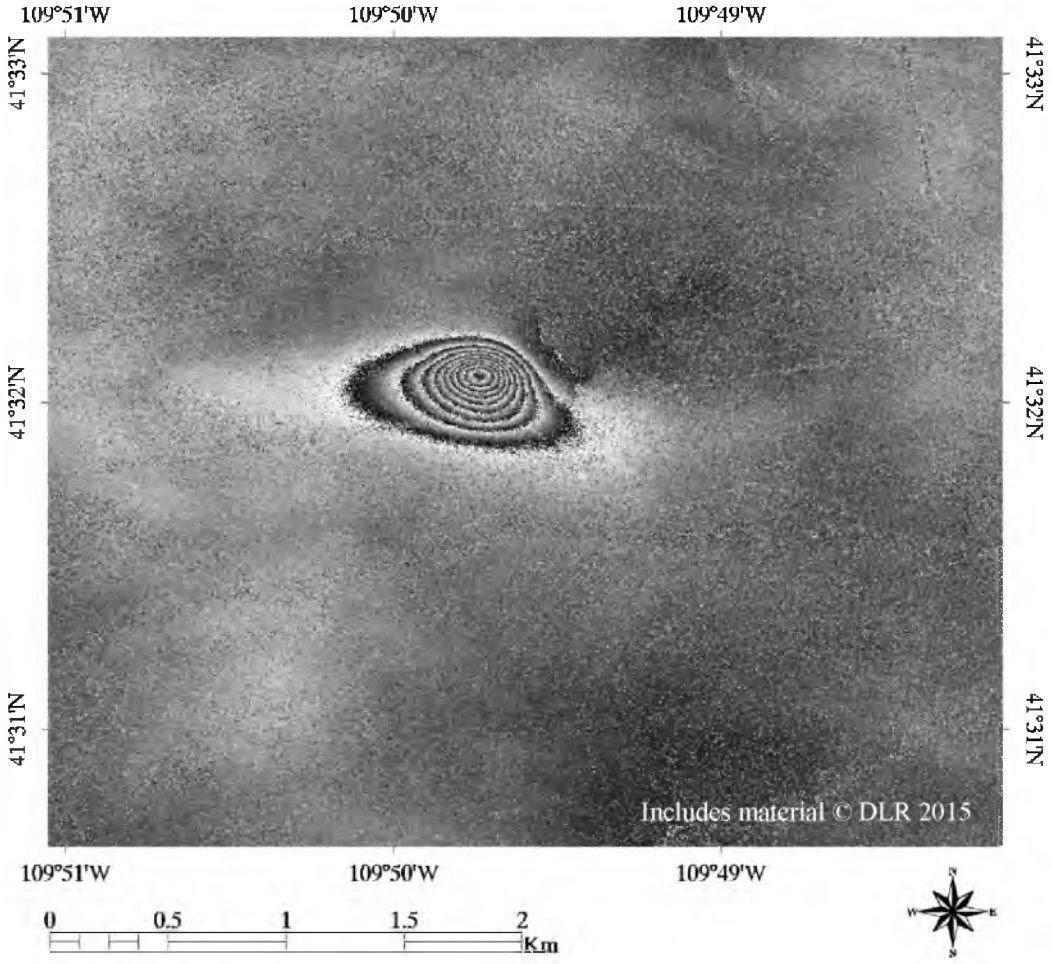

FIGURE 4.2 Differential interferogram (X-band) from the southwest Wyoming region: July 27, 2015 to August 7, 2015

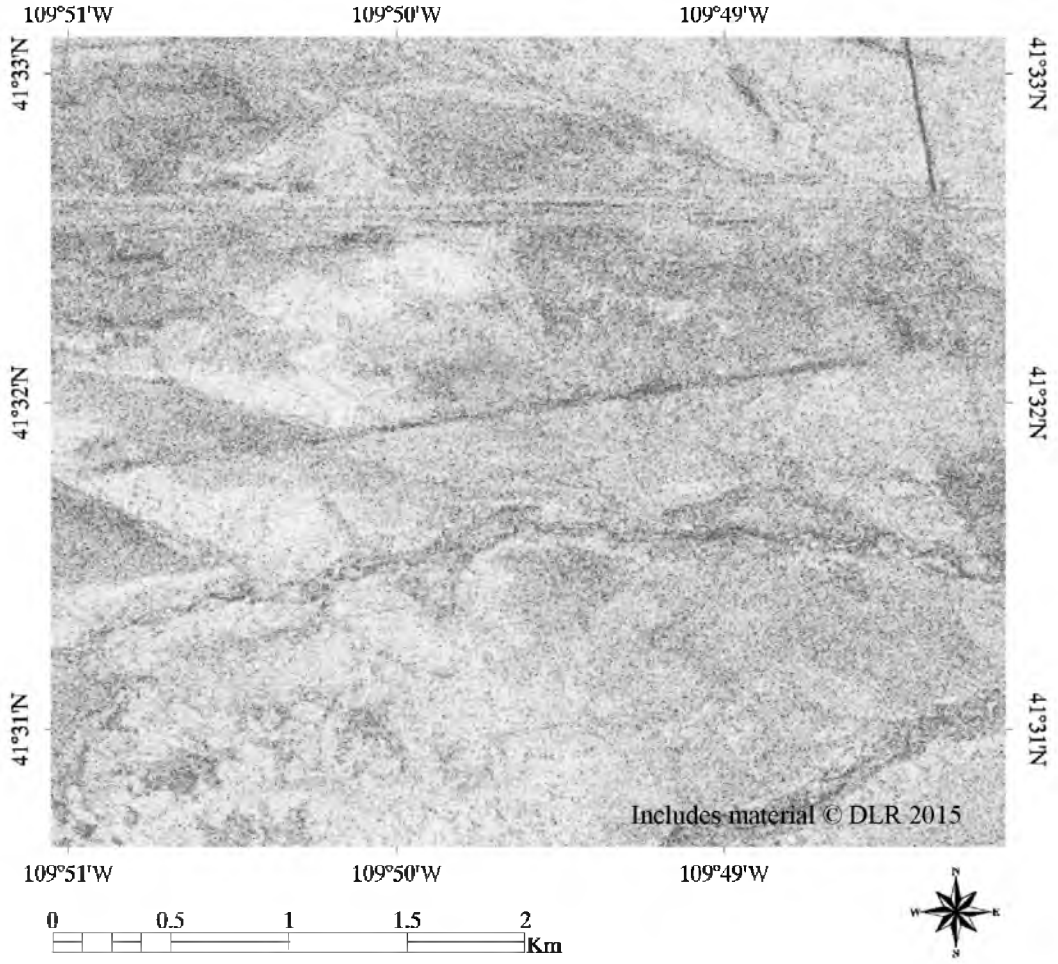

FIGURE 4.3 Coherence data (X-band) from the southwest Wyoming region: July 27, 2015 to August 7, 2015

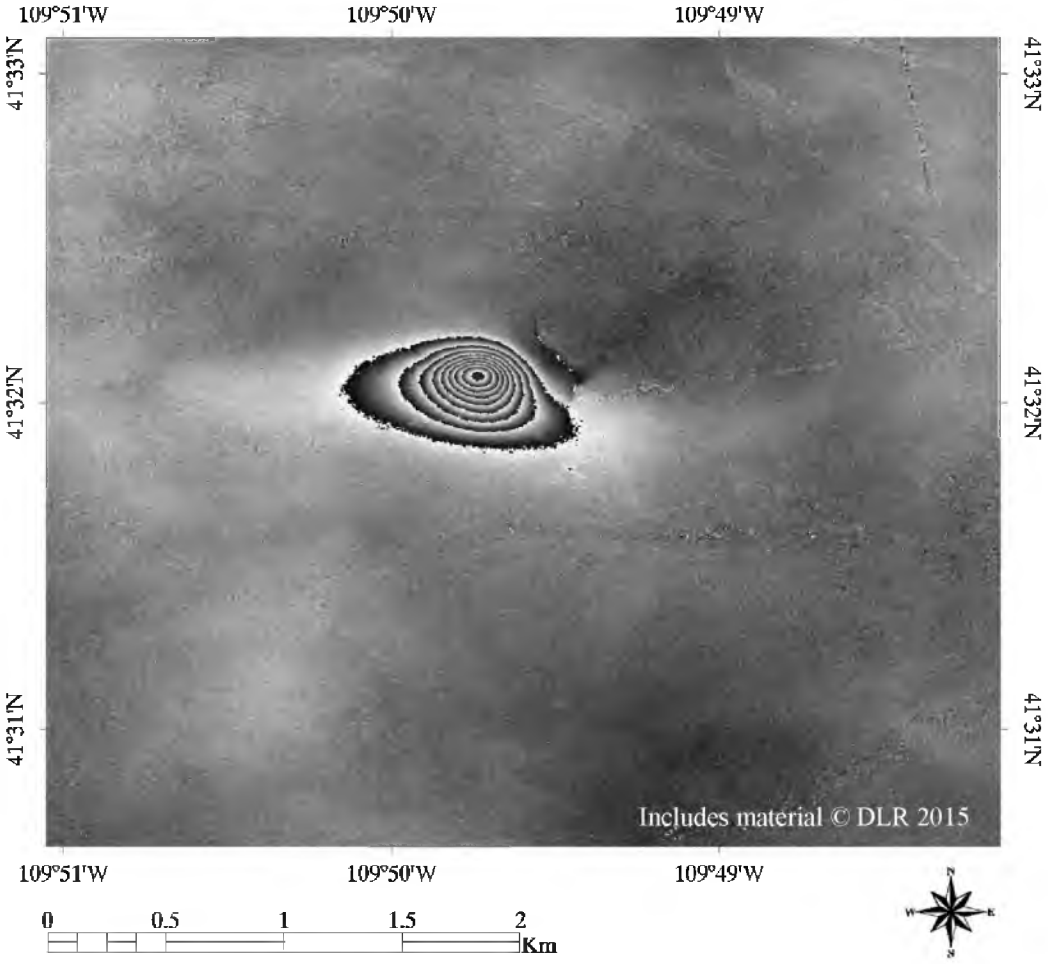

FIGURE 4.4 Boxcar filtered differential interferogram (X-band) from the southwest Wyoming region: July 27, 2015 to August 7, 2015

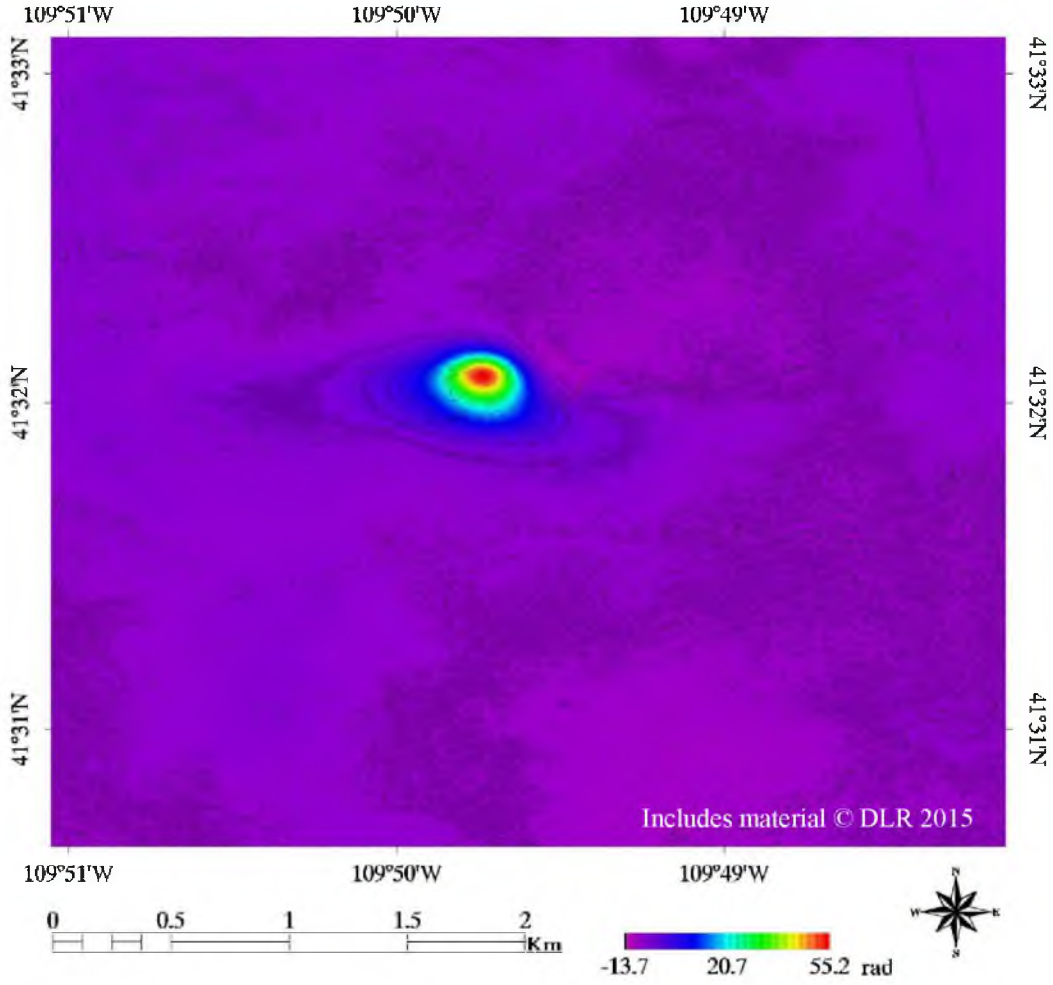

FIGURE 4.5 Unwrapped differential interferogram (X-band) from the southwest Wyoming region: July 27, 2015 to August 7, 2015

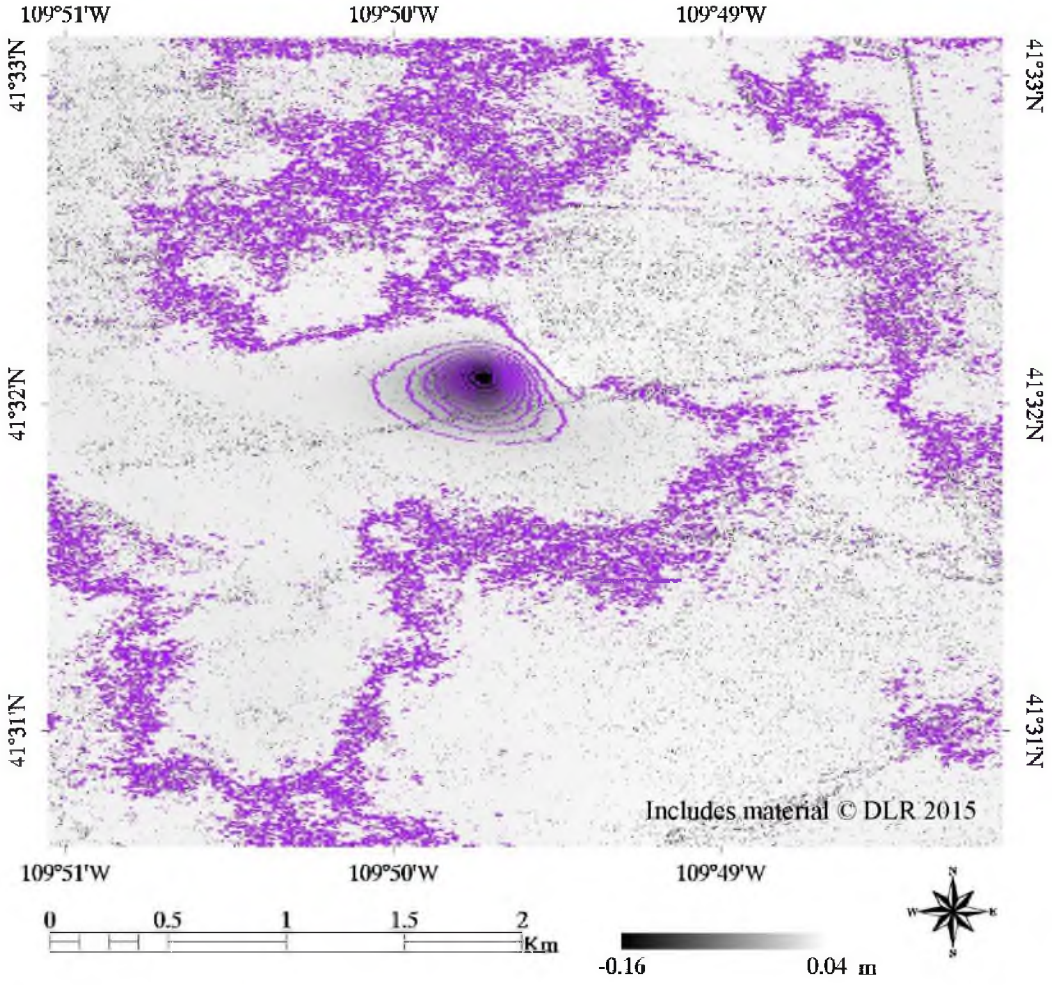

FIGURE 4.6 Vertical deformation map (X-band) from the southwest Wyoming region: July 27, 2015 to August 7, 2015. Displacement is contoured from 0 to −0.15 m with a 0.015-m increment.

CHAPTER 5

SEISMIC DATA

5.1 Introduction

MIS, seismicity that results from the rapid release of strain energy generated by mining, can directly impact mine safety and has been well researched. Gibowicz (2009), Gibowicz and Lasocki (2001), and Maleki et al. (1995) present significant literature on induced seismicity in mine environments. MIS is often a function of mine development, but it depends strongly on operational and geological conditions, and the characteristics of MIS are significantly variable. Overall, very few seismic events disrupt mine development, but differentiating between normal seismicity and seismicity potentially indicative of rock failures near mine openings is not trivial, and MIS remains an important topic in mining engineering research.

One purpose of this study is to investigate relationships between subsidence and MIS in the Wasatch Plateau and the Green River Basin. This chapter includes a brief review of literature on MIS in the Wasatch Plateau and the Green River Basin, an introduction to the seismic catalogs used in this study, and a summary of the characteristics of MIS during the study period. The dates, origin times, locations, and magnitudes of the cataloged events used in this study are presented in Tables 5.1 to 5.5.

5.2 MIS in the Wasatch Plateau

Underground coal mines in the Wasatch Plateau and Book Cliffs coal fields exhibit significant MIS (Arabasz et al. 1997; Arabasz and Pechmann 2001; Ellenberger et al. 2001). In these regions, MIS is generally correlated with mine development (Boltz et al. 2014; Pankow et al. 2008), but these correlations are largely variable (Arabaz et al. 1997). The consequences of MIS in the central Utah region are also largely variable. The majority of MIS is benign, but seismicity has been associated with catastrophic failures, including the 2007 Crandall Canyon mine collapse (Kubacki et al. 2014; Pechmann et al. 2008). Additionally, the Wasatch Plateau and Book Cliffs are tectonically active, and not all of the seismicity in the central Utah coal fields is necessarily induced (Arabasz et al. 2007), but discriminating between induced and tectonic seismicity in this region is challenging (Stein et al. 2015).

The trona district in southwest Wyoming also exhibits significant MIS, but in this region, correlations between seismicity and mine advance have not been as clearly demonstrated. Compared to the central Utah coal fields, the level of cataloged seismicity in the trona district is relatively low, and events are often difficult to associate to specific mines (Arabasz and Pechmann 2001). Like the central Utah coal fields, the consequences of MIS in the trona district are variable. Although the cataloged seismicity tends to be relatively large magnitude, around 3, there are few reported impacts to mine production. MIS is associated with catastrophic failures in this region, including collapses in 1995 and 2000 at the Solvay mine (Pechmann et al. 1995; Arabasz and Pechmann 2001).

5.3 Seismic Catalogs

For the central Utah study region, the seismic events identified in this study were derived from the University of Utah Seismograph Stations (UUSS, www.quake.utah.edu) earthquake catalog. These events are based on data continually recorded by the UUSS regional seismic network, which has been active since 1978 (Arabasz et al. 1997), and the cataloged events are described by the origin time, epicenter, depth, and magnitude. In this catalog the event magnitudes are reported as either Richter local magnitude (M_L) or coda magnitude (M_C), although for small earthquakes M_L and M_C do not correspond exactly (Pechmann et al. 2006), in this study no discrimination is made. In the central Utah region, the UUSS catalog is complete at magnitude of roughly 1.5 (Pankow et al. 2008), and events with magnitudes greater than 1.5 are systematically identified.

The UUSS catalog was also used to identify events in the southwest Wyoming region. For this region the resolution of the UUSS regional seismic network is relatively low and the magnitude of completeness is on the order of 3.0 (UUSS 2016). To supplement the UUSS catalog in this region, the Array Network Facility (ANF, anf.ucsd.edu) catalog, which uses seismic data collected by the EarthScope Transportable Array (TA) of broadband seismometers (Astiz et al. 2014), was used. The TA was active across southwest Wyoming from November 2007 through May 2009, and for this period, the seismic instrument density and azimuthal coverage are good.

5.4 Characteristics of Mining Induced Seismicity (MIS)

For the central Utah region, Table 5.1 lists the origin time, location, and magnitude of the UUSS catalog events that occurred from November 21, 2006 to

December 24, 2007. During this period there were 97 events, a rate of about 90 events per year, with magnitudes ranging from 0.99 to 2.84. Only four events had magnitudes greater than 2.5. Table 5.2 lists the origin time, location, and magnitude of the UUSS catalog events that occurred from November 29, 2009 to February 16, 2011. During this period there were 353 events, a rate of about 290 events per year, with magnitudes ranging from 0.90 to 2.60. Three events had magnitudes greater than 2.5. Table 5.3 lists the origin time, location, and magnitude for the UUSS catalog events that occurred from June 1 to November 30, 2015. During this period there were six events, a rate of about 12 events per year, with magnitudes ranging from 0.92 to 1.67.

For the southwest Wyoming region, Table 5.4 lists the origin time, location, and magnitude for the UUSS cataloged events that occurred from November 19, 2007 to March 29, 2011. Only four seismic events were cataloged with magnitudes ranging from 2.59 to 3.51. All four of the UUSS cataloged events occurred during the period from November 2007 through May 2009 when the TA was active in southwest Wyoming and are included in the ANF catalog. Because of differences in data analysis and processing, the catalogs report marginally different magnitudes and locations for these events. For the November 2007 through May 2009 period, the ANF catalog includes two relatively low magnitude events that are not included in the UUSS catalog. Table 5.5 lists the origin time, location, and magnitude for the all six of the ANF catalog events. These events have magnitudes ranging from 1.65 to 3.58. Only the UUSS network was active in the Wyoming regions for the period imaged by TerraSAR-X, June 2 to November 3, 2015, and during this period no events were cataloged.

Table 5.1 November 21, 2006 to December 24, 2007 seismic events—Utah region

Date	Time, h:min:s	Latitude	Longitude	Magnitude
December 11, 2006	7:31:13.81	38° 58.97'	111° 27.38'	2.48
January 5, 2007	11:12:22.76	38° 59.31'	111° 19.85'	2.22
January 5, 2007	22:25:38.18	38° 59.42'	111° 19.40'	1.72
January 6, 2007	23:51:04.93	38° 59.47'	111° 19.45'	1.82
January 7, 2007	1:22:01.42	38° 59.68'	111° 19.86'	1.90
January 7, 2007	4:52:50.56	39° 00.07'	111° 19.44'	1.68
January 8, 2007	3:59:08.12	38° 59.76'	111° 19.52'	1.81
January 9, 2007	6:12:30.61	38° 59.40'	111° 20.16'	1.67
January 9, 2007	6:15:35.27	38° 59.06'	111° 19.41'	1.44
January 13, 2007	19:26:53.74	38° 59.36'	111° 19.47'	1.74
January 13, 2007	21:07:21.08	38° 59.68'	111° 20.23'	1.60
January 14, 2007	1:44:24.57	38° 59.31'	111° 20.28'	2.69
January 15, 2007	14:09:46.50	38° 58.93'	111° 19.24'	1.54
January 15, 2007	16:38:25.95	38° 59.18'	111° 19.82'	1.62
January 20, 2007	3:53:01.36	38° 59.34'	111° 19.64'	1.46
January 20, 2007	9:39:30.97	38° 59.14'	111° 19.58'	1.48
January 20, 2007	10:14:43.78	38° 59.17'	111° 19.50'	1.55
January 20, 2007	12:48:29.54	38° 59.22'	111° 20.02'	1.73
January 20, 2007	16:18:26.31	38° 59.46'	111° 19.58'	1.92
January 20, 2007	21:24:52.05	38° 59.03'	111° 19.30'	1.58
January 21, 2007	2:01:35.87	38° 59.73'	111° 19.34'	1.51
January 21, 2007	14:55:32.93	38° 58.99'	111° 19.18'	1.75
January 22, 2007	17:24:48.61	38° 59.16'	111° 19.57'	2.11
January 23, 2007	17:51:43.33	38° 59.07'	111° 19.99'	1.40
January 25, 2007	5:06:09.62	38° 58.93'	111° 19.17'	1.41
January 26, 2007	6:51:37.97	38° 59.21'	111° 18.60'	1.56
January 26, 2007	19:54:58.42	38° 58.94'	111° 19.68'	1.74
January 31, 2007	0:33:09.80	38° 59.56'	111° 19.65'	1.83
February 9, 2007	15:18:20.37	38° 59.30'	111° 19.65'	1.73
February 17, 2007	19:12:20.31	38° 58.94'	111° 19.52'	1.44
February 20, 2007	2:18:51.06	38° 59.15'	111° 19.40'	1.57
February 25, 2007	1:07:33.50	39° 00.00'	111° 19.45'	1.62
March 27, 2007	4:10:17.10	38° 59.58'	111° 27.60'	2.67
April 5, 2007	4:19:03.72	38° 55.42'	111° 27.71'	1.46
April 25, 2007	0:18:53.59	38° 58.93'	111° 26.51'	1.54

Table 5.1 Continued

Date	Time, h:min:s	Latitude	Longitude	Magnitude
May 23, 2007	22:13:16.61	38° 58.21'	111° 26.57'	1.81
August 20, 2007	16:50:31.04	38° 59.08'	111° 19.83'	1.52
October 18, 2007	8:58:37.30	38° 59.85'	111° 23.53'	1.61
October 19, 2007	13:40:47.54	38° 59.71'	111° 23.53'	2.02
October 19, 2007	18:24:28.56	38° 59.71'	111° 23.56'	1.71
October 24, 2007	2:56:53.67	38° 59.64'	111° 23.53'	1.50
October 24, 2007	5:07:51.41	38° 59.65'	111° 23.63'	1.56
October 25, 2007	0:17:03.51	38° 59.82'	111° 18.65'	1.58
October 25, 2007	11:39:59.86	38° 59.74'	111° 23.78'	1.87
October 25, 2007	12:45:51.49	38° 59.76'	111° 23.44'	1.89
October 27, 2007	15:54:28.68	38° 59.55'	111° 23.51'	1.58
October 27, 2007	18:51:02.29	38° 59.48'	111° 23.25'	1.36
October 28, 2007	8:17:18.01	38° 59.63'	111° 23.44'	1.65
October 31, 2007	3:22:45.52	38° 59.80'	111° 23.83'	2.84
November 4, 2007	18:59:45.29	38° 59.83'	111° 23.74'	1.43
November 9, 2007	6:29:19.44	38° 59.61'	111° 23.53'	1.65
November 9, 2007	9:28:32.43	38° 59.63'	111° 23.75'	2.21
November 9, 2007	9:46:39.25	38° 59.97'	111° 23.77'	2.50
November 9, 2007	9:47:41.13	38° 59.04'	111° 24.09'	0.99
November 9, 2007	10:51:52.34	39° 00.06'	111° 23.98'	1.56
November 9, 2007	14:47:09.37	39° 00.01'	111° 22.52'	1.70
November 10, 2007	18:53:25.86	38° 59.58'	111° 23.35'	1.64
November 14, 2007	13:29:17.27	38° 59.87'	111° 23.77'	1.65
November 15, 2007	2:52:51.98	38° 59.28'	111° 23.47'	1.47
November 15, 2007	17:51:58.44	38° 59.45'	111° 22.90'	1.19
November 17, 2007	5:10:36.94	38° 59.52'	111° 23.60'	2.15
November 17, 2007	22:47:50.04	38° 59.87'	111° 23.75'	1.71
November 18, 2007	0:40:59.29	38° 59.60'	111° 23.49'	2.01
November 19, 2007	9:04:46.17	38° 59.77'	111° 23.86'	2.55
November 21, 2007	12:43:47.19	38° 59.62'	111° 23.59'	1.90
November 22, 2007	4:02:55.63	38° 59.38'	111° 23.48'	1.19
November 23, 2007	2:21:34.06	38° 59.60'	111° 23.55'	1.44
November 28, 2007	9:28:10.70	38° 59.18'	111° 21.35'	1.60
November 28, 2007	13:23:23.09	38° 59.53'	111° 24.27'	2.15
November 28, 2007	19:42:49.23	38° 59.74'	111° 23.21'	1.56

Table 5.1 Continued

Date	Time, h:min:s	Latitude	Longitude	Magnitude
November 29, 2007	7:37:45.32	38° 59.83'	111° 23.71'	2.24
November 29, 2007	7:58:11.70	38° 59.70'	111° 23.77'	1.72
November 30, 2007	19:31:24.16	38° 59.40'	111° 23.49'	1.95
December 1, 2007	18:33:09.87	38° 59.72'	111° 23.08'	2.28
December 3, 2007	7:32:20.42	38° 59.56'	111° 23.49'	2.03
December 4, 2007	8:46:18.04	38° 59.71'	111° 23.71'	1.97
December 4, 2007	14:19:50.88	38° 59.49'	111° 23.73'	1.90
December 4, 2007	21:13:12.94	38° 59.68'	111° 23.98'	2.34
December 5, 2007	12:28:18.53	38° 59.43'	111° 23.23'	2.02
December 7, 2007	0:01:22.87	38° 59.73'	111° 23.59'	1.19
December 7, 2007	2:13:02.96	38° 59.75'	111° 24.37'	2.42
December 7, 2007	4:56:13.67	39° 00.07'	111° 23.98'	1.83
December 8, 2007	17:12:29.80	38° 59.73'	111° 23.97'	2.45
December 12, 2007	2:27:07.39	38° 59.83'	111° 23.94'	2.27
December 12, 2007	12:27:51.66	38° 59.44'	111° 23.70'	1.66
December 13, 2007	11:58:04.94	38° 59.63'	111° 23.45'	1.47
December 13, 2007	15:01:33.34	38° 59.50'	111° 23.51'	1.38
December 14, 2007	18:18:45.60	38° 59.04'	111° 21.80'	1.08
December 16, 2007	17:01:38.71	38° 59.99'	111° 23.39'	1.56
December 17, 2007	16:52:12.82	38° 59.38'	111° 23.40'	1.58
December 18, 2007	6:28:54.32	38° 59.93'	111° 24.12'	1.60
December 19, 2007	9:25:16.13	38° 59.51'	111° 23.45'	1.76
December 19, 2007	10:21:08.86	38° 59.49'	111° 23.56'	1.76
December 19, 2007	17:15:59.72	38° 59.74'	111° 23.58'	1.46
December 20, 2007	13:14:00.97	38° 59.23'	111° 23.31'	1.56
December 21, 2007	9:06:21.25	38° 58.83'	111° 23.30'	1.57
December 21, 2007	23:51:05.68	39° 00.04'	111° 22.89'	1.49

Table 5.2 November 29, 2009 to February 16, 2011 seismic events—Utah region

Date	Time, h:min:s	Latitude	Longitude	Magnitude
November 29, 2009	11:38:31.77	38° 59.56'	111° 22.84'	1.56
December 2, 2009	6:40:04.05	38° 59.61'	111° 23.07'	2.26
December 2, 2009	10:53:40.47	38° 59.52'	111° 23.05'	1.52
December 3, 2009	12:00:29.14	38° 59.86'	111° 23.10'	1.74
December 5, 2009	1:21:42.80	38° 59.42'	111° 23.51'	1.95
December 7, 2009	20:23:03.05	38° 59.61'	111° 23.03'	1.72
December 7, 2009	20:39:53.47	38° 59.47'	111° 23.16'	1.74
December 9, 2009	7:47:55.92	38° 58.97'	111° 23.17'	1.73
December 11, 2009	4:18:59.63	38° 59.71'	111° 23.52'	1.62
December 11, 2009	9:09:22.02	38° 59.60'	111° 23.21'	1.63
December 11, 2009	9:13:44.12	38° 59.99'	111° 22.69'	2.06
December 11, 2009	10:37:51.12	38° 59.94'	111° 23.34'	2.13
December 11, 2009	11:05:57.68	38° 59.78'	111° 23.25'	1.43
December 11, 2009	21:57:33.54	38° 59.65'	111° 23.58'	2.32
December 11, 2009	22:10:59.85	38° 59.91'	111° 23.63'	1.41
December 12, 2009	18:58:55.30	38° 59.54'	111° 23.21'	1.93
December 16, 2009	1:30:12.84	38° 59.72'	111° 23.31'	1.27
December 18, 2009	11:44:15.76	38° 59.62'	111° 23.67'	1.50
December 18, 2009	15:47:09.78	38° 59.39'	111° 23.57'	2.16
December 18, 2009	20:20:29.23	38° 59.52'	111° 23.49'	1.69
December 19, 2009	0:32:08.42	38° 59.25'	111° 23.09'	1.92
December 21, 2009	4:55:52.05	38° 59.64'	111° 22.69'	2.15
December 22, 2009	7:48:04.12	38° 59.30'	111° 23.36'	1.87
January 1, 2010	17:16:19.10	38° 59.58'	111° 23.47'	2.42
January 1, 2010	23:43:06.51	38° 59.40'	111° 23.49'	2.12
January 5, 2010	18:16:56.14	38° 59.61'	111° 23.29'	2.40
January 6, 2010	12:33:49.45	38° 59.61'	111° 23.36'	1.71
January 6, 2010	21:45:42.25	38° 59.73'	111° 23.37'	2.38
January 7, 2010	21:43:15.25	38° 59.32'	111° 22.63'	1.74
January 12, 2010	20:52:50.24	38° 59.59'	111° 23.48'	2.47
January 18, 2010	5:57:59.22	39° 00.28'	111° 23.01'	1.23
January 22, 2010	3:12:42.13	38° 59.65'	111° 23.55'	2.20
January 27, 2010	20:33:03.73	38° 59.35'	111° 23.46'	2.35
January 28, 2010	10:15:17.09	38° 59.14'	111° 22.74'	1.46
January 28, 2010	14:10:59.41	38° 59.61'	111° 23.86'	2.35

Table 5.2 Continued

Date	Time, h:min:s	Latitude	Longitude	Magnitude
January 30, 2010	15:46:32.50	38° 59.37'	111° 23.66'	1.82
February 7, 2010	14:20:52.69	38° 59.53'	111° 23.21'	1.76
May 4, 2010	20:20:32.83	38° 58.96'	111° 21.65'	1.26
May 21, 2010	9:48:13.96	38° 59.09'	111° 23.34'	1.68
June 19, 2010	2:03:17.04	39° 00.22'	111° 23.02'	1.54
June 19, 2010	15:40:45.43	39° 00.33'	111° 22.69'	1.61
June 20, 2010	1:36:52.73	39° 00.67'	111° 23.57'	1.59
June 21, 2010	23:54:36.75	39° 00.26'	111° 23.21'	1.60
June 22, 2010	6:26:55.94	39° 00.03'	111° 23.03'	1.48
June 22, 2010	8:17:49.18	39° 00.57'	111° 22.88'	1.69
June 22, 2010	10:43:15.53	38° 59.83'	111° 22.65'	1.46
June 22, 2010	23:56:37.30	39° 00.60'	111° 22.67'	1.68
June 23, 2010	0:40:21.96	39° 01.16'	111° 22.49'	1.68
June 24, 2010	11:06:41.11	39° 00.81'	111° 22.29'	1.32
June 24, 2010	21:38:30.52	39° 00.46'	111° 22.52'	1.67
June 24, 2010	22:44:07.15	39° 00.09'	111° 22.74'	1.72
June 25, 2010	0:49:54.98	38° 59.78'	111° 22.69'	1.40
June 25, 2010	16:02:05.70	39° 02.43'	111° 17.24'	1.30
June 25, 2010	22:54:56.10	39° 00.40'	111° 23.02'	2.60
June 27, 2010	3:36:22.15	39° 00.64'	111° 22.81'	1.22
June 27, 2010	5:46:35.94	39° 00.02'	111° 22.75'	1.71
June 28, 2010	8:56:14.87	39° 00.43'	111° 23.15'	1.29
June 30, 2010	16:15:41.73	39° 01.05'	111° 22.34'	1.05
July 1, 2010	2:33:43.72	39° 00.24'	111° 22.37'	2.04
July 1, 2010	2:34:25.02	39° 00.05'	111° 19.48'	2.34
July 1, 2010	4:09:42.27	39° 00.26'	111° 22.86'	1.83
July 1, 2010	4:20:23.49	39° 00.55'	111° 23.03'	1.67
July 2, 2010	15:15:47.23	39° 00.28'	111° 22.37'	1.67
July 4, 2010	11:07:56.69	39° 00.50'	111° 22.99'	1.42
July 5, 2010	3:56:40.42	39° 00.53'	111° 22.92'	1.40
July 5, 2010	22:17:28.30	38° 59.74'	111° 22.42'	1.44
July 6, 2010	23:14:17.60	38° 59.13'	111° 21.61'	1.61
July 7, 2010	11:23:08.58	39° 00.59'	111° 22.91'	1.60
July 7, 2010	13:20:08.06	39° 00.26'	111° 22.67'	1.51
July 7, 2010	19:48:03.99	39° 00.83'	111° 22.98'	1.52

Table 5.2 Continued

Date	Time, h:min:s	Latitude	Longitude	Magnitude
July 8, 2010	22:43:49.00	38° 59.64'	111° 23.30'	1.68
July 9, 2010	8:53:34.90	39° 00.05'	111° 22.94'	1.35
July 9, 2010	12:59:13.57	38° 59.91'	111° 22.89'	1.62
July 9, 2010	18:53:55.50	39° 01.46'	111° 22.22'	1.44
July 10, 2010	3:50:02.97	39° 01.36'	111° 22.72'	1.43
July 11, 2010	1:06:42.58	39° 00.11'	111° 22.97'	1.51
July 11, 2010	2:20:56.59	38° 59.51'	111° 22.65'	1.40
July 11, 2010	6:22:22.80	39° 00.91'	111° 22.76'	1.39
July 11, 2010	17:23:45.53	38° 59.34'	111° 22.79'	1.67
July 14, 2010	5:49:16.45	38° 59.46'	111° 22.98'	1.73
July 14, 2010	22:45:28.63	39° 00.24'	111° 22.92'	1.61
July 15, 2010	13:36:04.65	39° 00.71'	111° 23.62'	1.57
July 16, 2010	20:13:22.55	39° 00.20'	111° 23.41'	1.66
July 17, 2010	0:18:20.43	39° 00.03'	111° 23.10'	1.34
July 17, 2010	5:23:52.82	39° 00.30'	111° 22.77'	1.67
July 17, 2010	5:31:45.34	39° 00.16'	111° 22.96'	1.49
July 17, 2010	5:35:20.48	38° 59.98'	111° 22.96'	1.55
July 17, 2010	17:09:50.61	38° 59.80'	111° 22.96'	1.41
July 18, 2010	0:37:55.49	38° 59.98'	111° 23.05'	1.63
July 18, 2010	5:55:34.81	38° 59.98'	111° 22.81'	1.74
July 20, 2010	12:47:57.95	39° 00.18'	111° 22.55'	1.81
July 20, 2010	17:05:06.31	38° 59.83'	111° 23.05'	1.74
July 21, 2010	8:40:39.41	38° 59.89'	111° 23.29'	2.06
July 21, 2010	11:49:54.81	39° 00.49'	111° 23.51'	1.63
July 21, 2010	13:21:25.67	38° 59.55'	111° 23.07'	1.78
July 22, 2010	13:30:57.82	38° 59.71'	111° 22.27'	1.52
July 23, 2010	13:02:27.92	38° 59.71'	111° 22.52'	1.59
July 24, 2010	3:22:52.43	39° 00.48'	111° 22.91'	1.64
July 24, 2010	22:07:57.03	39° 00.07'	111° 23.04'	1.69
July 28, 2010	15:33:24.10	39° 00.35'	111° 23.15'	1.67
July 29, 2010	8:49:52.74	39° 00.20'	111° 23.01'	1.22
July 29, 2010	17:07:24.70	39° 00.09'	111° 22.54'	1.20
July 29, 2010	19:34:09.43	38° 59.81'	111° 23.11'	2.31
July 29, 2010	20:23:58.45	39° 00.20'	111° 22.63'	1.25
July 30, 2010	8:26:21.88	39° 00.36'	111° 22.81'	1.75

Table 5.2 Continued

Date	Time, h:min:s	Latitude	Longitude	Magnitude
July 30, 2010	21:58:55.70	38° 59.82'	111° 22.95'	1.71
July 31, 2010	2:01:31.12	38° 59.81'	111° 22.83'	1.78
July 31, 2010	17:38:20.90	39° 00.29'	111° 22.60'	1.37
July 31, 2010	17:39:02.49	38° 59.05'	111° 22.82'	1.74
August 2, 2010	2:41:44.22	39° 00.18'	111° 23.04'	1.45
August 4, 2010	7:15:03.00	38° 59.91'	111° 22.72'	1.49
August 5, 2010	0:40:20.51	39° 00.26'	111° 22.50'	1.50
August 5, 2010	13:40:30.43	38° 59.71'	111° 22.36'	1.35
August 5, 2010	17:35:54.08	39° 01.14'	111° 22.74'	1.35
August 6, 2010	18:16:12.62	38° 59.90'	111° 23.19'	1.93
August 6, 2010	20:12:30.57	38° 59.30'	111° 22.58'	1.56
August 7, 2010	11:47:04.28	39° 00.19'	111° 22.94'	1.45
August 10, 2010	3:29:09.38	38° 59.79'	111° 22.83'	1.68
August 10, 2010	19:22:28.03	38° 59.79'	111° 22.55'	1.68
August 10, 2010	20:13:25.57	38° 59.72'	111° 22.40'	1.70
August 10, 2010	20:44:48.51	39° 00.35'	111° 22.26'	1.43
August 11, 2010	0:16:33.37	39° 00.22'	111° 22.34'	1.63
August 11, 2010	0:41:47.91	39° 00.33'	111° 22.74'	1.49
August 11, 2010	22:17:40.60	38° 59.81'	111° 22.92'	2.55
August 12, 2010	6:50:32.39	38° 59.77'	111° 22.81'	1.30
August 12, 2010	9:49:24.18	38° 59.98'	111° 22.12'	1.64
August 13, 2010	23:30:34.30	38° 59.08'	111° 23.06'	1.29
August 18, 2010	3:27:42.30	39° 00.29'	111° 22.92'	1.75
August 18, 2010	11:10:16.87	39° 00.02'	111° 22.62'	1.67
August 19, 2010	18:31:19.88	38° 59.70'	111° 22.62'	1.65
August 19, 2010	22:05:55.17	39° 00.11'	111° 22.69'	1.55
August 20, 2010	3:33:01.22	38° 59.84'	111° 23.22'	1.72
August 20, 2010	12:50:53.28	38° 59.78'	111° 22.11'	1.44
August 20, 2010	13:30:14.72	39° 00.14'	111° 22.43'	1.97
August 20, 2010	13:42:20.82	39° 00.26'	111° 21.94'	1.44
August 20, 2010	14:13:38.43	38° 59.84'	111° 22.53'	1.42
August 20, 2010	19:01:18.00	39° 00.36'	111° 22.48'	1.42
August 24, 2010	11:47:52.12	39° 00.29'	111° 21.83'	1.97
August 25, 2010	18:16:36.86	39° 00.12'	111° 22.88'	1.67
August 26, 2010	10:32:59.44	38° 59.99'	111° 22.97'	1.90

Table 5.2 Continued

Date	Time, h:min:s	Latitude	Longitude	Magnitude
September 5, 2010	18:11:19.86	38° 56.17'	111° 24.38'	1.35
September 25, 2010	20:17:28.31	38° 59.95'	111° 22.45'	1.68
September 27, 2010	20:43:17.90	39° 00.56'	111° 21.45'	1.53
September 28, 2010	14:23:39.60	39° 00.13'	111° 23.37'	1.27
September 29, 2010	11:58:34.52	38° 59.58'	111° 22.55'	1.62
October 2, 2010	18:32:40.33	39° 00.19'	111° 22.88'	1.46
October 10, 2010	10:46:03.50	38° 59.63'	111° 21.89'	1.46
October 10, 2010	19:56:31.07	39° 00.36'	111° 22.23'	1.35
October 12, 2010	4:12:43.74	39° 00.59'	111° 21.85'	1.77
October 13, 2010	17:52:29.57	39° 00.11'	111° 22.39'	1.38
October 14, 2010	4:42:57.07	39° 00.42'	111° 22.77'	1.67
October 14, 2010	6:28:46.14	39° 00.29'	111° 22.15'	1.61
October 16, 2010	14:08:21.18	38° 59.85'	111° 21.54'	0.90
October 17, 2010	13:04:20.69	39° 00.75'	111° 22.18'	1.56
October 17, 2010	13:36:03.50	39° 00.79'	111° 22.42'	1.36
October 17, 2010	23:39:05.76	39° 00.66'	111° 22.28'	1.48
October 20, 2010	2:51:06.29	39° 00.60'	111° 21.98'	1.53
October 20, 2010	5:24:21.66	39° 00.28'	111° 22.19'	1.64
October 20, 2010	5:37:03.88	39° 00.22'	111° 22.32'	1.94
October 20, 2010	8:34:10.09	39° 00.76'	111° 22.50'	1.73
October 20, 2010	9:23:26.56	38° 59.92'	111° 21.99'	1.48
October 20, 2010	9:50:58.50	39° 00.42'	111° 22.03'	1.26
October 20, 2010	12:26:08.01	39° 00.54'	111° 21.97'	1.43
October 21, 2010	7:29:53.04	39° 00.71'	111° 21.90'	1.49
October 21, 2010	11:56:43.67	39° 00.45'	111° 22.66'	1.55
October 21, 2010	12:29:52.75	39° 00.53'	111° 22.38'	1.55
October 21, 2010	12:43:44.98	39° 00.55'	111° 22.51'	1.43
October 21, 2010	15:38:07.44	39° 00.68'	111° 21.88'	1.24
October 21, 2010	20:39:45.51	39° 00.24'	111° 22.82'	1.49
October 21, 2010	22:58:10.30	39° 00.46'	111° 22.67'	1.74
October 22, 2010	9:14:38.20	39° 00.23'	111° 22.52'	1.56
October 23, 2010	3:13:55.83	38° 59.88'	111° 22.16'	1.28
October 25, 2010	6:30:33.38	38° 59.96'	111° 21.83'	1.92
October 25, 2010	14:50:30.32	39° 01.22'	111° 21.30'	1.30
October 25, 2010	21:17:01.99	39° 00.79'	111° 22.03'	1.58

Table 5.2 Continued

Date	Time, h:min:s	Latitude	Longitude	Magnitude
October 26, 2010	1:07:06.02	39° 00.27'	111° 22.45'	1.67
October 26, 2010	23:13:29.09	39° 00.12'	111° 22.44'	1.58
October 27, 2010	11:08:22.56	38° 59.17'	111° 22.45'	1.34
October 28, 2010	22:55:19.93	39° 00.70'	111° 22.40'	1.47
October 29, 2010	17:11:56.64	38° 59.97'	111° 21.84'	1.47
October 29, 2010	23:27:56.92	39° 00.74'	111° 22.22'	1.82
November 1, 2010	5:15:56.58	39° 00.06'	111° 22.79'	1.28
November 1, 2010	21:52:57.64	39° 00.68'	111° 22.47'	1.57
November 3, 2010	1:55:14.07	39° 00.62'	111° 22.59'	1.52
November 3, 2010	7:53:38.71	39° 00.01'	111° 22.28'	1.45
November 3, 2010	8:07:09.98	39° 00.52'	111° 22.35'	1.51
November 3, 2010	9:14:33.30	38° 59.97'	111° 22.15'	1.23
November 3, 2010	9:43:48.37	39° 00.46'	111° 21.42'	1.37
November 3, 2010	14:00:21.73	39° 00.31'	111° 21.38'	1.52
November 3, 2010	16:21:46.26	38° 59.94'	111° 22.50'	1.54
November 3, 2010	19:38:21.90	39° 00.92'	111° 20.17'	1.63
November 5, 2010	7:23:57.63	39° 00.28'	111° 22.59'	1.60
November 5, 2010	16:45:18.51	39° 00.26'	111° 21.91'	1.52
November 5, 2010	21:54:49.42	38° 59.49'	111° 22.25'	1.11
November 6, 2010	6:17:40.20	39° 00.59'	111° 22.45'	1.19
November 6, 2010	19:03:44.29	39° 00.46'	111° 21.81'	1.62
November 7, 2010	3:18:58.04	39° 00.77'	111° 20.83'	1.51
November 9, 2010	6:26:27.91	39° 00.58'	111° 22.20'	1.53
November 9, 2010	9:57:17.77	39° 00.93'	111° 21.35'	1.51
November 9, 2010	10:12:19.01	39° 00.42'	111° 22.42'	1.56
November 10, 2010	5:17:02.63	38° 59.76'	111° 22.04'	1.19
November 10, 2010	13:12:20.06	38° 59.87'	111° 21.53'	1.13
November 10, 2010	15:47:54.53	39° 00.04'	111° 22.62'	1.40
November 10, 2010	16:53:54.82	38° 59.88'	111° 22.90'	1.39
November 10, 2010	18:00:35.76	39° 00.09'	111° 22.35'	1.46
November 12, 2010	3:03:15.51	38° 59.44'	111° 21.77'	1.30
November 12, 2010	16:53:22.09	39° 00.57'	111° 22.44'	1.38
November 13, 2010	0:35:33.74	38° 59.91'	111° 22.13'	1.40
November 13, 2010	10:14:54.36	39° 00.35'	111° 22.14'	1.52
November 13, 2010	16:38:47.12	39° 00.48'	111° 21.84'	1.50

Table 5.2 Continued

Date	Time, h:min:s	Latitude	Longitude	Magnitude
November 13, 2010	21:46:22.72	39° 00.58'	111° 22.47'	1.54
November 14, 2010	12:33:13.62	39° 00.22'	111° 22.32'	1.39
November 15, 2010	2:46:41.99	39° 01.50'	111° 21.15'	1.46
November 15, 2010	4:32:26.70	39° 00.86'	111° 22.26'	1.54
November 15, 2010	22:07:54.17	38° 59.99'	111° 22.29'	1.47
November 16, 2010	13:00:48.61	39° 00.23'	111° 22.64'	1.46
November 17, 2010	6:50:37.88	39° 00.31'	111° 22.50'	1.19
November 18, 2010	9:06:04.52	39° 00.41'	111° 22.53'	1.44
November 18, 2010	19:24:56.33	39° 00.13'	111° 21.92'	1.68
November 19, 2010	6:33:32.34	39° 00.10'	111° 22.82'	1.56
November 19, 2010	10:12:07.69	39° 00.01'	111° 20.91'	1.40
November 19, 2010	11:57:24.37	39° 00.09'	111° 22.28'	1.36
November 19, 2010	18:05:22.09	39° 00.27'	111° 21.63'	1.79
November 20, 2010	1:17:22.90	38° 59.39'	111° 21.46'	1.34
November 20, 2010	15:09:36.88	39° 00.34'	111° 24.27'	1.22
November 21, 2010	5:23:19.29	39° 00.60'	111° 21.45'	1.73
November 21, 2010	8:56:12.18	39° 00.04'	111° 21.39'	1.58
November 22, 2010	22:46:38.39	38° 59.91'	111° 22.25'	1.60
November 23, 2010	8:35:04.48	39° 00.52'	111° 22.69'	1.41
November 24, 2010	20:22:15.31	38° 59.43'	111° 22.70'	1.40
November 25, 2010	6:42:50.44	39° 00.13'	111° 22.48'	1.06
November 25, 2010	7:48:41.68	39° 00.05'	111° 21.92'	1.45
November 25, 2010	9:39:16.84	39° 00.94'	111° 21.82'	1.43
November 25, 2010	20:03:25.93	39° 00.28'	111° 19.68'	1.23
November 25, 2010	21:46:36.66	39° 00.53'	111° 22.12'	1.38
November 26, 2010	13:40:32.31	38° 59.79'	111° 21.99'	1.43
November 29, 2010	8:09:11.46	38° 59.72'	111° 22.24'	1.78
November 30, 2010	10:59:38.32	38° 59.91'	111° 22.46'	1.74
November 30, 2010	16:02:18.41	39° 00.03'	111° 22.39'	1.54
December 1, 2010	11:34:38.34	39° 00.08'	111° 22.49'	1.63
December 1, 2010	13:59:27.18	39° 00.31'	111° 21.90'	1.26
December 1, 2010	19:13:21.93	39° 00.21'	111° 22.57'	1.27
December 2, 2010	9:02:56.39	39° 00.26'	111° 22.14'	1.66
December 2, 2010	12:33:44.40	38° 59.33'	111° 22.55'	1.18
December 2, 2010	20:15:02.44	39° 00.03'	111° 22.63'	1.32

Table 5.2 Continued

Date	Time, h:min:s	Latitude	Longitude	Magnitude
December 3, 2010	5:53:25.47	38° 59.27'	111° 22.64'	1.51
December 4, 2010	12:00:22.79	39° 00.01'	111° 22.81'	1.52
December 4, 2010	14:08:43.15	38° 59.61'	111° 22.45'	1.08
December 6, 2010	5:57:49.29	38° 59.69'	111° 21.79'	1.21
December 6, 2010	11:20:10.17	39° 00.27'	111° 22.35'	1.50
December 6, 2010	19:00:08.80	38° 59.93'	111° 22.18'	1.38
December 6, 2010	22:18:58.33	39° 00.25'	111° 21.99'	1.46
December 7, 2010	2:46:39.08	38° 58.40'	111° 21.19'	1.49
December 7, 2010	16:39:05.46	39° 00.07'	111° 22.40'	1.74
December 7, 2010	19:17:17.61	38° 59.95'	111° 22.90'	1.37
December 7, 2010	22:27:59.01	38° 59.75'	111° 22.26'	1.43
December 7, 2010	23:03:33.20	38° 59.93'	111° 22.94'	1.62
December 8, 2010	2:14:05.26	38° 59.70'	111° 22.12'	1.27
December 8, 2010	5:14:41.42	39° 00.15'	111° 22.86'	1.72
December 8, 2010	7:25:01.59	39° 00.56'	111° 22.54'	1.30
December 8, 2010	13:06:33.47	38° 59.42'	111° 22.15'	1.19
December 10, 2010	10:57:09.69	39° 00.59'	111° 22.07'	1.32
December 10, 2010	21:10:23.02	38° 58.45'	111° 23.67'	1.35
December 10, 2010	22:45:29.34	38° 59.74'	111° 23.34'	1.70
December 10, 2010	23:54:03.57	38° 59.61'	111° 22.17'	1.48
December 11, 2010	3:06:00.68	39° 00.36'	111° 22.58'	1.53
December 12, 2010	11:11:59.07	39° 00.68'	111° 22.12'	1.63
December 12, 2010	20:32:29.72	38° 59.93'	111° 22.49'	1.40
December 13, 2010	21:34:59.81	38° 58.50'	111° 24.20'	1.40
December 14, 2010	5:26:32.62	38° 59.44'	111° 22.58'	1.65
December 14, 2010	9:29:19.17	39° 00.54'	111° 21.86'	1.34
December 14, 2010	9:35:07.18	38° 59.53'	111° 22.22'	1.51
December 14, 2010	10:32:31.51	38° 59.77'	111° 22.36'	1.59
December 14, 2010	11:56:37.91	38° 59.76'	111° 22.71'	1.72
December 14, 2010	12:25:40.28	38° 59.85'	111° 22.06'	1.15
December 14, 2010	12:30:49.73	38° 59.92'	111° 22.39'	1.37
December 14, 2010	17:33:59.13	39° 00.99'	111° 22.85'	1.43
December 14, 2010	21:25:19.48	39° 00.22'	111° 22.56'	1.45
December 14, 2010	23:24:42.74	38° 59.95'	111° 23.08'	1.48
December 15, 2010	3:28:33.12	38° 59.99'	111° 22.61'	1.69

Table 5.2 Continued

Date	Time, h:min:s	Latitude	Longitude	Magnitude
December 15, 2010	8:41:34.15	38° 59.72'	111° 21.92'	1.17
December 15, 2010	13:30:24.58	39° 00.19'	111° 22.55'	1.78
December 16, 2010	0:16:36.73	38° 59.75'	111° 23.87'	1.57
December 16, 2010	7:43:46.11	38° 59.97'	111° 22.20'	1.52
December 16, 2010	8:50:52.47	38° 59.95'	111° 22.07'	1.39
December 16, 2010	10:17:13.28	39° 00.78'	111° 21.64'	1.25
December 16, 2010	11:19:58.99	38° 59.70'	111° 22.91'	1.32
December 16, 2010	13:24:27.56	38° 59.76'	111° 22.48'	1.00
December 16, 2010	17:01:08.82	39° 00.35'	111° 22.64'	1.83
December 16, 2010	22:37:03.10	38° 59.94'	111° 22.07'	1.79
December 17, 2010	2:23:02.67	38° 59.69'	111° 21.73'	2.17
December 17, 2010	7:49:06.84	39° 00.00'	111° 22.26'	1.52
December 17, 2010	16:44:15.29	38° 59.91'	111° 22.78'	1.73
December 17, 2010	17:17:06.84	38° 59.95'	111° 22.79'	2.14
December 17, 2010	21:13:33.50	39° 00.06'	111° 22.80'	1.57
December 17, 2010	23:47:36.82	38° 59.54'	111° 20.72'	2.20
December 18, 2010	0:49:23.29	38° 59.81'	111° 22.43'	1.73
December 18, 2010	21:53:35.45	38° 59.74'	111° 22.24'	1.62
December 19, 2010	1:39:54.31	39° 00.17'	111° 22.44'	1.56
December 19, 2010	11:11:13.48	38° 59.64'	111° 22.16'	1.59
December 19, 2010	18:39:20.67	39° 00.08'	111° 22.55'	1.82
December 20, 2010	14:13:04.42	38° 59.76'	111° 22.30'	1.47
December 20, 2010	14:29:09.65	38° 59.71'	111° 21.96'	1.36
December 20, 2010	20:40:50.98	39° 00.45'	111° 22.60'	1.25
December 21, 2010	6:12:10.09	39° 00.15'	111° 22.81'	1.82
December 23, 2010	9:50:21.17	38° 59.81'	111° 22.05'	1.07
December 23, 2010	9:54:49.15	38° 59.86'	111° 22.68'	1.71
December 23, 2010	11:19:38.55	39° 00.21'	111° 23.08'	1.69
December 23, 2010	15:35:04.23	39° 00.19'	111° 22.39'	1.78
December 23, 2010	23:01:22.61	39° 00.19'	111° 22.69'	2.11
December 23, 2010	23:43:20.42	39° 00.06'	111° 22.98'	2.15
December 23, 2010	23:54:47.04	39° 00.11'	111° 22.61'	2.04
December 24, 2010	0:13:58.27	38° 59.64'	111° 22.35'	1.63
December 24, 2010	5:43:00.88	38° 59.34'	111° 22.50'	1.62
December 24, 2010	23:16:18.83	39° 00.18'	111° 21.85'	1.86

Table 5.2 Continued

Date	Time, h:min:s	Latitude	Longitude	Magnitude
December 25, 2010	0:06:03.39	38° 59.68'	111° 21.83'	1.67
December 26, 2010	12:34:26.45	39° 00.10'	111° 22.42'	1.48
December 27, 2010	12:37:24.38	39° 00.40'	111° 22.56'	1.13
December 27, 2010	13:40:21.35	39° 00.59'	111° 23.31'	1.38
December 27, 2010	22:05:33.49	38° 59.91'	111° 22.42'	1.46
December 28, 2010	3:32:12.34	38° 59.77'	111° 22.85'	1.06
December 28, 2010	16:01:54.30	38° 59.63'	111° 22.97'	1.48
December 28, 2010	21:06:00.32	38° 59.77'	111° 23.03'	1.51
December 29, 2010	8:11:49.72	39° 00.43'	111° 22.25'	1.17
December 30, 2010	2:01:41.84	38° 59.84'	111° 22.29'	1.70
January 1, 2011	13:42:01.64	38° 59.84'	111° 22.04'	1.25
January 1, 2011	14:18:04.18	38° 59.96'	111° 21.28'	1.61
January 2, 2011	19:00:02.54	39° 00.15'	111° 21.34'	1.83
January 3, 2011	10:53:42.57	39° 00.55'	111° 22.74'	1.27
January 4, 2011	12:15:32.73	38° 59.84'	111° 22.02'	1.40
January 4, 2011	16:27:50.96	38° 59.53'	111° 22.24'	1.55
January 4, 2011	22:11:09.17	39° 00.19'	111° 22.29'	1.72
January 5, 2011	4:37:06.76	39° 00.11'	111° 22.82'	1.73
January 5, 2011	5:00:40.38	39° 00.39'	111° 21.55'	1.43
January 5, 2011	13:50:35.67	39° 00.0'	111° 22.81'	1.85
January 5, 2011	17:32:30.43	39° 00.14'	111° 21.90'	1.69
January 5, 2011	18:23:07.61	39° 00.03'	111° 22.97'	2.44
January 5, 2011	19:21:10.40	39° 00.32'	111° 23.23'	1.79
January 5, 2011	23:10:11.67	39° 00.45'	111° 22.58'	1.68
January 6, 2011	0:38:33.21	38° 59.86'	111° 22.84'	1.67
January 7, 2011	3:12:24.67	39° 00.43'	111° 22.03'	1.49
January 10, 2011	19:14:36.41	38° 59.99'	111° 22.75'	1.58
January 15, 2011	6:19:48.11	38° 59.71'	111° 22.53'	1.38
January 16, 2011	12:37:47.08	39° 00.27'	111° 22.62'	1.67
January 18, 2011	9:40:19.12	38° 59.52'	111° 22.22'	1.24
January 18, 2011	23:37:48.77	38° 59.88'	111° 22.98'	2.35
January 19, 2011	10:25:12.79	38° 59.42'	111° 23.65'	1.64
January 20, 2011	14:27:39.54	39° 00.77'	111° 22.20'	1.63
January 26, 2011	10:51:22.24	39° 00.43'	111° 22.01'	1.41
January 27, 2011	10:18:57.43	38° 59.63'	111° 23.09'	1.69

Table 5.2 Continued

Date	Time, h:min:s	Latitude	Longitude	Magnitude
January 30, 2011	3:12:51.95	38° 59.01'	111° 22.89'	2.03
February 9, 2011	11:58:45.14	38° 59.95'	111° 22.47'	1.56

Table 5.3 June 1, 2015 to November 30, 2015 seismic events—Utah region

Date	Time, h:min:s	Latitude	Longitude	Magnitude
June 26, 2015	19:12:50.95	38° 56.74'	111° 22.14'	1.06
August 9, 2015	2:34:27.52	38° 56.08'	111° 22.14'	0.92
October 8, 2015	8:13:47.06	38° 57.56'	111° 22.44'	1.67
October 9, 2015	2:29:43.56	38° 58.65'	111° 22.71'	1.30
November 4, 2015	16:38:20.14	38° 59.82'	111° 22.10'	1.11
November 19, 2015	14:28:45.8	38° 57.71'	111° 22.55'	1.25

Table 5.4 November 19, 2007 to March 29, 2011 UUSS catalog seismic events—Wyoming region

Date	Time, h:min:s	Latitude	Longitude	Magnitude
November 22, 2007	2:29:36.46	41° 37.98'	109° 44.17'	3.42
December 22, 2007	5:59:46.45	41° 37.64'	109° 55.08'	2.59
February 9, 2008	17:41:49.85	41° 40.06'	109° 53.32'	3.32
March 7, 2009	2:45:10.18	41° 40.21'	109° 55.39'	3.51

Table 5.5 November 2007 to May 2009 ANF catalog seismic events—Wyoming region

Date	Time, h:min:s	Latitude	Longitude	Magnitude
November 22, 2007	2:29:36	41° 37.80'	109° 44.40'	3.40
December 22, 2007	5:59:46	41° 37.64'	109° 55.08'	2.59
January 20, 2008	12:03:31	41° 40.12'	109° 54.17'	1.65
February 9, 2008	17:41:49	41° 39.03'	109° 53.83'	3.58
July 16, 2008	7:38:03	41° 37.07'	109° 50.66'	2.21
March 7, 2009	2:45:10	41° 40.20'	109° 55.20'	3.50

CHAPTER 6

SUBSIDENCE AND SEISMICITY—UTAH REGION

6.1 Introduction

DInSAR can be a viable technique for measuring small surface displacements with high temporal and spatial resolutions. Using DInSAR to quantify mine subsidence has potential to clearly define subsidence dynamics and may identify relationships between subsidence and MIS. This chapter presents results of the application of DInSAR for mine subsidence monitoring for one mine in the Wasatch Plateau region of central Utah. First, general characteristics of the geology, vegetation, and subsidence of the Wasatch Plateau study region are described. Next, subsidence monitoring results using L-band and X-band DInSAR are presented. For the periods DInSAR generated measureable subsidence, subsidence maps are presented and the temporal progression of subsidence is defined. Finally, cataloged seismicity and surface deformations are compared.

6.2 Geology, Vegetation, and Subsidence Characteristics

The Wasatch Plateau is characterized by rugged topography with flat topped mesas and steeply incised canyons. The subalpine region of the Wasatch Plateau is heavily vegetated; grasses, forbs, and low shrubs are dominant. Steep northern exposures

at higher elevations are heavily forested by spruce and alpine fir. At lower elevations, on steep southern exposures, aspen, pine, and tall shrubs are common (Ellison 1954). The Wasatch Plateau is geologically complex and exists in a region of transition from the Colorado Plateau to the east and the Basin and Range Province to the west (Arabasz et al. 2007). Dominant structures include northward trending normal faults and grabens, vertical joints, and vertical strike-slip faults (Pankow et al. 2008). Figure 6.1 shows a TerraSAR-X image of a region of the Wasatch Plateau. In this image, topographic features of the Wasatch Plateau are discernable.

In the study region, coal has been mined from the Upper and Lower Hiawatha seams. These seams are present in the lower 75 to 110 m of the Blackhawk Formation (Mesaverde Group), which has a total thickness ranging from 190 to 245 m. Prominent near seam geology includes the Castlegate and the Star Point Sandstones, both massive, medium to course grained sandstones. The Castlegate Sandstone overlays the Blackhawk Formation and has a thickness ranging from 45 to 150 m. The Star Point Sandstone, lies beneath the Blackhawk Formation and has a thickness ranging from 25 to 300 m (Doelling 1972). Significant MIS is attributed to the presence of these sandstones.

The Wasatch Plateau mine imaged for this study has a mining height ranging from 2.6 to 3.8 m and an overburden thickness ranging from 305 to 550 m. Maximum vertical subsidence typically occurs near the center of the longwall panels with a magnitude of 1.5 to 1.8 m. The average reported angle of draw is 15° (Monroe, 2014). Panel widths have ranged from 170 to 335 m, but the subsidence is likely subcritical; increasing the panel width would likely increase the subsidence magnitude. The horizontal component of subsidence is small, 0.15 m in tension and 0.19 m in

compression. Additionally, subsidence is associated with surface cracking. The cracks have apertures up to 0.15 m, and are oriented parallel to the longwall gateroads, parallel to the longwall face, and subparallel to the dominant joint set which strikes at N21°W in the mining region (Goodrich et al. 1999).

6.3 L-Band DInSAR Results

For the central Utah study region, 10 interferograms were generated using L-band data from ALOS in intervals over the period from December 6, 2006 to February 1, 2011. The interferometric data parameters are summarized in Table 4.5. Phase fringes due to surface displacement are identifiable in all 10 interferograms, but all of the images have topographic artifacts and the overall image quality is variable, with average coherence ranging from 0.30 to 0.63. Significantly, the coherence of the interferograms seems to be more affected by seasonal variation in the surface conditions than by the length of the imaging period, which ranges from 46 to 184 days. The interferograms generated from image pairs with one image acquired in December have relatively low coherence regardless of the imaging period. Additionally, in the majority of the interferograms, the regions with the largest displacements have relatively low coherence, and in some areas the deformations rates were too high to be measured coherently and the phases saturated. Overall for subsidence monitoring using L-band SAR data from ALOS, interferograms with short temporal baselines and small spatial baselines have the most distinct and interpretable phase fringes.

6.4 Displacement Mapping (L-Band) and Seismicity

Four interferograms were generated in intervals during the period from December 6, 2006 to December 9, 2007. Vertical displacement maps derived from these interferograms are presented in Figures 6.2 to 6.5. These figures show 5-cm subsidence contours starting at a vertical displacement of −5 cm. Figure 6.6 shows a cumulative displacement map for the December 6, 2006 to December 9, 2007 period. In this image, subsidence is contoured every 10 cm starting from a vertical displacement of −10 cm. In all of the figures, seismic events are red and low coherence pixels are white. Additionally, in these figures, two regions (identified as 1 and 2) are affected by subsidence. For each region, maximum subsidence magnitudes for each period and for the cumulative subsidence data are presented in Table 6.1. Figures 6.7 to 6.9 show magnitude versus time plots of the seismicity occurring within 15 days of the imaging periods. In these figures, events spatially clustered near the regions affected by subsidence are identified in black and events that are significantly displaced from the regions affected by subsidence are identified in green. No magnitude time plot is presented for the June 8 to September 8, 2007 period; only one event was cataloged during this period. For each period, seismic event rates for both of the regions affected by subsidence are presented in Table 6.1. Finally, Figure 6.10 to 6.13 show time series profiles of subsidence along the section lines defined in Figure 6.6. Gaps in the profiles result from missing data caused by low coherence pixels.

Six interferograms were generated in intervals during the period from December 14, 2009 to February 1, 2011. Vertical displacement maps derived from these interferograms are presented in Figures 6.14 to 6.19. The figures show 5-cm subsidence

contours starting at a vertical displacement of −5 cm. Figure 6.20 shows a cumulative displacement map for the December 14, 2009 to February 1, 2011 period. In this image, subsidence is contoured every 10 cm starting from a vertical displacement of −10 cm. In all of the figures, seismic events are shown in red and low coherence pixels are white. In these figures, only one region is affected by subsidence. For this region, the maximum subsidence magnitudes for each period and for the cumulative subsidence data are presented in Table 6.2. Figures 6.21 to 6.26 show magnitude versus time plots of the seismicity occurring within 15 days of the imaging periods. Again, events spatially clustered near the regions affected by subsidence are identified in black and events that are significantly displaced from the regions affected by subsidence are identified in green. Seismic event rates are presented in Table 6.2. Finally, Figure 6.27 shows time series profiles of subsidence along the section line AA' defined in Figure 6.20.

From the data, several observations are significant. First, for the December 6, 2006 to December 9, 2007 period, the maximum subsidence in region 1 was only 0.95 m and the maximum subsidence in region 2 was only 0.38 m. Using conventional aerial surveys, maximum subsidence on the order of 2 m was reported for both of these regions. It is likely that the imaging period did not capture the full development of subsidence in either region. For the December 14, 2009 to February 1, 2011 period, the maximum subsidence was 1.8 m, which is within 20 cm of the reported 2-m maximum subsidence. The maximum subsidence measured by DInSAR may be underestimated as a result of poor coherence in regions of large displacement.

Next, from the cumulative maps (Figures 6.6 and 6.20), three distinctive groups of seismicity are apparent. Two groups of events spatially cluster near regions 1 and 2.

These events are shown in black in the magnitude versus time plots (Figures 6.7 through 6.9 and 6.21 through 6.26). Over relatively long periods, these two groups of events appear spatially well correlated with subsidence. In the third group, the events are not spatially clustered and are kilometers from the regions affected by subsidence. These events are shown in green in the magnitude versus time plots. Although these events may be induced, their spatial and temporal characteristics are significantly different from the events that spatially cluster near regions 1 and 2.

In the cumulative subsidence maps the majority of the seismicity appears spatially well correlated with surface displacements, but over shorter periods, spatial correlation between seismicity and subsidence is less consistent. Several periods with significant displacement have relatively low levels of seismicity. Lack of correlation is most evident in region 1 during the period from December 6, 2006 to June 8, 2007. The surface subsides over 70 cm during this period, but no seismicity spatially correlates with subsidence. Generally for the study region, seismicity appears to lag subsidence. This lag is indicated both spatially in the shorter period data, where significant displacements occur but there is little or no seismicity, and in the magnitude time plots, where periods of no seismicity are followed by periods of fairly regular seismicity.

Inconsistent relationships between subsidence and seismicity are further illustrated in Figure 6.28. This figure shows the maximum subsidence rate plotted versus the seismic event rate for each region affected by subsidence for each imaging period. In general, low subsidence rates are associated with low seismic event rates. For higher subsidence rates, more than 1 cm/d, the seismic event rates vary more significantly from less than one event per day to a maximum of close to 1.7 events per day. But as a general

trend, higher rates of subsidence are associated with higher rates of seismicity.

6.5 X-Band DInSAR Results

For the Wasatch Plateau study region, 15 interferograms were generated using X-band SAR data in intervals over the period from June 7 to November 22, 2015. The interferometric data parameters are summarized in Table 4.7. Phase fringes due to surface displacement are identifiable in the majority of the interferograms; the area affected by subsidence is identified by the white box in Figure 6.29. Though fringes are identifiable, they are difficult to precisely interpret and to unwrap. The average coherence of the inteferograms ranges from 0.50 to 0.66, but in the X-band data, coherence has a strong spatial dependence. Coherence is generally high over the valley floors and low in the vegetated subalpine regions. Additionally, though the TerraSAR-X imaging periods are short, at most 33 days, variable surface conditions in the subalpine regions contribute to low coherence and significant phase noise. Some of the interferograms have strong topographic artifacts, and these artifacts reduce the phase clarity, especially in regions where there are large topographic changes. Finally, in some of the interferograms, large displacement rates cause phase saturation which also reduces the interpretability of the phase fringes.

As result of difficulty interpreting and unwrapping the interferometric fringes, displacement data were not derived from the X-band interferograms. All 15 of the filtered differential interferograms for the Wasatch Plateau study region generated using X-band data are presented the Appendix. In these figures, colored outlines bound the phase fringes due to subsidence. Two of the interferograms (Figures A.1 and A.2) were

generated using data from orbit 159, which has a descending track and a look angle of 24°. Thirteen of the interfeograms (Figures A.3 through A.15) were generated using data from orbit 30, which has an ascending track and look angle of 37°. Overall, the interferograms from orbit 30 have better coherence and better defined fringes in both the subalpine and valley floor regions of the Wasatch Plateau. However, two of the interferograms (Figures A.12 and A.15) generated from the orbit 30 data do not have definable phase fringes due to subsidence. The interferogram from October 9 to October 20, 2015 (Figure A.12) is relatively coherent and it is likely that no surface displacement took place during this period. The coherence of the November 11 to November 22, 2015 interferogram (Figure A.15) is poor, especially in the subalpine regions of the Wasatch Plateau, and seasonal variation ground cover likely contributed to the loss of phase data for this period.

Though the maximum subsidence magnitudes are difficult to precisely quantify in the X-band inteferograms, the subsidence extent is identifiable in most of the data, and in some cases, the magnitudes and rates of subsidence can be reasonably estimated. Figure 6.30 shows the June 10, 2015 to June 21, 2015 interferogram with the subsidence boundaries for the consecutive periods from June 10 to November 1, 2015 overlain. In this figure, though the subsidence magnitudes are not precisely quantified, the general progression of subsidence is definable. Also, in the June 10, 2015 to June 21, 2015 interferogram presented in this figure, there are at least seven fringes due to subsidence (outlined in red) indicating a maximum vertical displacement of more than 13 cm and a maximum subsidence rate of more than 1 cm/d.

During the TerraSAR-X imaging period from June 7 to November 22, 2015, both

the extent and rate of subsidence in the Wasatch Plateau study region were significant, but only six seismic events were cataloged near the mining region. These events, identified in red in Figure 6.29, are all measurably displaced from the actively subsiding region. It is possible that the events are not mining induced, but they may indicate dynamic failures in mined out regions where the surface is stable. The lack of seismicity spatially correlated with subsidence during the June 7 to November 22, 2015 period supports the argument that, in this mining region, seismicity is significantly delayed during some periods of active mining.

Table 6.1 Maximum subsidence magnitudes and seismic event rates: December 6, 2006 to December 9, 2007

Period	Region 1		Region 2	
	Maximum Subsidence Magnitude, cm	Seismic Event Rate, No/d	Maximum Subsidence Magnitude, cm	Seismic Event Rate, No/d
December 6, 2006 – June 8, 2007 (184 days)	70	-	38	0.17
June 8, 2007 – September 8, 2007 (92 days)	24	-	-	0.01
September 8, 2007 – October 24, 2007 (46 days)	26	0.11	-	-
October 24, 2007 – December 9, 2007 (46 days)	48	0.89	-	-
December 6, 2006 – December 9, 2007 (368 days)	95	0.13	38	0.09

Table 6.2 Maximum subsidence magnitudes and seismic event rates: December 14, 2009 to February 1, 2011

Period	Region 1	
	Maximum Subsidence Magnitude, cm	Seismic Event Rate, No/d
December 14, 2009 – May 1, 2010 (138 days)	59	0.15
May 1, 2010 – June 16, 2010 (46 days)	48	0.04
June 16, 2010 – August 1, 2010 (46 days)	98	1.50
August 1, 2010 – September 16, 2010 (46 days)	60	0.67
September 16, 2010 – December 17, 2010 (92 days)	84	1.68
December 17, 2010 – February 1, 2011 (46 days)	59	1.20
December 14, 2009 – February 1, 2011 (414 days)	178	0.81

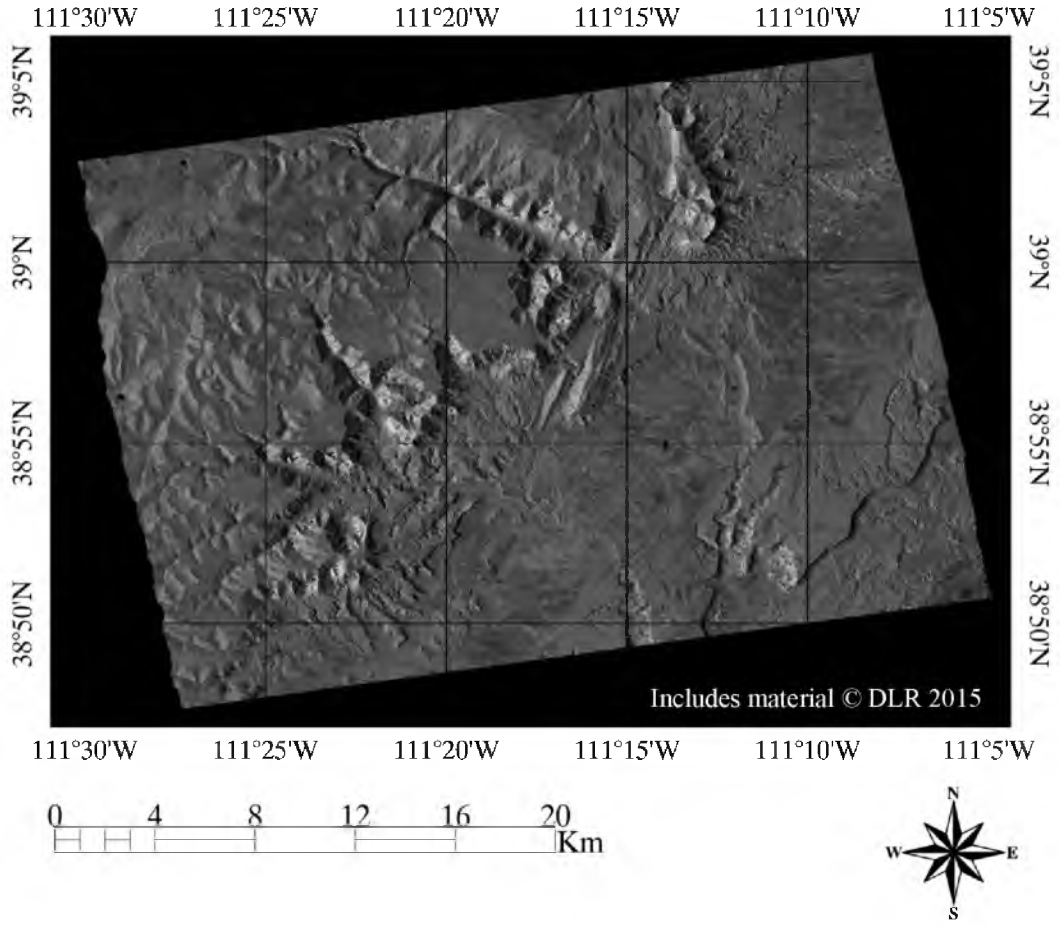

FIGURE 6.1 TDX-1 intensity image of the Wasatch Plateau study region (October 20, 2015)

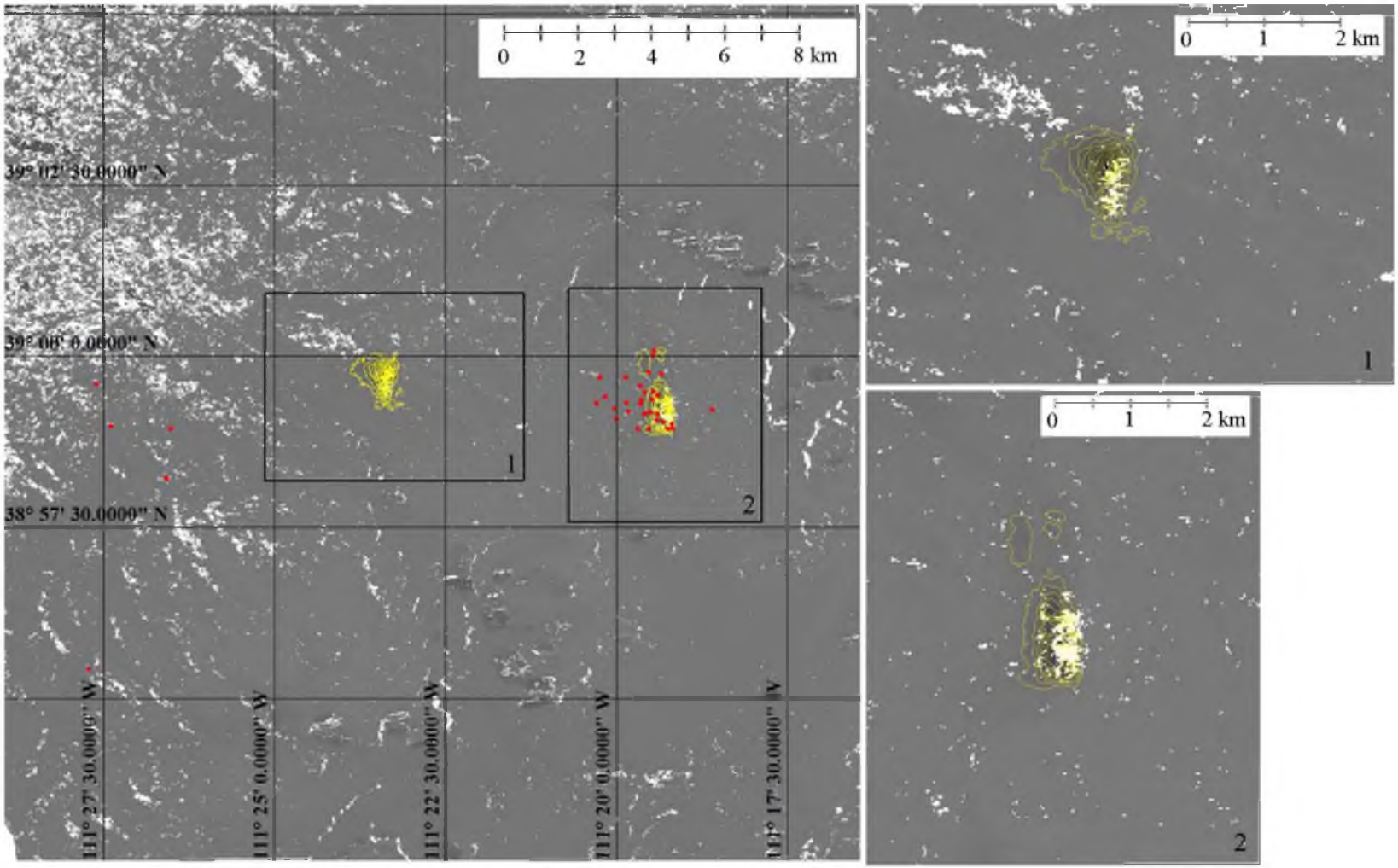

FIGURE 6.2 Displacement maps (L-band) and seismic event locations (red): December 6, 2006 to June 8, 2007 (184 days). Subsidence is contoured every 5 cm starting at −5 cm of vertical displacement.

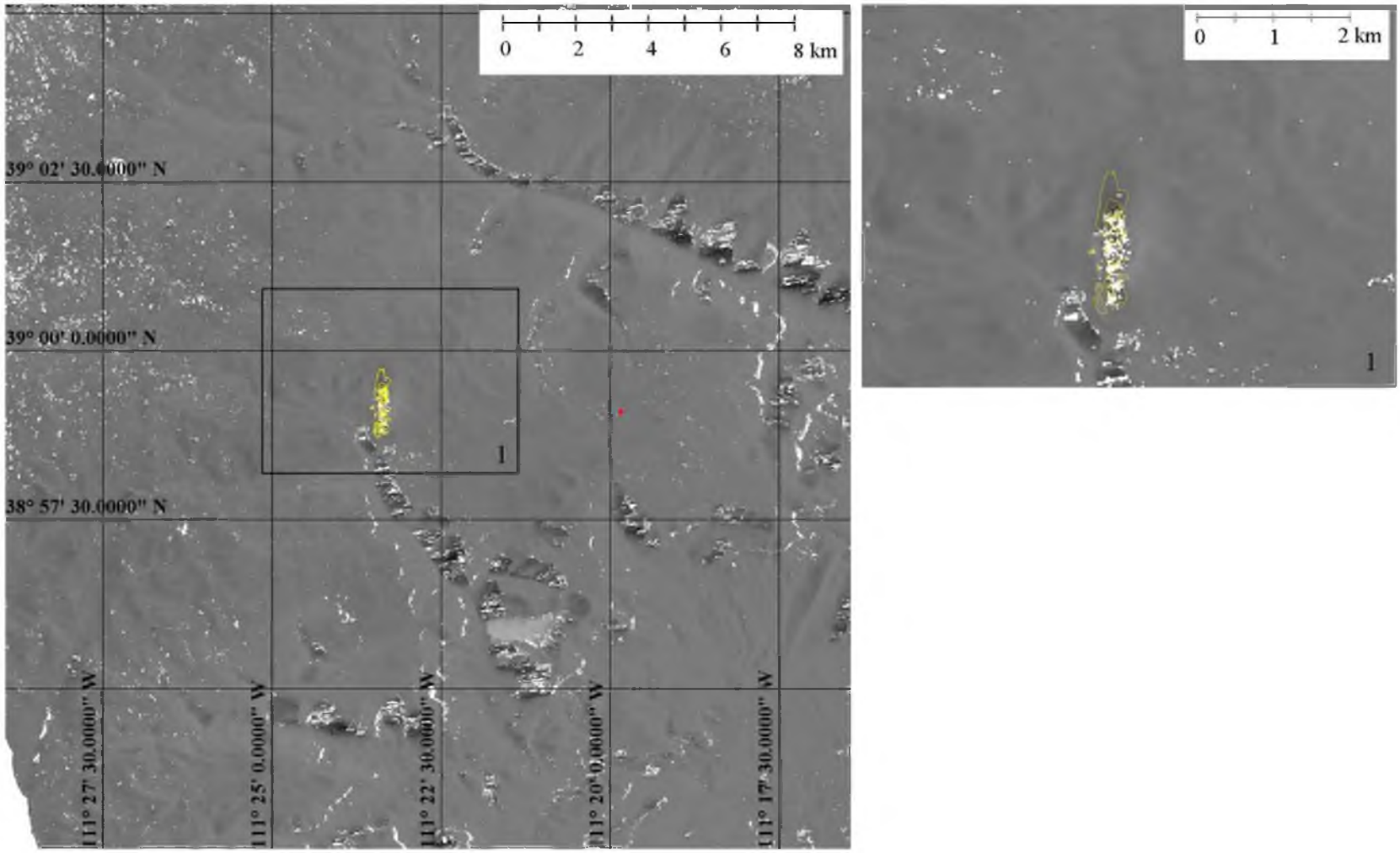

FIGURE 6.3 Displacement maps (L-band) and seismic event location (red): June 8, 2007 to September 8, 2007 (92 days). Subsidence is contoured every 5 cm starting at −5 cm of vertical displacement.

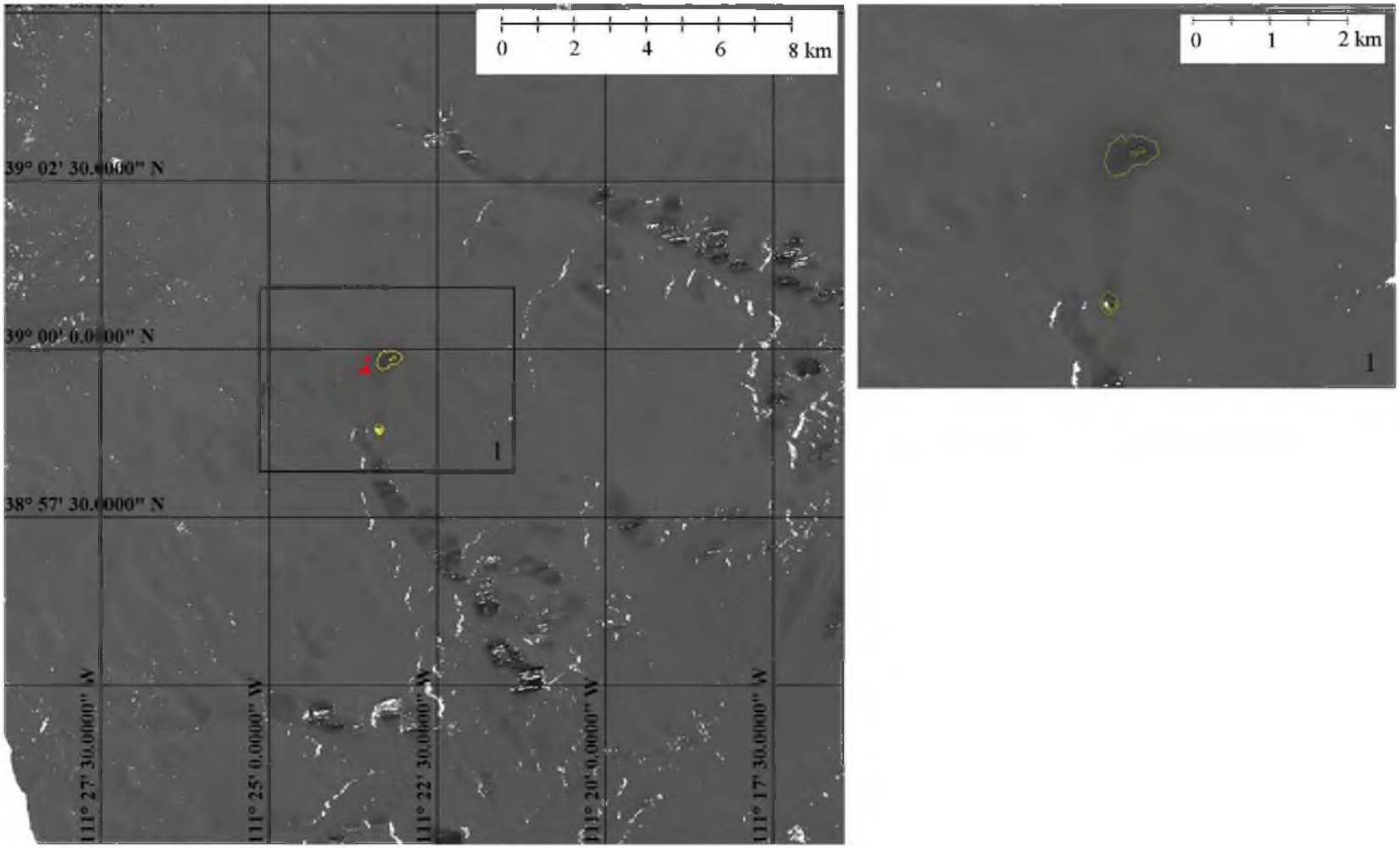

FIGURE 6.4 Displacement maps (L-band) and seismic event locations (red): September 8, 2007 to October 24, 2007 (46 days). Subsidence is contoured every 5 cm starting at −5 cm of vertical displacement.

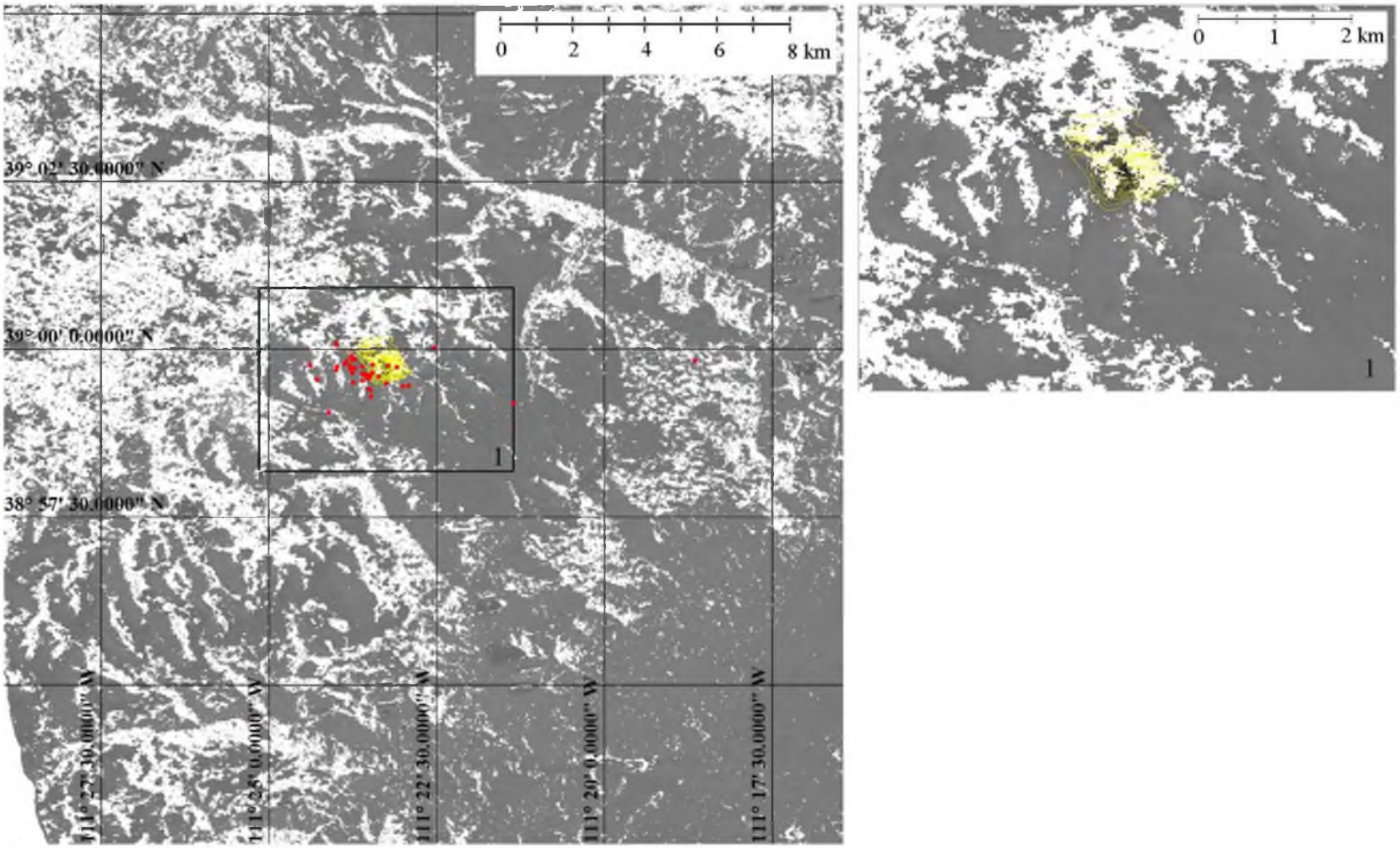

FIGURE 6.5 Displacement maps (L-band) and seismic event locations (red): October 24, 2007 to December 9, 2007 (46 days). Subsidence is contoured every 5 cm starting at −5 cm of vertical displacement.

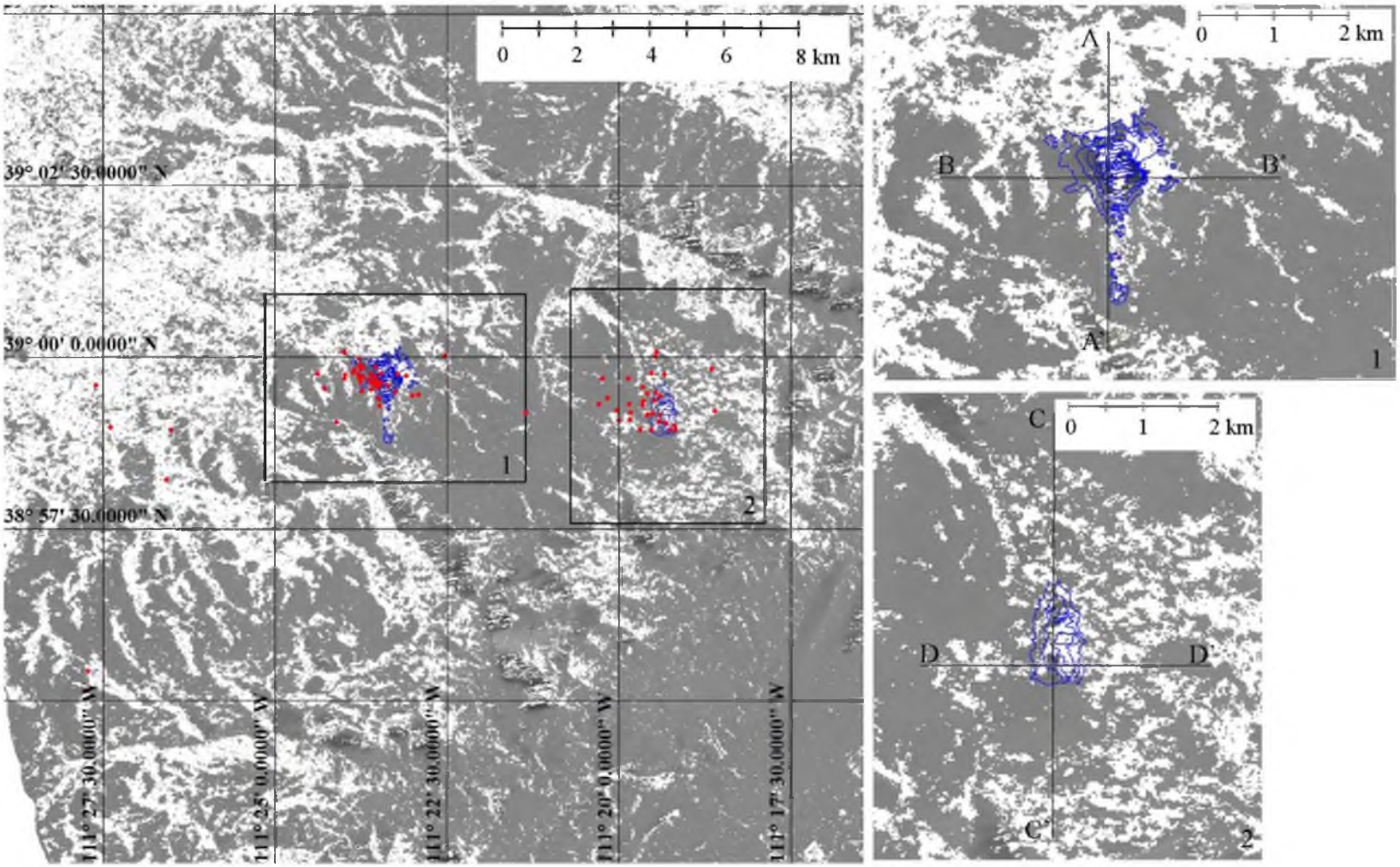

FIGURE 6.6 Cumulative displacement maps (L-band) and seismic event locations (red): December 6, 2006 to December 9, 2007 (368 days). Subsidence is contoured every 10 cm starting at −10 cm of vertical displacement.

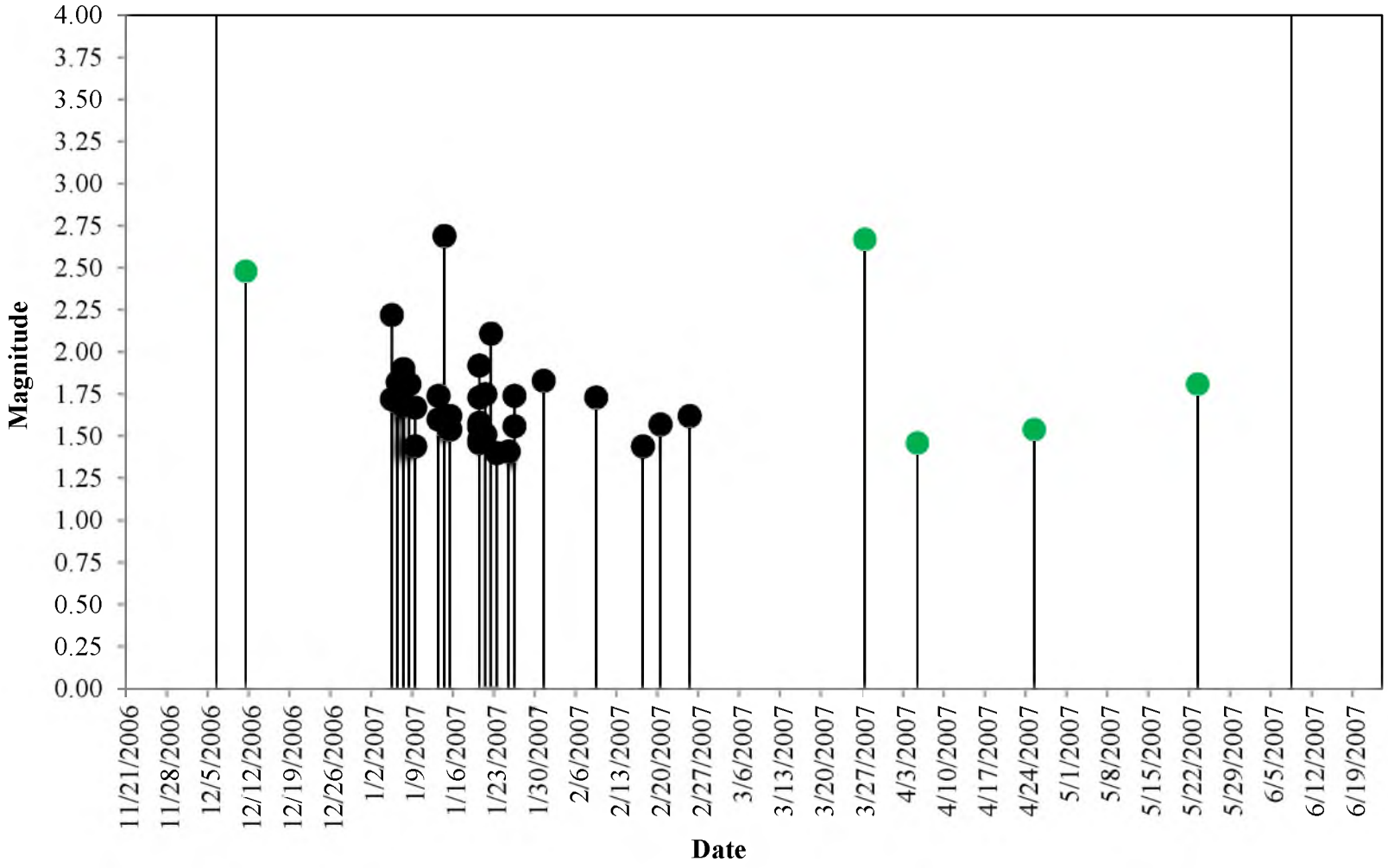

FIGURE 6.7 Magnitude and time of seismicity occurring within 15 days of the December 6, 2006 to June 8, 2007 period. Events identified in green are significantly displaced from the subsided regions.

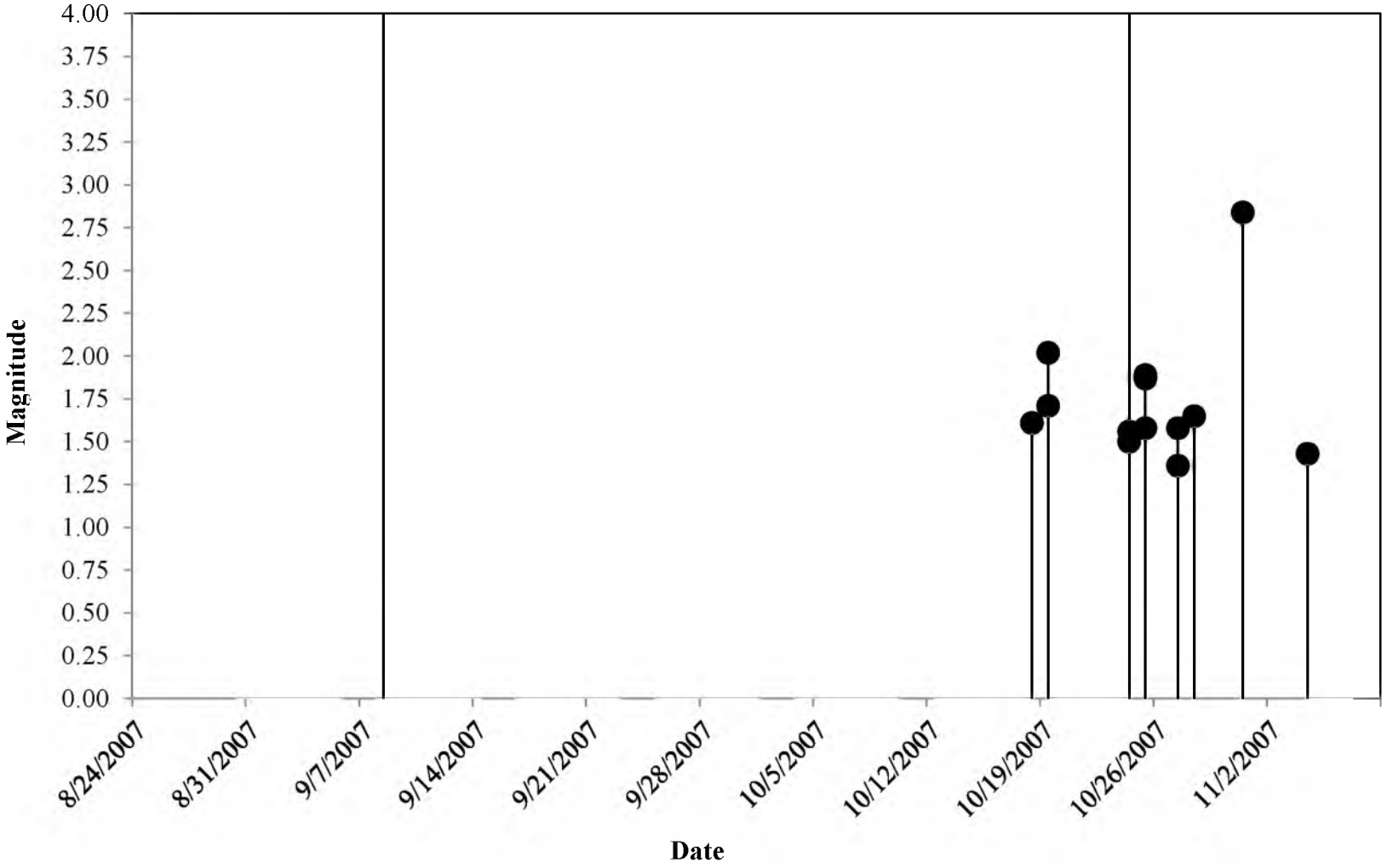

FIGURE 6.8 Magnitude and time of seismicity occurring within 15 days of the September 8, 2007 to October 24, 2007 period

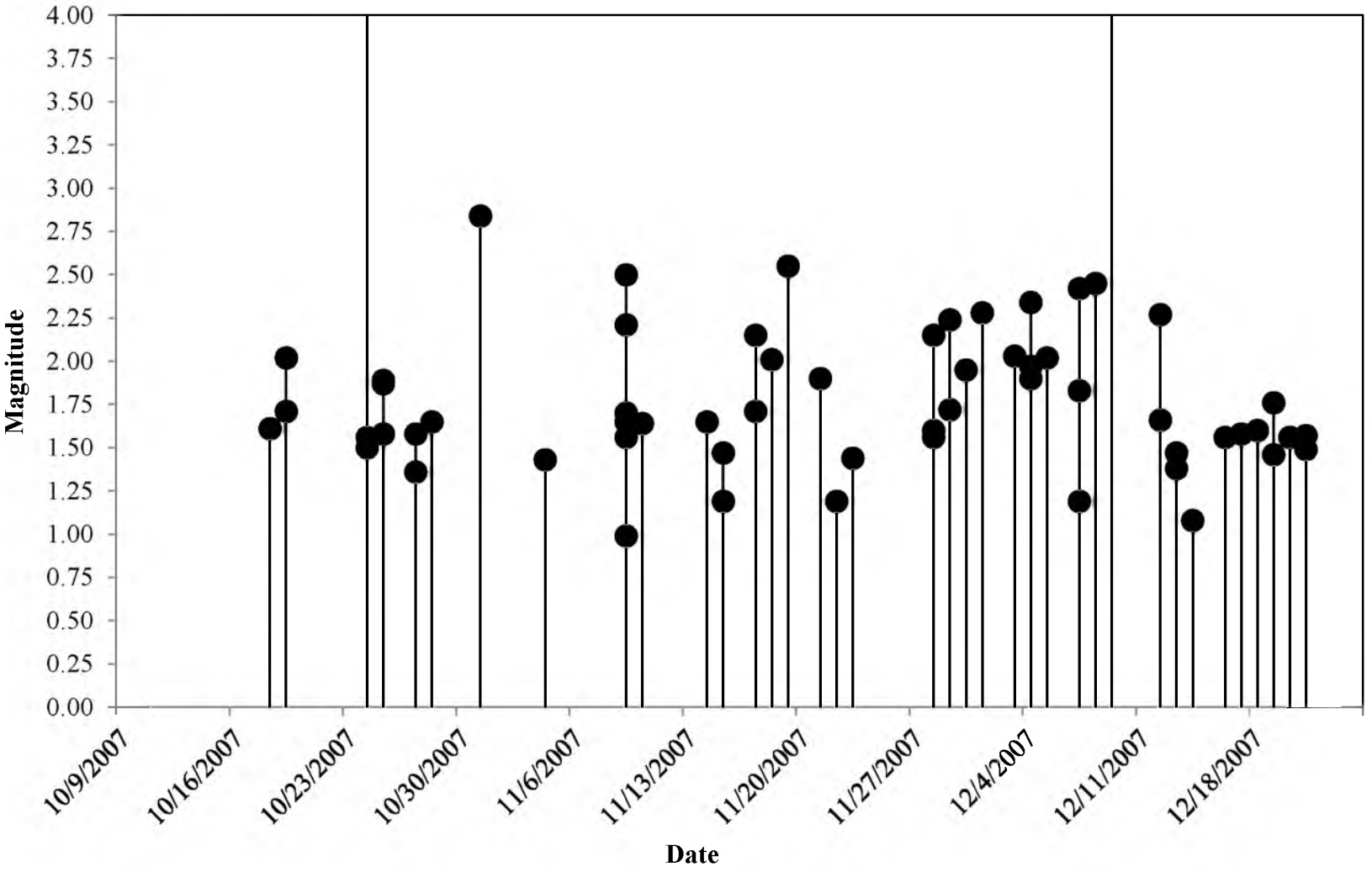

FIGURE 6.9 Magnitude and time of seismicity occurring within 15 days of the October 24, 2007 to December 9, 2007 period

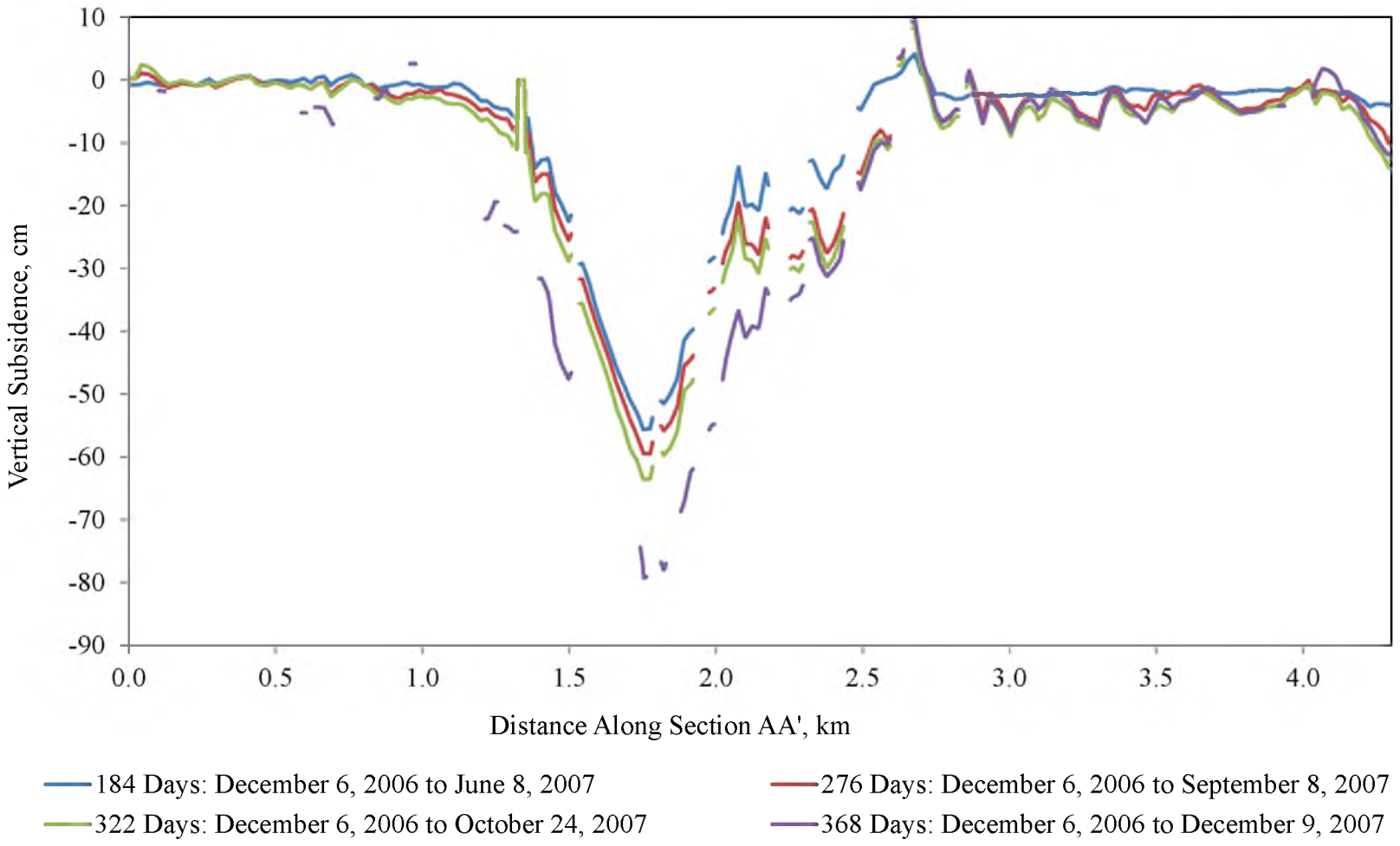

FIGURE 6.10 Time series subsidence profiles of section AA' from Figure 6.6

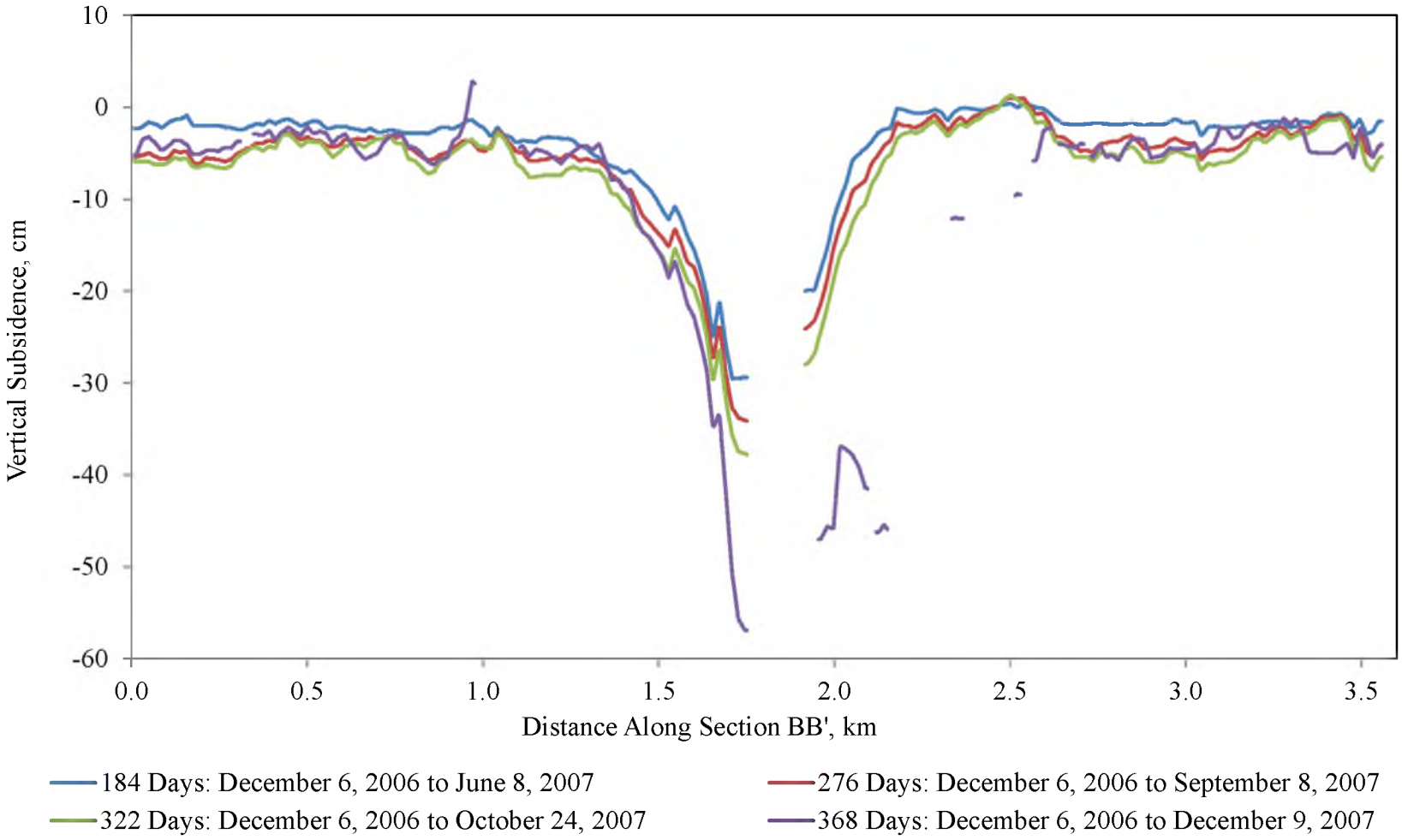

FIGURE 6.11 Time series subsidence profiles of section BB' from Figure 6.6

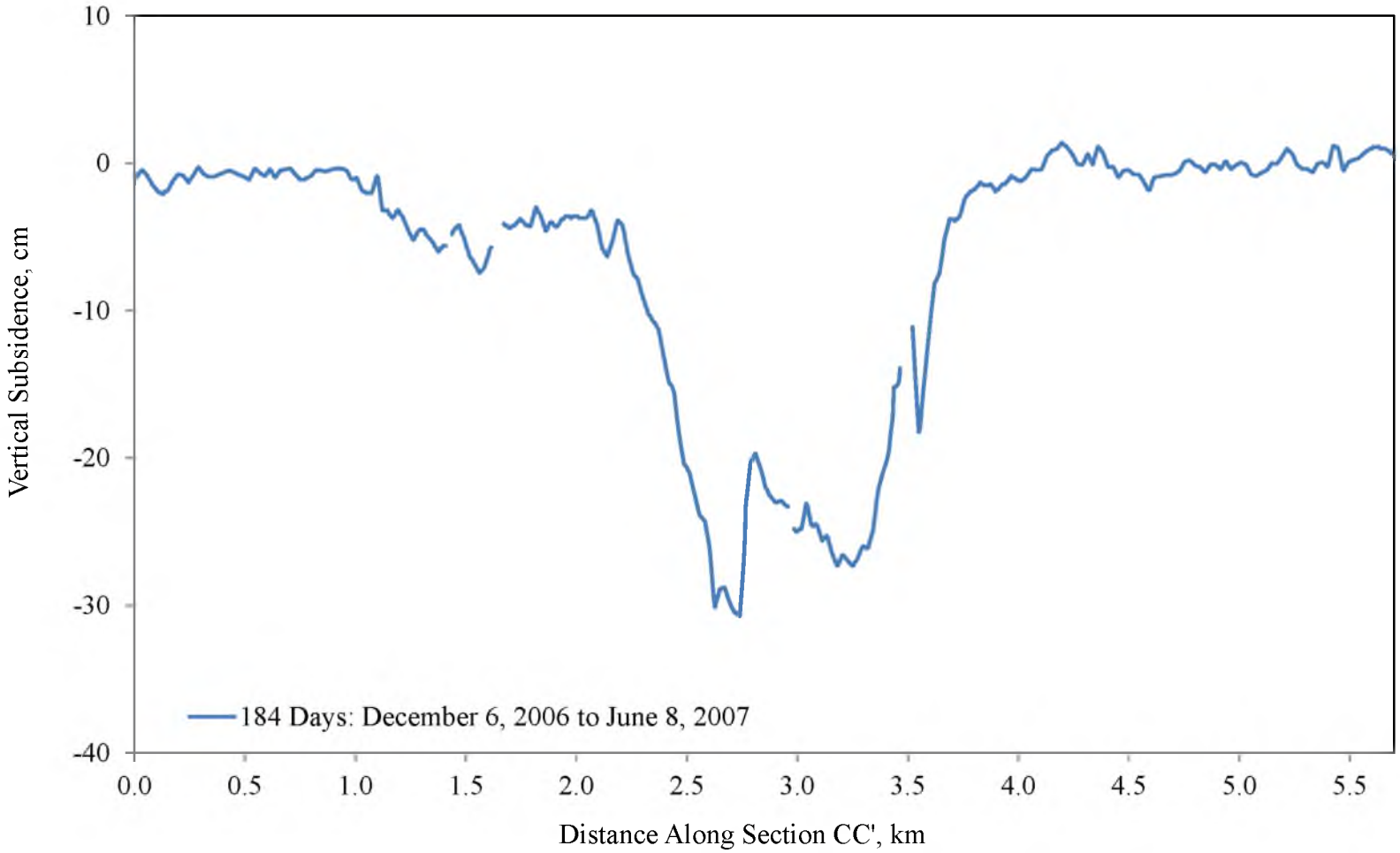

FIGURE 6.12 Time series subsidence profiles of section CC' from Figure 6.6

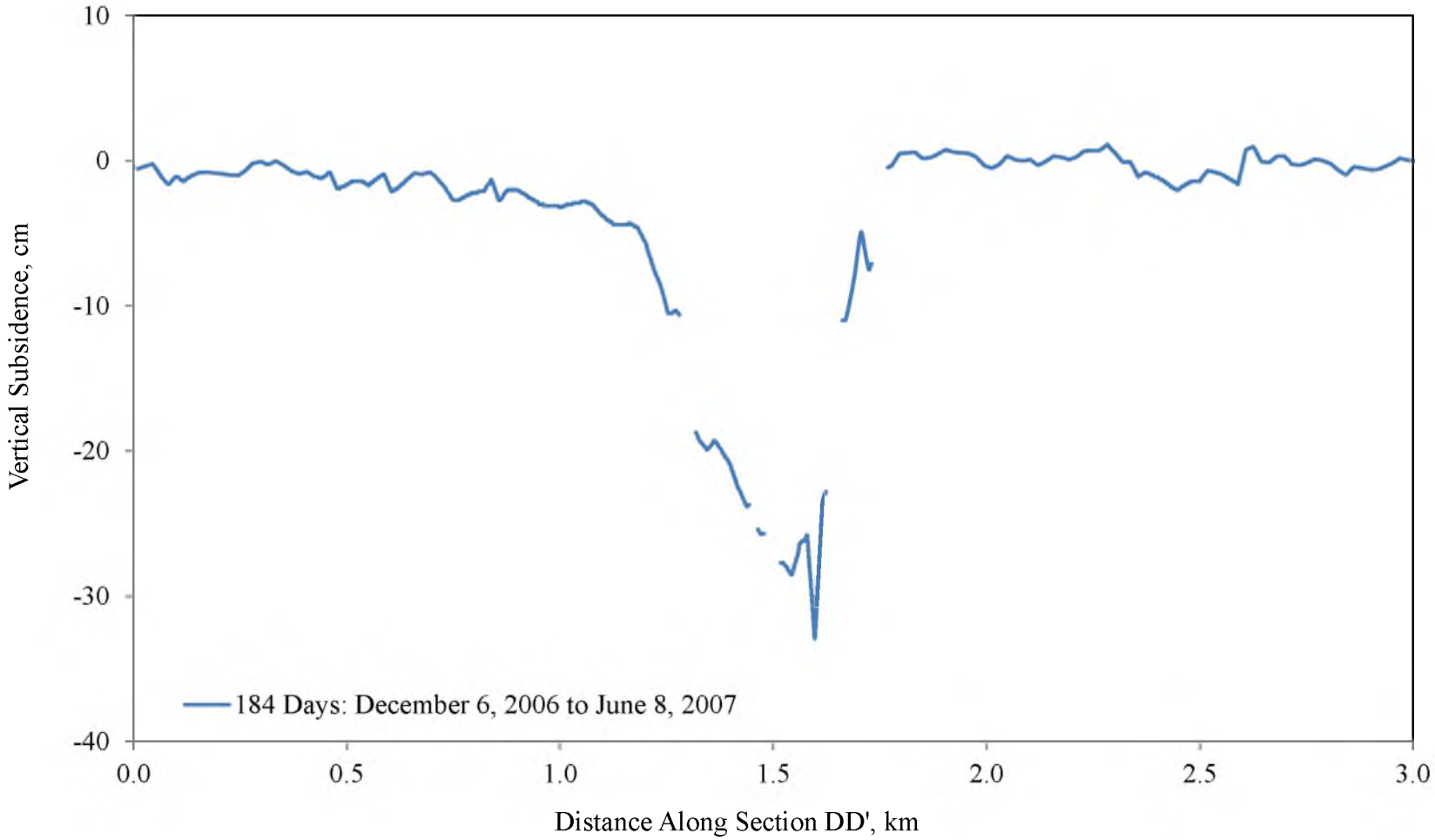

FIGURE 6.13 Time series subsidence profiles of section DD' from Figure 6.6

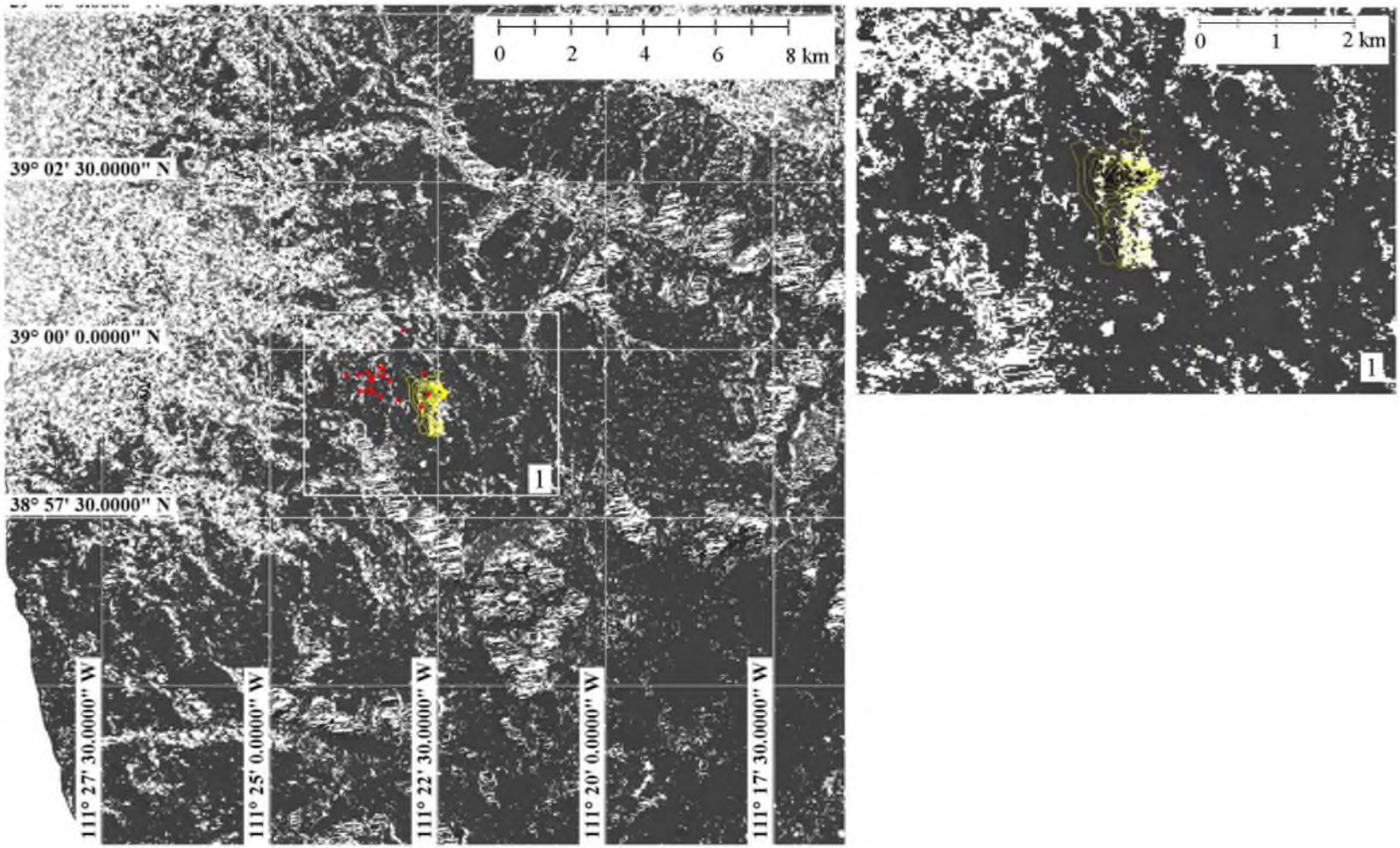

FIGURE 6.14 Displacement maps (L-band) and seismic event locations (red): December 14, 2009 to May 1, 2010 (138 days). Subsidence is contoured every 5 cm starting at −5 cm of vertical displacement.

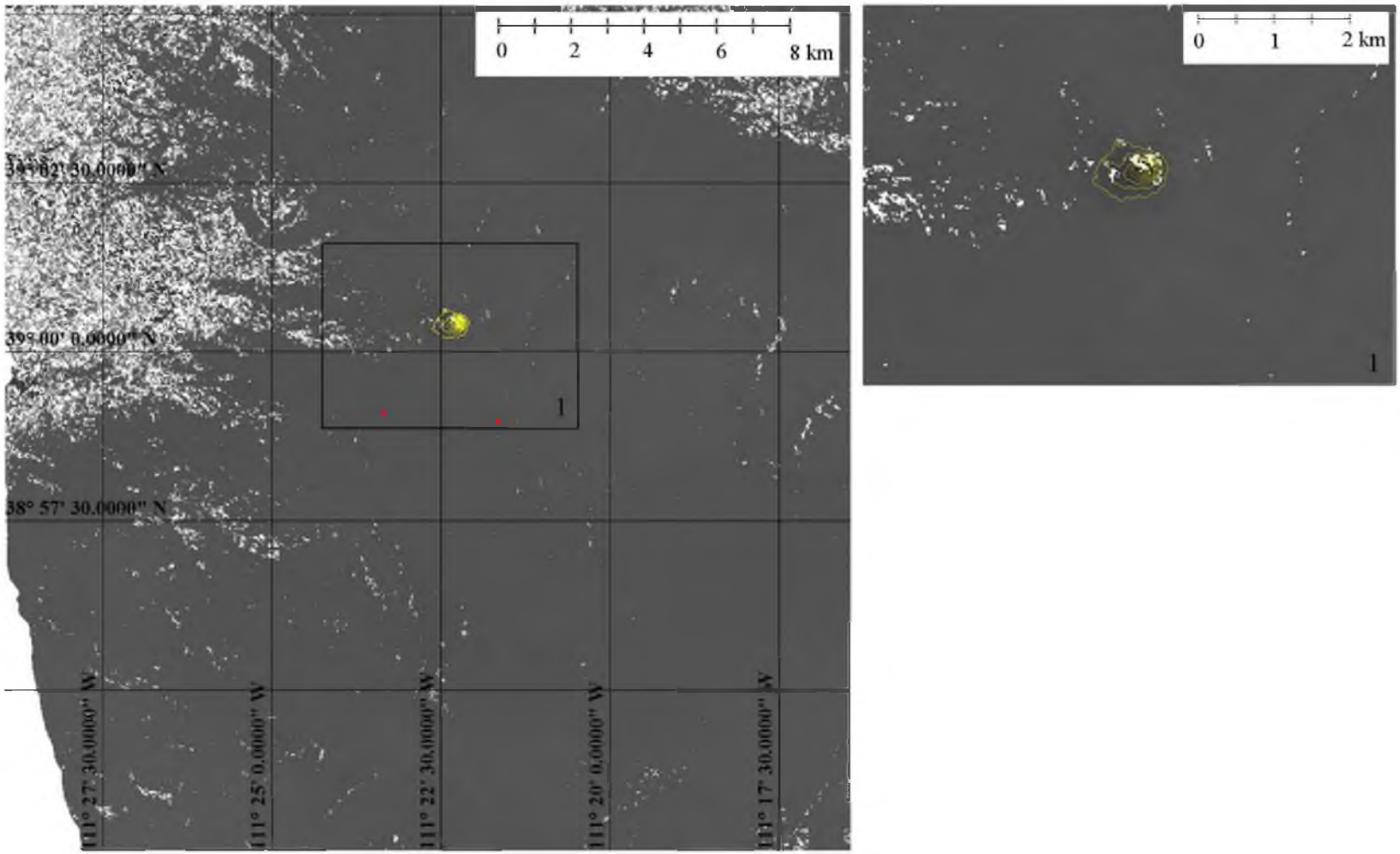

FIGURE 6.15 Displacement maps (L-band) and seismic event locations (red): May 1, 2010 to June 16, 2010 (46 days). Subsidence is contoured every 5 cm starting at −5 cm of vertical displacement.

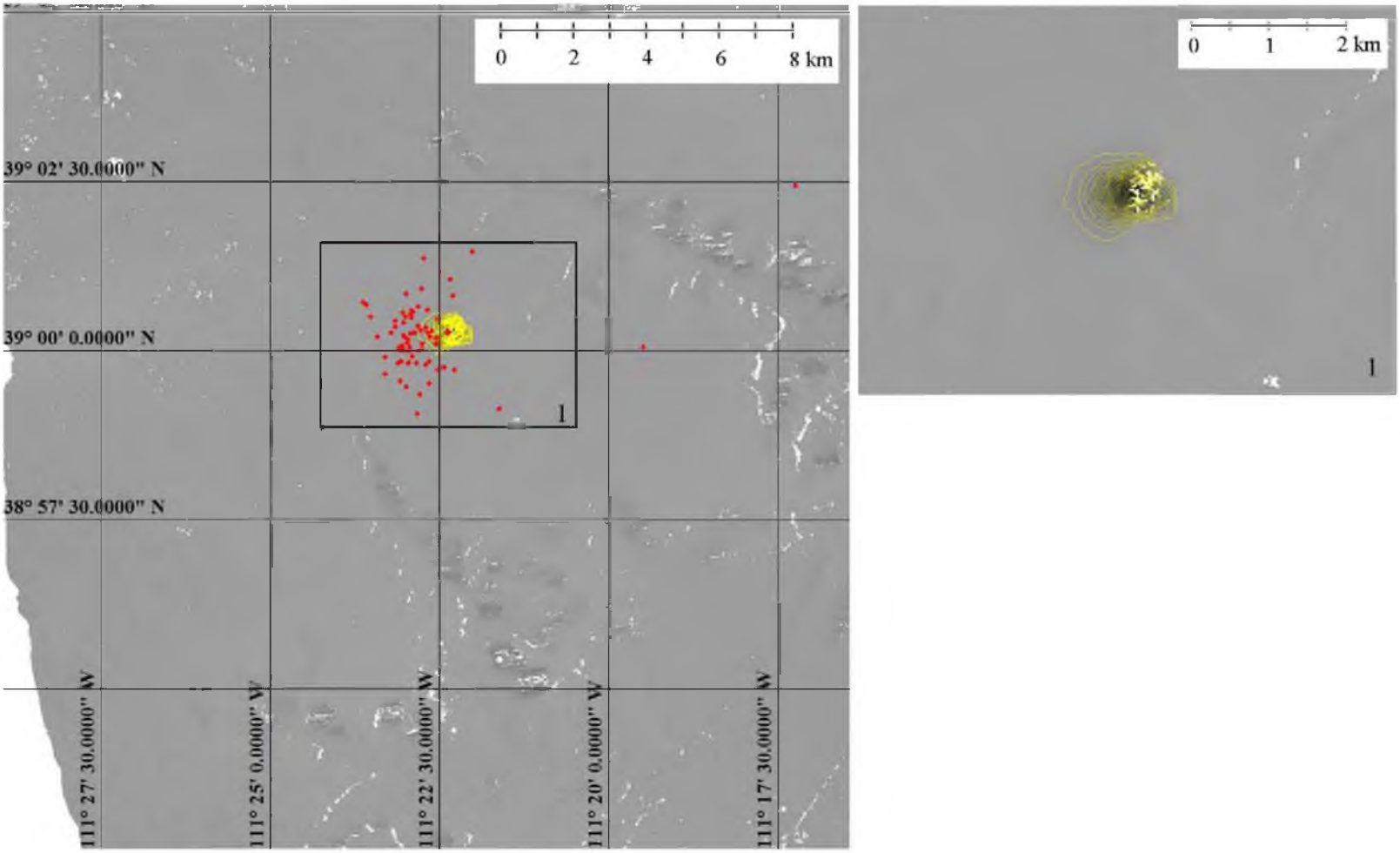

FIGURE 6.16 Displacement maps (L-band) and seismic event locations (red): June 16, 2010 to August 1, 2010 (46 days). Subsidence is contoured every 5 cm starting at −5 cm of vertical displacement.

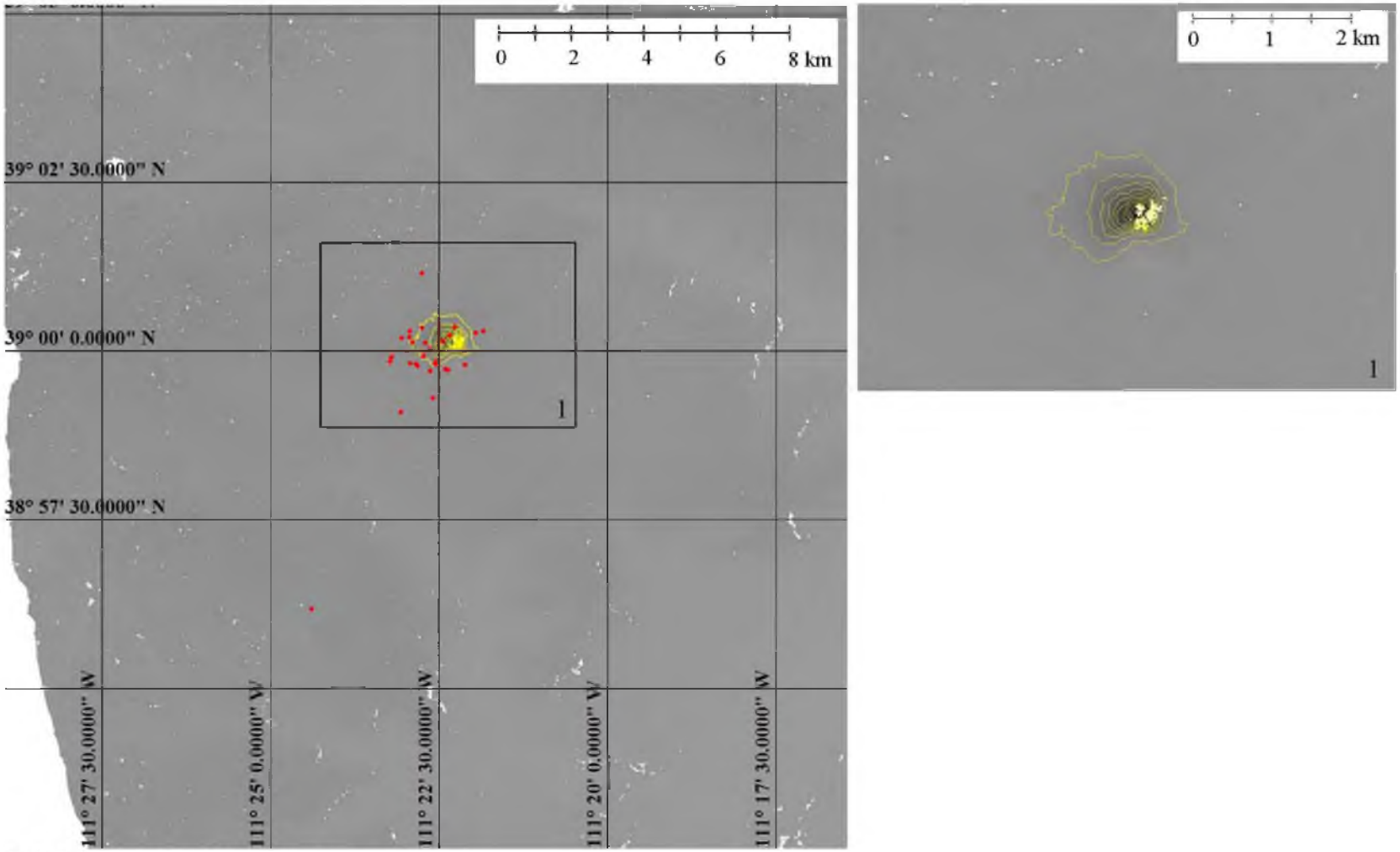

FIGURE 6.17 Displacement maps (L-band) and seismic event locations (red): August 1, 2010 to September 16, 2010 (46 days). Subsidence is contoured every 5 cm starting at −5 cm of vertical displacement.

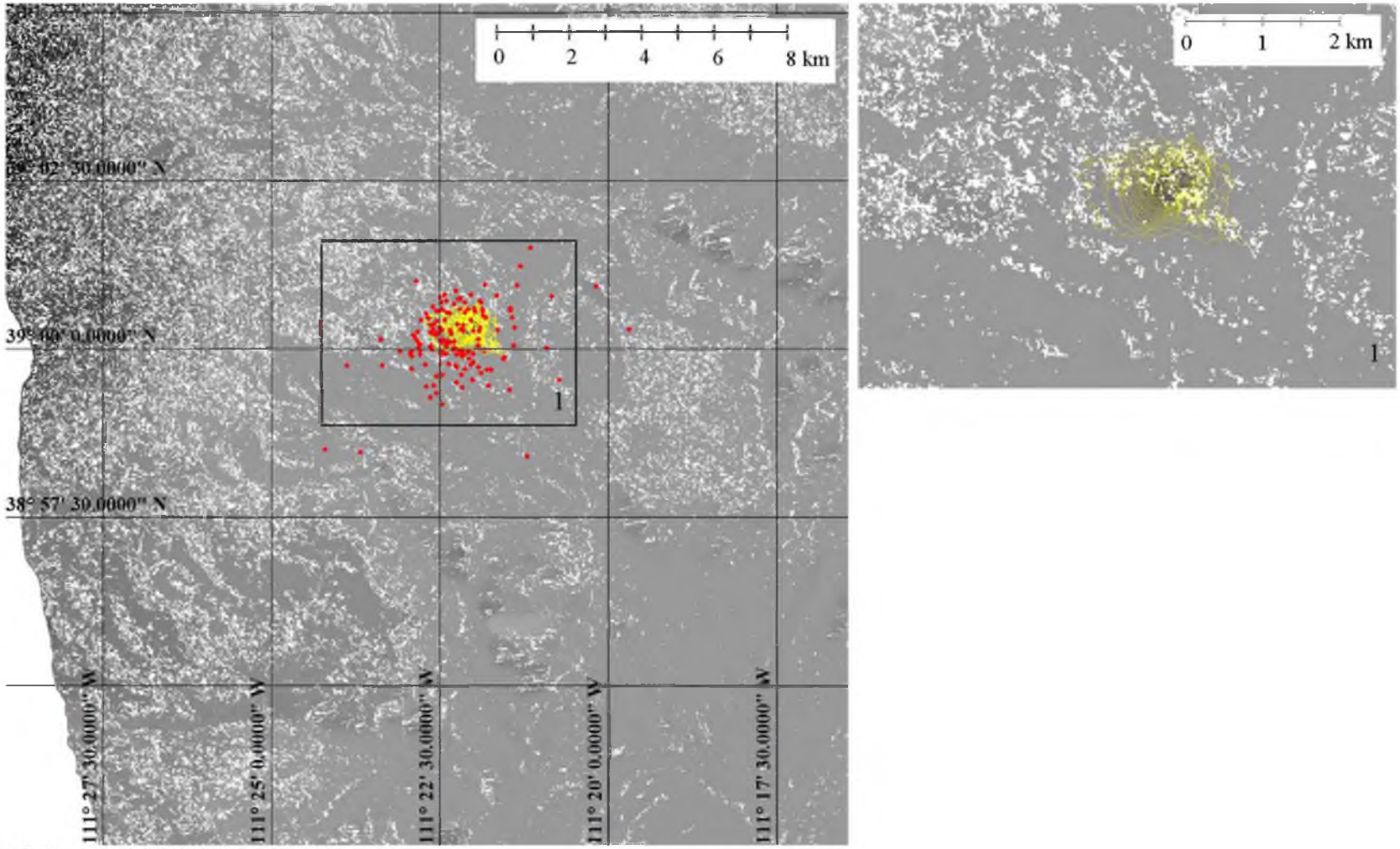

Includes material © JAXA/METI 2010

FIGURE 6.18 Displacement maps (L-band) and seismic event locations (red): September 16, 2010 to December 17, 2010 (92 days). Subsidence is contoured every 5 cm starting at −5 cm of vertical displacement.

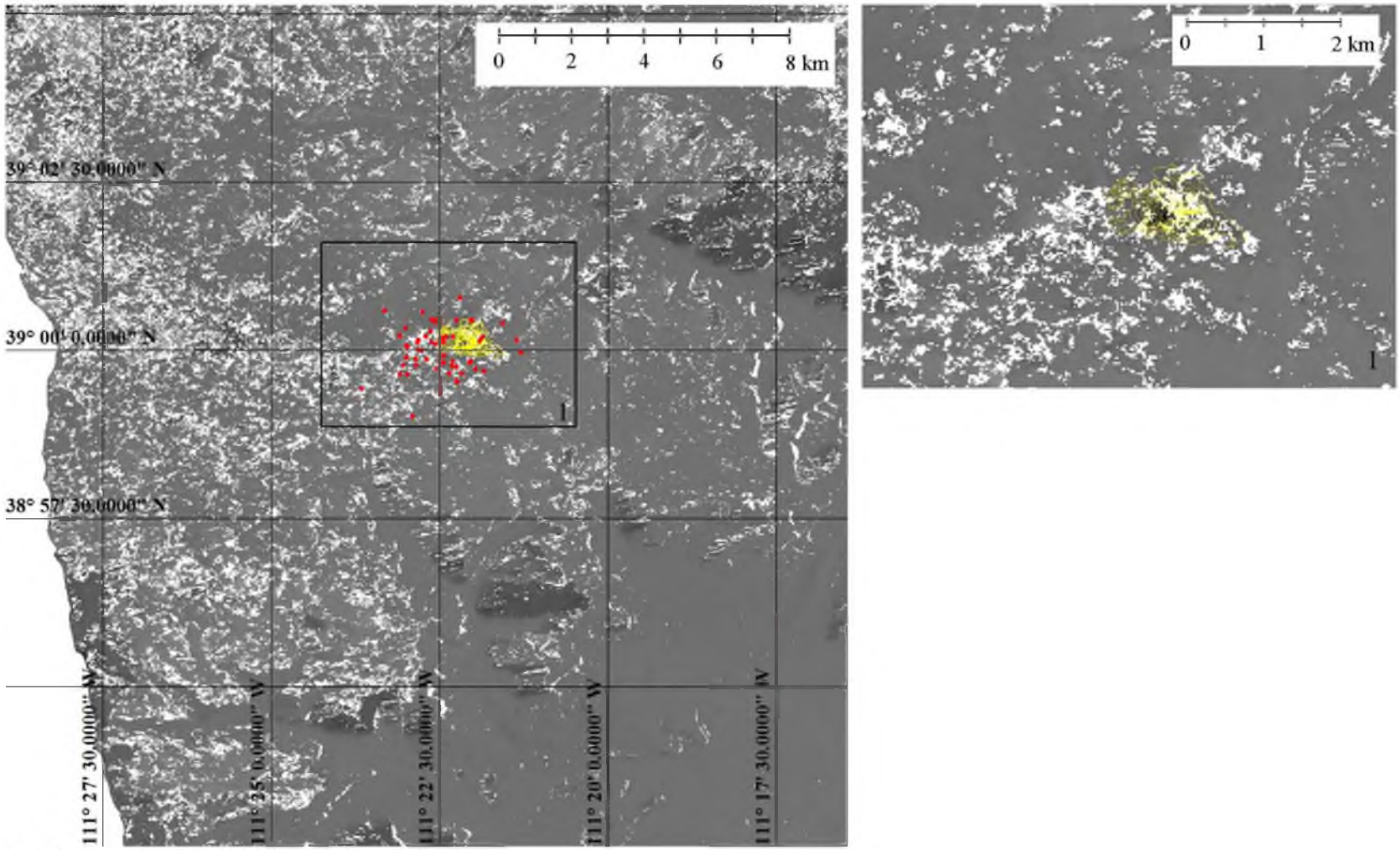

Includes material © JAXA/METI 2010 and 2011

FIGURE 6.19 Displacement maps (L-band) and seismic event locations (red): December 17, 2010 to February 1, 2011 (46 days). Subsidence is contoured every 5 cm starting at −5 cm of vertical displacement.

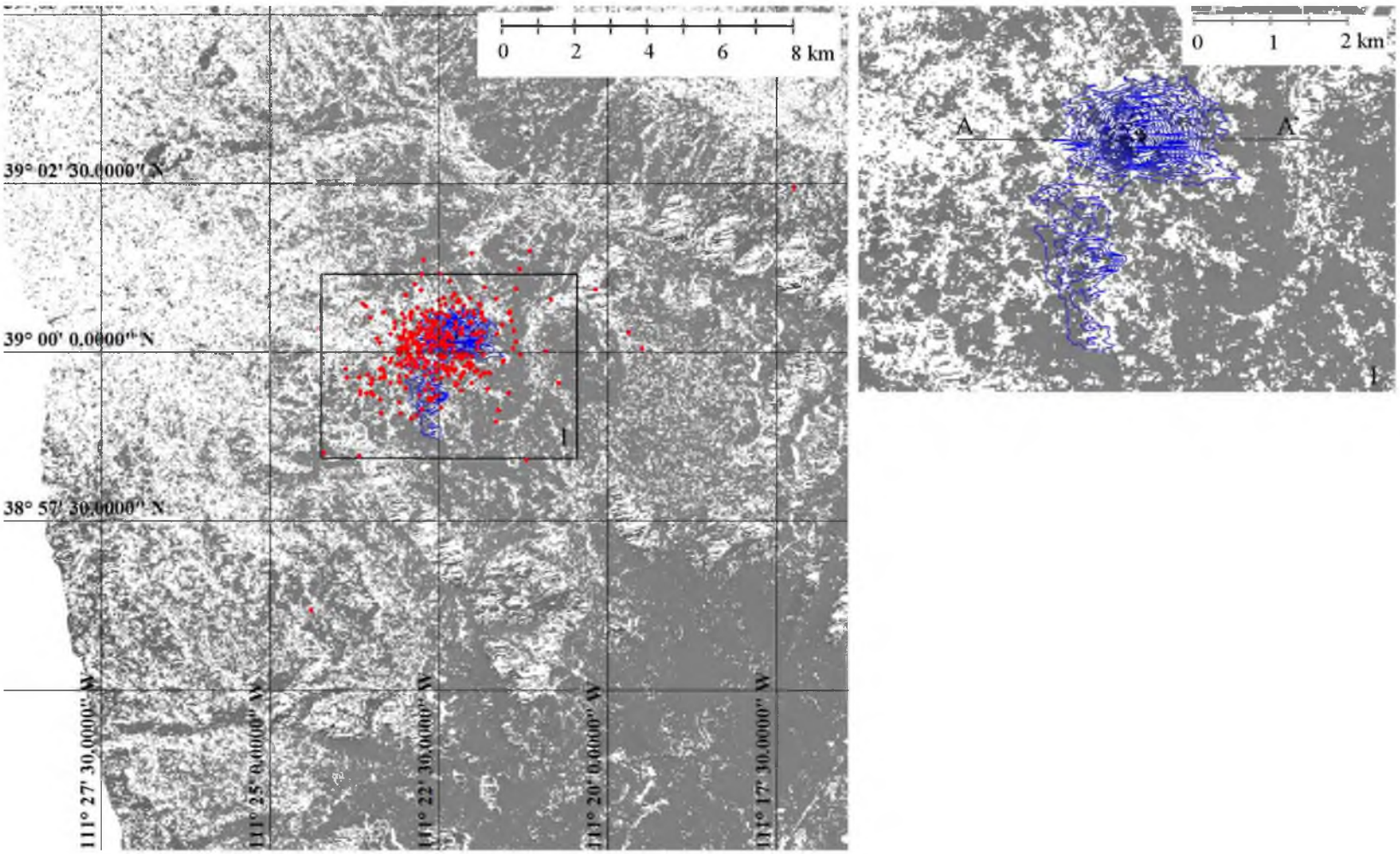

FIGURE 6.20 Cumulative displacement maps (L-band) and seismic event locations (red): December 14, 2009 to February 1, 2011 (414 days). Subsidence is contoured every 10 cm starting at −10 cm of vertical displacement.

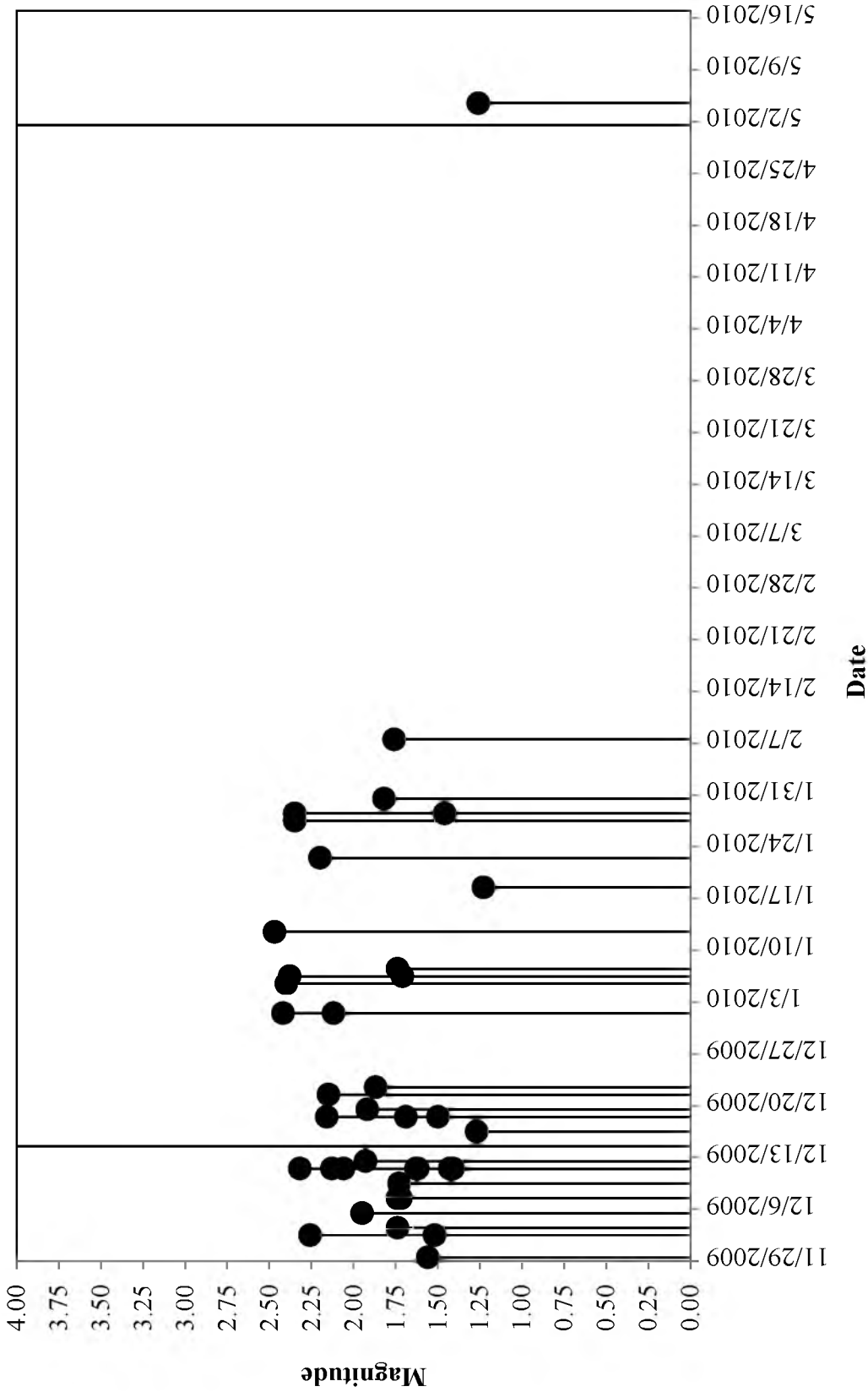

FIGURE 6.21 Magnitude and time of seismicity occurring within 15 days of the December 14, 2009 to May 1, 2010 period

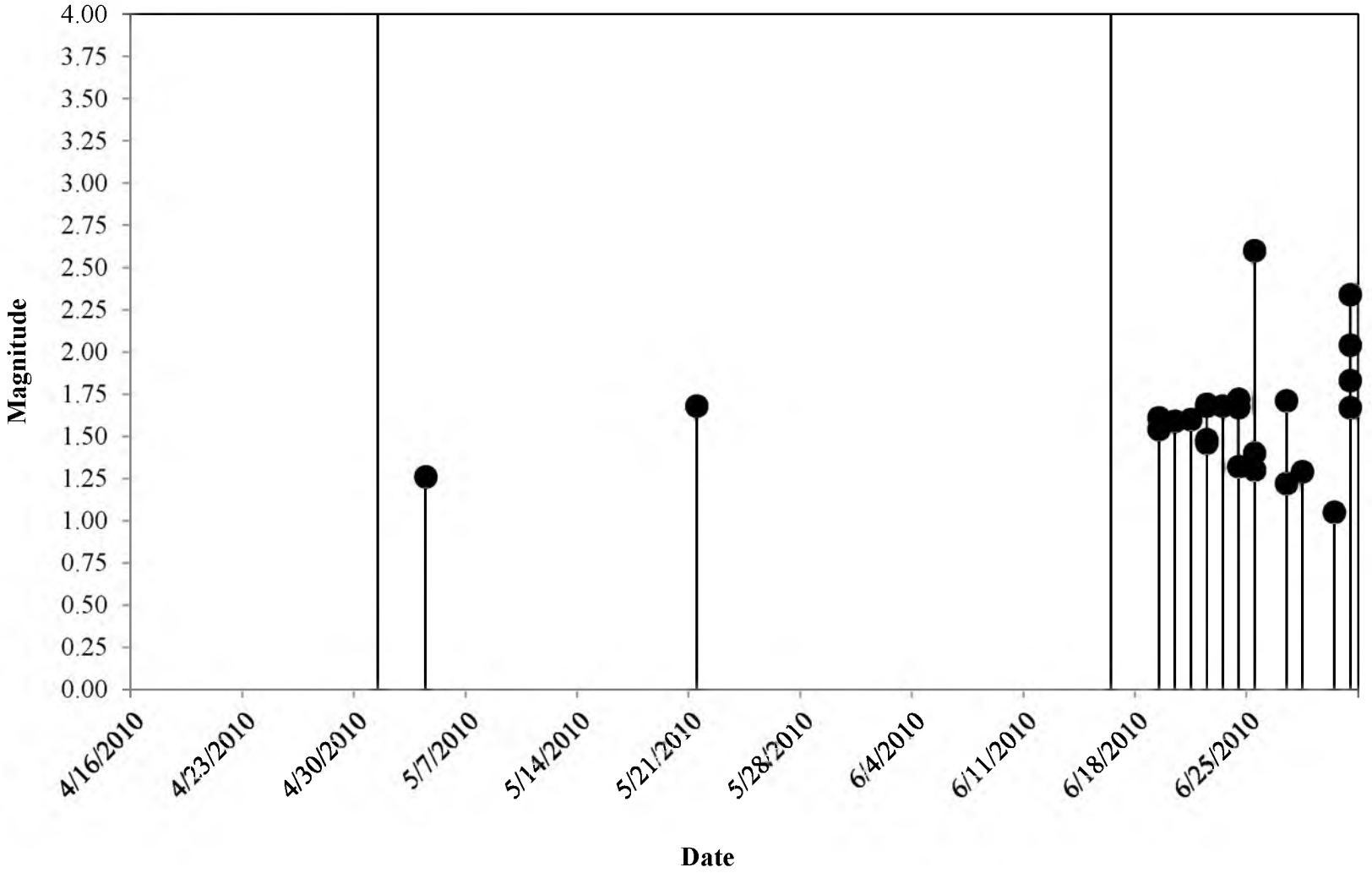

FIGURE 6.22 Magnitude and time of seismicity occurring within 15 days of the May 1, 2010 to June 16, 2010 period

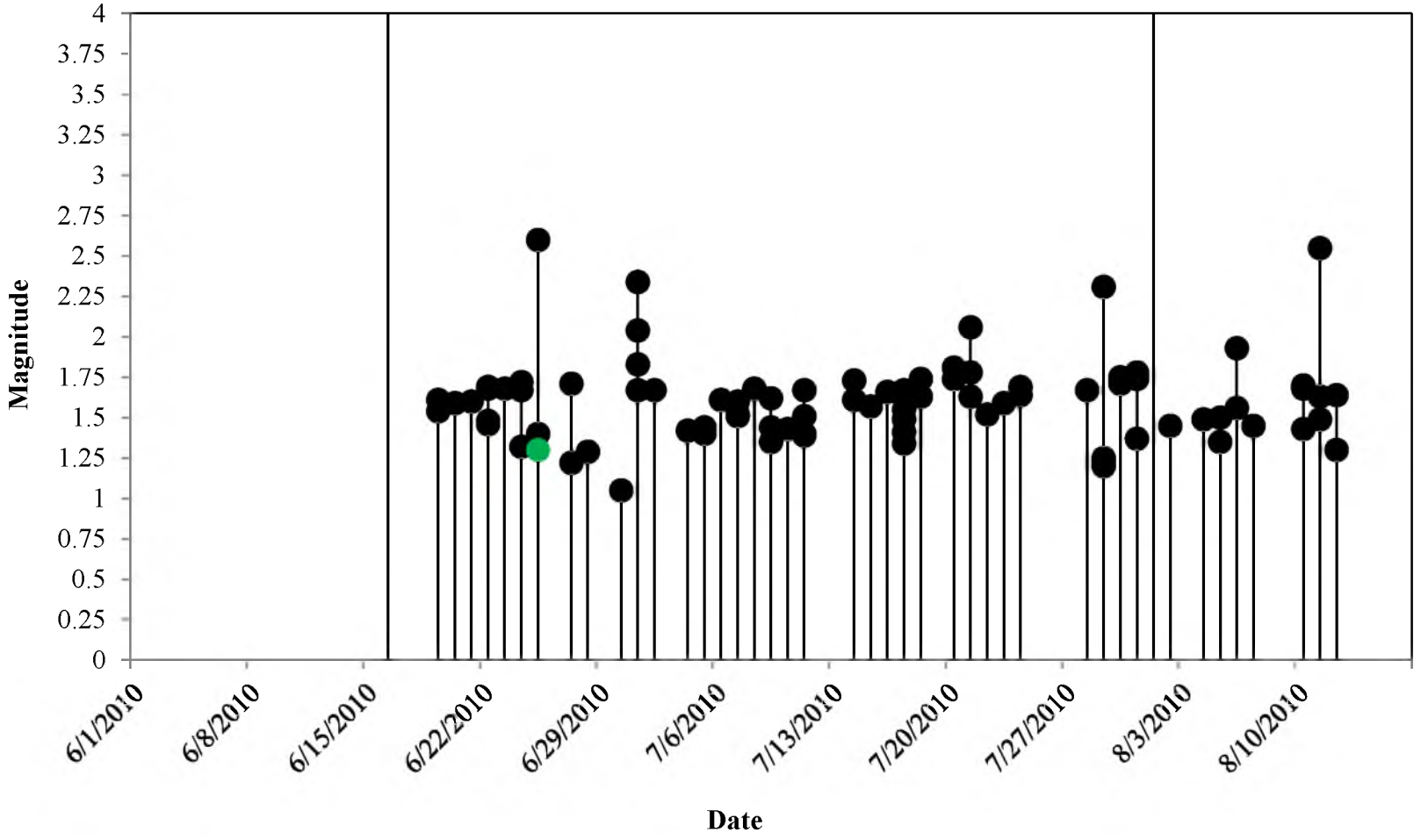

FIGURE 6.23 Magnitude and time of seismicity occurring within 15 days of the June 16, 2010 to August 1, 2010 period. Events identified in green are significantly displaced from the subsided regions.

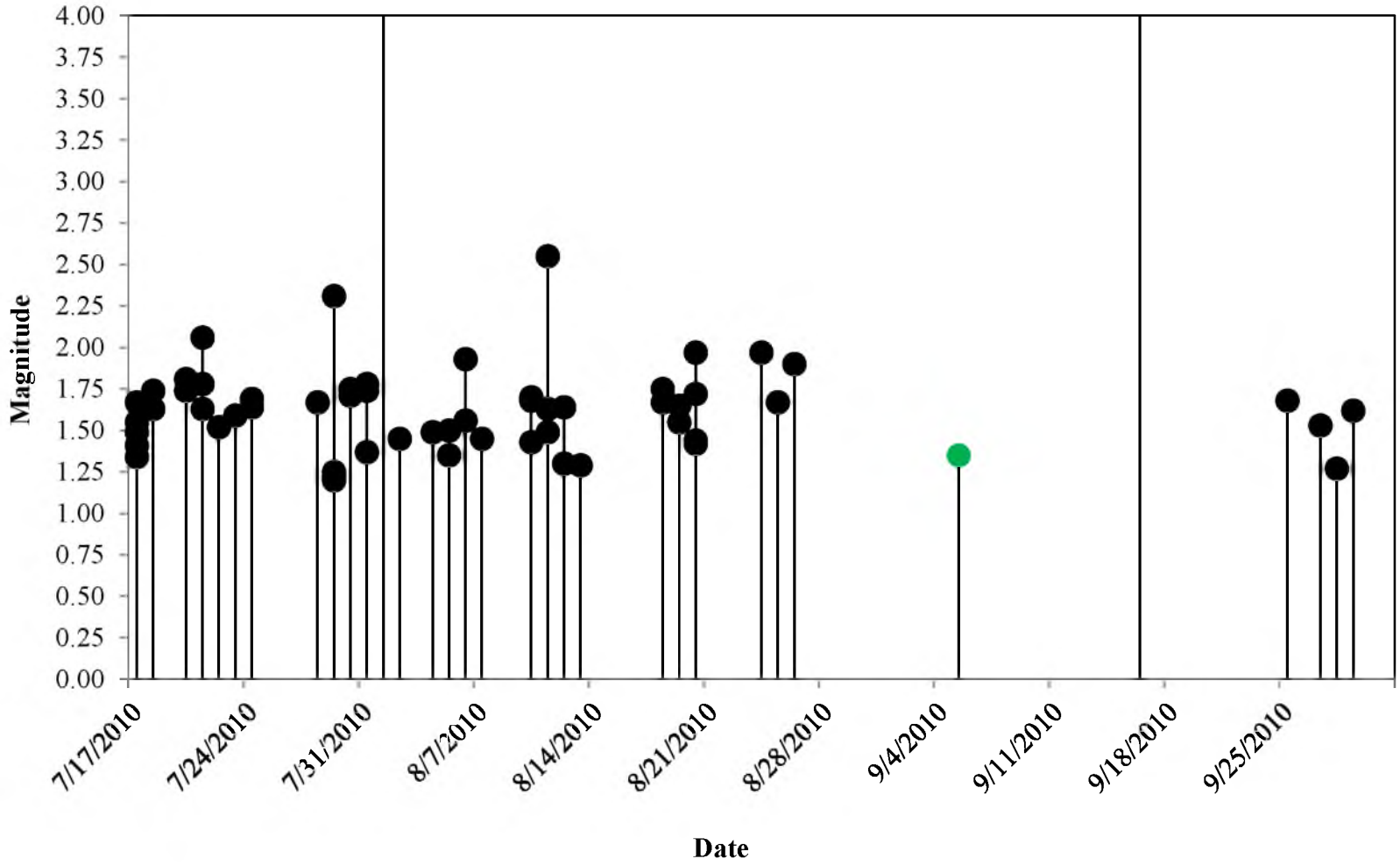

FIGURE 6.24 Magnitude and time of seismicity occurring within 15 days of the August 1, 2010 to September 16, 2010 period. Events identified in green are significantly displaced from the subsided regions.

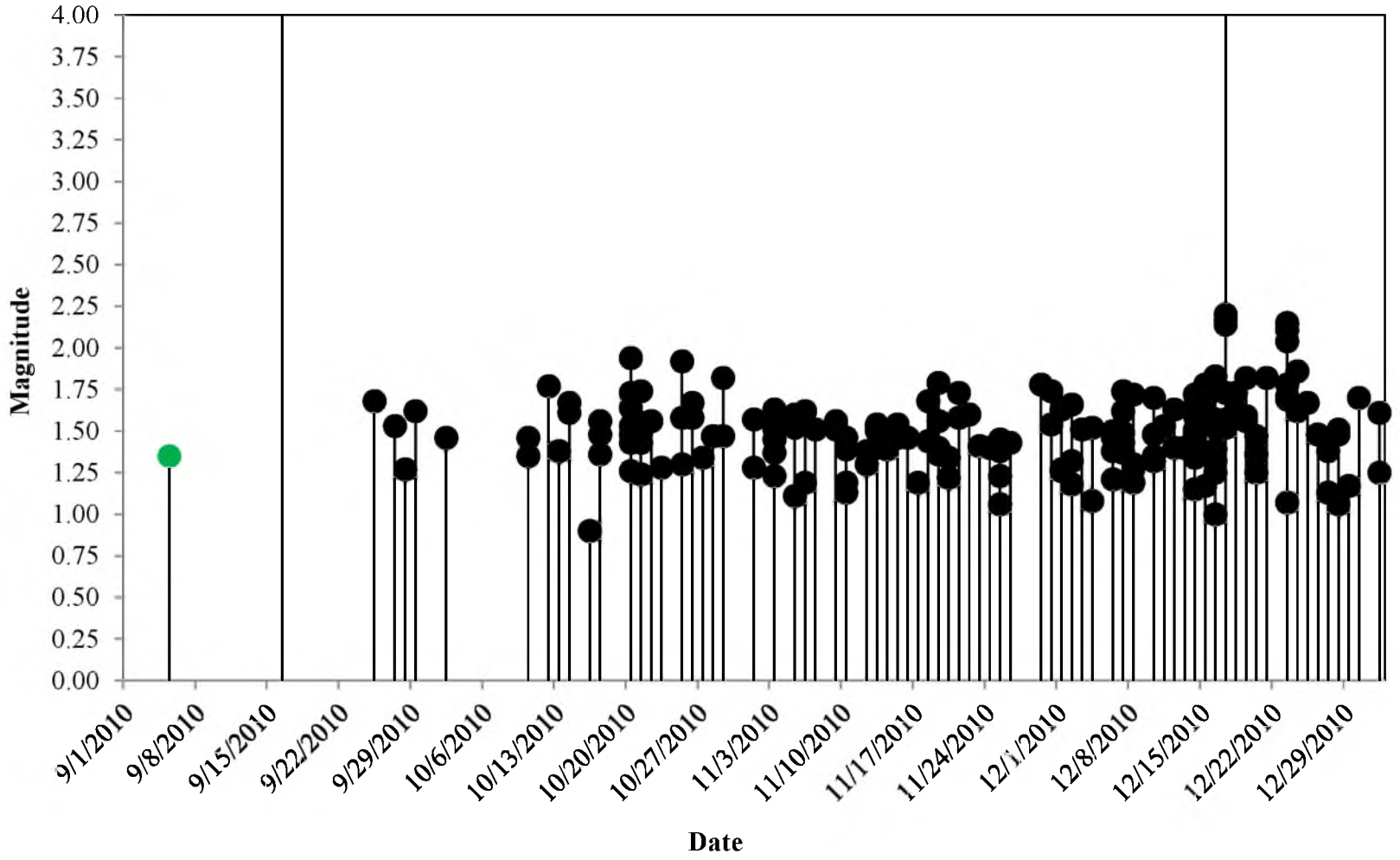

FIGURE 6.25 Magnitude and time of seismicity occurring within 15 days of the September 16, 2010 to December 17, 2010 2015 period. Events identified in green are significantly displaced from the subsided regions.

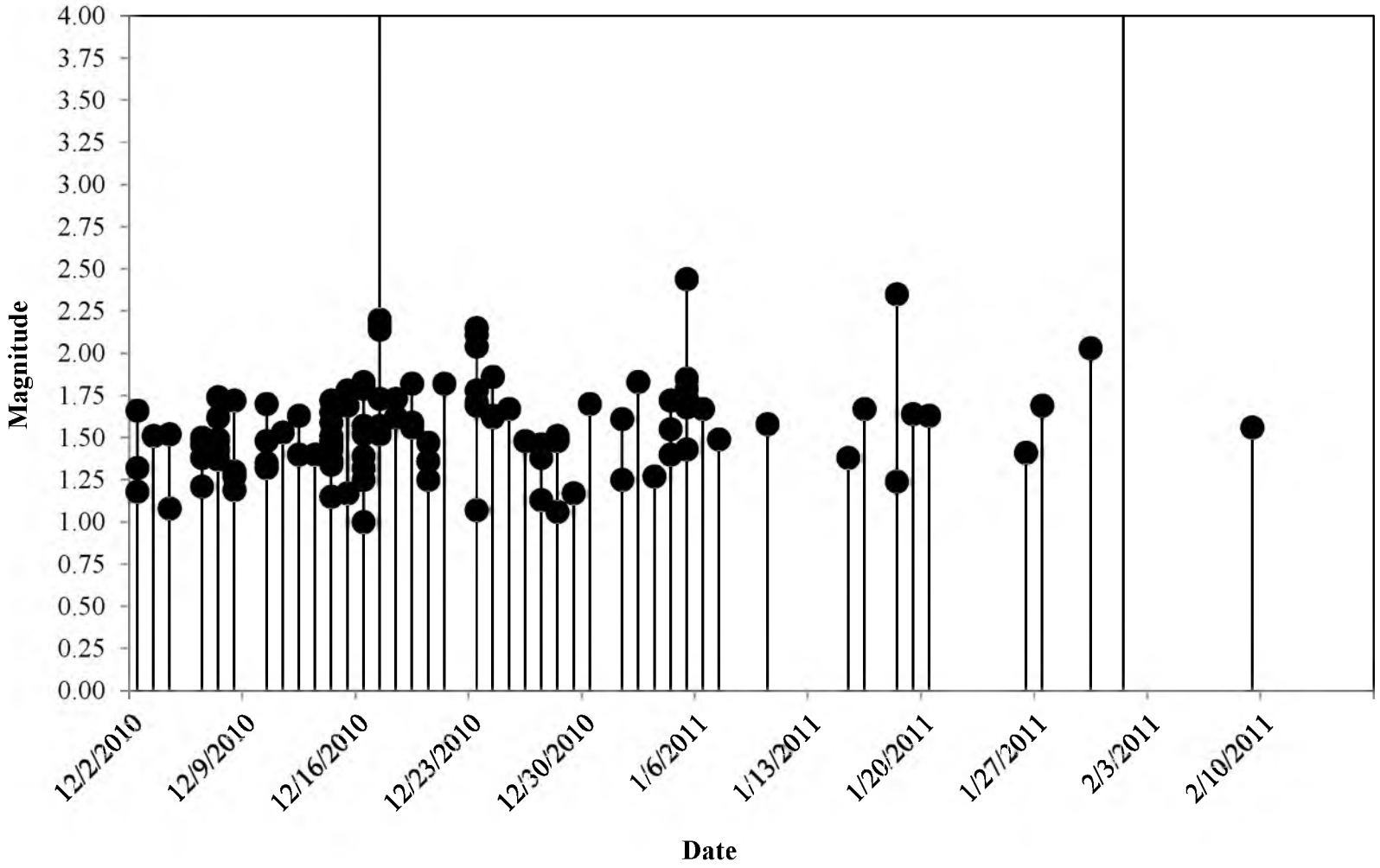

FIGURE 6.26 Magnitude and time of seismicity occurring within 15 days of the December 17, 2010 to February 1, 2011 period

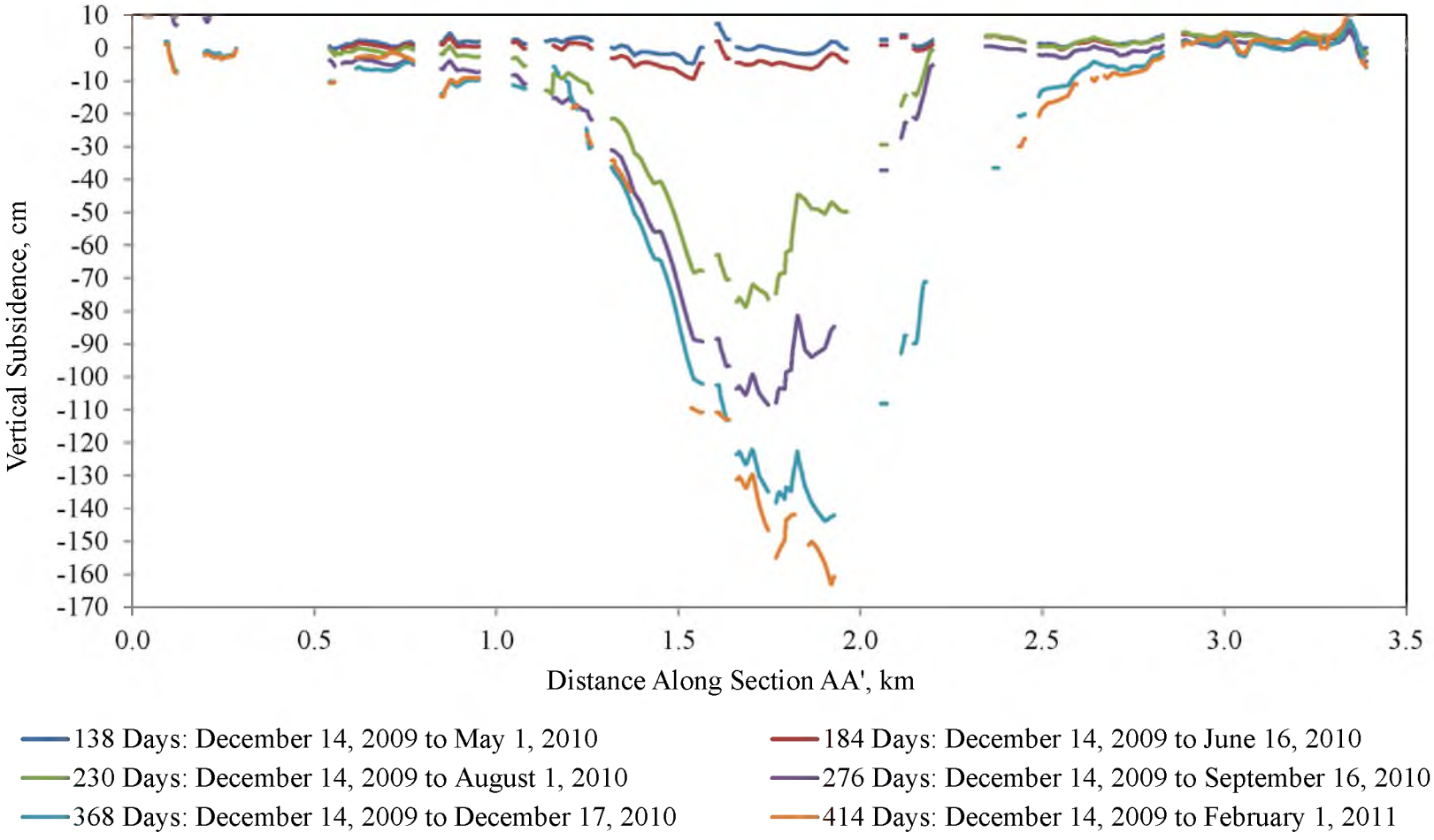

FIGURE 6.27 Time series subsidence profiles of section AA' from Figure 6.20

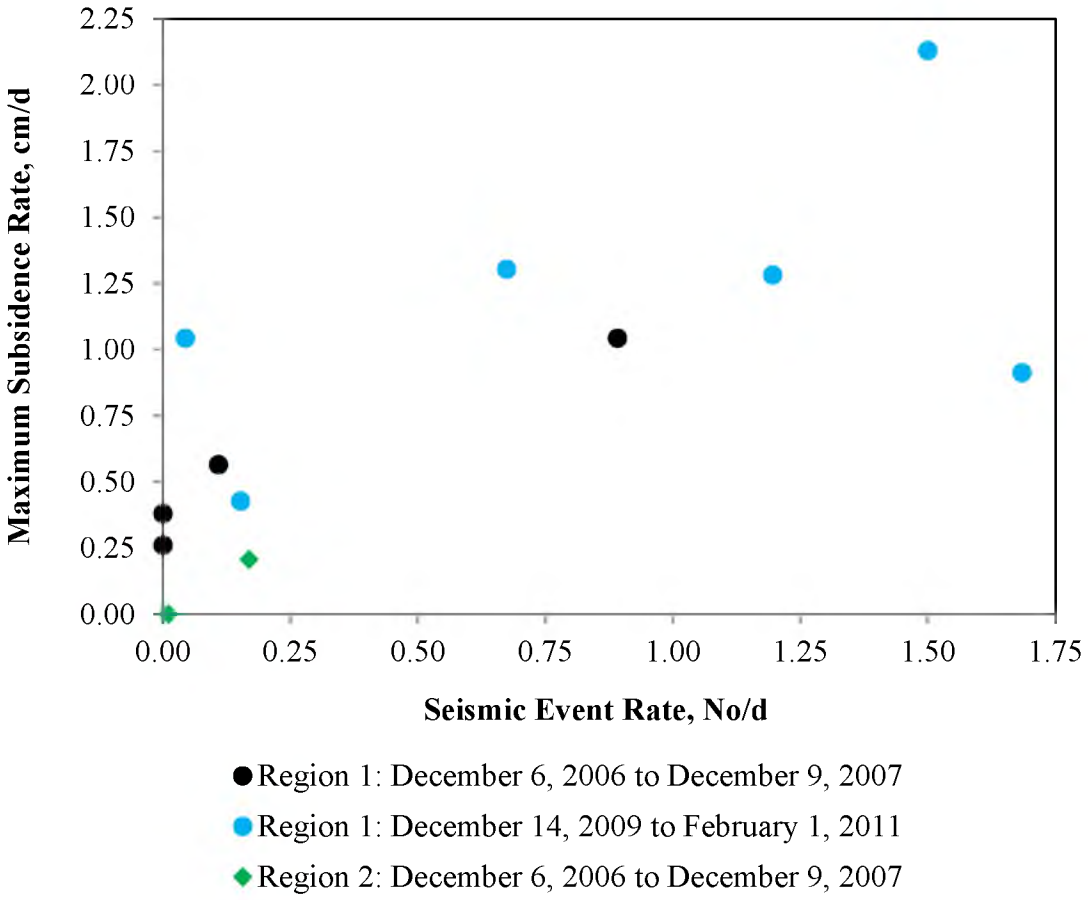

FIGURE 6.28 Maximum subsidence rate versus seismic event rate

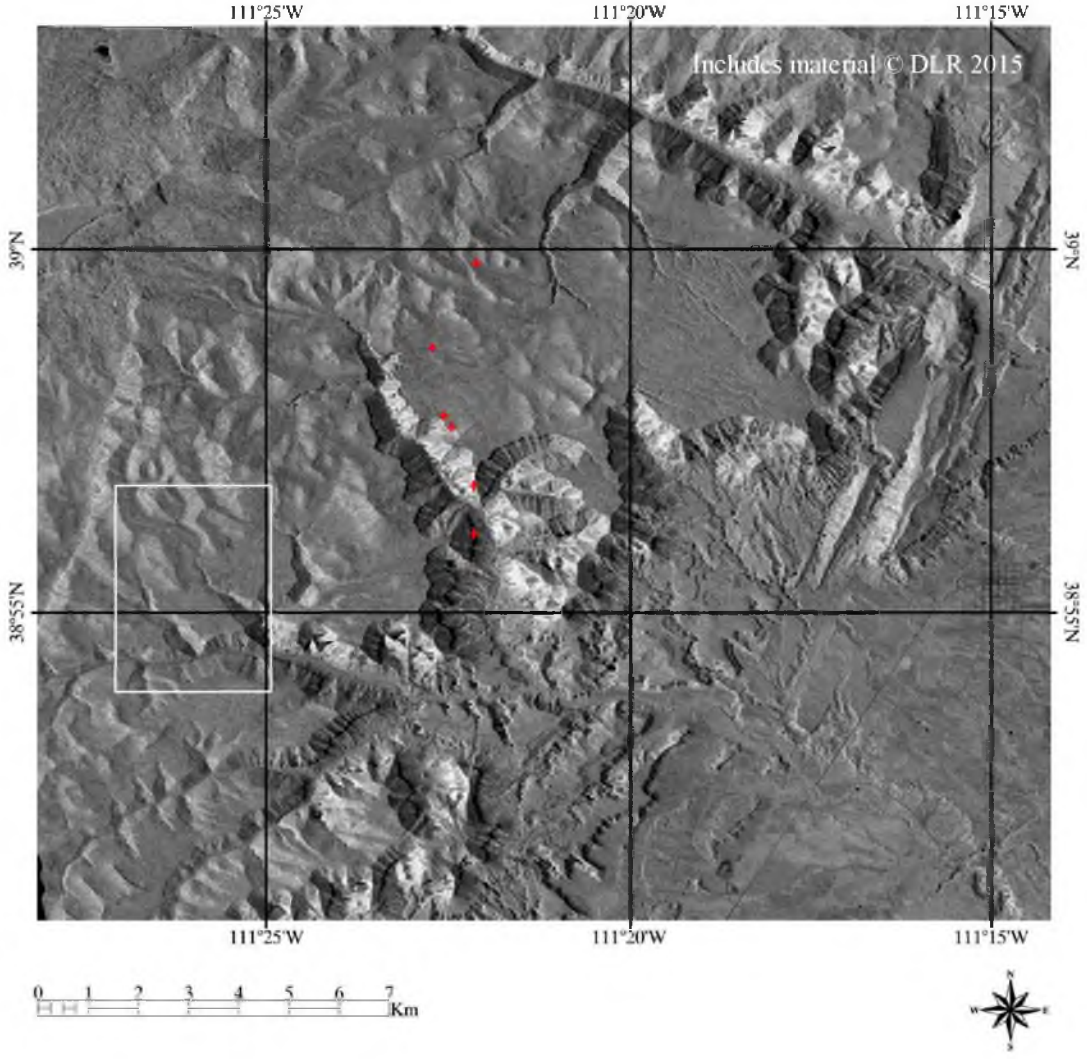

FIGURE 6.29 Region impacted by subsidence (white box) and seismic event locations (red): June 7, 2015 to November 22, 2015

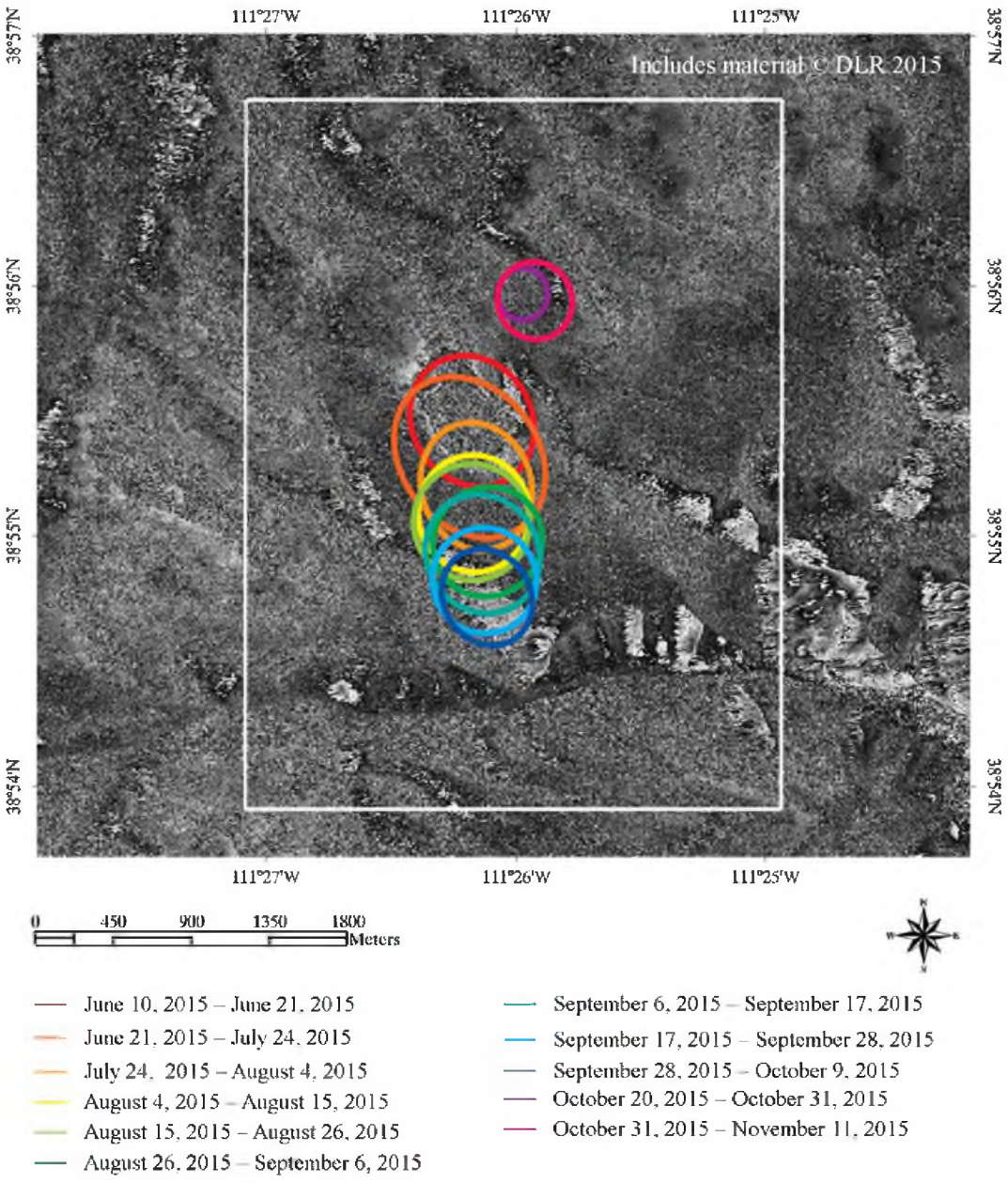

FIGURE 6.30 June 10, 2015 to June 21, 2015 interferogram (X-band) and subsidence progression by period

CHAPTER 7

SUBSIDENCE AND SEISMICITY—WYOMING REGION

7.1 Introduction

This chapter presents results of the application of DInSAR for mine subsidence monitoring in the Green River Basin of southwest Wyoming. First, general characteristics of geology and vegetation in the Green River Basin are described. Next, subsidence monitoring results using L-band and X-band DInSAR are presented. Vertical displacement maps are presented and the temporal progression of subsidence is defined. Additionally, cataloged seismicity and surface deformations are compared.

7.2 Geology and Vegetation Characteristics

The Green River Basin is a large, shallow synclinal basin. In this basin, elevations vary from 1,830 m to 2,900 m, and the topography is strongly influenced by differential erosion of faulted and folded sedimentary and volcanic rocks. Characteristic of a high, semiarid plateau, the Green River Basin is sparsely vegetated with low desert shrubs and grasses (Roehler, 1992). Strata in the basin are flat lying, except near the margins which are more structurally complex. The largest faults in the region are present along the northern flank of the Uinta Mountains and the southern flank of the Wind River

Mountains (Bradley 1964). Figure 7.1 shows a TerraSAR-X image of a region of the Green River Basin. Topography typical of the basin—rolling plains interrupted by ridges and buttes—is apparent.

In the Green River Basin, trona is present in bedded deposits in the Wilkins Peak Member of the Green River Formation. The Wilkins Peak Member is up to 370 m thick in the subsurface and is overlain by the Laney Shale Member and underlain by the Tipton Shale Member (Harris 1985). The Tipton Shale Member consists mostly of shales, oil shales, and thin sandstones. The Laney Shale Member consists mostly of marlstone, tuff, sandstone, shale, and limestone, and is more than 180 m thick near Green River, Wyoming. The Tower Sandstone is a prominent strata present near the base of the Laney Shale Member and consists of complex, extensive sand-filled channels and beds (Bradley 1964). The Tower Sandstone has typical thicknesses from 15 to 25 m (Bradley 1964), but sandstones thicker than 120 m have been encountered above the trona beds (Fischer 1964; Wilson and Rao 1982). Twenty-five of the trona beds are extensive and have thickness greater than 0.9 m. Only the thickest beds are mined conventionally, with mining heights typically ranging from 2.5 to 3.5 m (Agapito et al. 2000; Wilson and Rao 1982). Beds at depths greater than 550 m are not mined conventionally (Richardson et al. 1999).

7.3 L-Band DInSAR Results

Twelve interferograms were generated using L-band data from ALOS for the trona mining region in the Green River Basin in intervals over the period from December 4, 2007 to March 14, 2011. The interferometric data parameters are summarized in Table

4.6. Average coherence of the interferograms ranges from 0.26 to 0.60, and elapsed times range from 46 to 460 days. Phase fringes due to surface displacement are identifiable in all 12 of the interferograms, and overall the fringes are distinct. Because the topography in the trona bearing region of the Green River Basin is gentle, topographic artifacts in the interferogram are not significant. The coherence of the interferograms seems to be more affected by seasonal variation in the surface conditions than by the length of the imaging period; all of the interferograms generated from image pairs with one image acquired in January have low average coherence, despite short elapsed times. Additionally, some of the interferograms have fairly low coherence in the regions with the largest displacements, and in the interferograms with the longest elapsed times (184 and 460 days), large displacements cause the phases to saturate. Other regions of low coherence include tailings ponds associated with the trona mines and the Green River. Overall, L-band SAR data from ALOS generate strong phase fringes in the trona mining region. The interfreograms with small spatial and temporal baselines produced distinct phase fringes in regions of large displacement, but even the interferograms with long elapsed times and large magnitude spatial baselines have interpretable fringes.

7.4 Displacement Mapping (L-Band) and Seismicity

Vertical displacement maps derived from each of the 12 interferograms generated for the trona mining region using L-band data are presented in Figures 7.2 to 7.13. These figures cover intervals during the period from December 4, 2007 to March 14, 2011, and show 5-cm subsidence contours starting at a vertical displacement of −5 cm. Figure 7.14 shows a cumulative displacement map for the entire period from December 4, 2007 to

March 14, 2011. In this image subsidence is contoured every 10 cm starting from a vertical displacement of −10 cm. In all of these figures, seismic events from the ANF catalog are red, seismic events from the UUSS catalog are blue, and low coherence pixels are white. Finally, Figures 7.15 to 7.20 show time series profiles of subsidence along the section lines defined in Figure 7.14. Gaps in the profiles result from missing data due to low coherence pixels.

Based on the vertical displacement data, two types of subsidence are characteristic of the trona mining region: large magnitude subsidence that results from longwall mining and lower magnitude subsidence that results from trona dissolution. From the cumulative displacement map (Figure 7.14), region 1 and 2 demonstrate low magnitude subsidence due to dissolution; regions 3 and 4 show both low magnitude subsidence due to dissolution and large magnitude subsidence due to longwall production. Significantly, the maximum cumulative subsidence due to longwall mining in regions 3 and 4 are similar, 150 cm and 140 cm, respectively, but over shorter periods the characteristics of longwall mine subsidence are considerably different (Figures 7.2 to 7.13). Variability of the subsidence characteristics likely results from differences in the mining parameters, including different panel widths and development rates. For the trona mines with high extraction ratios, maximum subsidence is typically on the order of 1.5 to 2 m (Fischer 1986; FMC Granger 2012).

The maximum cumulative subsidence derived from L-band DInSAR is reasonable but may be slightly underestimated due to phase saturation. Because deformation rates due to subsidence tend to be large, phase noise and phase saturation can make the phases difficult to interpret and to unwrap, which can lead to wavelength level (or greater) errors

in subsidence measurements. These errors tend to be more significant in interferograms that cover longer periods; larger deformation gradients occur over longer periods. Subsidence can be measured accurately over relatively long periods by pairing images over shorter periods when the deformation gradients are lower, and accumulating the subsidence additively.

Finally, though subsidence in the trona mining region is significant, the level of seismicity is low. From the cumulative displacement map (Figure 7.14), the cataloged seismicity is spatially fairly well corrected with regions of subsidence over long periods. Over shorter periods (Figures 7.2 to 7.13) spatial correlation between seismicity and subsidence is less consistent. From the data in this study, it is difficult to define decisively if seismicity occurs in advance of surface displacement or if seismicity is delayed. It is probably significant that, over longer periods, seismic events tend to spatially cluster in regions where subsidence rates are low and subsidence is likely a result of dissolution. MIS in the Green River Basin tends to be relatively large magnitude and may indicate failure in strong overburden strata due to high stress. Increases in the extraction ratio due to dissolution might lead to significant increases in overburden stress.

7.5 X-Band DInSAR Results

Using X-band data from TerraSAR-X, 12 interferograms were generated for the trona mining region in the Green River Basin in intervals over the period from June 2 to November 3, 2015. The interferometric data parameters are summarized in Table 4.8. Average coherence of the inteferograms is high, ranging from 0.55 to 0.78. Two regions in the interferograms, 1 and 2 in Figure 7.1, disclose subsidence. In all of the data, phase

fringes due to surface displacement are distinct, with only one exception. In the interferogram with the longest elapsed time (33 days), there is significant phase saturation in the region with the largest displacement. Topographic artifacts in the interferograms are minimal. In these data, coherence is strongly affected by the length of the imaging period: the longest period interferogram has the lowest average coherence. Seasonal variation in surface conditions, specifically the presence of snow and changes in soil moisture content, could reduce the coherence, but the interferograms from June to November are not significantly affected by variations in the surface conditions. Overall, in Green River Basin, X-band data generate strong, interpretable phase fringes, but short imaging periods (11 day) are necessary for high coherence and to limit phase saturation in regions with large displacements. Again, accumulating subsidence additively generates accurate subsidence measurement over relatively long periods.

7.6 Displacement Mapping (X-Band)

Displacement data for region 1 (Figure 7.1) derived from each of the 12 interferograms generated using X-band data are presented in Figures 7.21 to 7.32. These figures cover intervals during the period from June 2, 2015 to November 3, 2015. Except for Figure 7.22, the figures show 1-cm subsidence contours starting at a vertical displacement of −1 cm. Profiles of subsidence are also presented in the figures. Figure 7.22 shows the phase fringes due to subsidence for the 33 day period from June 13, 2015 to July 16, 2015. Because of significant signal noise and phase saturation, vertical displacements were not estimated for region 1 for this period. Figure 7.33 shows a cumulative displacement map for the 110 day period from July 16, 2015 to November 3,

2015. In this image, subsidence is contoured every 5 cm starting from a vertical displacement of −5 cm. In Figures 7.21 to 7.33, low coherence pixels are white. Finally, Figures 7.34 and 7.35 show time series profiles of subsidence along the section lines defined in Figure 7.33. Gaps in the profiles result from missing data due to low coherence pixels.

Displacement data for region 2 (Figure 7.1) derived from each of the 12 interferograms generated using X-band data are presented in Figures 7.36 to 7.47. These figures cover intervals during the period from June 2, 2015 to November 3, 2015 and show 1-cm subsidence contours starting at a vertical displacement of −1 cm. Profiles of subsidence are also presented. Figure 7.48 shows a cumulative displacement map for region 2 for the 154 day period from June 2, 2015 to November 3, 2015. In this figure subsidence is contoured every 5 cm starting from a vertical displacement of −5 cm. In all of the figures, low coherence pixels are white. Finally, Figures 7.49 and 7.50 show time series profiles of subsidence along the section lines defined in Figure 7.48. Gaps in the profiles result from missing data due to low coherence pixels.

Again, two types of subsidence are characteristics of the trona mining region: large magnitude subsidence resulting from longwall mining and lower magnitude subsidence resulting from trona dissolution. Longwall mine subsidence is clear in regions 1 and 2, but the characteristics of the longwall subsidence in these regions are different. In region 1, maximum subsidence resulting from longwall mining occurs at an average rate of 0.72 cm/d, and in region 2 maximum subsidence resulting from longwall mining occurs at an average rate of 0.26 cm/d. Again, differences in the subsidence characteristic are likely due to different mining parameters. Notably in both regions, profiles of

subsidence due to longwall mining show upward displacement on the order of a centimeter, near the subsidence boundaries. Upward displacements of this magnitude are consistent with displacements measured in the trona region (FMC Granger 2012). In addition to longwall subsidence, subsidence due to dissolution occurs in region 2. This subsidence is relatively low magnitude, less than 0.1 cm/d, but it is apparent in the subsidence profiles in Figures 7.36 to 7.47, as well as in the cumulative subsidence data.

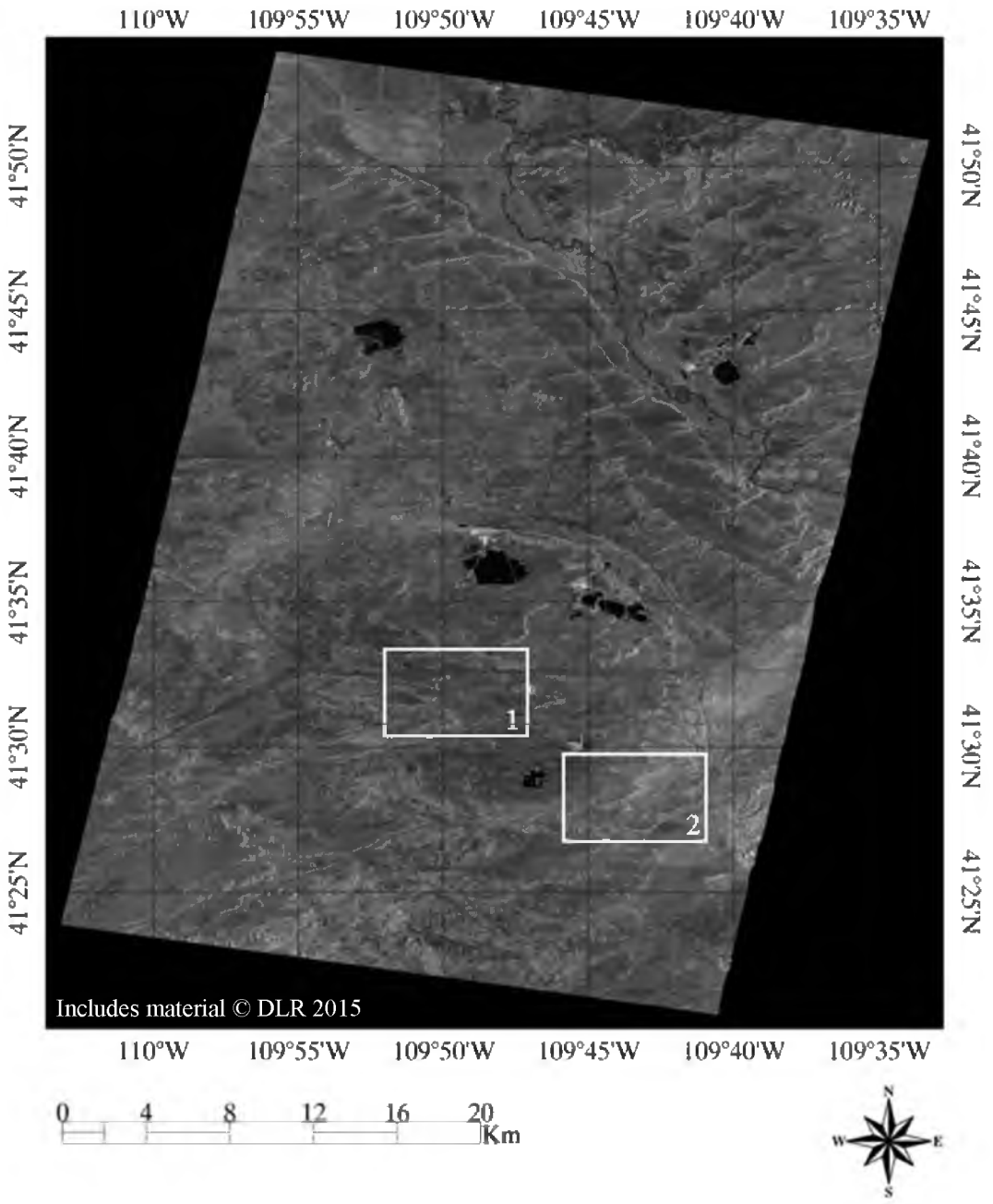

FIGURE 7.1 TSX-1 intensity image of a region in the Green River Basin (June 2, 2015)

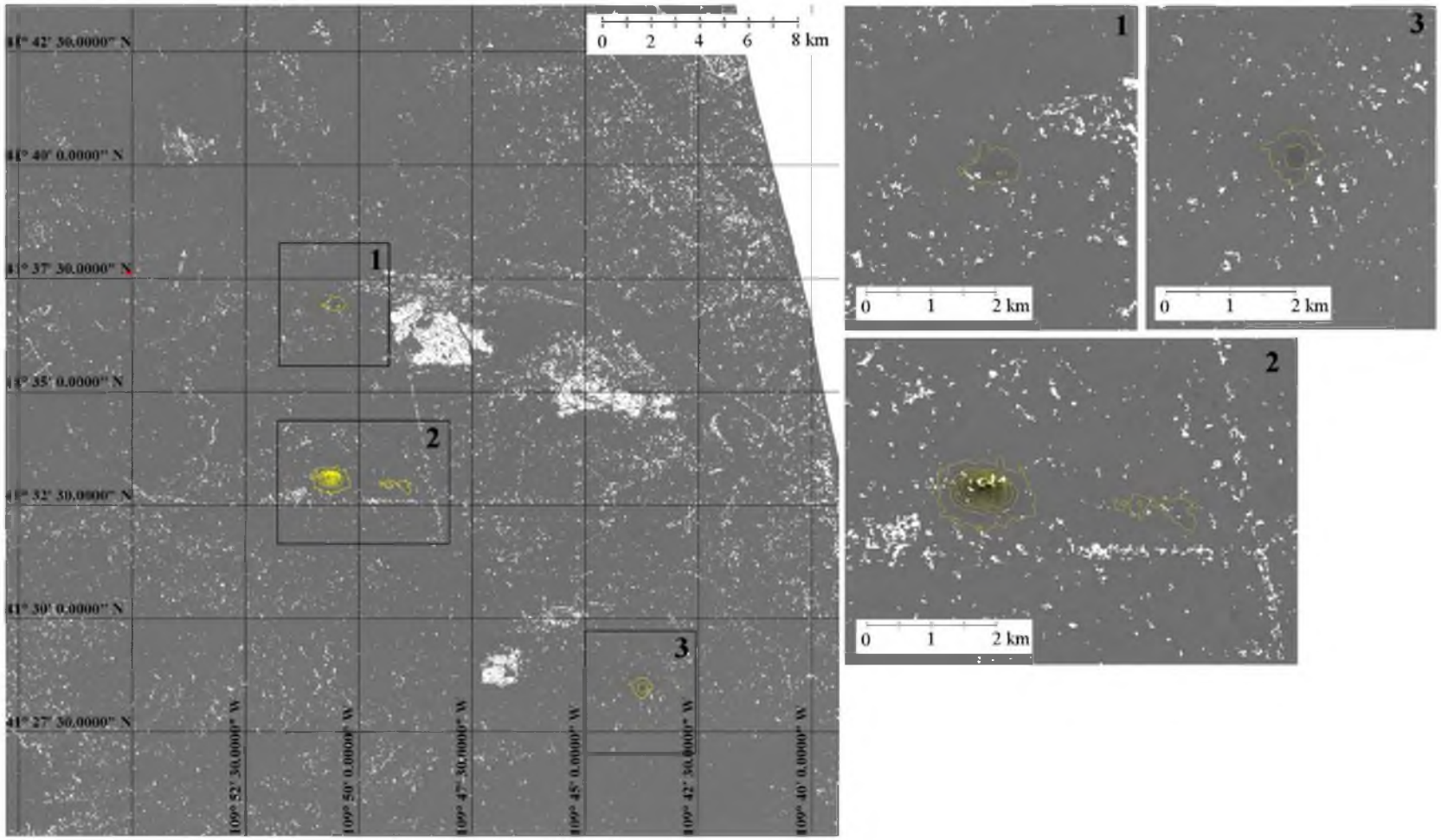

FIGURE 7.2 Displacement maps (L-band) and ANF catalog seismic event location (red): December 4, 2007 to January 19, 2008 (46 days). Subsidence is contoured every 5 cm starting at −5 cm of vertical displacement.

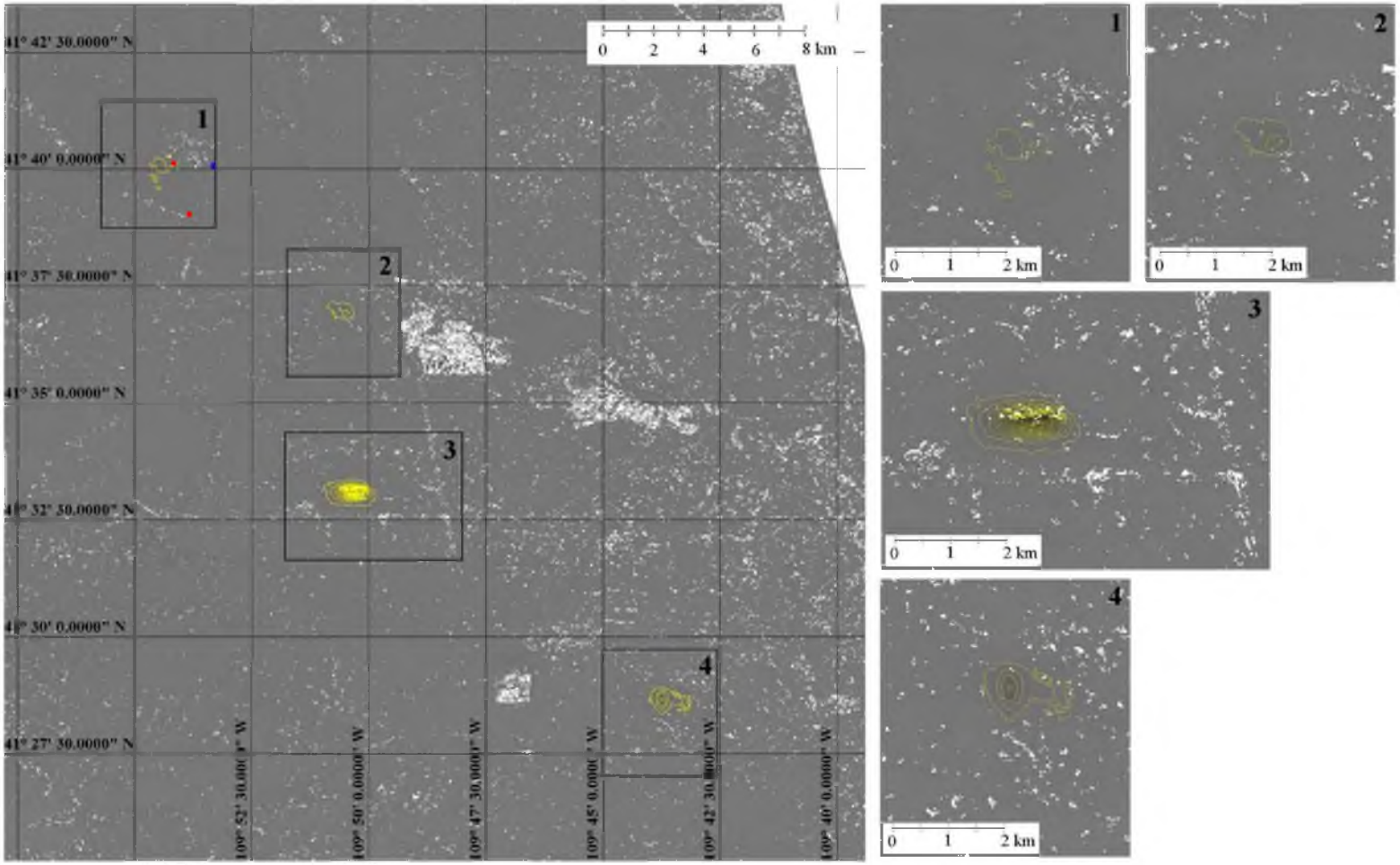

FIGURE 7.3 Displacement maps (L-band) and seismic event locations: January 19, 2008 to April 20, 2008 (92 days). ANF catalog events are shown in red, and the UUSS catalog event is shown in blue. Subsidence is contoured every 5 cm starting at −5 cm of vertical displacement.

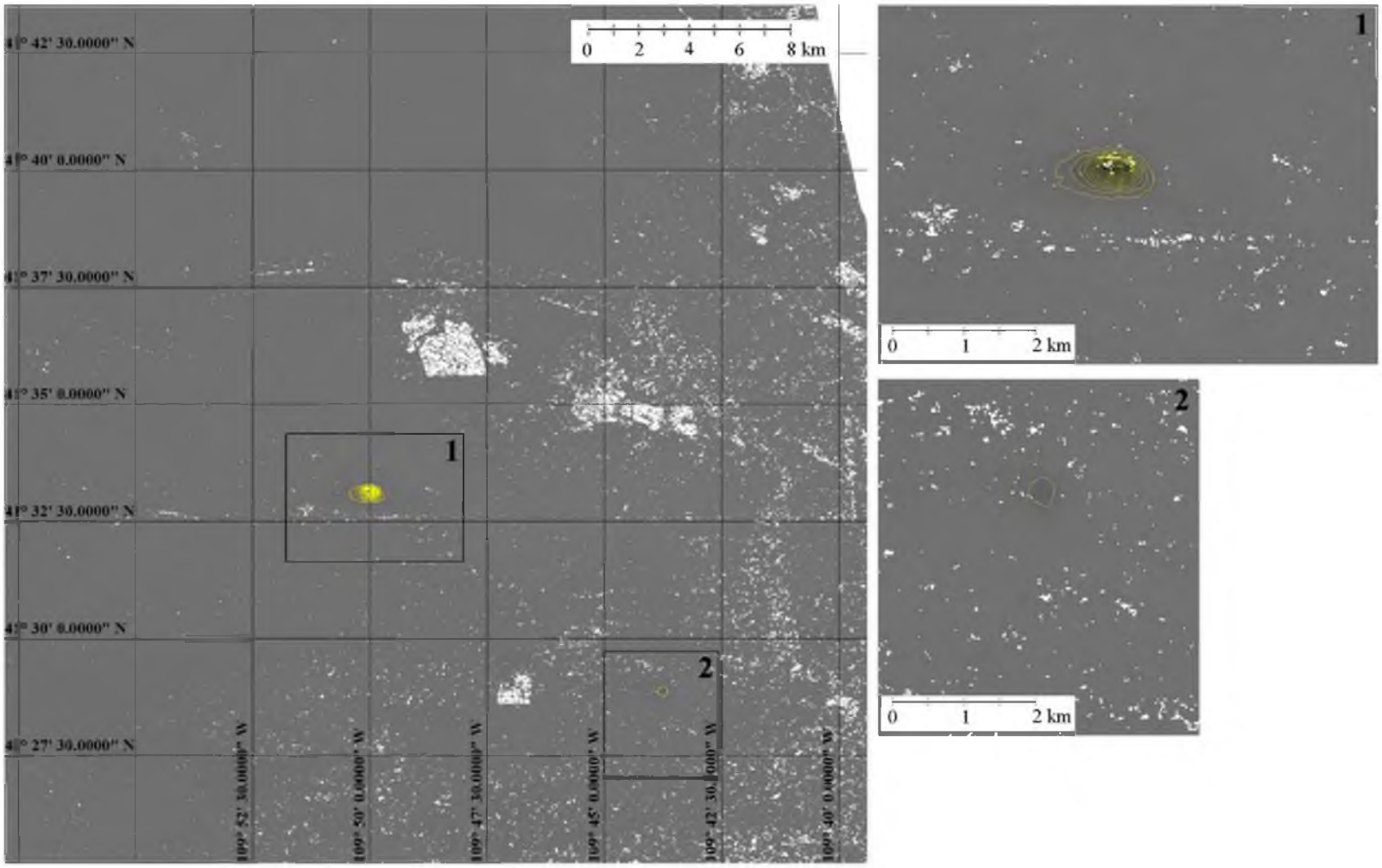

FIGURE 7.4 Displacement maps (L-band): April 20, 2008 to June 5, 2008 (46 days). Subsidence is contoured every 5 cm starting at −5 cm of vertical displacement.

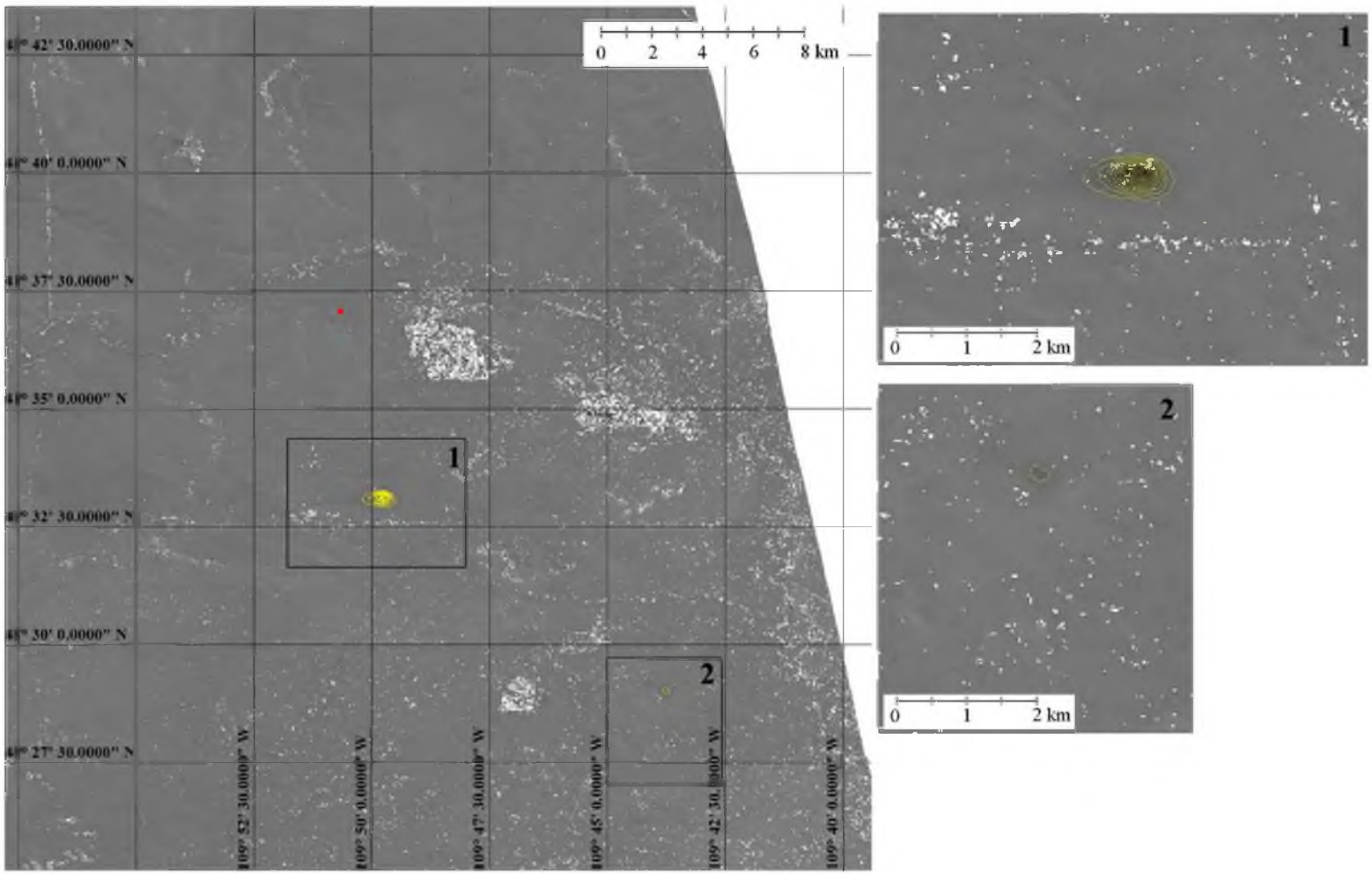

Includes material © JAXA/METI 2008

FIGURE 7.5 Displacement maps (L-band) and ANF catalog seismic event location (red): June 5, 2008 to July 21, 2008 (46 days). Subsidence is contoured every 5 cm starting at −5 cm of vertical displacement.

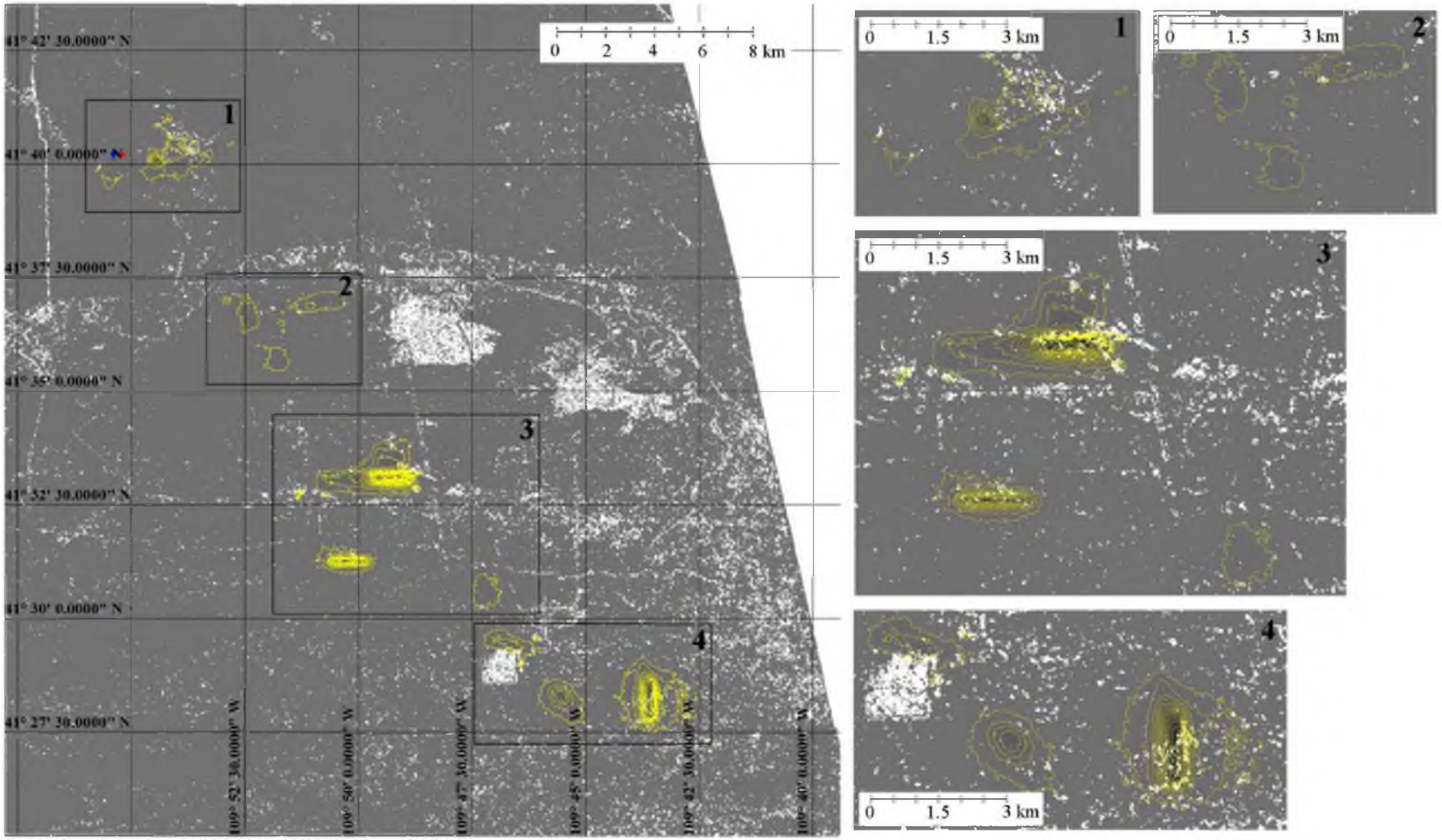

FIGURE 7.6 Displacement maps (L-band) and seismic event location: July 21, 2008 to October 24, 2009 (460 days). ANF catalog event is shown in red, and UUSS catalog event is shown in blue. Subsidence is contoured every 5 cm starting at −5 cm of vertical displacement.

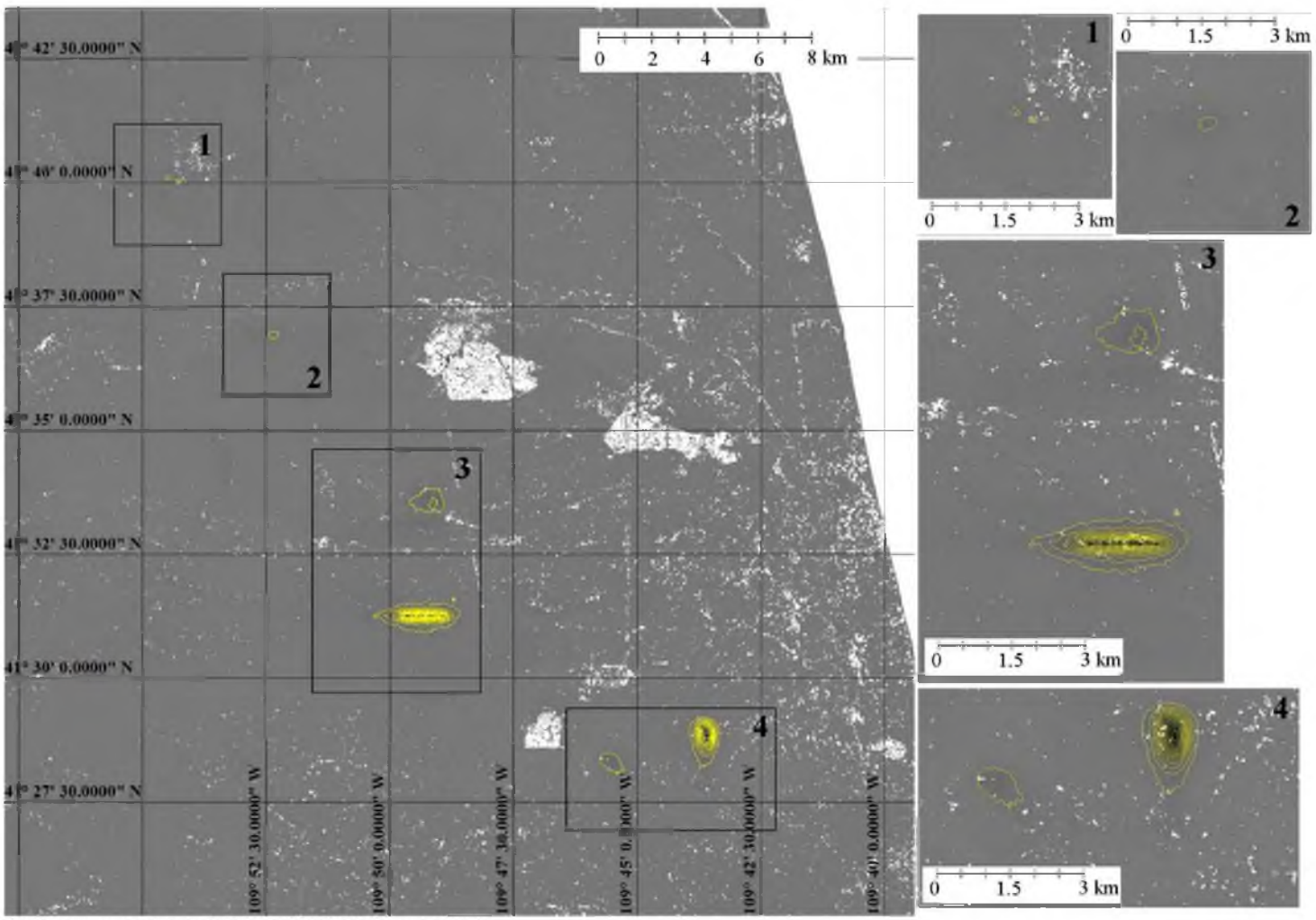

FIGURE 7.7 Displacement maps (L-band): October 24, 2009 to April 26, 2010 (184 days). Subsidence is contoured every 5 cm starting at −5 cm of vertical displacement.

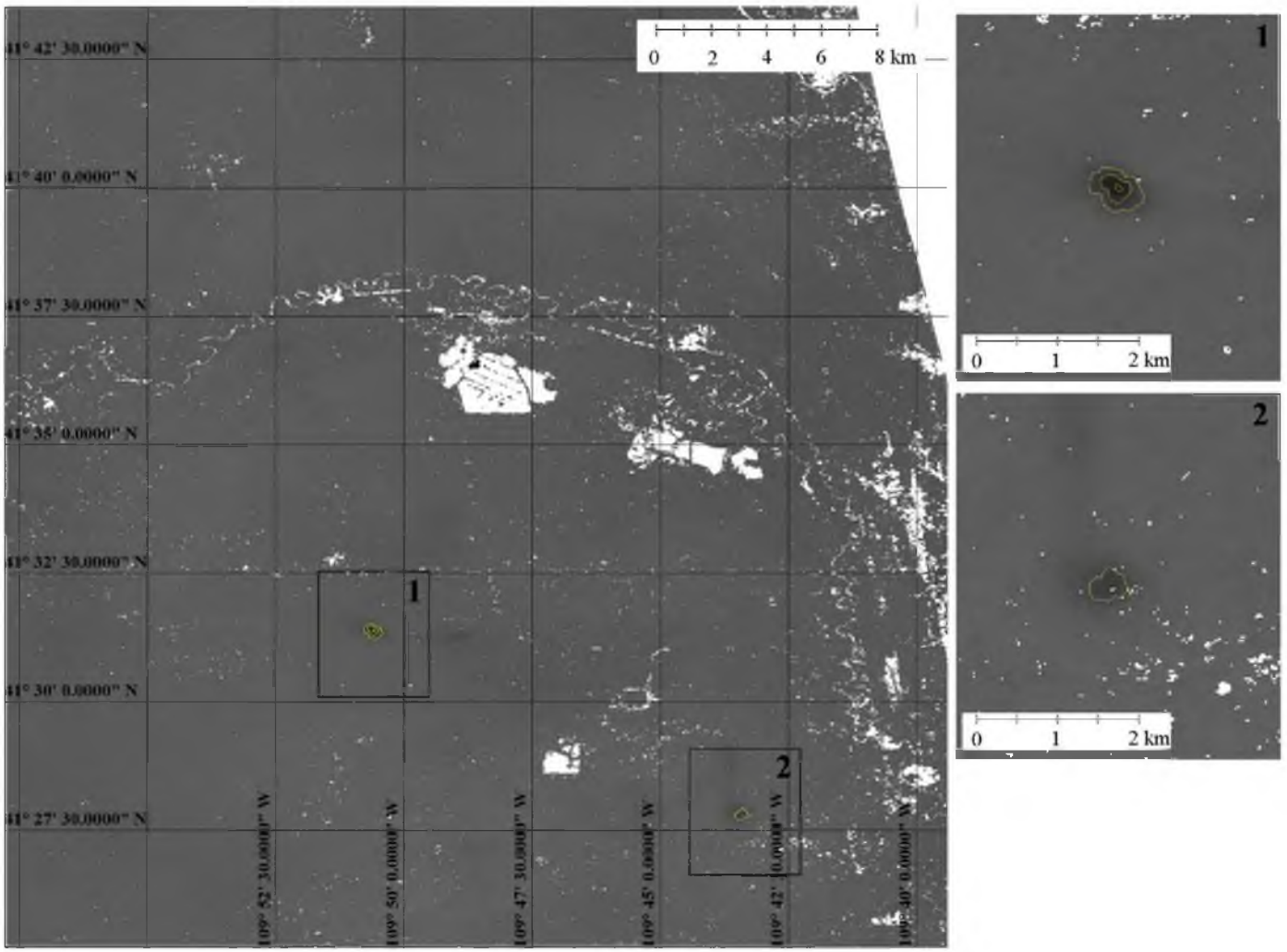

FIGURE 7.8 Displacement maps (L-band): April 26, 2010 to June 11, 2010 (46 days). Subsidence is contoured every 5 cm starting at −5 cm of vertical displacement.

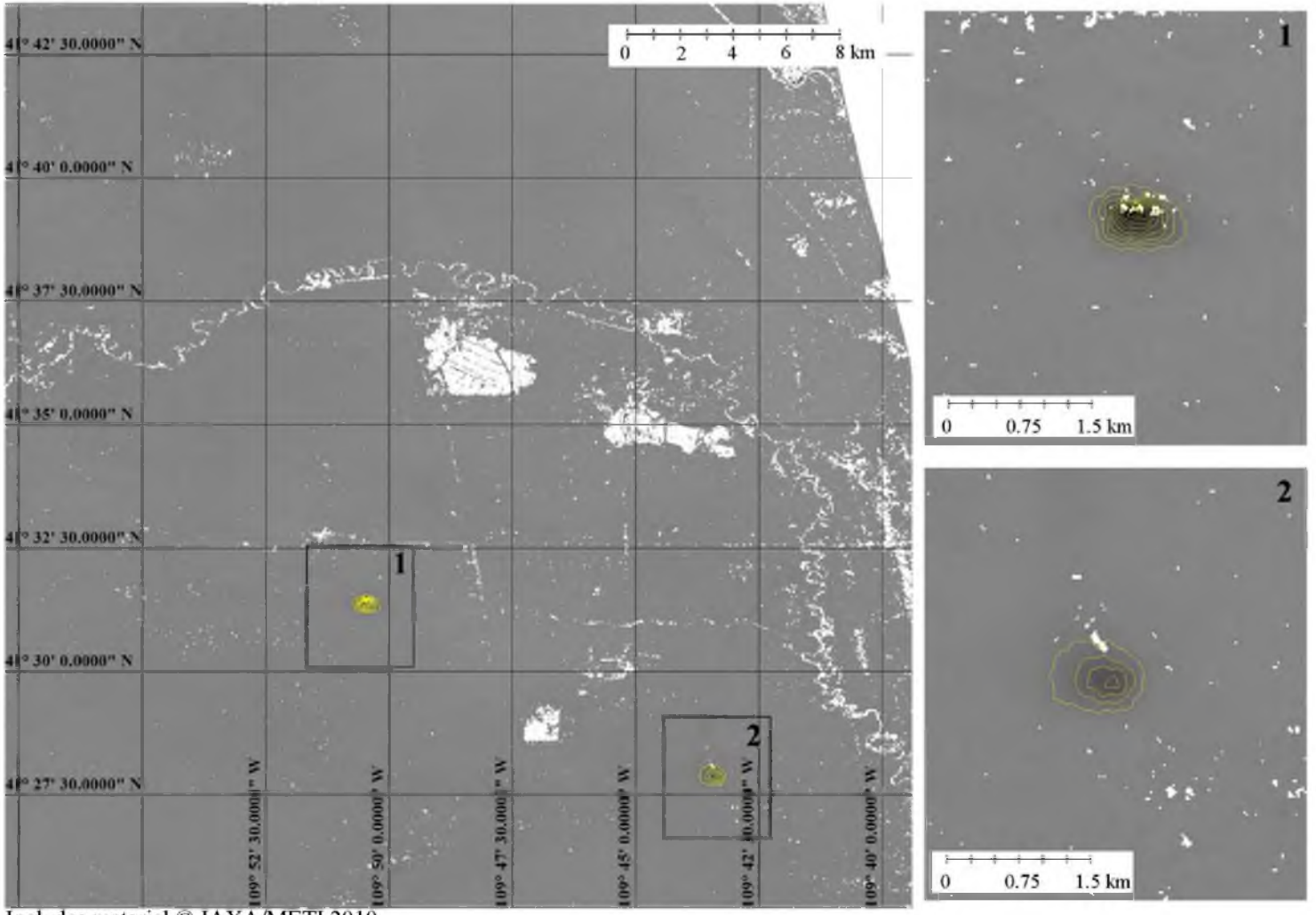

FIGURE 7.9 Displacement maps (L-band): June 11, 2010 to July 27, 2010 (46 days). Subsidence is contoured every 5 cm starting at −5 cm of vertical displacement.

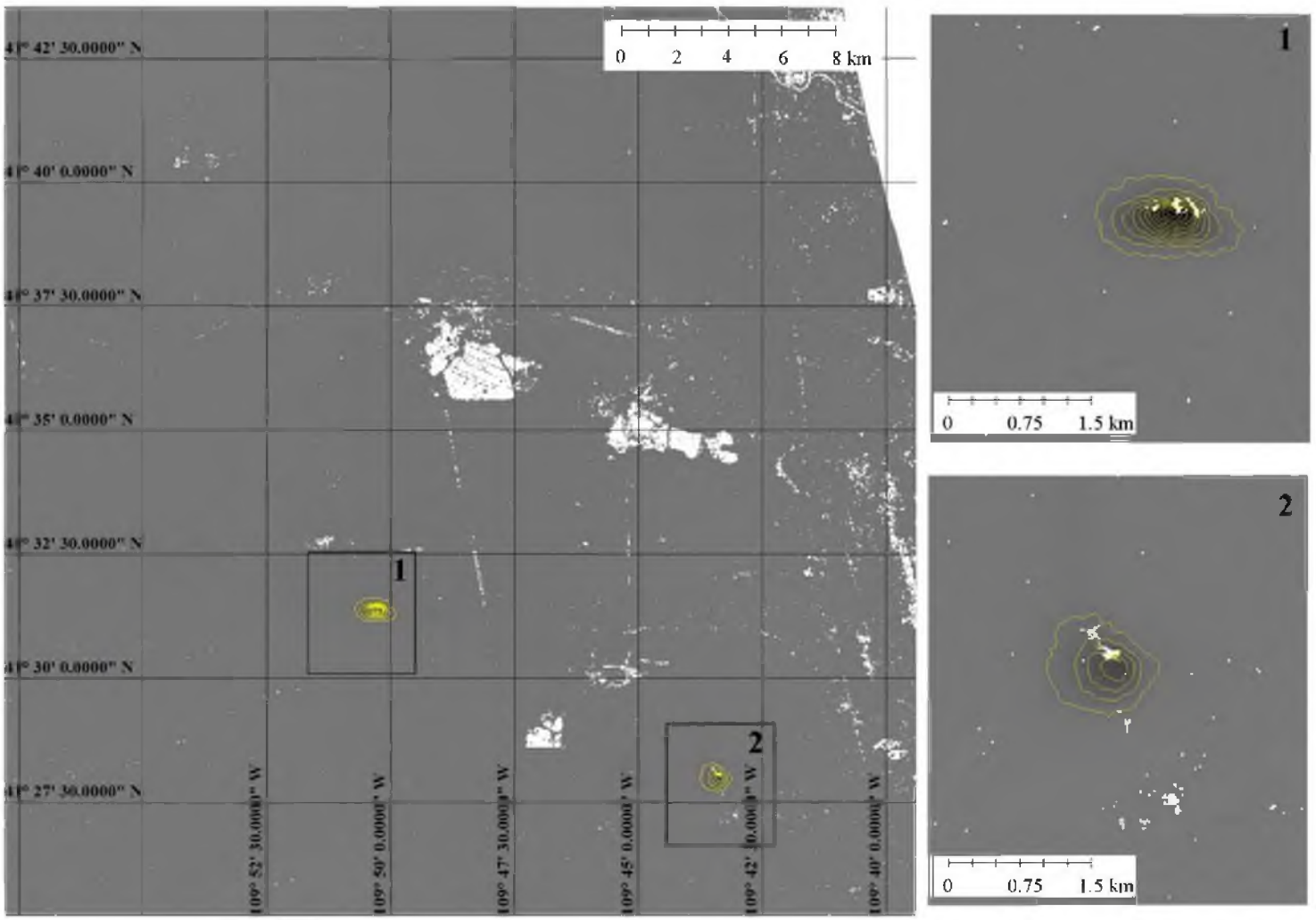

FIGURE 7.10 Displacement maps (L-band): July 27, 2010 to September 11, 2010 (46 days). Subsidence is contoured every 5 cm starting at −5 cm of vertical displacement.

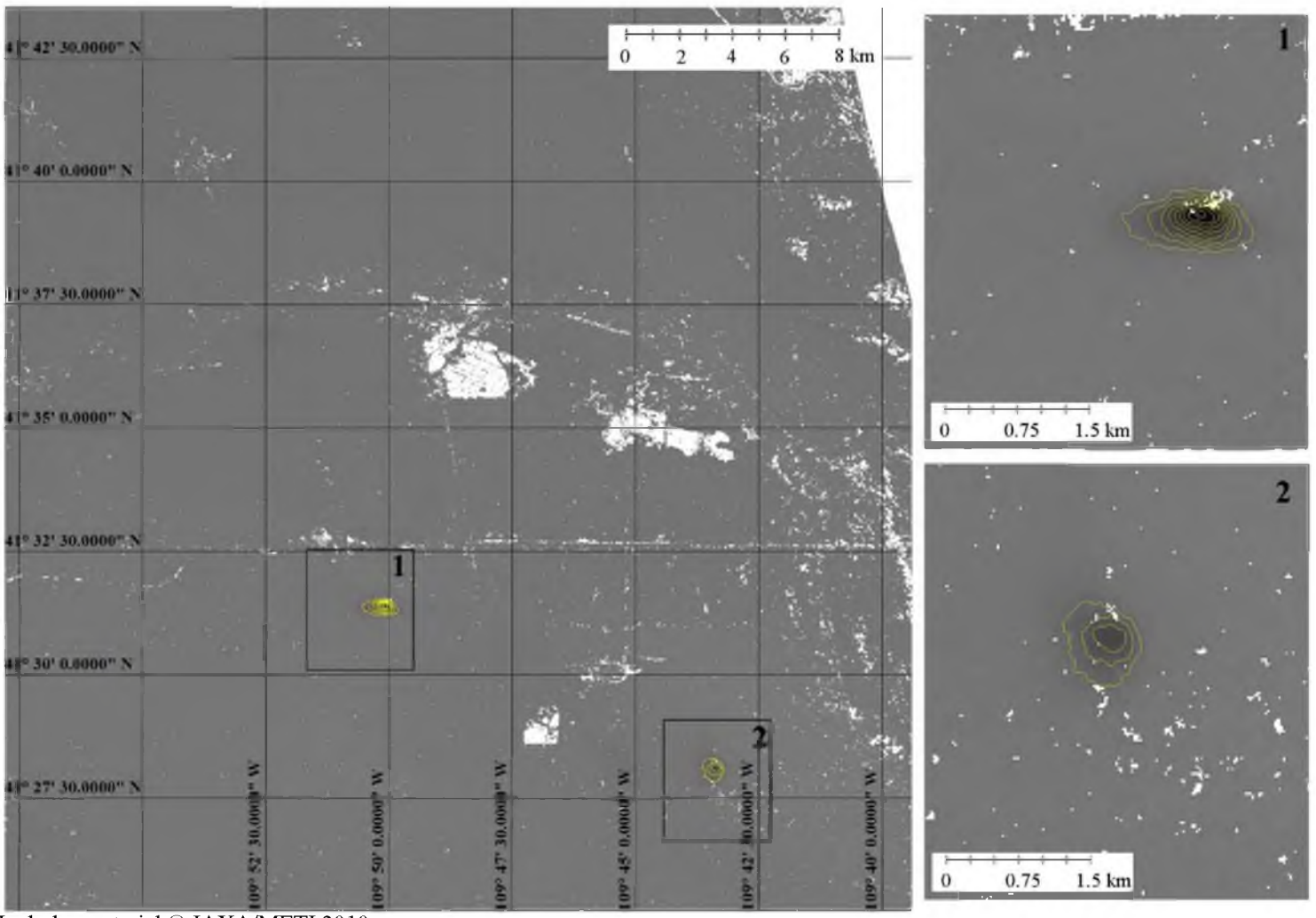

Includes material © JAXA/METI 2010

FIGURE 7.11 Displacement maps (L-band): September 11, 2010 to October 27, 2010 (46 days). Subsidence is contoured every 5 cm starting at -5 cm of vertical displacement.

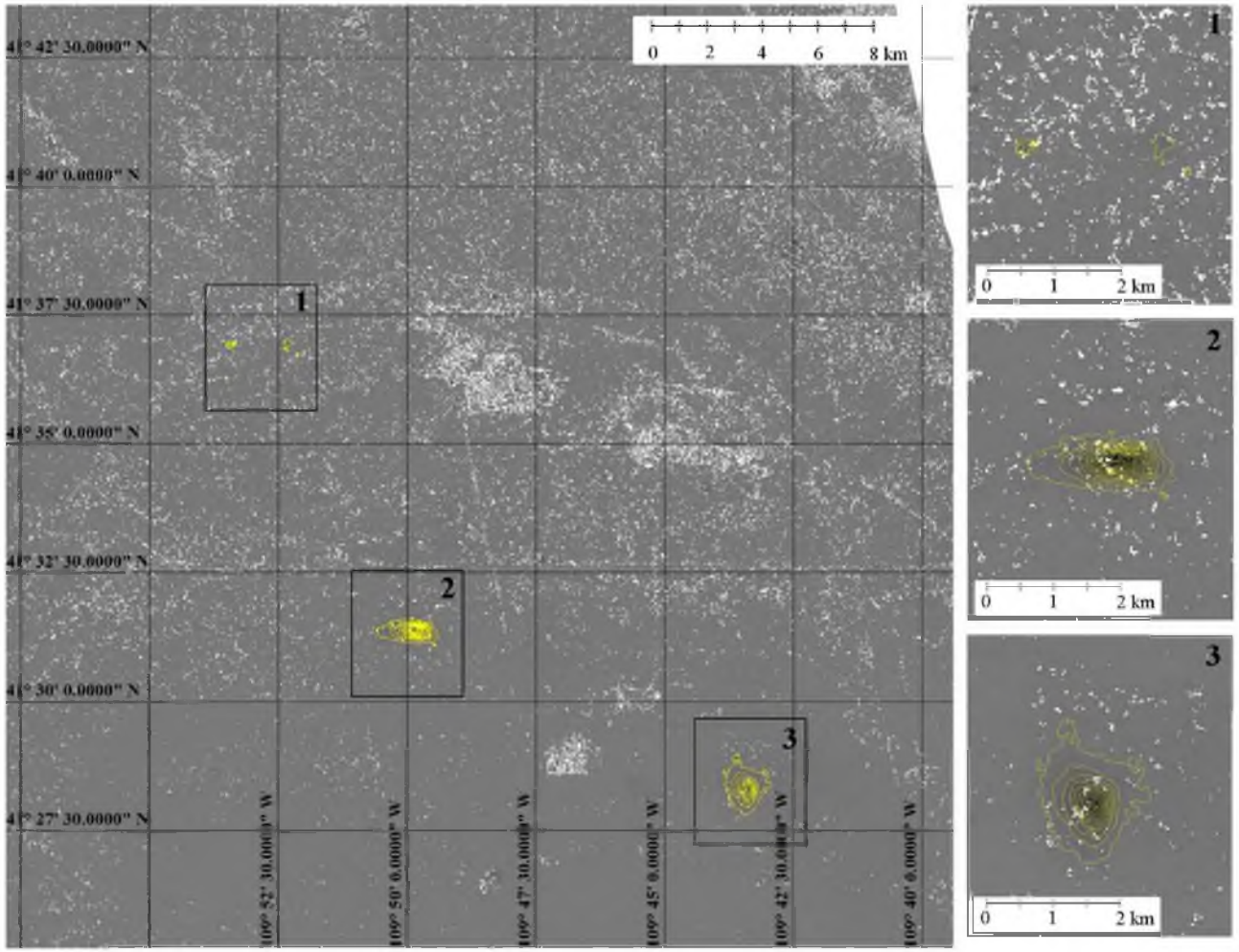

Includes material © JAXA/METI 2010 and 2011

FIGURE 7.12 Displacement maps (L-band): October 27, 2010 to January 27, 2011 (92 days). Subsidence is contoured every 5 cm starting at −5 cm of vertical displacement.

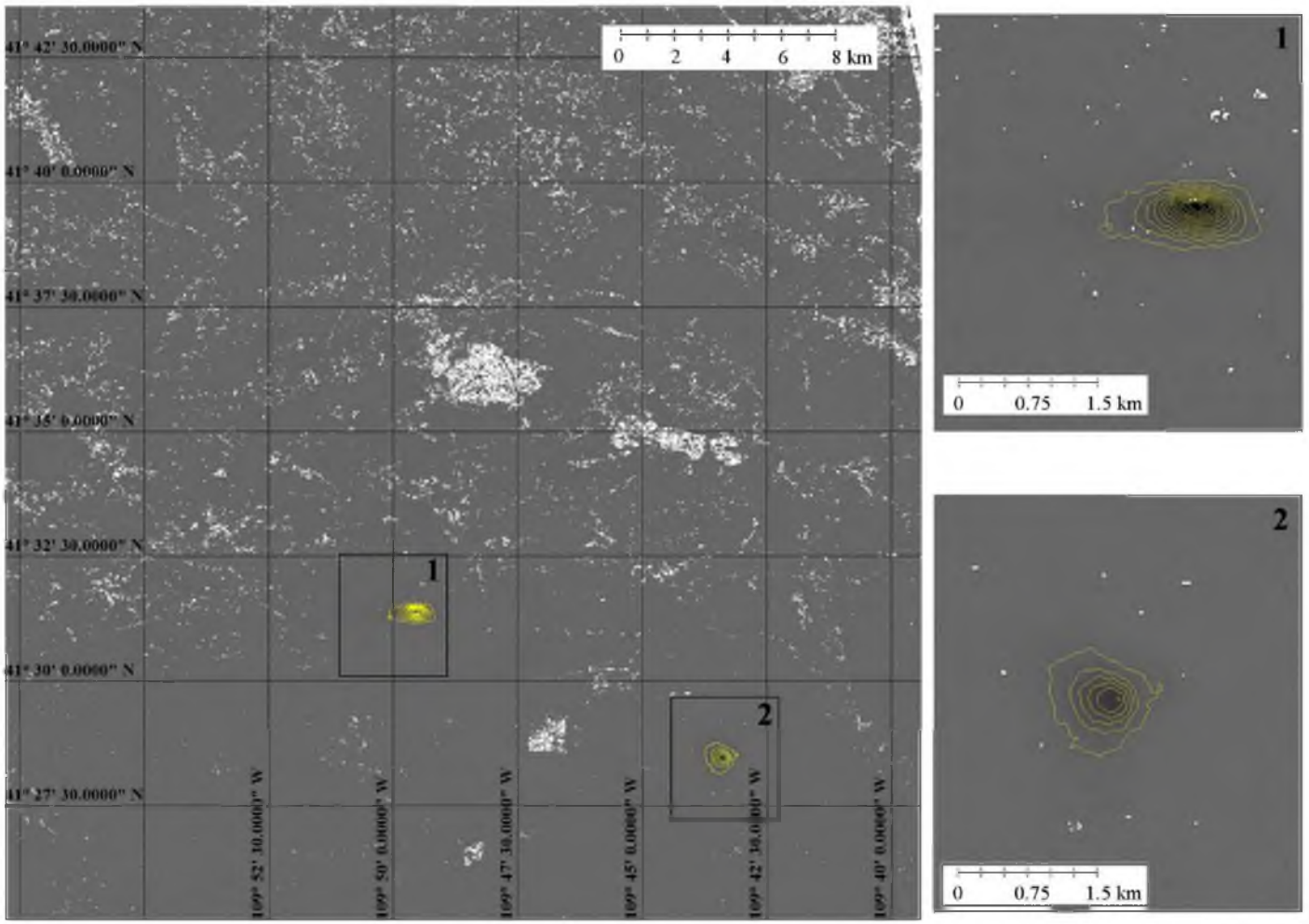

Includes material © JAXA/METI 2011

FIGURE 7.13 Displacement maps (L-band): January 27, 2011 to March 14, 2011 (46 days). Subsidence is contoured every 5 cm starting at −5 cm of vertical displacement.

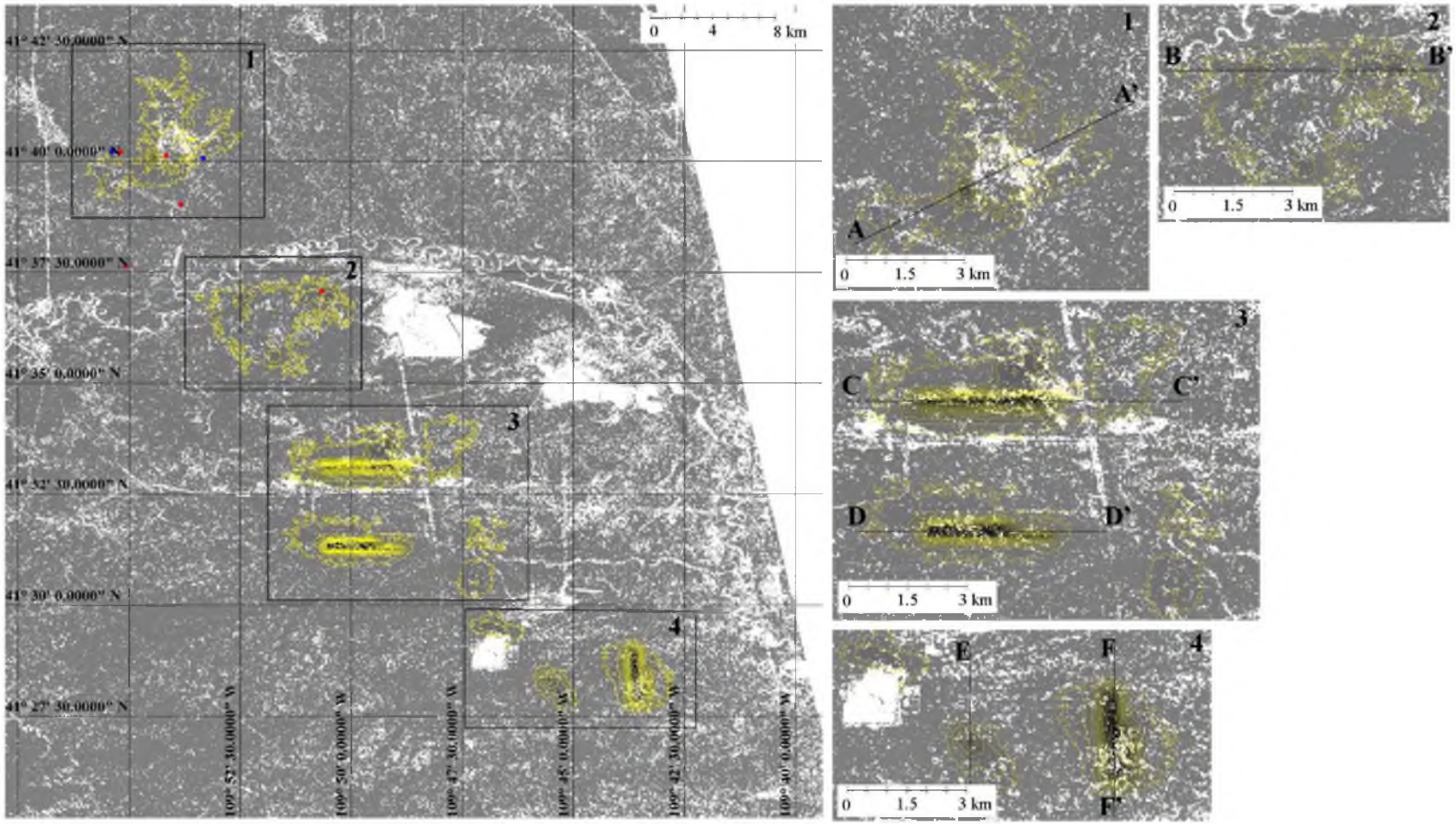

Includes material © JAXA/METI 2007, 2008, 2009, 2010, and 2011

FIGURE 7.14 Cumulative displacement maps (L-band) and seismic event locations: December 4, 2007 to March 14, 2011 (1,196 days). ANF catalog events are shown in red, and UUSS catalog events are shown in blue. Subsidence is contoured every 10 cm starting at −10 cm of vertical displacement.

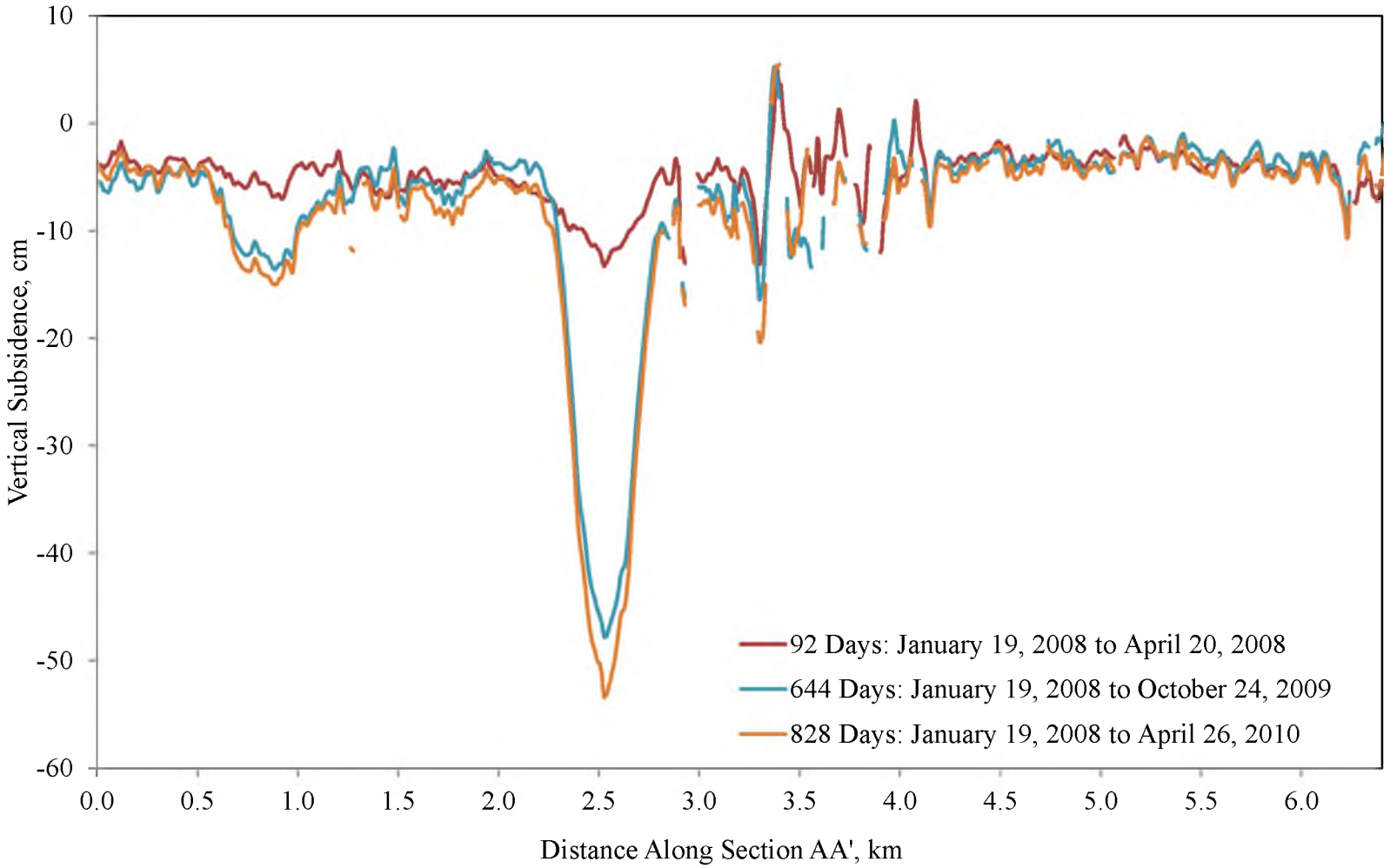

FIGURE 7.15 Time series subsidence profiles of section AA' from Figure 7.14

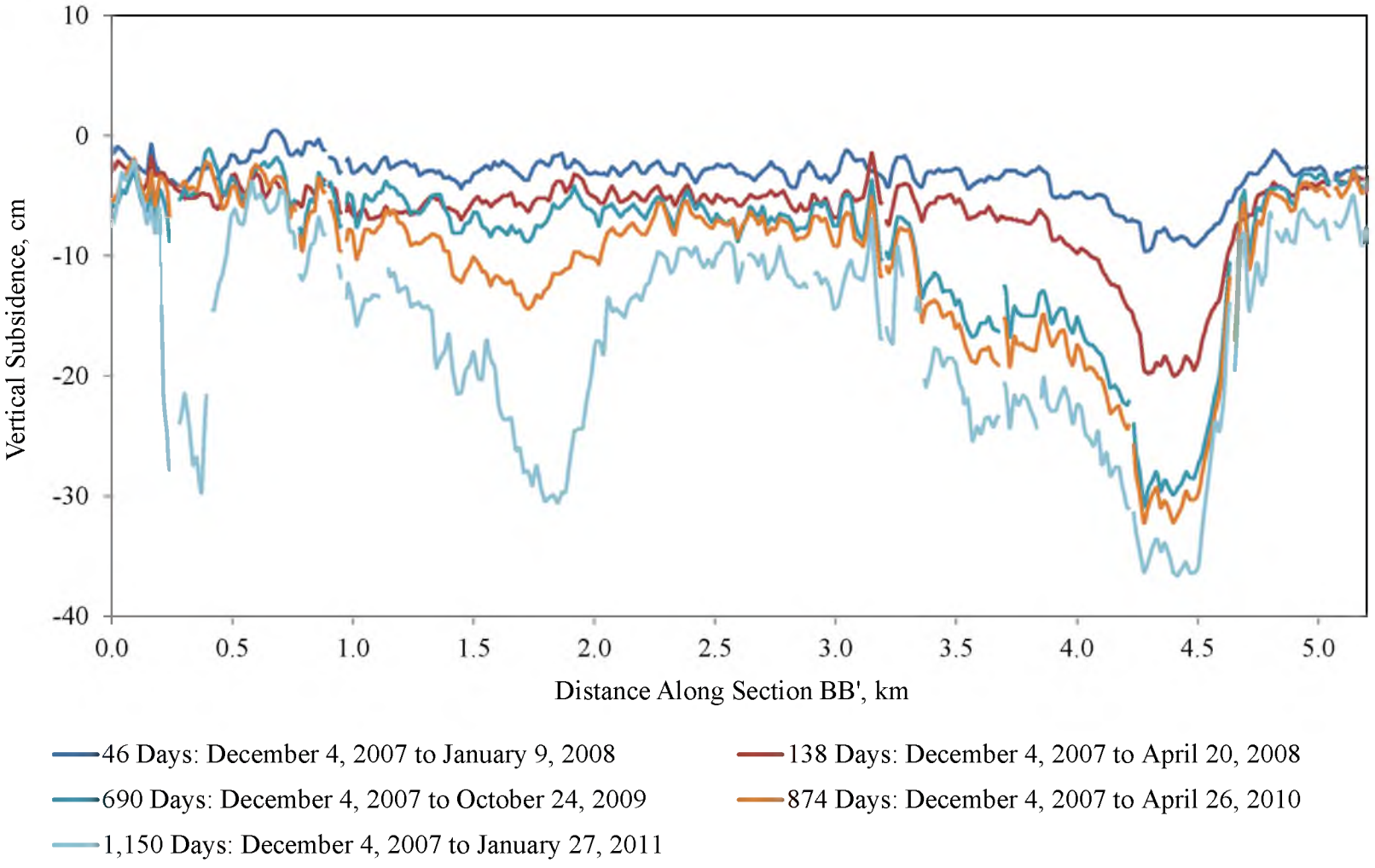

FIGURE 7.16 Time series subsidence profiles of section BB' from Figure 7.14

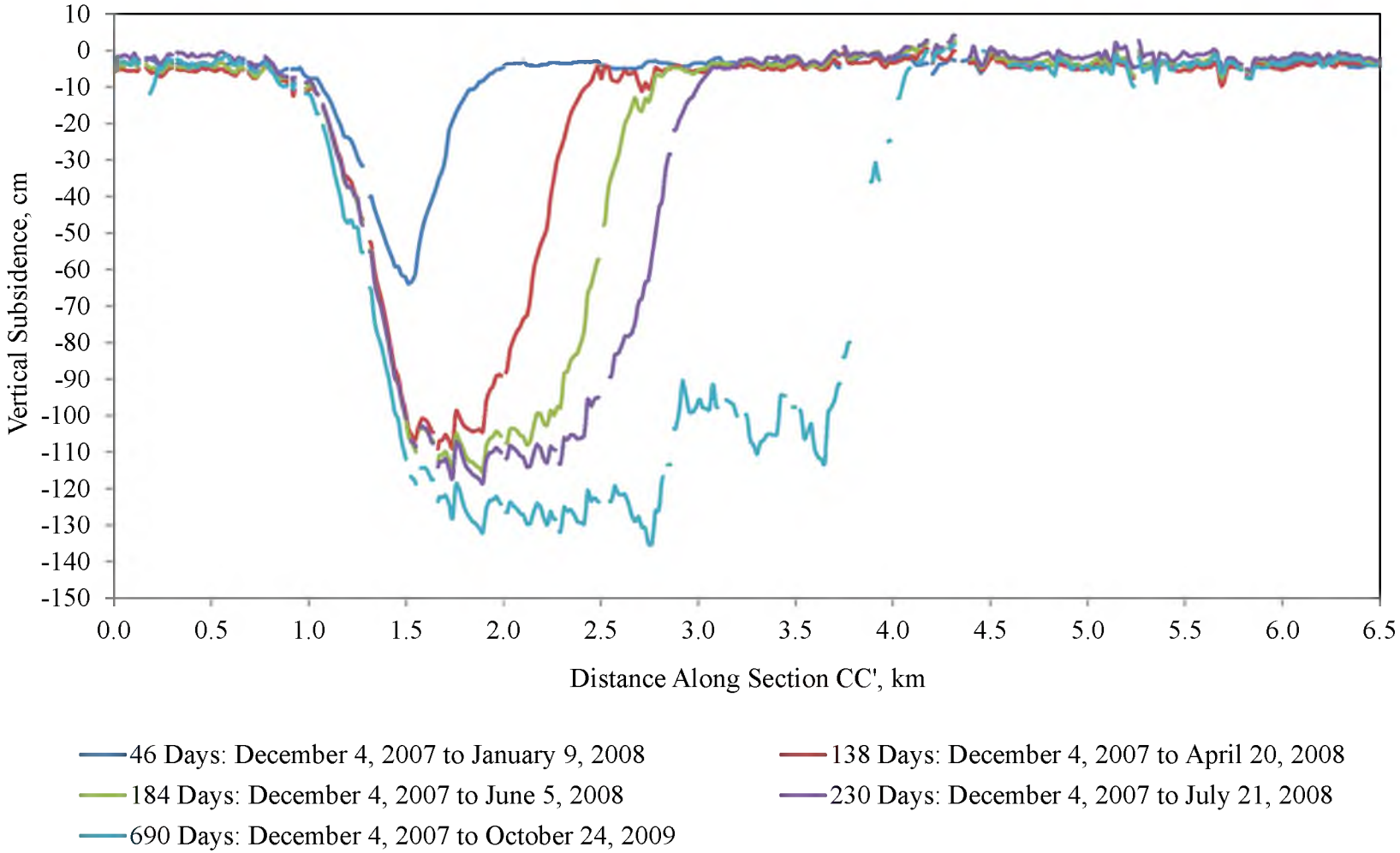

FIGURE 7.17 Time series subsidence profiles of section CC' from Figure 7.14

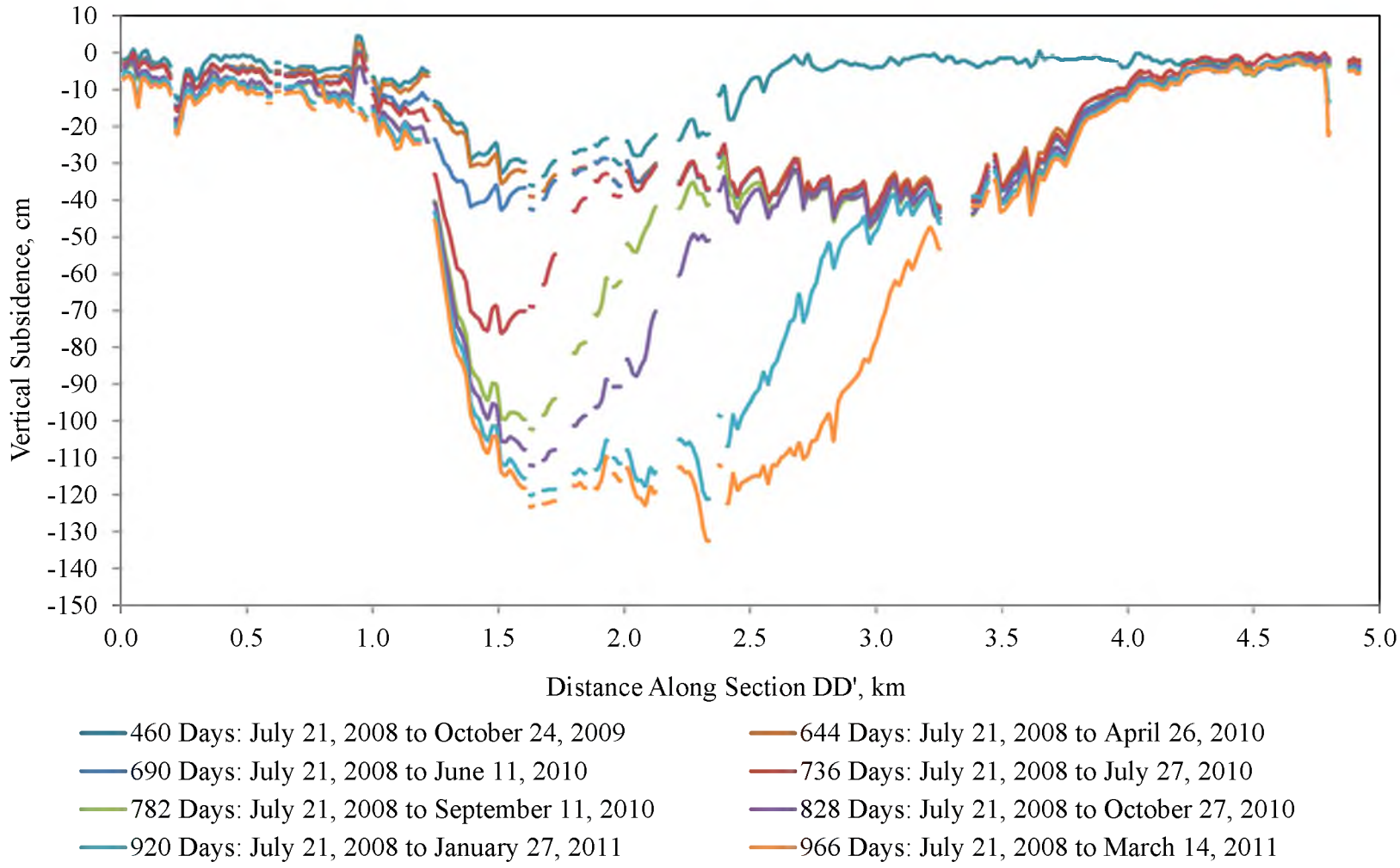

FIGURE 7.18 Time series subsidence profiles of section DD' from Figure 7.14

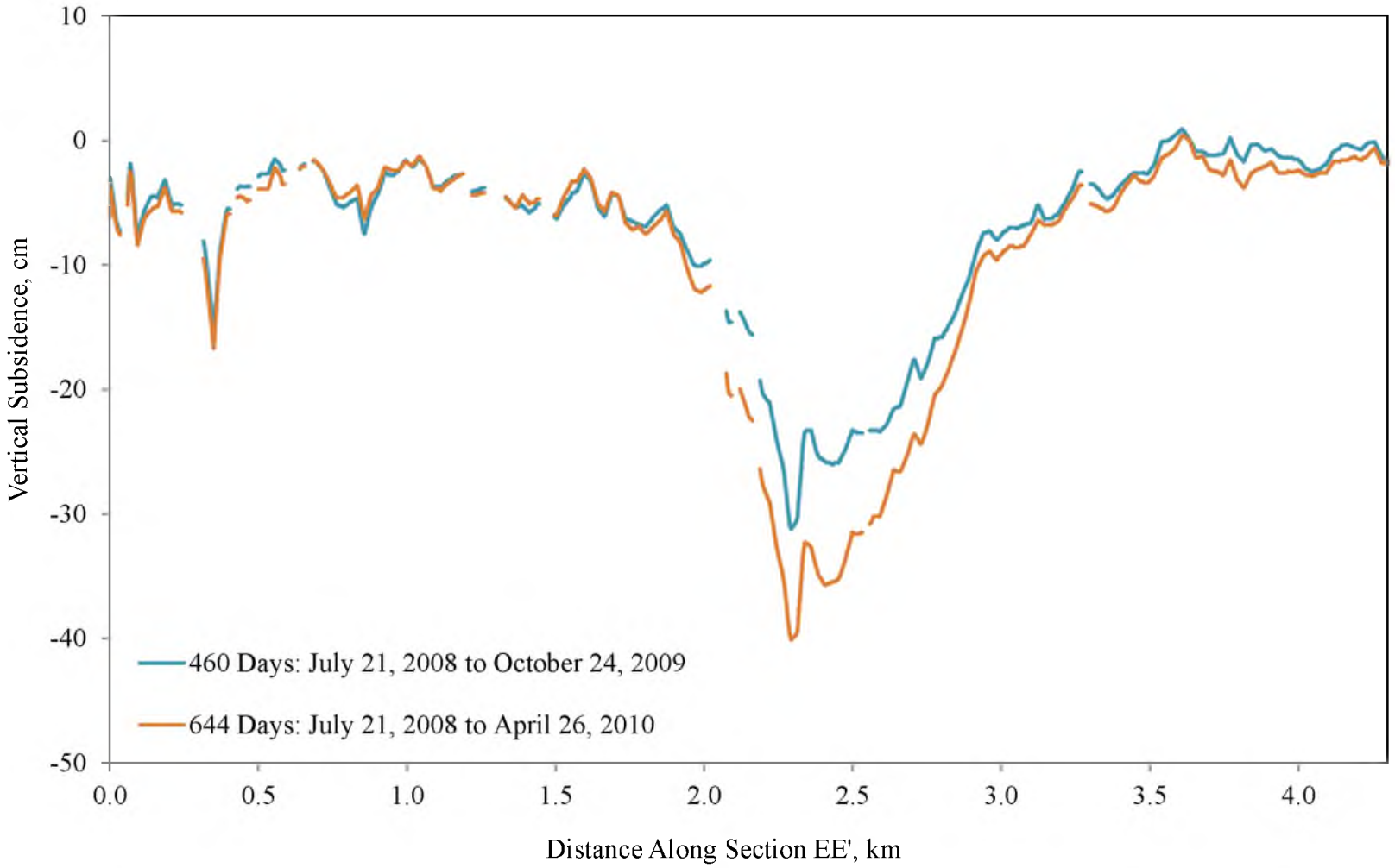

FIGURE 7.19 Time series subsidence profiles of section EE' from Figure 7.14

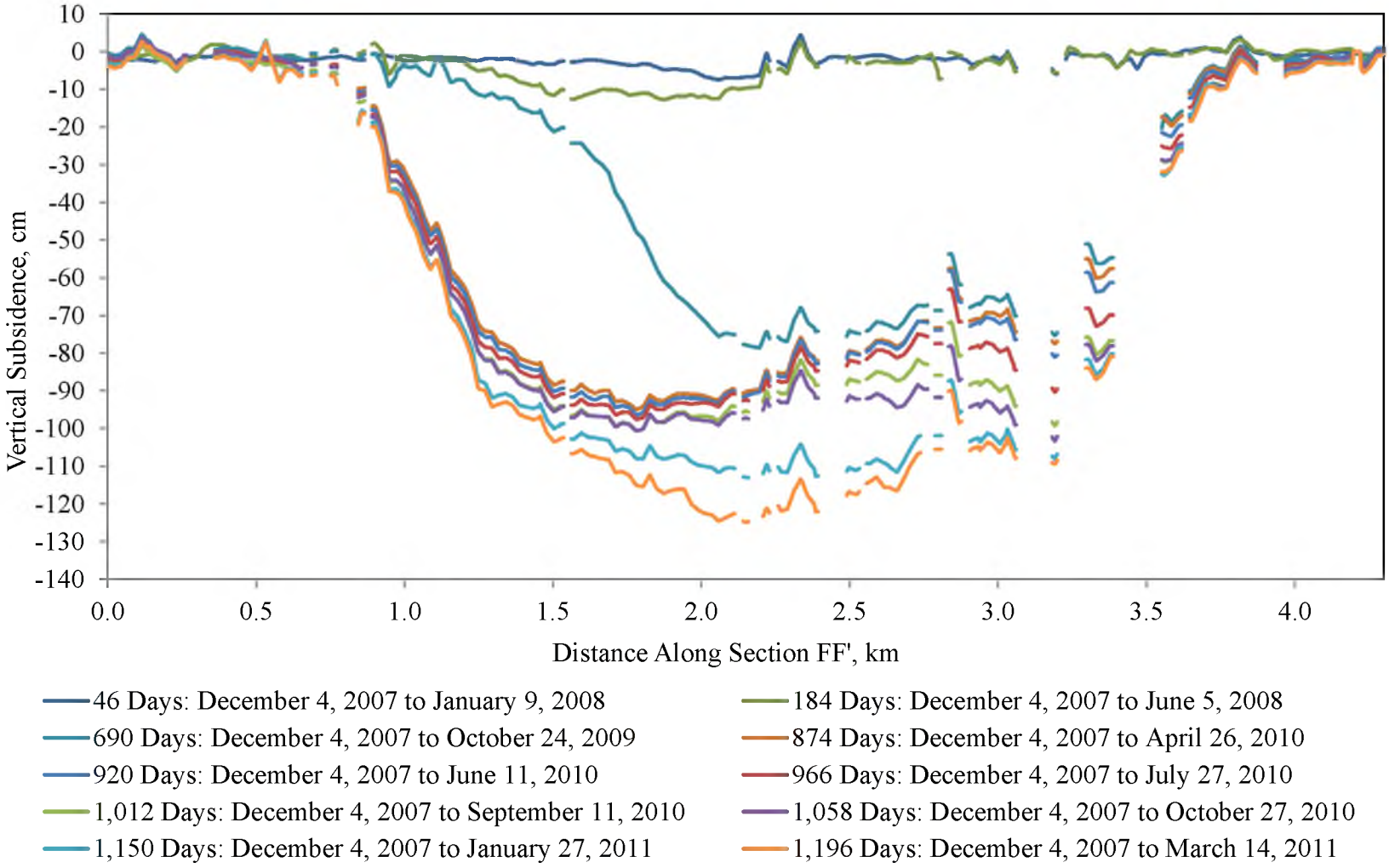

FIGURE 7.20 Time series subsidence profiles of section FF' from Figure 7.14

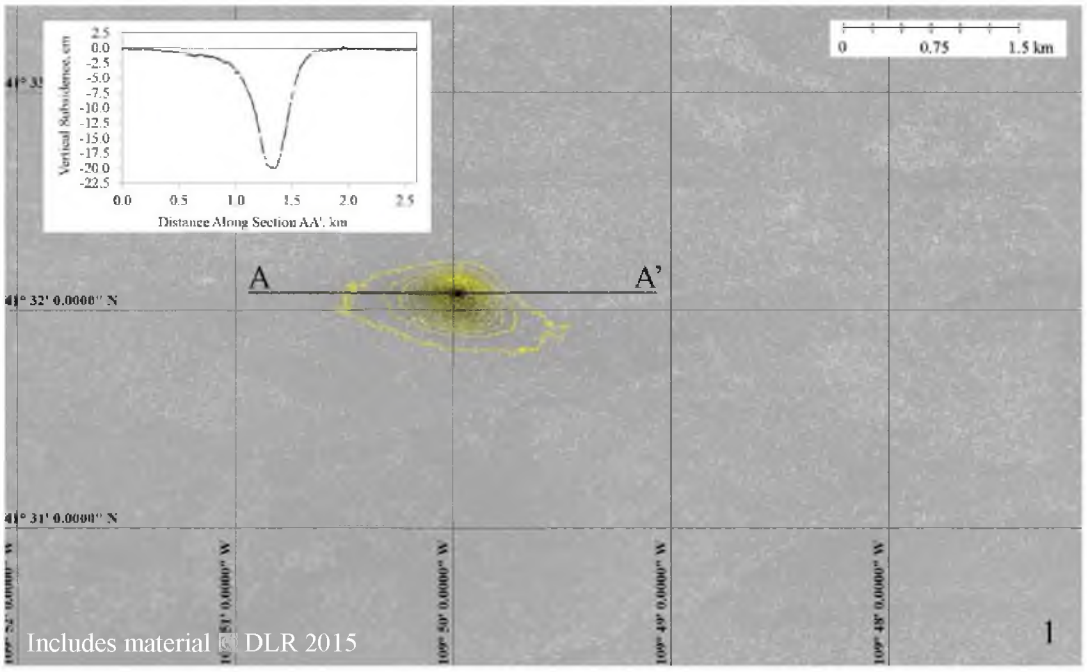

FIGURE 7.21 Region 1 displacement map (X-band): June 2, 2015 to June 13, 2015 (11 days). Subsidence is contoured every 1 cm starting at −1 cm of vertical displacement.

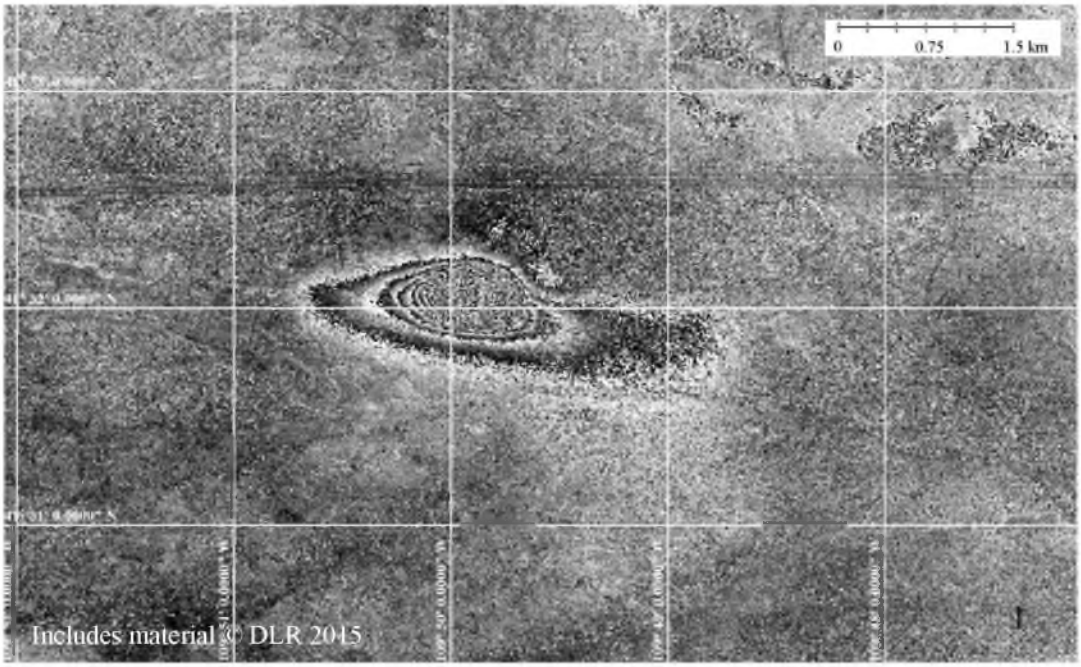

FIGURE 7.22 Region 1 filtered differential interferogram (X-band) with significant signal noise and phase saturation in region of maximum displacement: June 13, 2015 to July 16, 2015 (33 days)

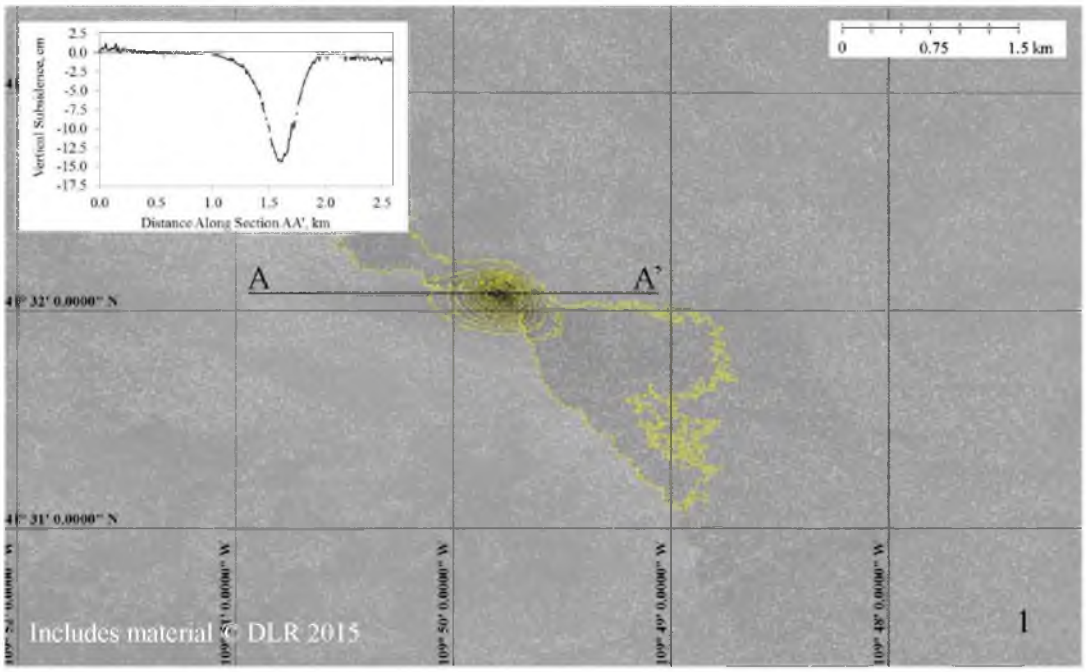

FIGURE 7.23 Region 1 (X-band) displacement map: July 16, 2015 to July 27, 2015 (11 days). Subsidence is contoured every 1 cm starting at −1 cm of vertical displacement.

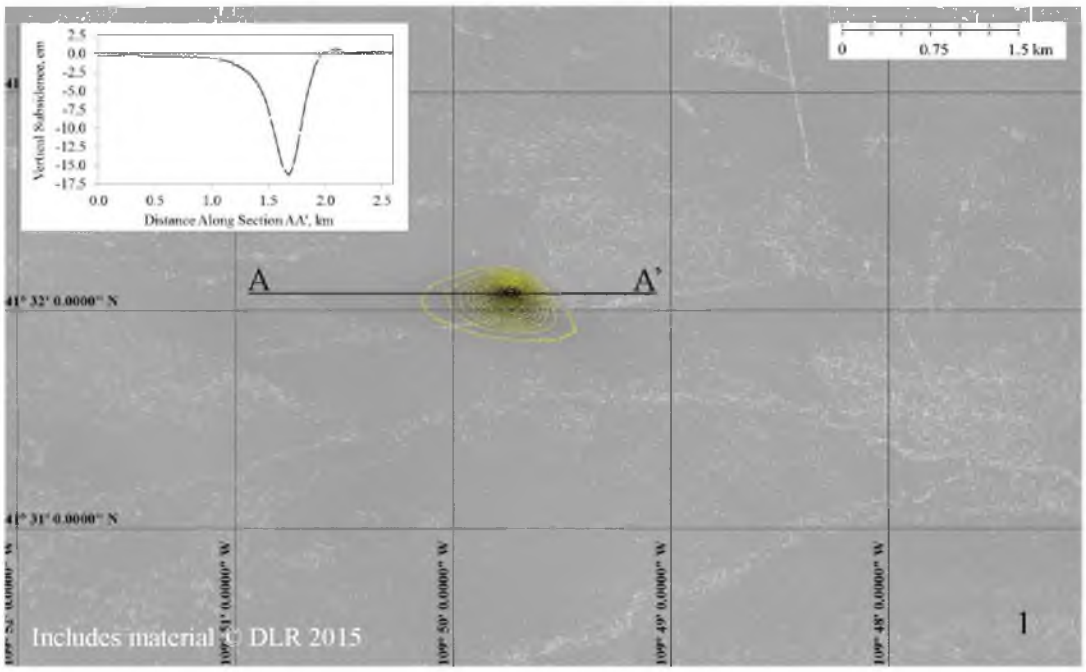

FIGURE 7.24 Region 1 displacement map (X-band): July 27, 2015 to August 7, 2015 (11 days). Subsidence is contoured every 1 cm starting at −1 cm of vertical displacement.

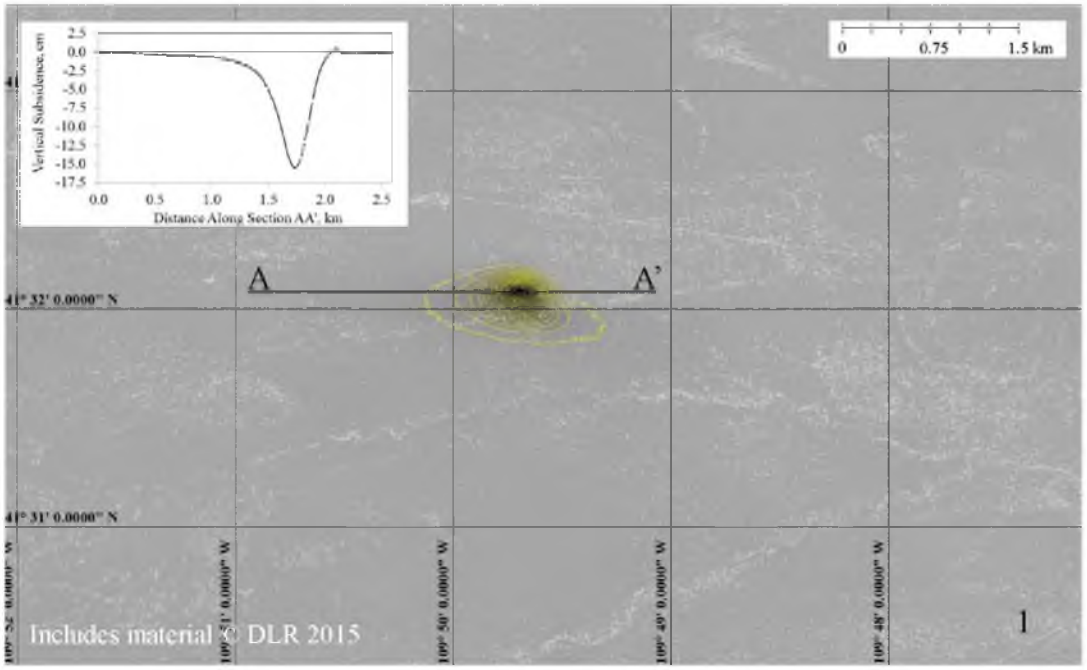

FIGURE 7.25 Region 1 displacement map (X-band): August 7, 2015 to August 18, 2015 (11 days) Subsidence is contoured every 1 cm starting at −1 cm of vertical displacement.

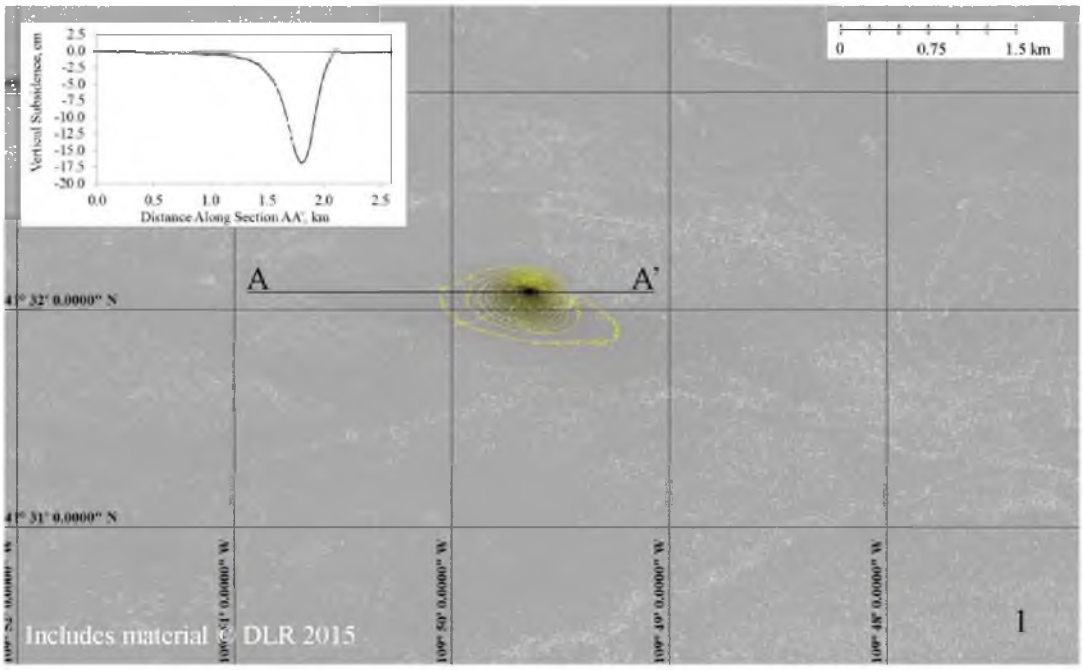

FIGURE 7.26 Region 1 displacement map (X-band): August 18, 2015 to August 29, 2015 (11 days). Subsidence is contoured every 1 cm starting at −1 cm of vertical displacement.

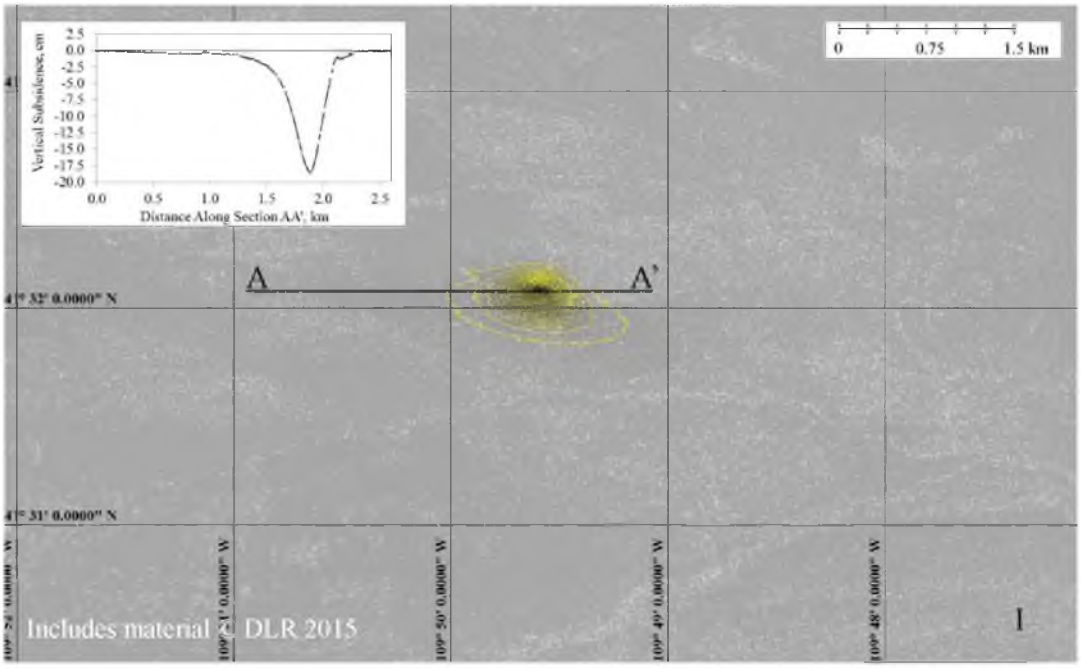

FIGURE 7.27 Region 1 displacement map (X-band): August 29, 2015 to September 9, 2015 (11 days). Subsidence is contoured every 1 cm starting at −1 cm of vertical displacement.

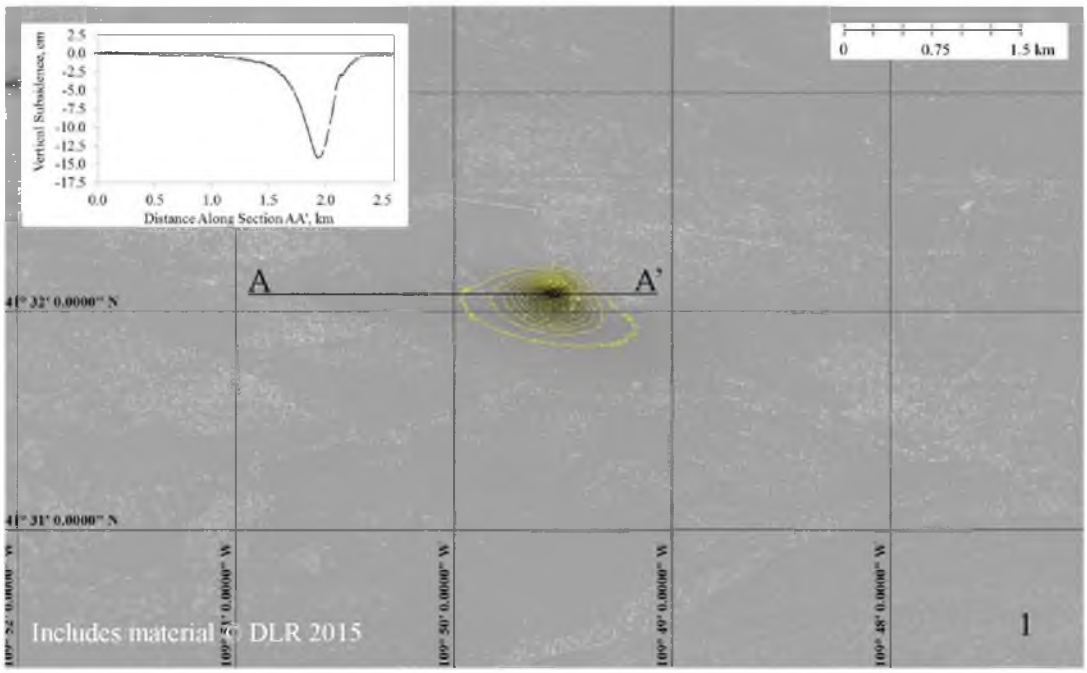

FIGURE 7.28 Region 1 displacement map (X-band): September 9, 2015 to September 20, 2015 (11 days). Subsidence is contoured every 1 cm starting at −1 cm of vertical displacement.

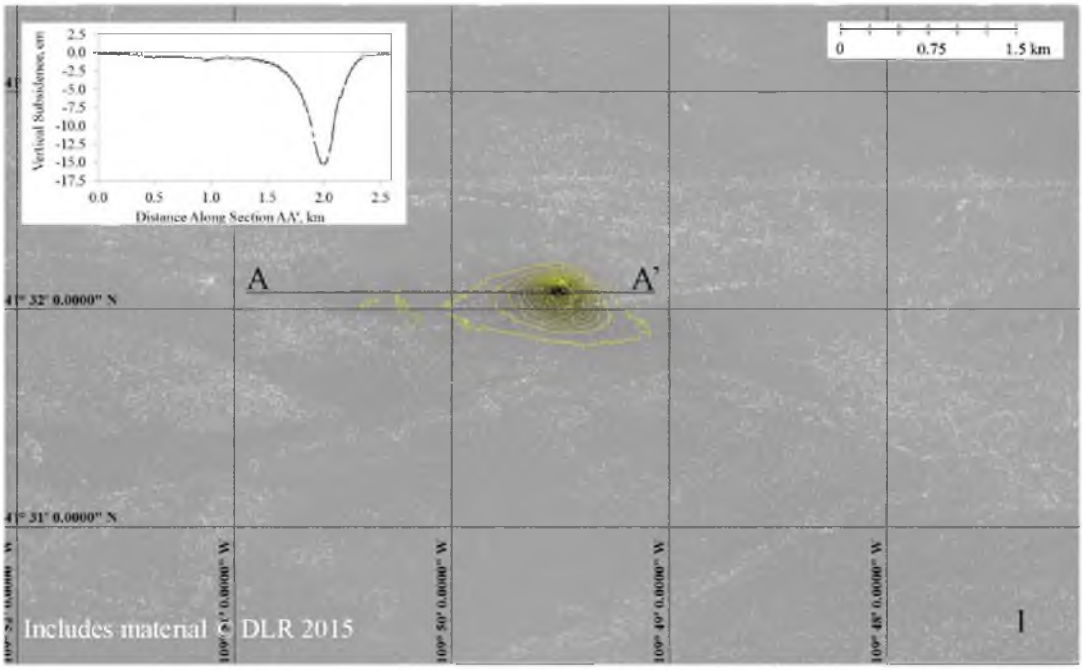

FIGURE 7.29 Region 1 displacement map (X-band): September 20, 2015 to October 1, 2015 (11 days). Subsidence is contoured every 1 cm starting at −1 cm of vertical displacement.

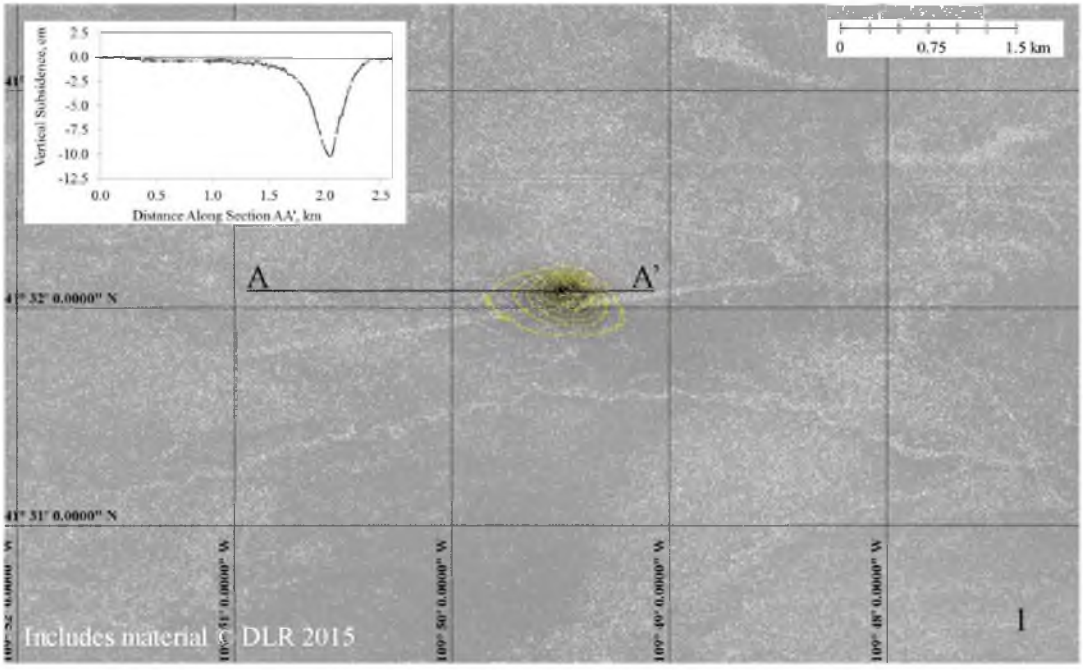

FIGURE 7.30 Region 1 displacement map (X-band): October 1, 2015 to October 12, 2015 (11 days). Subsidence is contoured every 1 cm starting at −1 cm of vertical displacement.

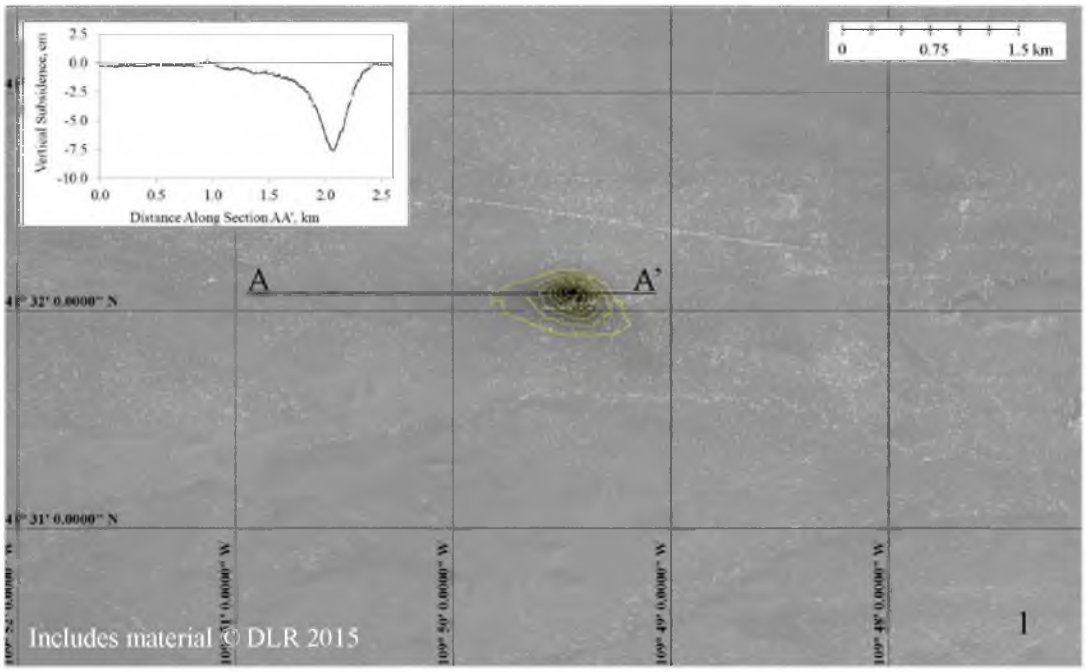

FIGURE 7.31 Region 1 displacement map (X-band): October 12, 2015 to October 23, 2015 (11 days). Subsidence is contoured every 1 cm starting at −1 cm of vertical displacement.

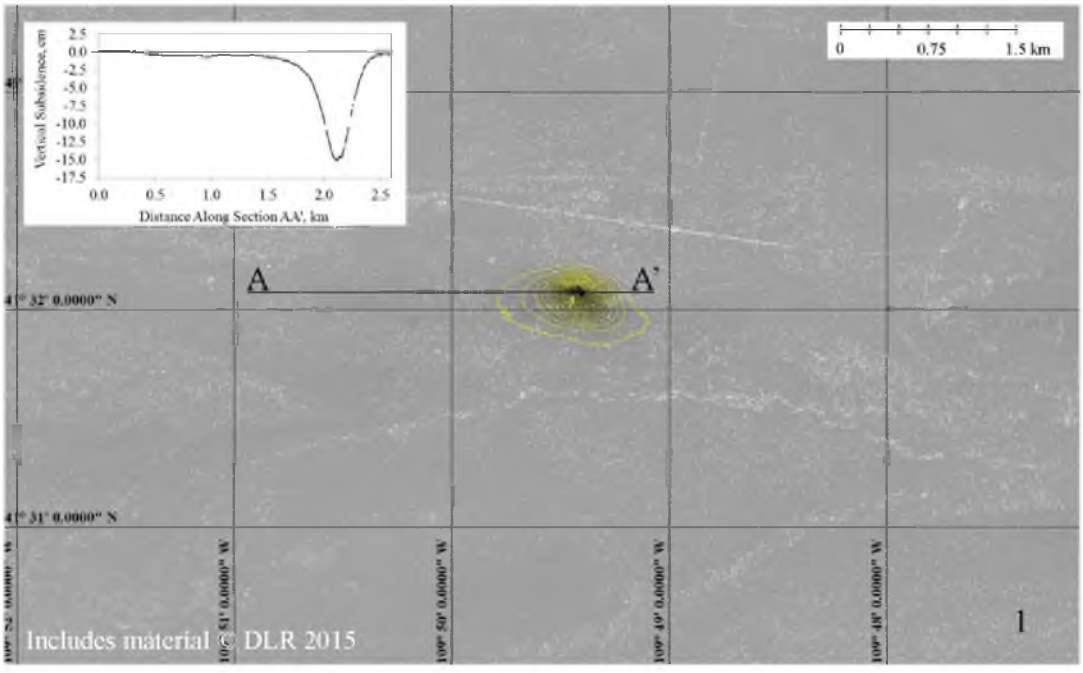

FIGURE 7.32 Region 1 displacement map (X-band): October 23, 2015 to November 3, 2015 (11 days). Subsidence is contoured every 1 cm starting at −1 cm of vertical displacement.

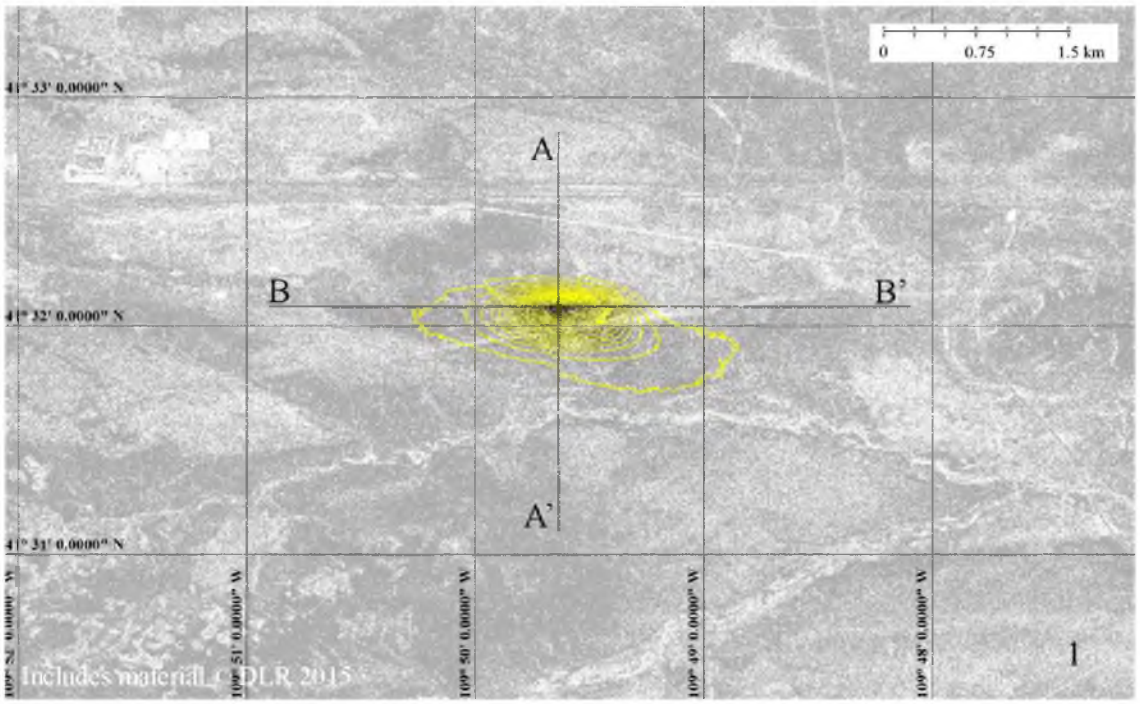

FIGURE 7.33 Region 1 cumulative displacement map (X-band): July 16, 2015 to November 3, 2015 (110 days). Subsidence is contoured every 5 cm starting at −5 cm of vertical displacement.

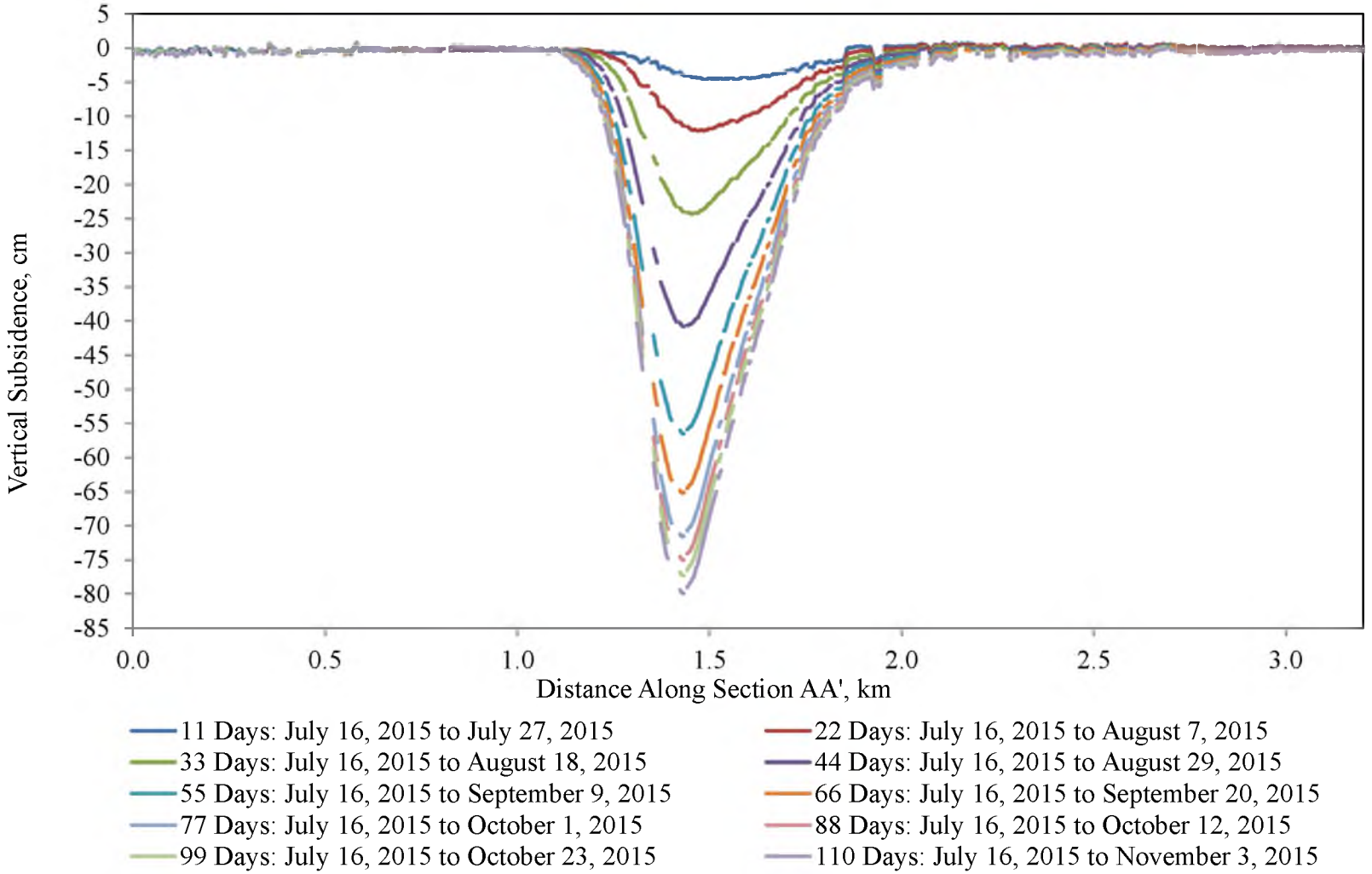

FIGURE 7.34 Time series subsidence profiles of section AA' from Figure 7.33

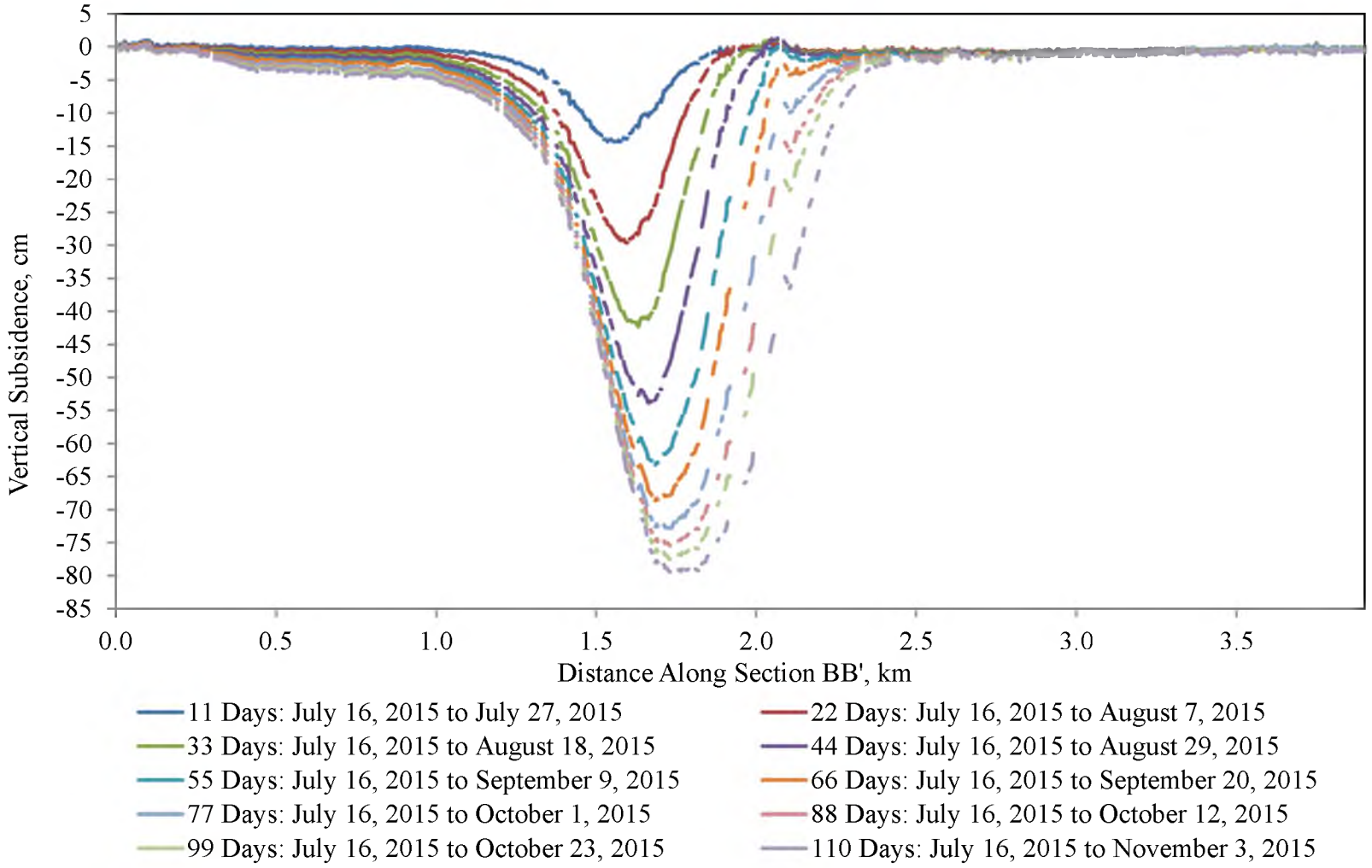

FIGURE 7.35 Time series subsidence profiles of section BB' from Figure 7.33

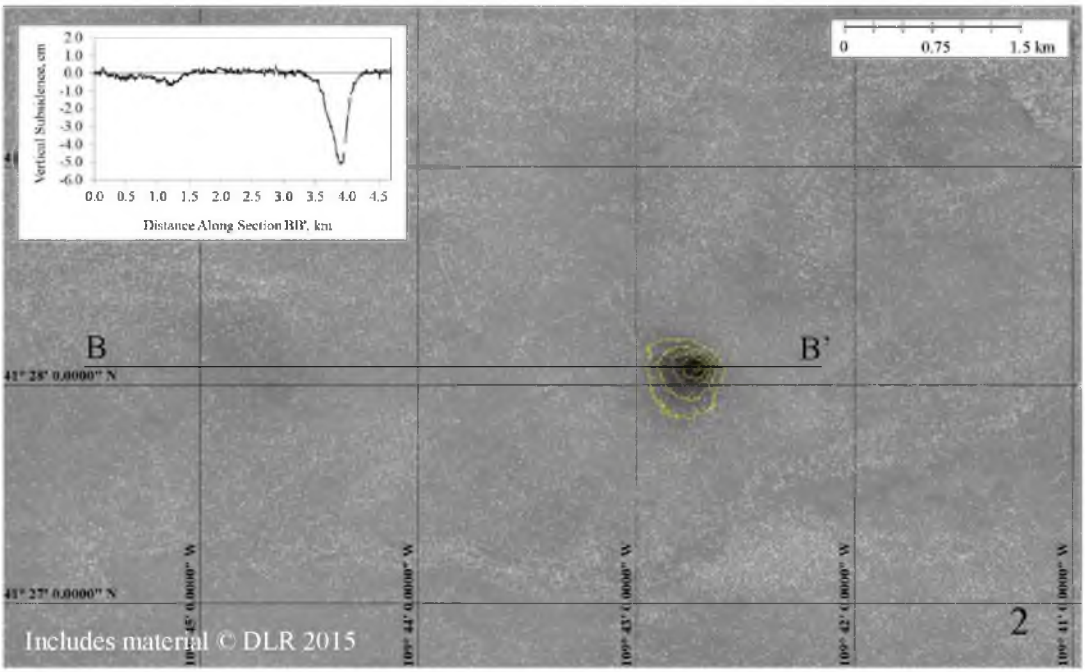

FIGURE 7.36 Region 2 displacement map (X-band): June 2, 2015 to June 13, 2015 (11 days). Subsidence is contoured every 1 cm starting at -1 cm of vertical displacement.

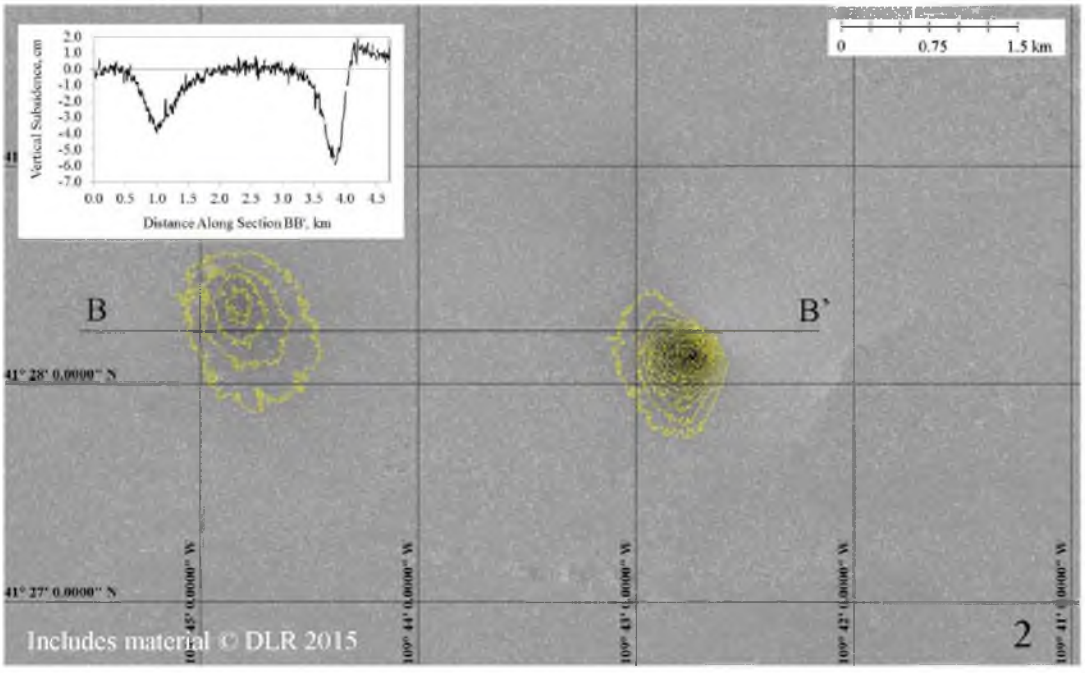

FIGURE 7.37 Region 2 displacement map (X-band): June 13, 2015 to July 16, 2015 (33 days). Subsidence is contoured every 1 cm starting at −1 cm of vertical displacement.

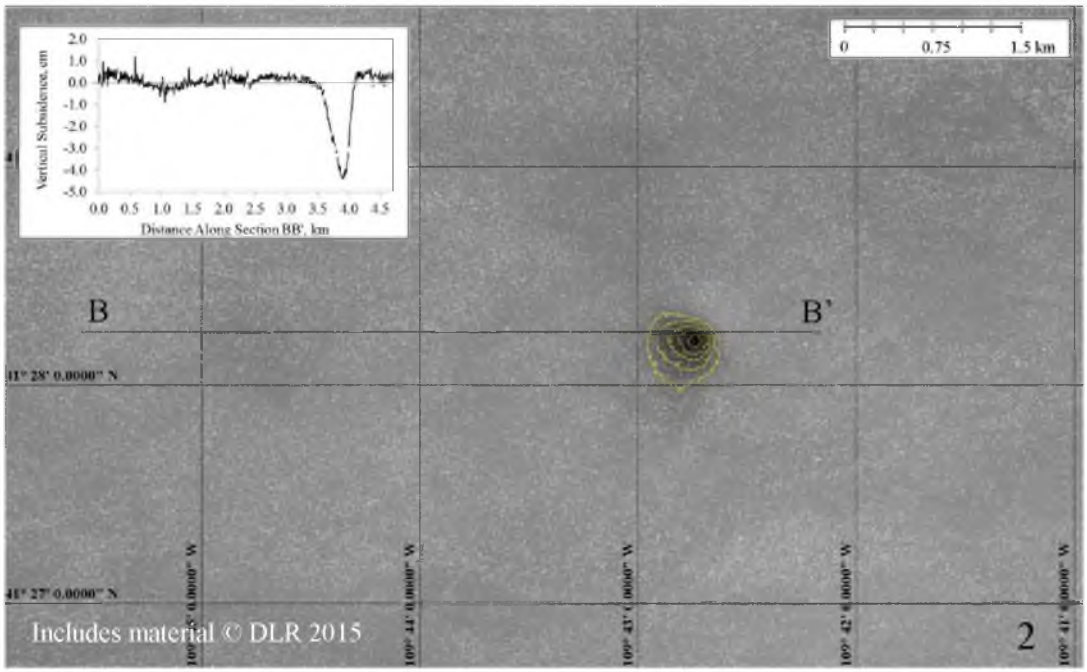

FIGURE 7.38 Region 2 displacement map (X-band): July 16, 2015 to July 27, 2015 (11 days). Subsidence is contoured every 1 cm starting at -1 cm of vertical displacement.

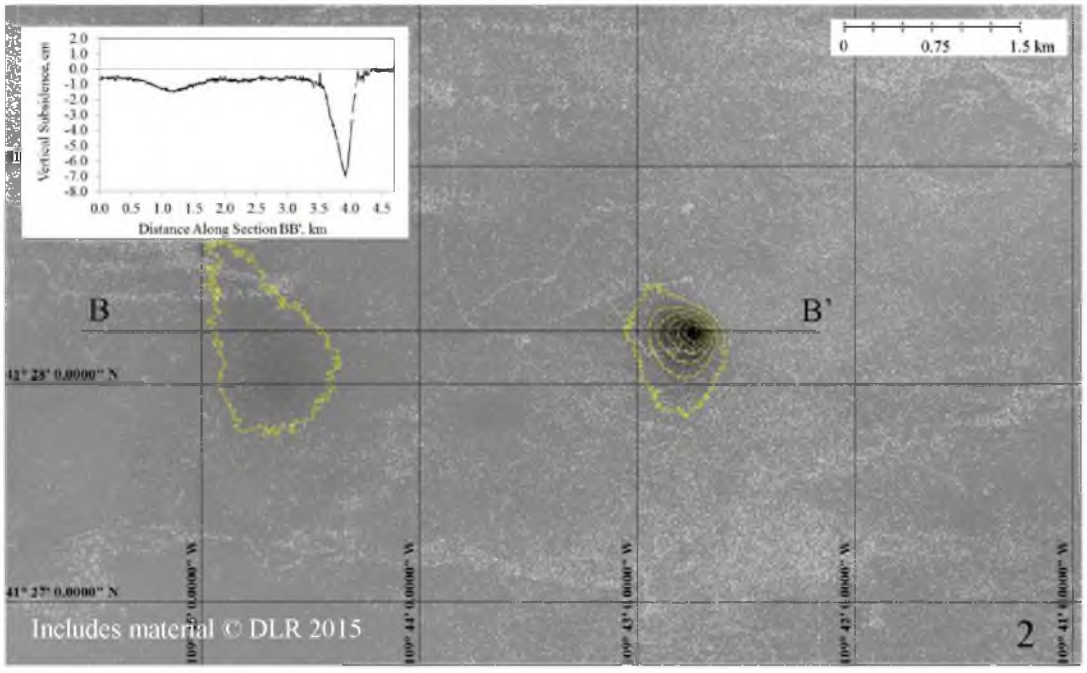

FIGURE 7.39 Region 2 displacement map (X-band): July 27, 2015 to August 7, 2015 (11 days). Subsidence is contoured every 1 cm starting at −1 cm of vertical displacement.

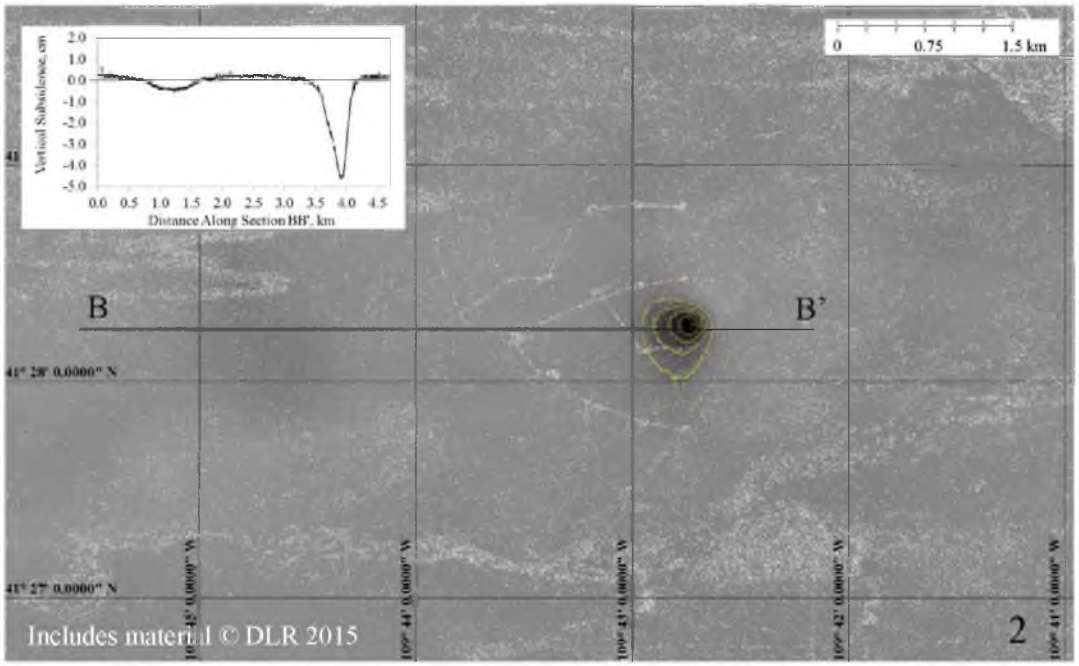

FIGURE 7.40 Region 2 displacement map (X-band): August 7, 2015 to August 18, 2015 (11 days). Subsidence is contoured every 1 cm starting at −1 cm of vertical displacement.

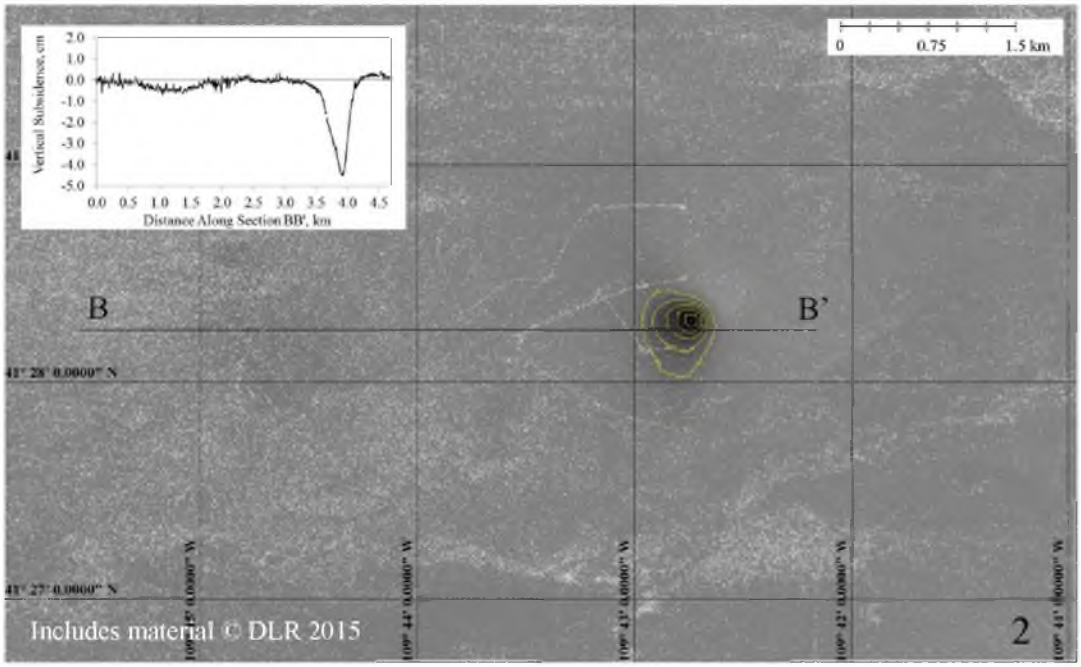

FIGURE 7.41 Region 2 displacement map (X-band): August 18, 2015 to August 29, 2015 (11 days). Subsidence is contoured every 1 cm starting at −1 cm of vertical displacement.

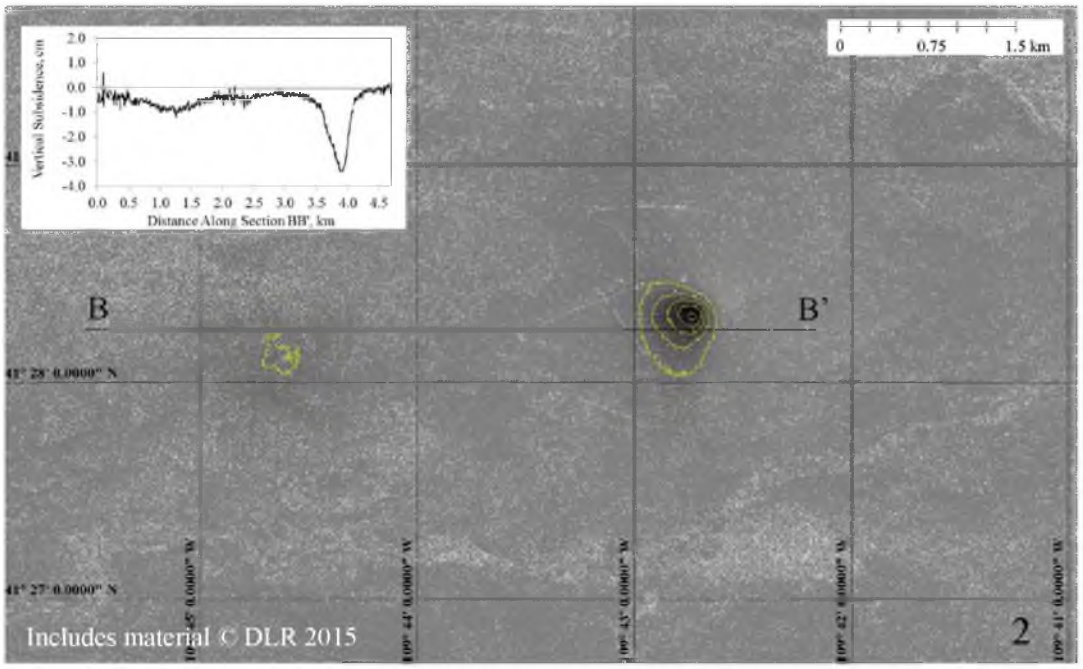

FIGURE 7.42 Region 2 displacement map (X-band): August 29, 2015 to September 9, 2015 (11 days). Subsidence is contoured every 1 cm starting at −1 cm of vertical displacement.

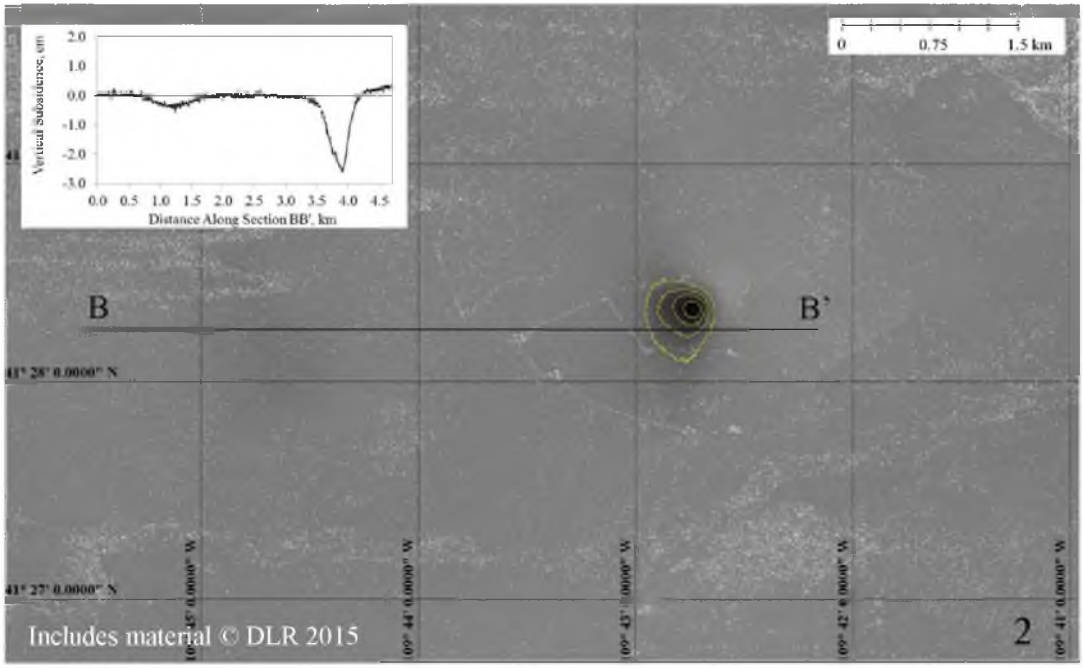

FIGURE 7.43 Region 2 displacement map (X-band): September 9, 2015 to September 20, 2015 (11 days). Subsidence is contoured every 1 cm starting at −1 cm of vertical displacement.

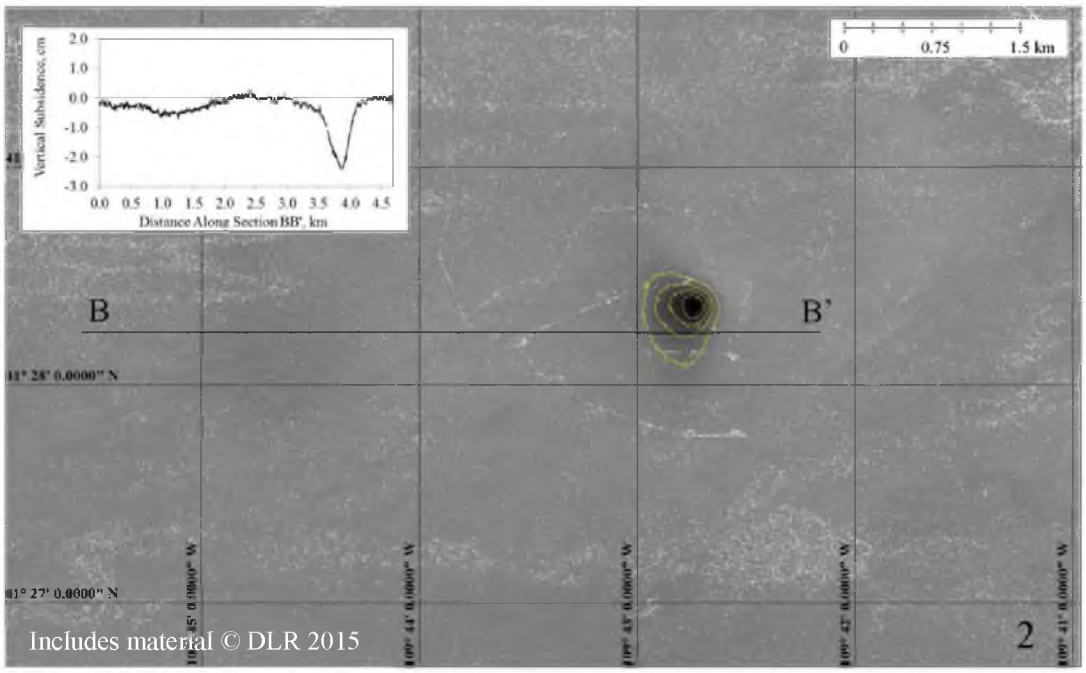

FIGURE 7.44 Region 2 displacement map (X-band): September 20, 2015 to October 1, 2015 (11 days). Subsidence is contoured every 1 cm starting at −1 cm of vertical displacement.

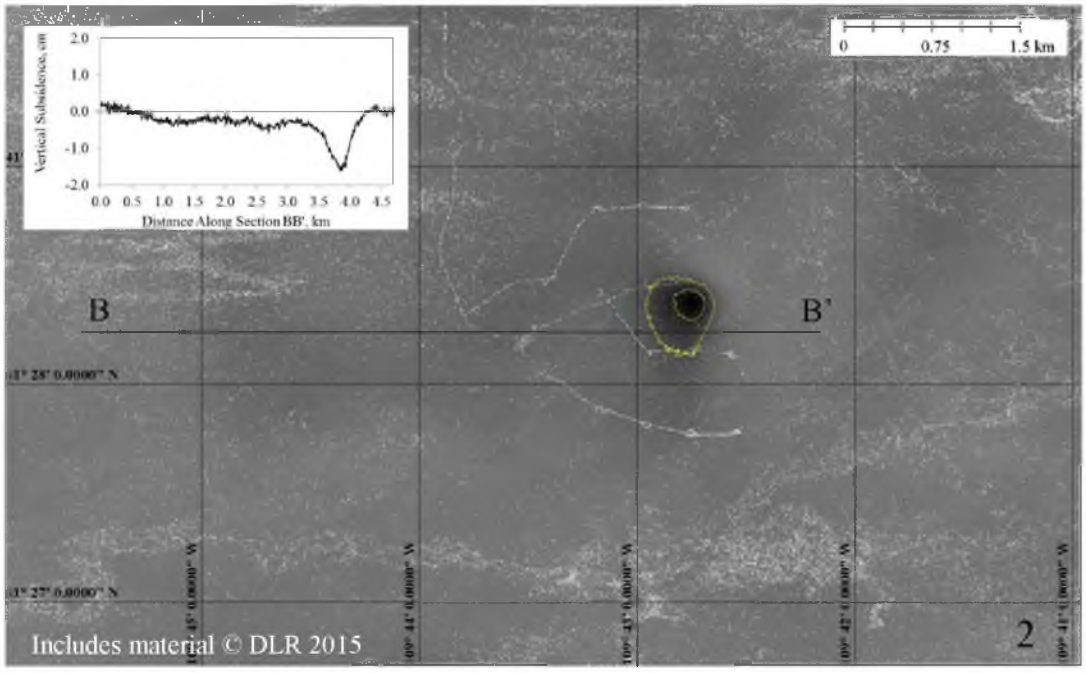

FIGURE 7.45 Region 2 displacement map (X-band): October 1, 2015 to October 12, 2015 (11 days). Subsidence is contoured every 1 cm starting at −1 cm of vertical displacement.

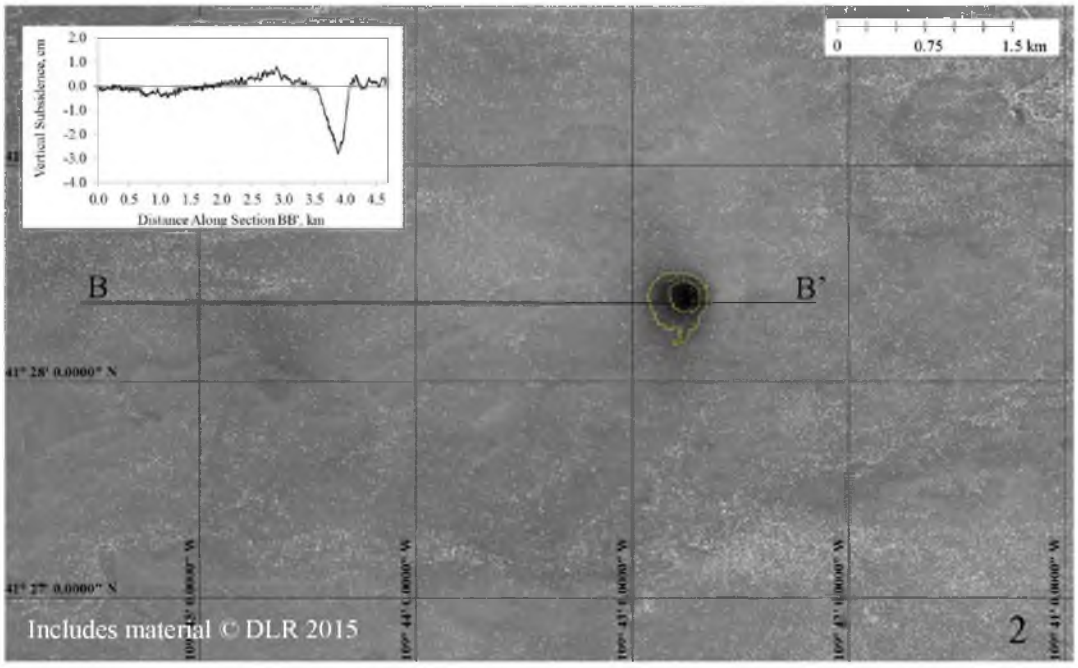

FIGURE 7.46 Region 2 displacement map (X-band): October 12, 2015 to October 23, 2015 (11 days). Subsidence is contoured every 1 cm starting at −1 cm of vertical displacement.

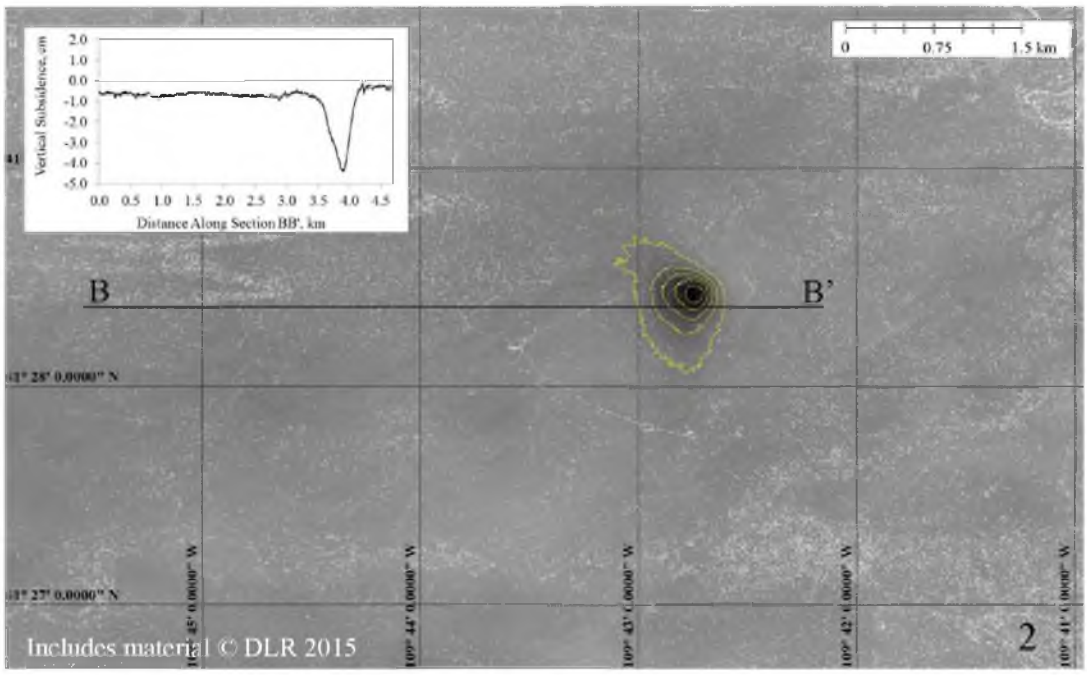

FIGURE 7.47 Region 2 displacement map (X-band): October 23, 2015 to November 3, 2015 (11 days). Subsidence is contoured every 1 cm starting at −1 cm of vertical displacement.

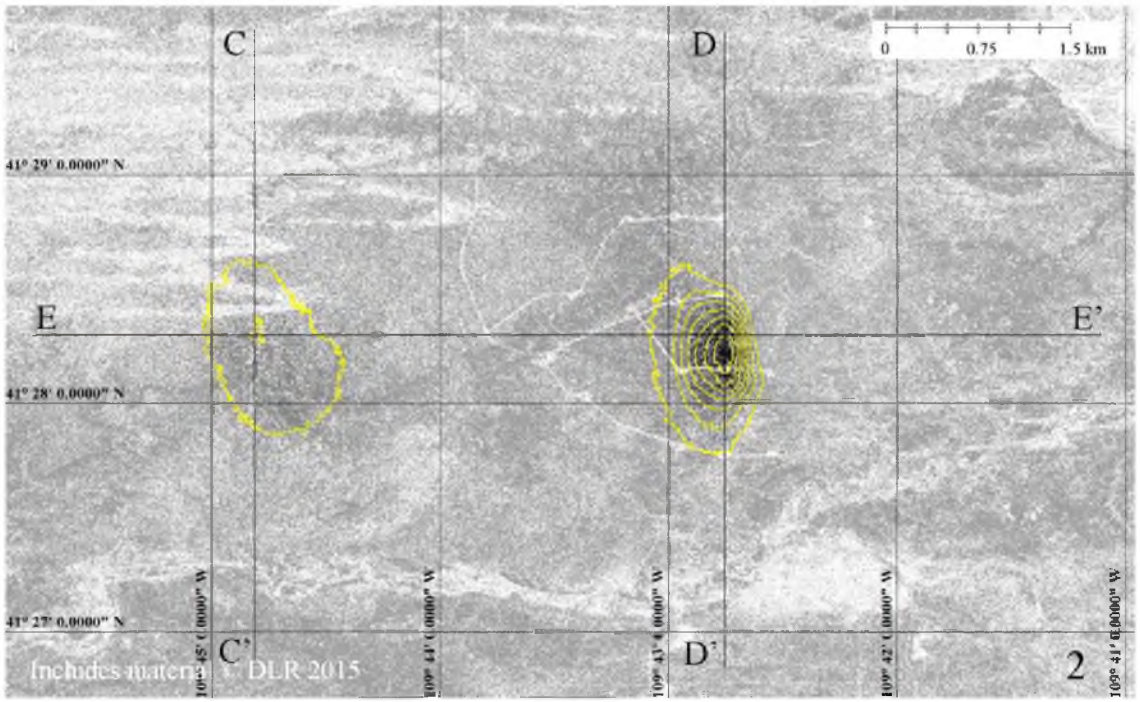

FIGURE 7.48 Region 2 cumulative displacement map (X-band): June 2, 2015 to November 3, 2015 (154 days). Subsidence is contoured every 5 cm starting at −5 cm of vertical displacement.

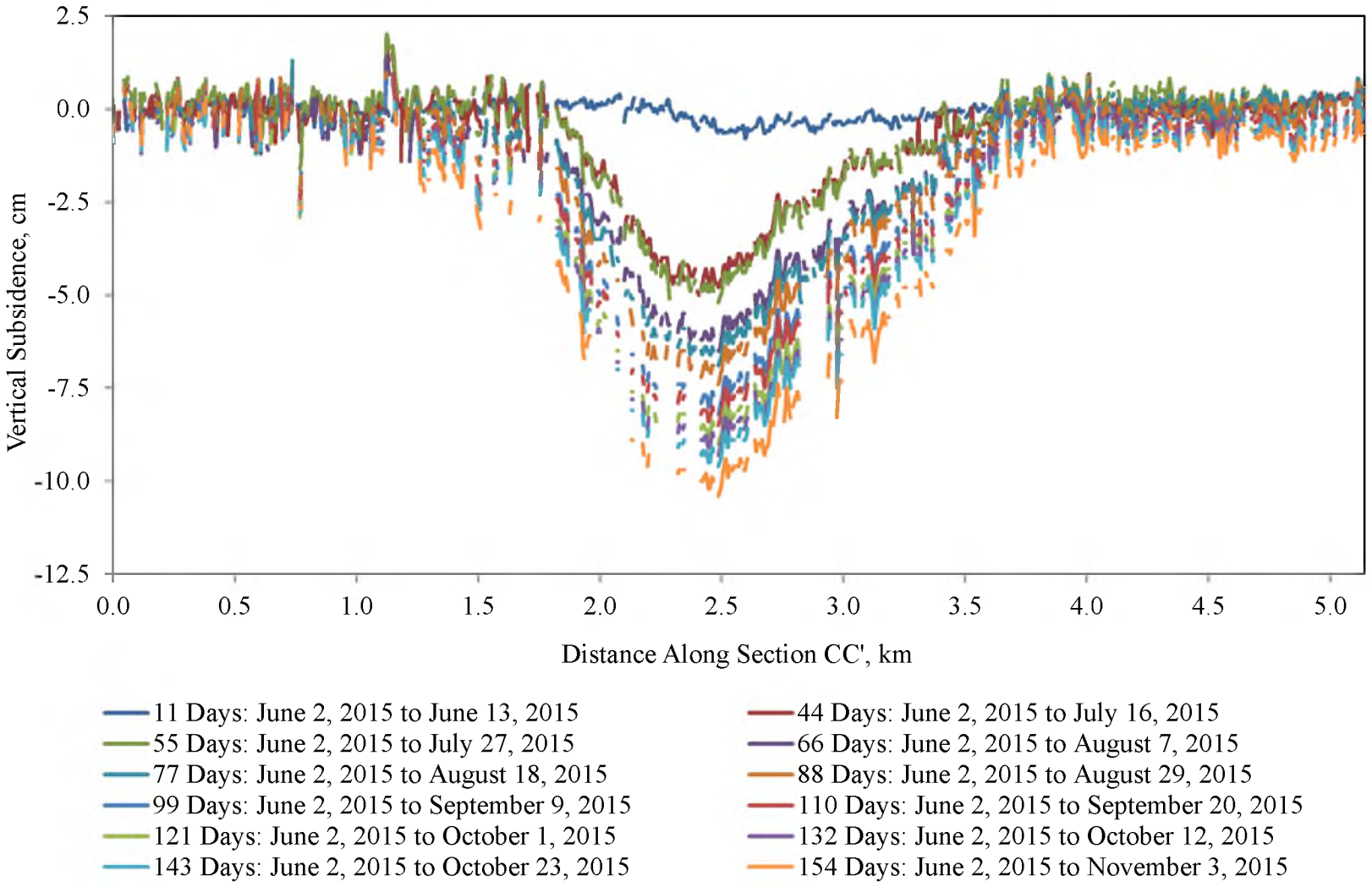

FIGURE 7.49 Time series subsidence profiles of section CC' from Figure 7.48

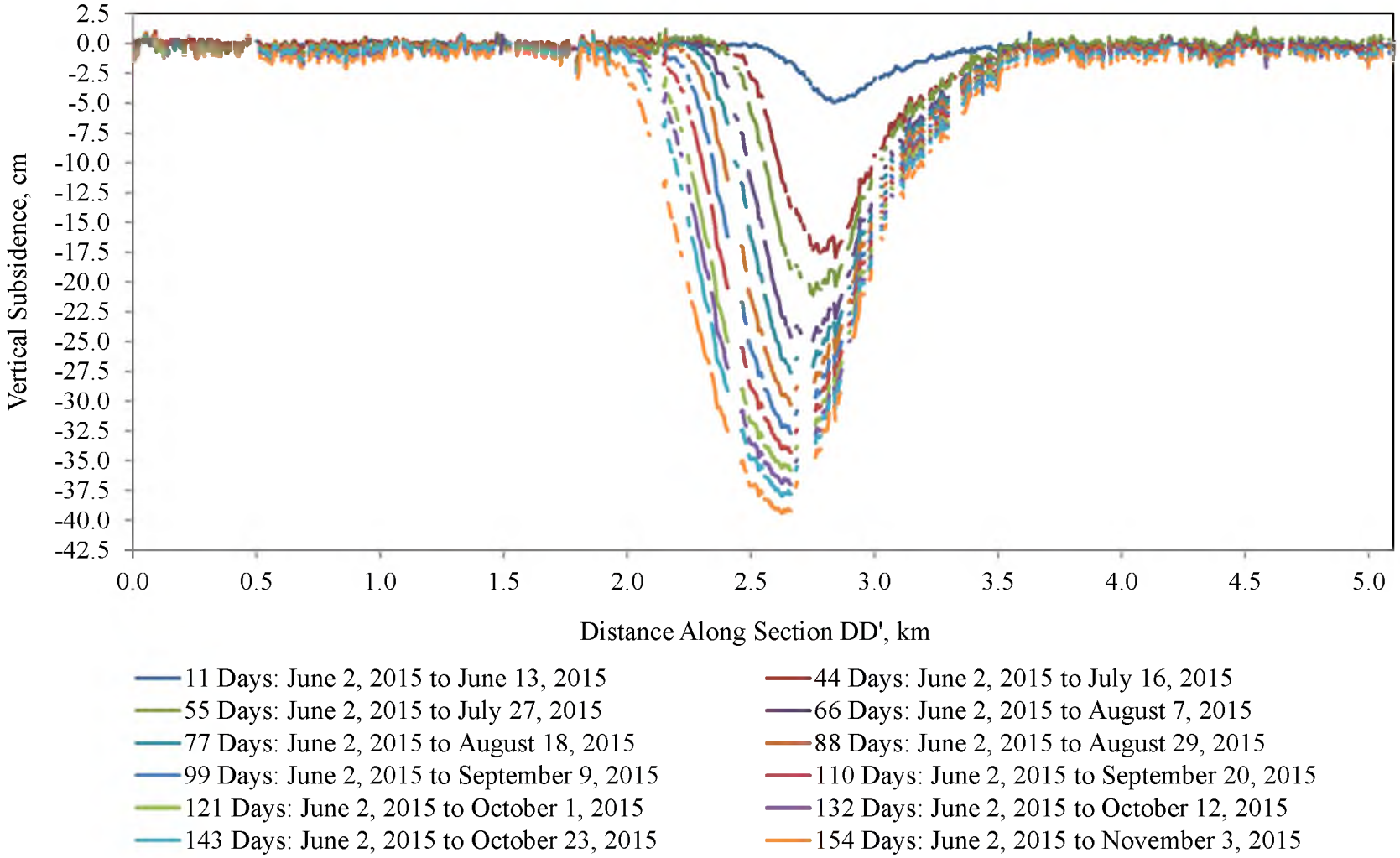

FIGURE 7.50 Time series subsidence profiles of section DD' from Figure 7.48

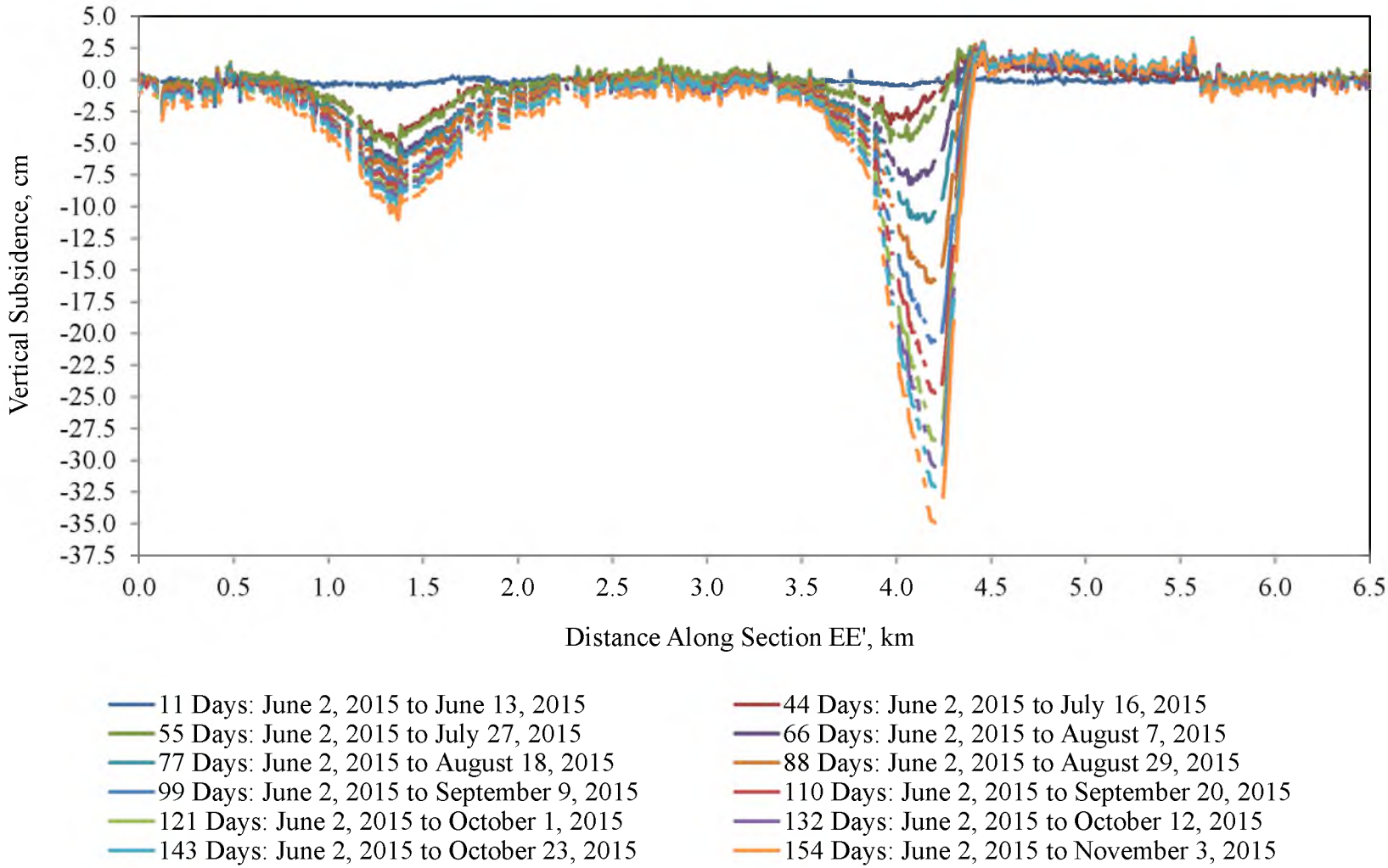

FIGURE 7.51 Time series subsidence profiles of section EE' from Figure 7.48

CHAPTER 8

CONCLUSIONS AND RECOMMENDATIONS

8.1 Conclusions

In this research, the application of DInSAR for subsidence monitoring was evaluated for active underground mining in the Wasatch Plateau study region in central Utah and in the Green River Basin in southwest Wyoming. DInSAR was performed using L-band data from ALOS and X-band data from TerraSAR-X. Both the central Utah region and the southwest Wyoming region are affected by significant subsidence, but the topographic and vegetative characteristics, which strongly influence DInSAR, are different.

In the Green River Basin, gentle topography and sparse vegetation contribute to good subsidence measurement using both L-band and X-band DInSAR. L-band interferograms are interpretable even over periods longer than a year, and using L-band DInSAR it is possible to monitory yearly subsidence on a regional scale with a high data density. X-band SAR has a much shorter wavelength and is more sensitive to deformation, and as a result, the X-band interferograms are significantly less stable over long periods. The average coherence of the X-band interferograms is considerably

reduced over periods longer than one cycle (11 days), and regions of large displacement are affected by phase saturation.

Although the X-band data are less stable than L-band data, in the Green River Basin, shorter period, higher resolution X-band data are better for defining the spatial and temporal progression of subsidence. Subsidence characteristics that are difficult to identify definitively in the L-band data are clear in the X-band data. Generally, in the southwest Wyoming region, the X-band data show strong asymmetry in the development of subsidence between the headgate and tailgate entries (Figures 7.34 and 7.51), and there is some asymmetry in the subsidence due to dissolution (Figure 7.49). Locally, some uplift is associated with longwall subsidence near edges of the subsidence troughs (Figures 7.35 and 7.48). Where the rate of longwall advance is high, there is a tail in the subsidence that trails the longwall advance (Figure 7.35). This tail is less prevalent where the longwall advance is slower (Figure 7.50).

In the Wasatch Plateau, vegetation and rugged topography significantly and negatively affect the application of L-band and X-band DInSAR for subsidence monitoring. Generally, L-band performed better than X-band in the Wasatch Plateau study region, but compared to the Green River Basin, the Wasatch Plateau L-band interferograms are less stable over long periods. Using L-band data over shorter periods, displacements can be measured, but because of low coherence in regions of large displacement, the maximum subsidence is likely underestimated. Again, because of the relatively low spatial resolution of the L-band images, subsidence characteristics in the time series data are difficult to define. In the X-band interferograms, regions affected by subsidence are definable but subsidence is difficult to precisely quantify.

Finally, relationships between subsidence and MIS, and the overall characteristics (rates and magnitudes) of MIS in central Utah and southwest Wyoming are different. In the Wasatch Plateau study region, significant surface displacement tends to precede seismicity, but generally, lower rates of subsidence are associated with lower rates of seismicity and higher rates of subsidence are associated with higher rates of seismicity (Figure 6.28). Typically, subsidence appears to closely follow longwall advance and seismic event rates tend to be relatively high. Event magnitudes tend to be fairly consistent and to be relatively low, less than 2.5 (Figures 6.7 to 6.9 and 6.21 to 6.26). In the Green River Basin, seismicity is only spatially correlated with surface displacements over long periods. Events tend to occur in areas where the surface displacements measured during the study period are small. These areas seem to be associated with secondary solution mining of room and pillar sections, and for these areas in the available data, the magnitude of events tends to be relatively large, often near 3, and the rate of events tends to be low. In areas affected by longwall mining, subsidence appears to closely follow longwall advance; however, in these areas, no major events were cataloged which suggests that longwall mining may be effective for reducing the magnitude of MIS.

Notably, the maximum subsidence measured by L-band DInSAR in the Wasatch Plateau, 180 cm over 414 days, is significantly more than maximum subsidence measure by L-band DInSAR in the Green River Basin, 150 cm over 690 days. The maximum subsidence in both regions is due to longwall mining. Lower magnitude seismicity, higher seismic event rates, and larger surface displacements in the study region of the Wasatch Plateau compared to the Green River Basin suggest further studies of regional

differences in MIS and of the dependence of MIS and subsidence on regional geology and mine parameters are justified.

8.2 Summary

- Using L-band DInSAR in the Wasatch Plateau study region, subsidence can be precisely measured. Interferograms with short spatial and temporal baselines generate the most interpretable results, but winter ground cover conditions and large displacement rates both affect the clarity of the interferometric phases.
- In the Wasatch Plateau study region, subsidence is not precisely measureable using X-band DInSAR. The X-band data are strongly affected by signal saturation due to large displacement rates and by variation in the ground cover conditions. However, the progression of subsidence is definable, and in many cases subsidence magnitudes and rates can be reasonably estimated.
- In the Green River Basin, subsidence can be precisely measured using L-band and X-band DInSAR. The X-band data evaluated in this study have higher spatial and temporal resolutions than the L-band data, and detailed characteristics of subsidence are more discernable in the X-band data. However, the L-band data are less affected by signal saturation and are stable over longer periods (months for L-band versus days for X-band).
- In addition, the data from the Green River Basin illustrate that measuring subsidence over long periods can be difficult because large deformation rates cause significant phase noise and saturation, and because temporal changes reduce the coherence. Subsidence can be measured accurately over long periods (years) by paring images

over shorter periods, when the deformation gradients are lower, and accumulating the subsidence additively.

- Generally, DInSAR with high spatial and temporal resolution has potential to provide timely and accurate reports of the magnitude, extent, and rate of subsidence, and also to identify periods when subsidence has ceased or is minimal. The appropriate band for subsidence monitoring depends on the monitoring period and on the regional surface characteristic and subsidence rates.
- Finally, though both the Wasatch Plateau study region and the Green River Basin and exhibit large displacement, relatively rapid subsidence, the characteristics (rates and magnitudes) of MIS are significantly different. In the Wasatch Plateau study region, seismicity tends to lag subsidence. Events tend to have magnitudes less than 2.5. Generally, lower rates of subsidence are associated with lower rates of seismicity and higher rates of subsidence are associated with higher rates of seismicity. In the Green River Basin, seismicity is only spatially correlated with surface displacements over long periods. Events tend to have magnitudes close to 3, and to occur near regions affected by solution mining where the surface displacements measured during the study period are small.

8.3 Recommendations

The success of DInSAR for mine subsidence monitoring depends on the radar band and on the spatial and temporal resolution of the data, but with increasing data availability, DInSAR has potential to become an important process for subsidence monitoring. Short period, high resolution subsidence data have potential to disclose lags

in subsidence that could indicate a lack of failure in the overburden strata and a hazardous increase in the potential energy. Measuring subsidence over short intervals for long periods could help establish the characteristics of subsidence in a mining region, including typical angles of draw and asymmetries in the trough shape. Subsidence characteristics have potential to impact design of barrier pillars between longwall panels, and could provide a basis for interpreting the overburden geology from subsidence patterns and for evaluating potential failure mechanisms. Characteristic subsidence could also be used to calibrate and validate empirical and numerical models to better predict future subsidence and more accurately model the development of stress over time.

Future research should be directed toward evaluating relationships between mine advance and subsidence. Development and extension of underground mine openings generates significant potential energy which can be estimated knowing the mining parameters, including the mining area, thickness, and depth. Defining relationships between potential energy freed by mining and potential energy consumed by subsidence over time has considerable implications for mine safety (Whyatt 2015). Without in-depth knowledge of strata properties and proper design of ground control support, unusual amounts of stored energy, indicated by a lack of controlled subsidence, may indicate higher potential for significant and damaging failure of the mining face and rock surrounding mine openings. DInSAR has been demonstrated as an effective method for accurately monitoring subsidence over short periods, and subsidence data from DInSAR could be used to quantify potential energy changes. Evaluating and defining relationships between generated potential energy and energy consumed through subsidence may help prevent events like the Crandall Canyon and the Solvay mine collapses.

APPENDIX

UTAH REGION X-BAND DIFFERENTIAL INTERFEROGRAMS

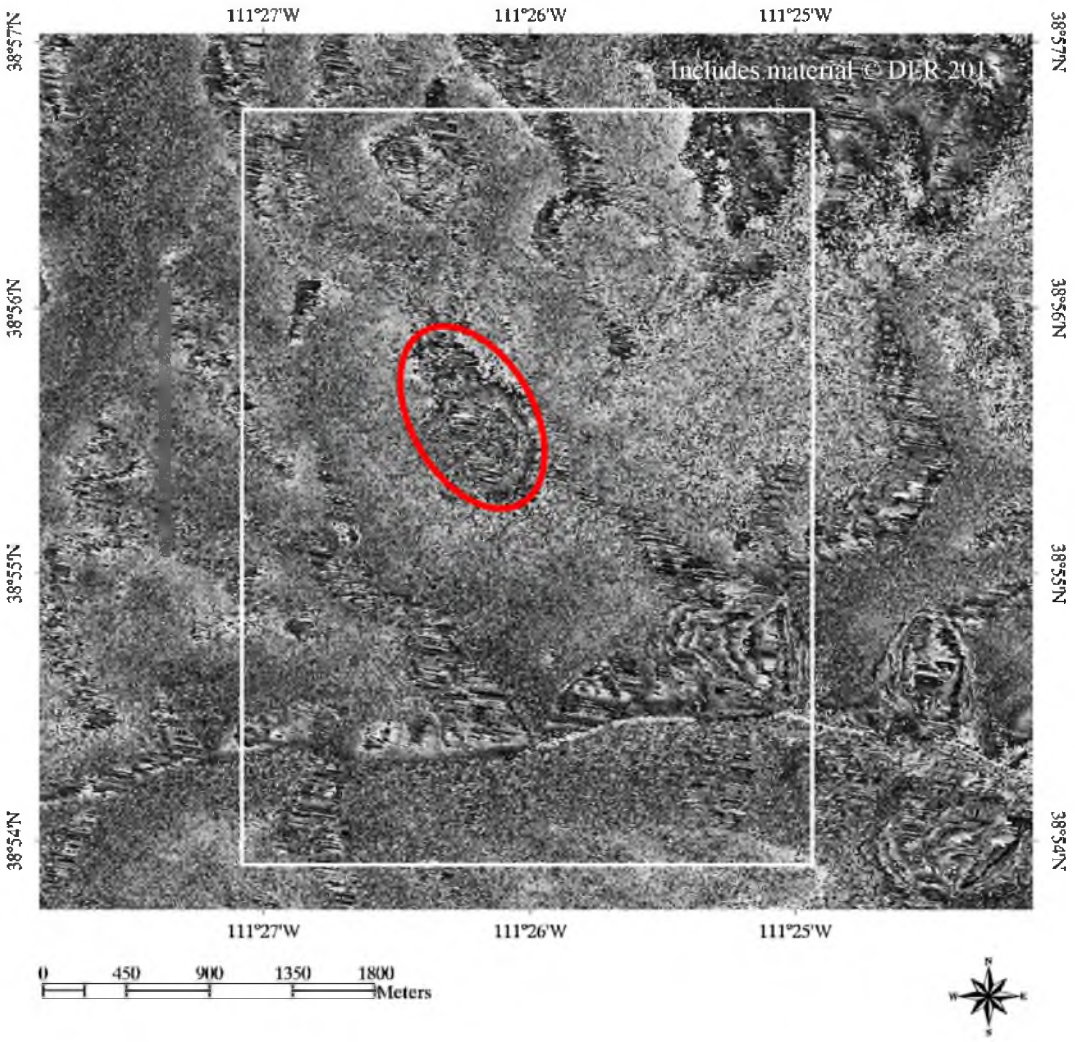

FIGURE A.1 X-band filtered differential interferogram: June 7, 2015 to June 18, 2015 (Orbit 159)

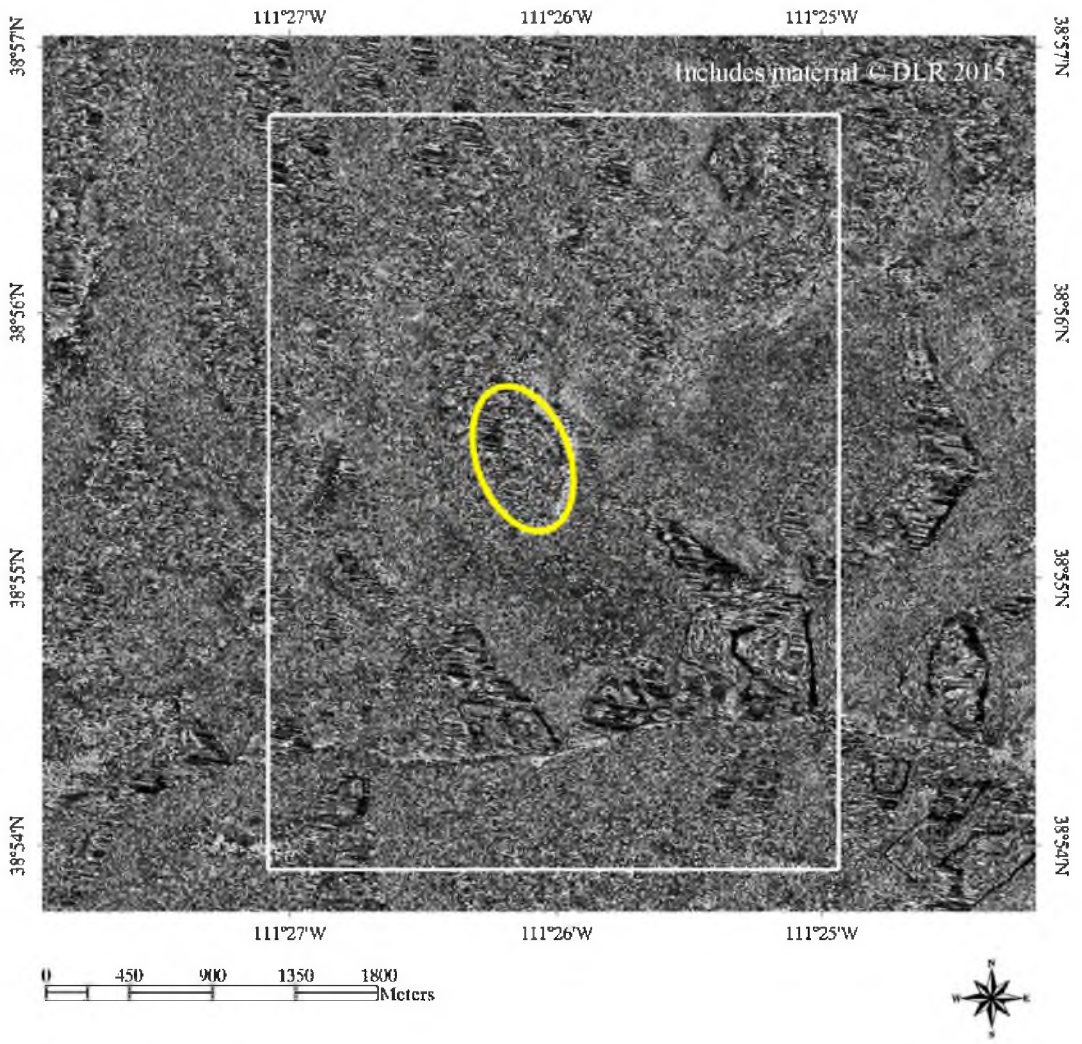

FIGURE A.2 X-band filtered differential interferogram: June 18, 2015 to July 10, 2015 (Orbit 159)

FIGURE A.3 X-band filtered differential interferogram: June 10, 2015 to June 21, 2015 (Orbit 30)

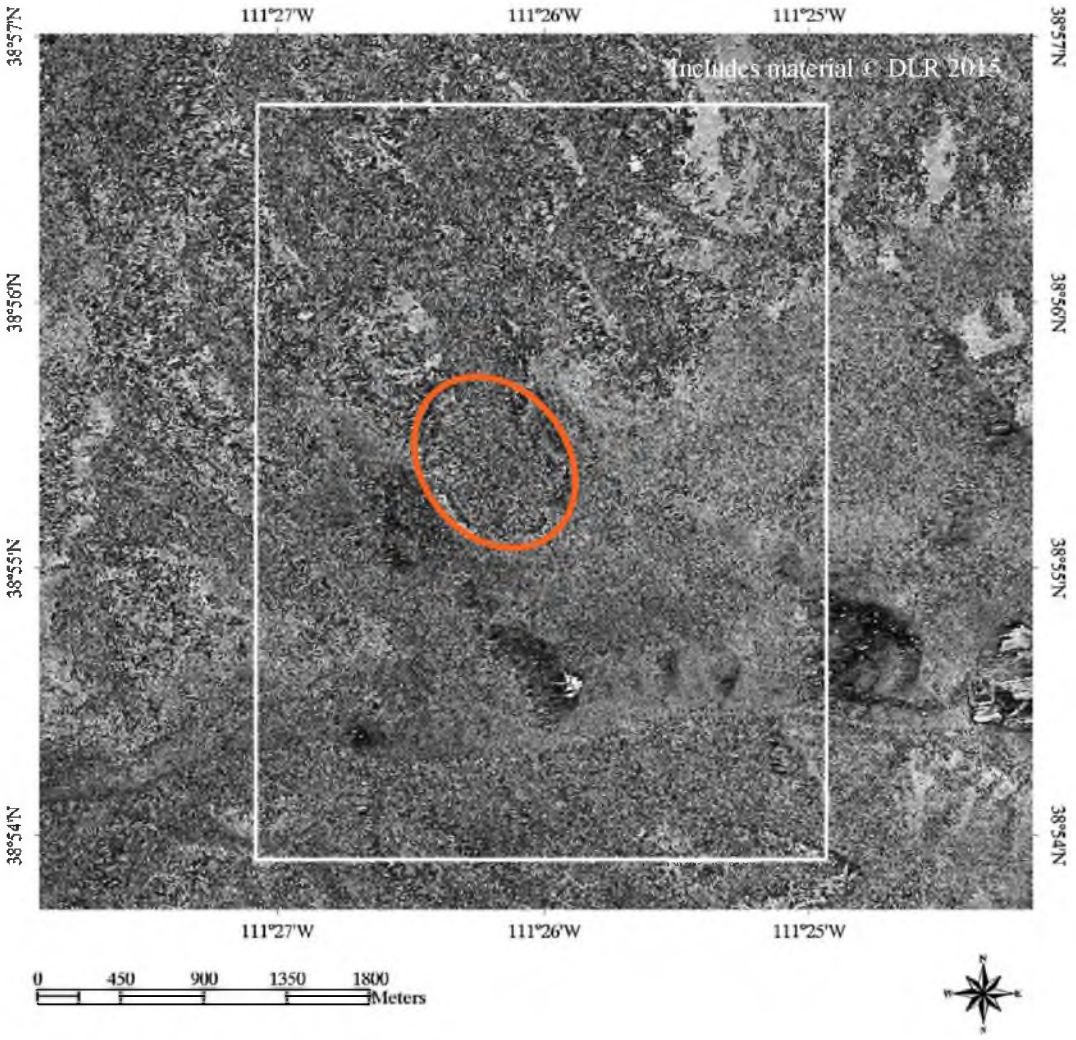

FIGURE A.4 X-band filtered differential interferogram: June 21, 2015 to July 24, 2015 (Orbit 30)

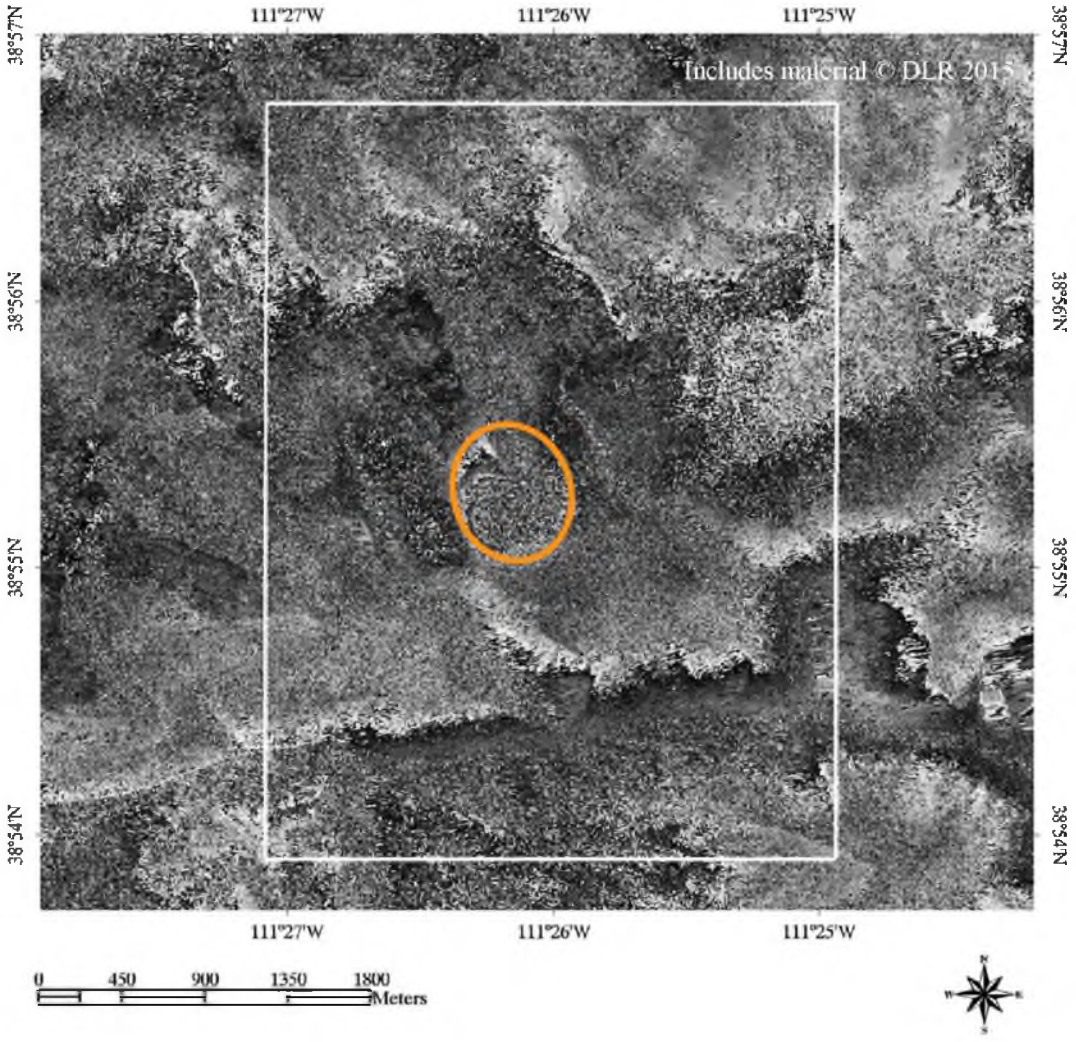

FIGURE A.5 X-band filtered differential interferogram: July 24, 2015 to August 4, 2015 (Orbit 30)

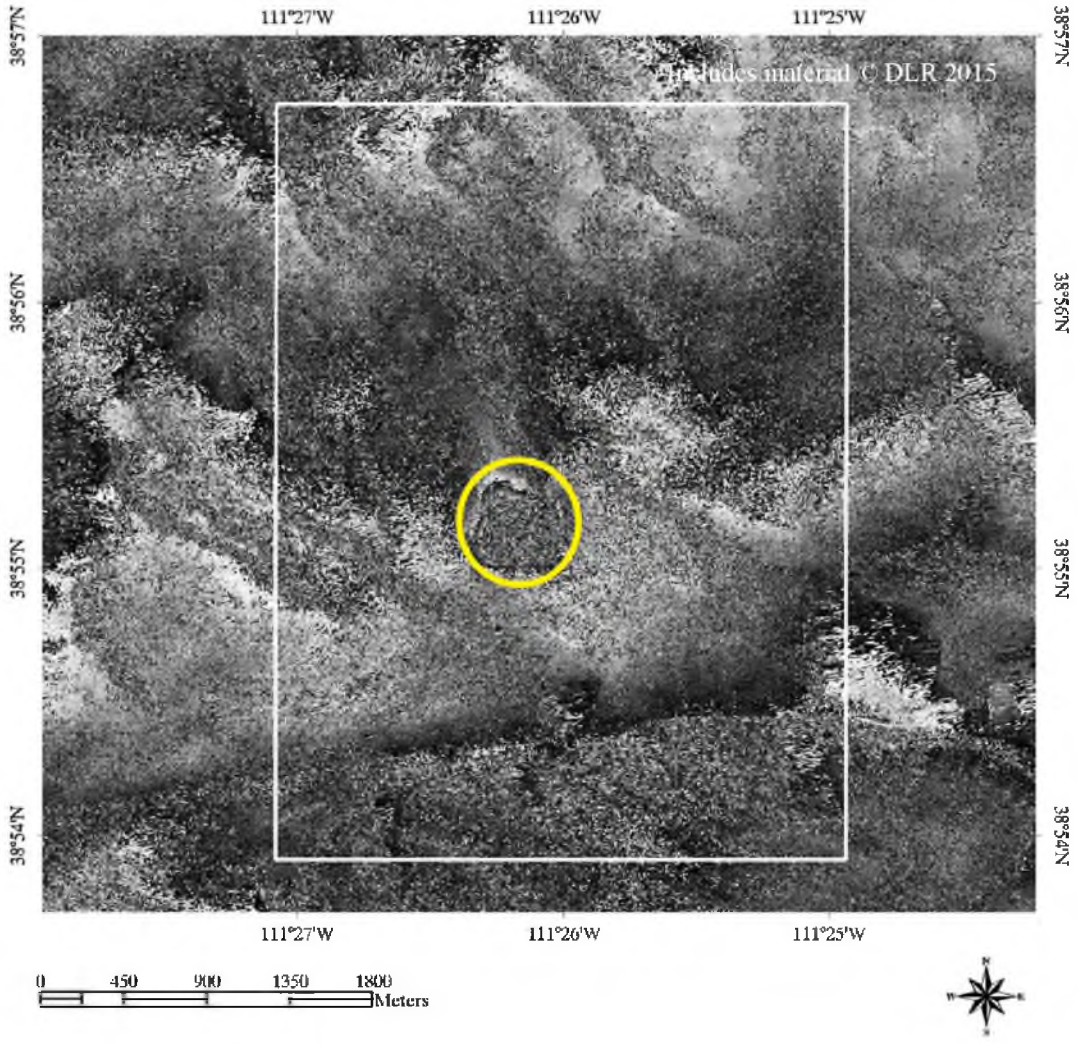

FIGURE A.6 X-band filtered differential interferogram: August 4, 2015 to August 15, 2015 (Orbit 30)

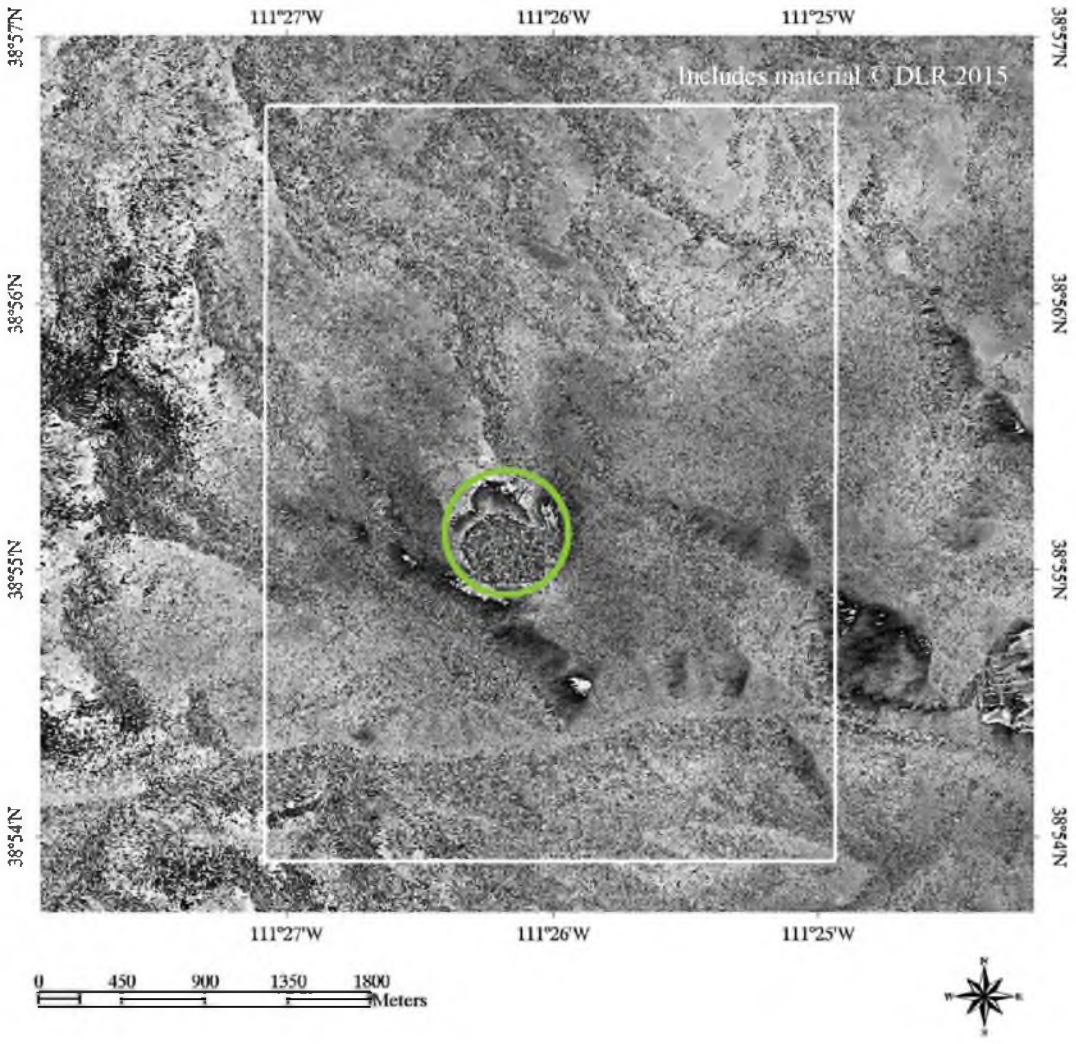

FIGURE A.7 X-band filtered differential interferogram:August 15, 2015 to August 26, 2015 (Orbit 30)

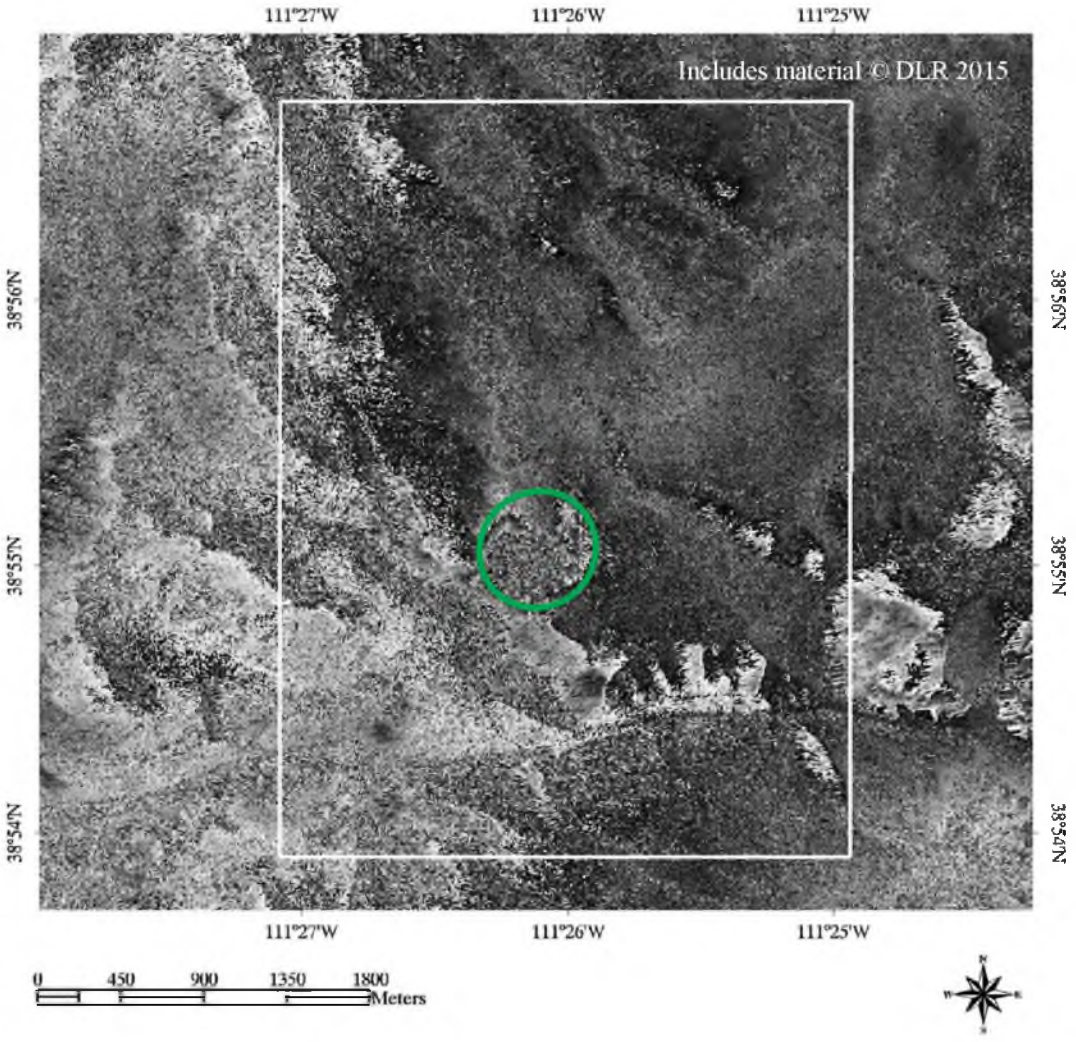

FIGURE A.8 X-band filtered differential interferogram: August 26, 2015 to September 6, 2015 (Orbit 30)

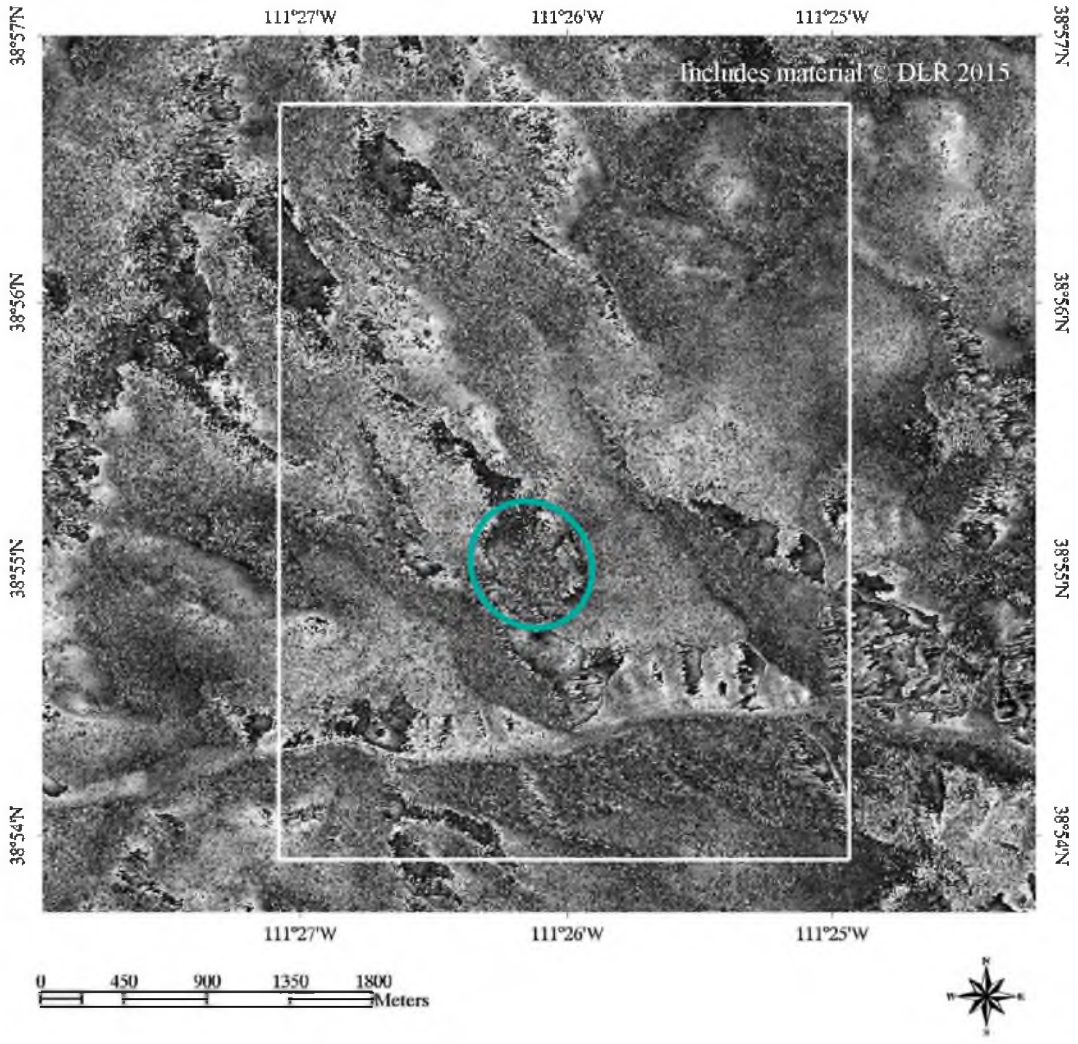

FIGURE A.9 X-band filtered differential interferogram: September 6, 2015 to September 17, 2015 (Orbit 30)

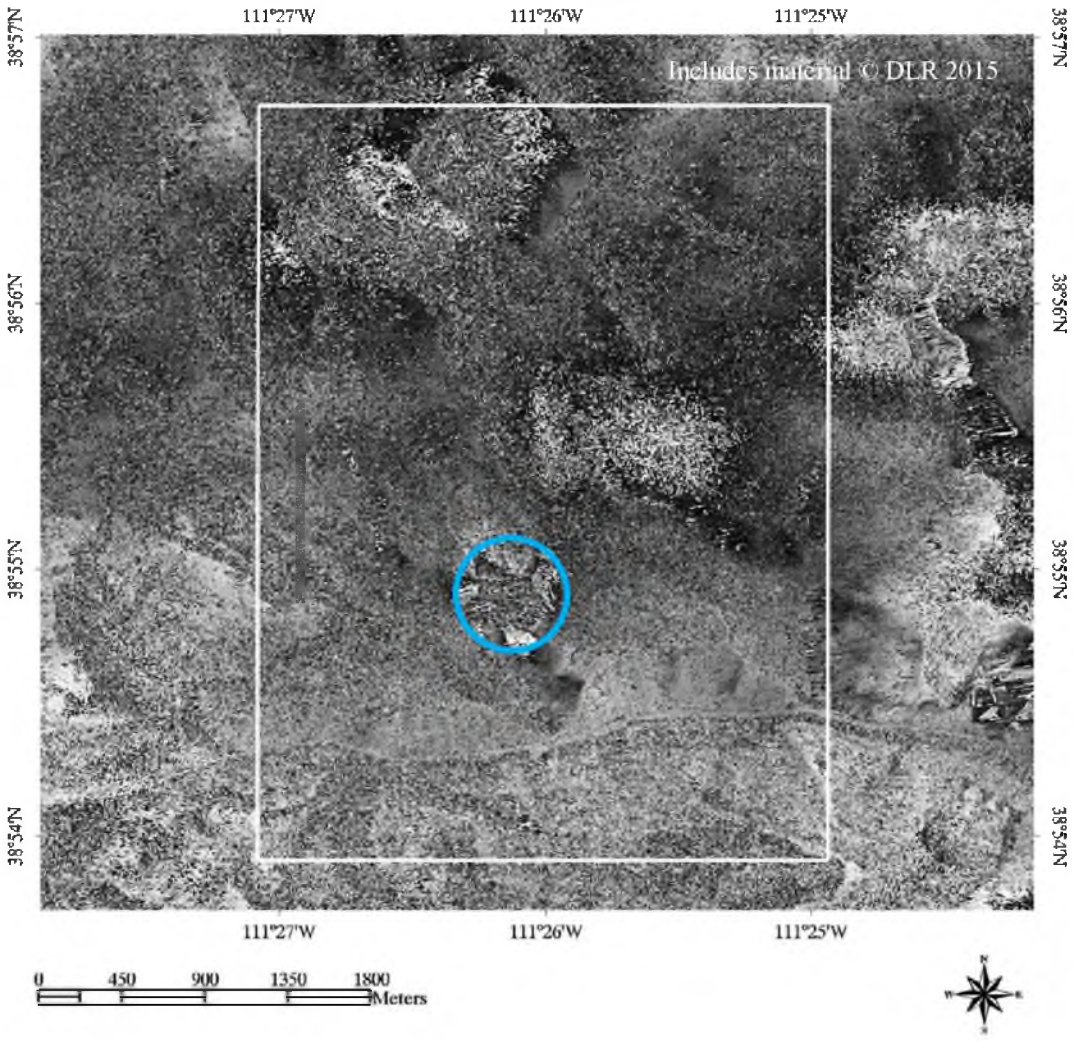

FIGURE A.10 X-band filtered differential interferogram: September 17, 2015 to September 28, 2015 (Orbit 30)

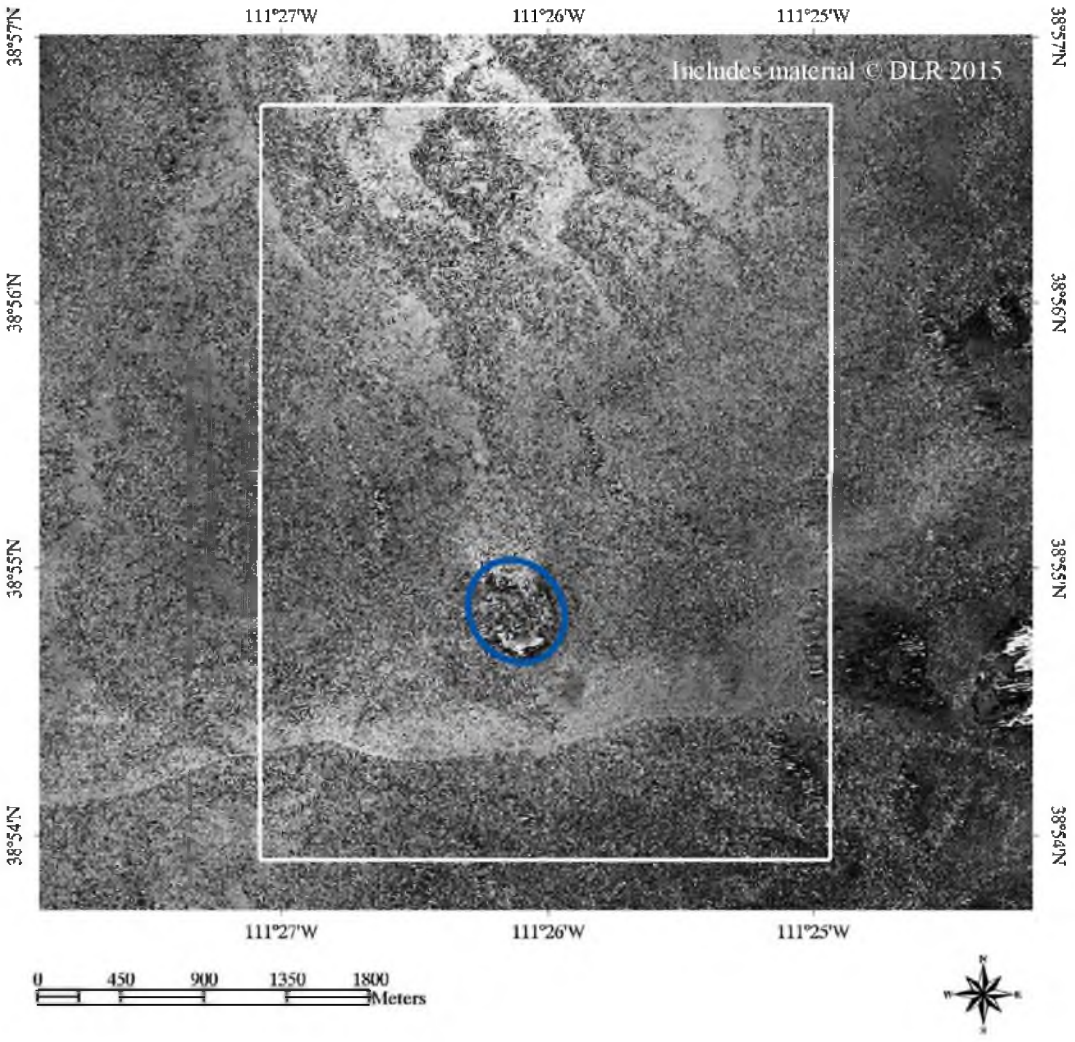

FIGURE A.11 X-band filtered differential interferogram: September 28, 2015 to October 9, 2015 (Orbit 30)

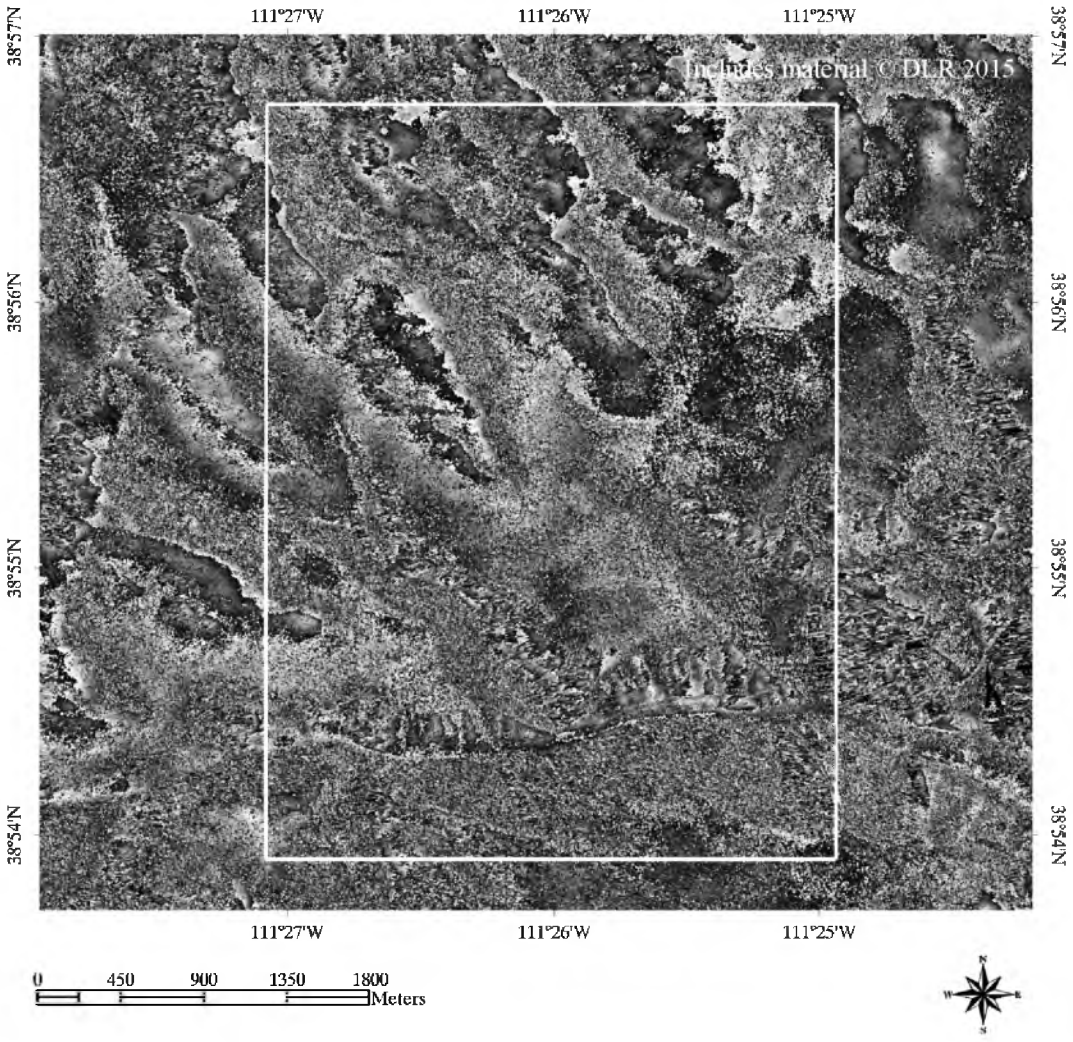

FIGURE A.12 X-band filtered differential interferogram: October 9, 2015 to October 20, 2015 (Orbit 30)

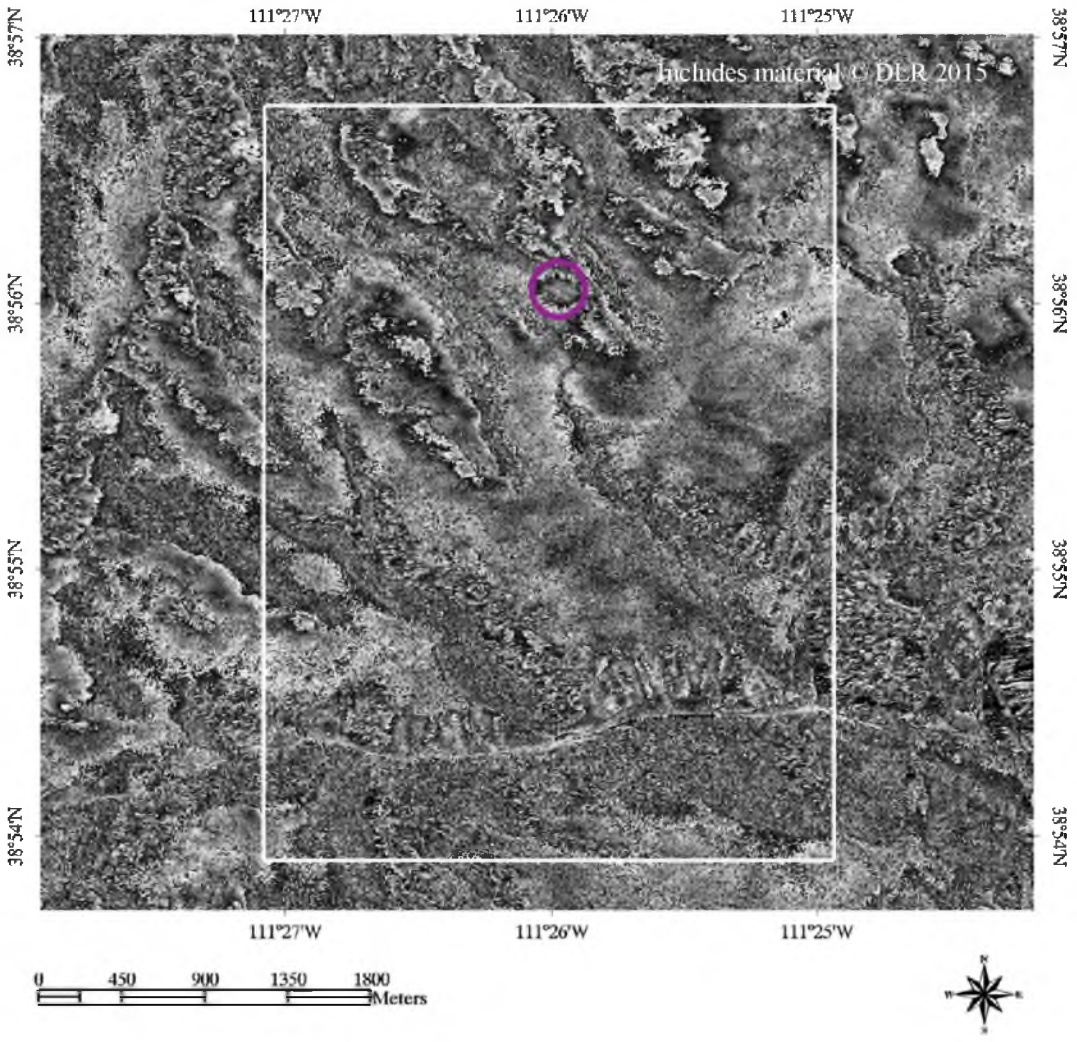

FIGURE A.13 X-band filtered differential interferogram: October 20, 2015 to October 31, 2015 (Orbit 30)

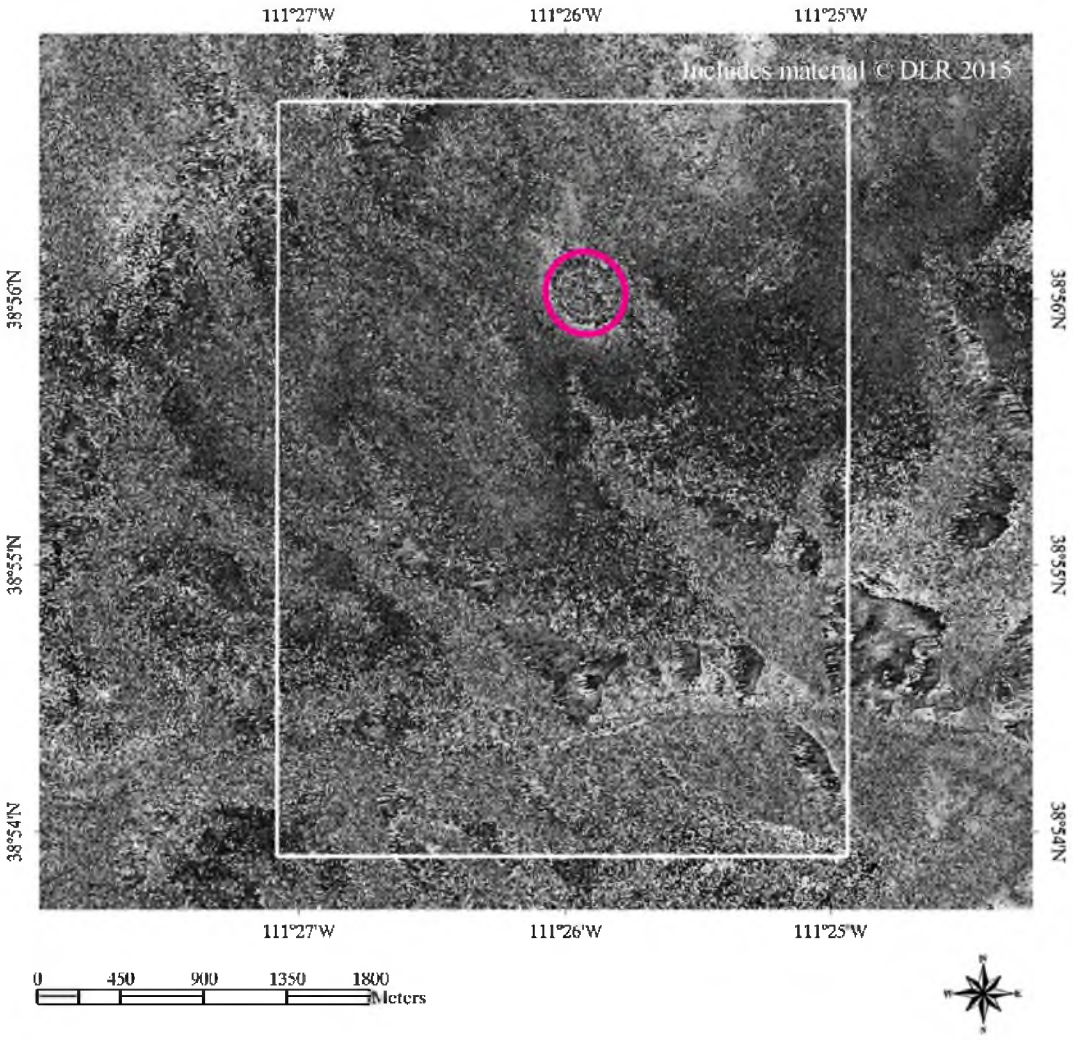

FIGURE A.14 X-band filtered differential interferogram: October 31, 2015 to November 11, 2015 (Orbit 30)

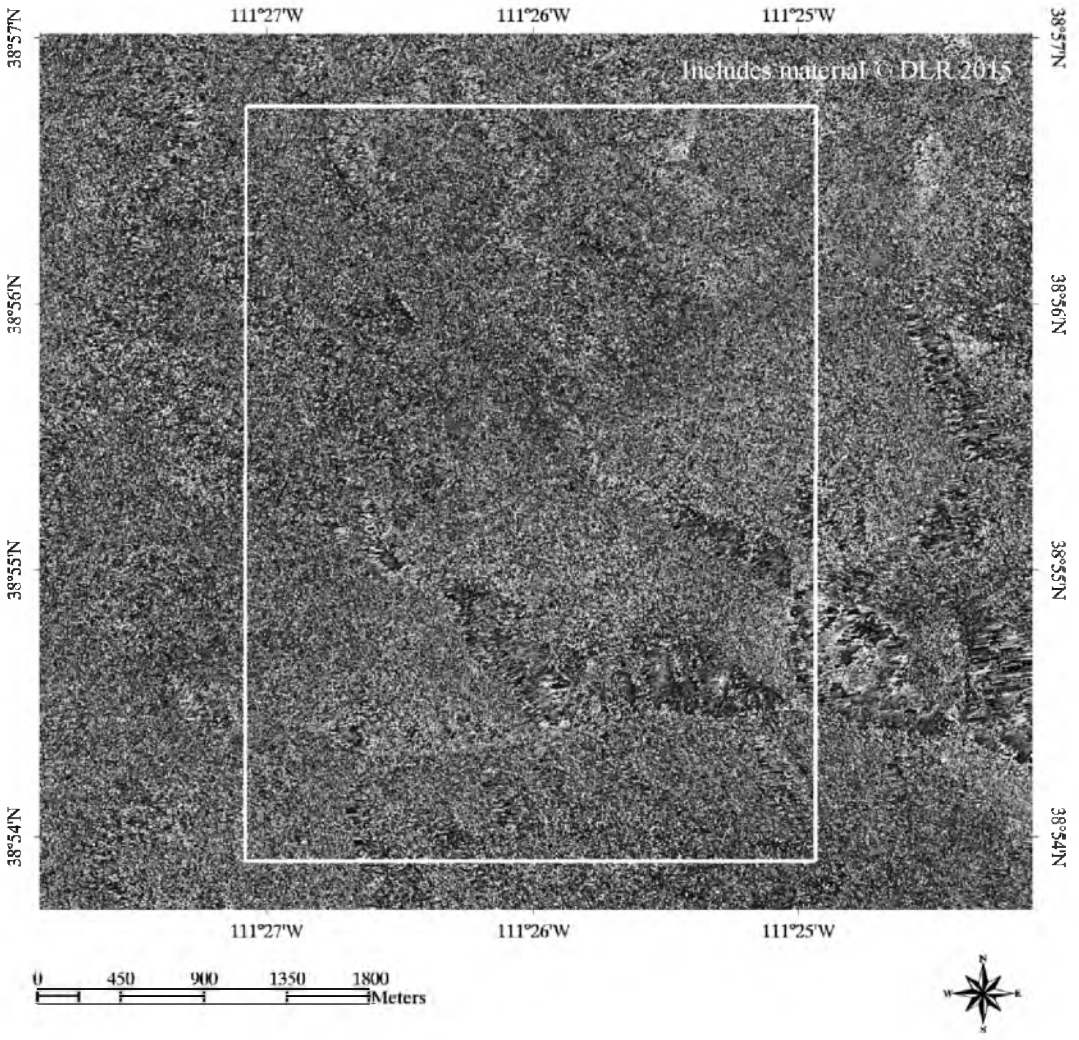

FIGURE A.15 X-band filtered differential interferogram: November 11, 2015 to November 22, 2015 (Orbit 30)

REFERENCES

30 U.S. Code Chapters 25. 1992. *Surface Mining Control and Reclamation.* www.law.cornell.edu/uscode/text/30/chapter-25. Accessed April 2015.

Adcock, T.W. 2013. Annual Report of the State Inspector of Mines of Wyoming. http://wyomingworkforce.org/employers-and-businesses/mines/Documents/2013%20Annua%20Rpt%20Final%203-21-14.pdf. Accessed June 2014.

Agapito, J.F.T, Goodrich, R.R., and Andrews, M.L. 2000. Two-seam mining stability at OCI's Big Island trona mine. *Min. Eng.* 52(4): 8–12.

ALTAMiRA. 2015. GlobalSAR. www.altamira-information.com/globalsar/view/globalsar-uses-all-globally-available-radar-satellites. Accessed May 2015.

Arabasz, W.J., Nava, S.J, and Phelps, W.T. 1997. Mining seismicity in the Wasatch Plateau and Book Cliffs coal mining districts, Utah, USA. In *Rockbursts and Seismicity in Mines*. Edited by S. J. Gibowicz and S. Lasocki. Rotterdam: A. A. Balkema.

Arabasz, W.J., Burlacu, R., and Pankow, K.L. 2007. An overview of historical and contemporary seismicity in central Utah. In *Central Utah—Diverse Geology of a Dynamic Landscape.* Edited by G.C. Willis, M.D. Hylland, D.L. Clark, and T.C. Chidsey. Publication 36. Salt Lake City, UT: Utah Geological Association. pp. 236–253.

Arabasz, W.J., and Pechmann, J.C. 2001. *Seismic Characterization of Coal-Mining Seismicity in Utah for CTBT Monitoring.* Internal Report UCRL-CR-143772. Livermore, CA: Lawrence Livermore National Laboratory.

ASF. 2015. About ALOS PALSAR. www.asf.alaska.edu/sar-data/palsar/about-palsar/. Accessed June 2015.

Astiz, L., Eakins J.A., Martynov V.G., Cox, T.A., Tytell, J., Reyes, J.C., Newman, R.L., Karasu, G.H., Mulder, T., White, M., Davis, G.A., Busby R.W., Hafner, K., Meyer J.C., and Vernon, F.L. 2014. The Array Network Facility seismic bulletin: Products and an unbiased view of United States seismicity. *Seismol. Res. Lett.* 85(3):576–593.

Bahuguna, P.P., Srivastava, A.M.C., and Saxena, N.C. 1991. A critical review of mine subsidence prediction methods. *Min. Sci. Technol.* 13(3):369–382.

Bamler, R. and Hartl, P. 1998. Synthetic aperture radar interferometry. *Inverse Prob.* 14:R1–R54.

Barron, L.R., DeMarco, M.J., and Kniesley, R.O. 1994. *Longwall Gate Road Stability in Four Deep Western US Coal Mines.* Information Circular IC-9406. Washington, DC: U.S. Department of Interior, Bureau of Mines.

Bauer, R.A. 2006. *Mine Subsidence in Illinois: Facts for Homeowners.* Circular 569. Champaign, IL: Illinois State Geological Survey.

Bauer, R.A. 2008. *Planned Coal Mine Subsidence in Illinois: A Public Information Booklet.* Circular 573. Champaign, IL: Illinois State Geological Survey.

Bessinger, S.L. 2011. Longwall mining. In *SME Mining Engineering Handbook,* 3rd ed. Edited by P. Darling. Englewood, CO: SME.

Boltz, M.S., Pankow, K.L., and McCarter, M.K. 2014. Fine details of mining-induced seismicity at the Trail Mountain coal mine using modified hypocentral relocation techniques. *Bull. Seismol. Soc. Am.* 104(1):193–203.

Bradley, W.H. 1964. *Geology of Green River Formation and Associated Eocene Rocks in Southwestern Wyoming and Adjacent Parts of Colorado and Utah.* Geological Survey Professional Paper 496–A. Washington, DC: U.S. Government Printing Office.

Brown, N.A. 1995. Union Pacific instrumental in developing Wyoming trona. *Min. Eng.* 47(2): 135–141.

Buckley, S.M. 2000. Radar interferometry measurement of land subsidence. Ph.D. dissertation, The University of Texas at Austin, TX.

Bullock R.L. 2011. Comparison of underground mining methods. In *SME Mining Engineering Handbook,* 3rd ed. Edited by P. Darling. Englewood, CO: SME.

Burgmann, R., Rosen, P.A., Fielding, E.J. 2000. Synthetic aperture radar interferometry to measure earth's surface topography and its deformation. *Annu. Rev. Earth Planet. Sci.* 28:169–209.

Carnec, C. and Delacourt, C. 2000. Three years of mining subsidence monitored by SAR interferometry, near Gardanne, France. *J. Appl. Geophys.* 43:43–54.

CEOS ESA. 2015. The CEOS database. http://database.eohandbook.com/database/missiontable.aspx. Accessed May 2015.

Costantini, M. 1998. A novel phase unwrapping method based on network programming. *IEEE Trans. Geosci. Remote Sens.* 36(3):813–821.

DLR. 2013. *TerraSAR-X Ground Segment Basic Product Specification Document*. TX-GS-DE-3302. Wessling, Germany: DLR.

DLR. 2015. TerraSAR-X—Science Services System —List of accepted proposals. http://terrasar-x.dlr.de/. Accessed June 2015.

Doelling, H.H. 1972. *Central Utah Coal Fields: Sevier-Sanpete, Wasatch Plateau, Book Cliffs and Emery.* Salt Lake City, UT: Utah Geological and Mineralogical Survey.

Dunrud, C.D. 1976. *Some Engineering and Geologic Factors Controlling Coal Mine Subsidence in Utah and Colorado.* Geological Survey Professional Paper 969. Washington, DC: U.S. Government Printing Office.

Dunrud, C.D. 1984. Coal mine subsidence—Western United States. *Rev. Eng. Geol.* 6:151–194. Accessed June 2014. doi: 10.1130/REG6-p151.

Dunrud, C.D., and Osterwald, F.W. 1980. *Effects of Coal Mine Subsidence in the Sheridan, Wyoming, Area.* Geological Survey Professional Paper 1164. Washington, DC: U.S. Government Printing Office.

Duro, J., Albiol, D. Mora, O. and Payàs, B. 2013. Application of advanced InSAR techniques for the measurement of vertical and horizontal ground motion in longwall minings. 13th Coal Operators' Conference. Wollongong, NSW, February 14–15.

Ellenberger, J.L., Heasley, K.A., Swanson, P.L. and Mercier, J. 2001. Three dimensional microseismic monitoring of a Utah longwall. In *Proceeding of the 38th U.S. Rock Mechanics Symposium*. Edited by D. Elsworth, J.P. Tinucci, and K.A. Heasley. Rotterdam, Netherlands: A.A.Balkema.

Ellison, L. 1954. Subalpine vegetation of the Wasatch Plateau, Utah. *Ecol. Monogr.* 24(2):89–184.

Fischer, W.G. 1964. How rock mechanics is applied to specific mining problems at the Westvaco mine. *Trans. SME* December: 435–443.

Fischer, W.G. 1986. Time dependent subsidence behavior at a Green River trona mine. In *Mine Subsidence*. Edited by M.M. Singh. Littleton, CO: SME.

Fiscor, S. 2014. The landscape for U.S. longwalls changes. *Coal Age*. February 21. www.coalage.com/features/3384-the-landscape-for-u-s-longwalls-changes.html#.U6Sr7MJOWpp. Accessed June 2014.

FMC Granger. 2012. *Annual Mining Report 2011–2012*. Lander, WY: Wyoming Division of Environmental Quality, Land Quality Division.

FMC Granger. 2013. *Annual Mining Report 2012–2013*. Lander, WY: Wyoming Division of Environmental Quality, Land Quality Division.

Foxall, W., Sweeney, J.J., and Walter, W.R., 1998. Identification of mine collapses, explosions and earthquakes using INSAR: A preliminary investigation. Presented at the 20th Seismic Research Symposium, Santa Fe, NM, September 21–23.

Foy, P. 2008. Utah coal mine closed over safety problems. *Insurance Journal.* April 4. www.insurancejournal.com/news/west/2008/04/04/88697.htm. Accessed June 2014.

Fry, R.C. 1986. Case study in monitoring mining induced subsidence using photogrammetry and conventional surveys. In *Proceedings 3rd Subsidence Workshop Due to Underground Mining*. Morgantown, WV: West Virginia University.

Gabriel, A.K., Goldstein, R.M., and Zebker, H.A. 1989. Mapping small elevation changes over large areas: Differential radar interferometry. *J Geophys. Res.* 94(B7):9183–9191.

Galloway, D., Jones, D.R., and Ingebritsen, S.E. 1999. *Land Subsidence in the United States*. Circular 1182. Reston, VA: U.S. Department of Interior, U.S. Geological Survey.

Gandhi, S. 2013. Industrial minerals review: Soda ash. *Min. Eng.* 65(7):103–104.

Ge, L., Chang, H.C., and Rizos, C. 2007. Mine subsidence monitoring using multi-source satellite SAR images. *Photogramm. Eng. Remote Sens.* 73(3):259–266.

Ge, L., Chang, H.C., Ng, A., and Rizos, C. 2008. Spaceborne radar interferometry for mine subsidence monitoring in Australia. In *First International Future Mining Conference and Exhibition 2008 Proceedings*. Carlton South, VIC: AusIMM.

Gibowicz, S.J. 2009. Seismicity induced by mining: Recent research. *Adv. Geophys.* 51:1–53.

Gibowicz, S.J. and Lasocki, S. 2001. Seismicity induced by mining: Ten years later. *Adv. Geophys.* 44: 39–181.

Goldstein, R.M., Zebker, H.A., and Werner, C.L. 1988. Satellite radar interferometry: Two-dimensional phase unwrapping. *Radio Sci.* 23(4):713–720.

Goldstein, R.M., Engelhardt, H., Kamb, B., and Frolich, R.M. 1993. Satellite radar interferometry for monitoring ice sheet motion: Application to an Antarctic ice stream. *Sci.* 262(5139):1525–1530.

Goodrich, R.R., Agapito, J.F.T., Sorensen, W.K., and Black, J. 1999. Subsidence behavior at the SUFCO coal mine, Utah. In *Rock Mechanics for Industry: Proceedings of the 37th U.S. Rock Mechanics Symposium*. Edited by B. Amadei, R.L. Kranz, G.A. Scott, and P.H. Smeallie. Rotterdam, Netherlands: Balkema.

Google. 2015. July 25, 2014 Sheridan, Wyoming. 44°53'00.33"N, 106°50'25.21"W, Eye Altitude 2.01 km. www.earth.google.com. Accessed April 2015.

Gray, R.E., and Bruhn, R.W. 1984. Coal mine subsidence—Eastern United States. *Rev. Eng. Geol.* 6:123–150. Accessed June 2014. doi: 10.1130/REG6-p123.

Hanssen, R. 2001. *Radar Interferometry: Data Interpretation and Error Analysis.* Dordrecht, Netherlands: Kluwer Academic.

Harris, R.E. 1985. Overview of the geology and production of Wyoming trona. *Min. Eng.* 37(10).

Harrison, J.P. 2011. Mine subsidence. In *SME Mining Engineering Handbook,* 3rd ed. Edited by P. Darling. Englewood, CO: SME.

Ismaya, F. 2010. The application of differential interferometric synthetic aperture radar to identify, measure, and analyze subsidence above underground coal mines in Utah. M.S. thesis, University of Utah, Salt Lake City, UT.

Ismaya, F., and Donovan, J. 2012. Applications of DInSAR for measuring mine-induced subsidence and constraining ground deformation model. In *Proceedings of the GeoCongress 2012: State of the Art Practice in Geotechnical Engineering*. Reston, Virginia: ASCE.

Jeran P.W., and Trevits, M.A. 1995. *Timing and Duration of Subsidence Due to Longwall Mining.* Report of Investigations 9552. Washington, DC: Department of Interior, Bureau of Mines.

Kratzsch, H. 1983. *Mining Subsidence Engineering*. New York: Springer—Verlag Berlin Heidelberg.

Kubacki, T., Koper, K.D., Pankow, K.L., and McCarter, M.K. 2014. Changes in mining-induced seismicity before and after the 2007 Crandall Canyon Mine collapse. *J. Geophys. Res. Solid Earth* 119: 4876–4889. Accessed February 2015. doi:10.1002/2014JB011037.

Kyle, J.I., Maxwell, D.K., and Alexander, B.L. 2011. In-situ techniques of solution mining. In *SME Mining Engineering Handbook,* 3rd ed. Edited by P. Darling. Englewood, CO: SME.

LaScola, J.C. 1988. *Comparison of Aerial and Ground Surveying of Subsidence Over an Active Longwall.* Report of Investigations 9214. Washington, DC: Department of Interior, Bureau of Mines.

Lu, Z. and Wicks, C., Jr. 2010. Characterizing 6 August 2007 Crandall Canyon mine collapse from ALOS PALSAR InSAR. *Geomatics Nat. Hazards Risk* 1(1): 85–93. Accessed July 2014. doi: 10.1080/19475701003648077.

Maleki, H., Wopat, P.F., Repsher, R.C., and Tuchman, R.J. 1995. *Proceedings: Mechanics and Mitigation of Violent Failure in Coal and Hard-Rock Mines.* Special Publication 01-95. Washington, DC: U.S. Department of Interior, Bureau of Mines.

Mannion, L.E. 1975. Wyoming trona. Presented at the SME Fall Meeting, Salt Lake City, UT, September 10–12.

Massonnet D., Rossi, M., Carmona, C., Adragna, F., Peltzer, G., Feigl, K., and Rabaute, T. 1993. The displacement field of the Landers earthquake mapped by radar interferometry. *Nat.* 364:138–142.

Massonnet D., and Feigl K.L. 1998. Radar interferometry and its application to changes in the Earth's surface. *Rev. Geophys.* 36(4):441–500.

Massonnet, D. and Souyris, J.C. 2008. *Imaging with Synthetic Aperture Radar.* Boca Raton, FL: EPFL Press, Taylor and Francis.

Monroe, J.K. 2014. *2014 Subsidence Report Canyon Fuel Company, LLC SUFCO.* Salt Lake City, UT: Utah Division of Oil, Gas, and Mining, Department of Natural Resources.

National Coal Board. 1975. *Subsidence Engineers' Handbook.* UK: Mining Department.

National Map. 2015. TNM Download (V1.0), Elevation Products (3DEP), 1/3 arc-second DEM. http://viewer.nationalmap.gov/basic/. Accessed November 2015.

National Research Council. 1991. *Mitigating Losses from Land Subsidence in the United States.* Washington, DC: National Academy Press.

Ng, A.H.M., Ge, L., Yan,Y., Li, X., Chang, H.C., Zhang, K., and Rizos, C. 2010. Mapping accumulated mine subsidence using small stack of SAR differential interferograms in the Southern coalfield of New South Wales, Australia. *Eng. Geol.* 115(1–2):1–15.

Nieto, A. 2011. Selection process for underground soft-rock mining. In *SME Mining Engineering Handbook,* 3rd ed. Edited by P. Darling. Englewood, CO: SME.

Pankow, K.L., McCarter, M.K., Arabasz, W.J., and Burlacu, R.L. 2008. Coal-mining-induced seismicity in Utah—Improving spatial resolution using double-difference relocations. In *Proceedings 27th International Conference on Ground Control in Mining*. Morgantown, WV: West Virginia University.

Pechmann, J.C., Walter, W.R., Nava, S.J., and Arabasz, W.J. 1995. The February 3, 1995, ML 5.1 seismic event in the trona mining district of southwestern Wyoming. *Seismol. Res. Lett.* 66(3):25–34.

Pechmann, J.C., Nava, S.J., Bernier, F.M., Terra, F.M., and Burlacu, R. 2006. Summary of UUSS magnitude determinations: 1981–2006. www.quake.utah.edu/EQCENTER/LISTINGS/magsum.htm. Accessed January 2016.

Pechmann, J.C., Arabasz, W.J., Pankow, K.L., Burlacu, R., and McCarter, M.K. 2008. Seismological report on the 6 August 2007 Crandall Canyon mine collapse in Utah, *Seismol. Res. Lett.* 79(5):620–636.

Peng, S.S. 2006. *Longwall Mining,* 2nd ed. Morgantown, WV: Syd S. Peng.

Perski, Z. 2000. The interpretation of ERS-1 and ERS-2 InSAR data for the mining subsidence monitoring in Upper Silesian coal basin, Poland. *Int. Arch. Photogramm. Remote Sens. Spatial Inf Sci.* 33.

Perski, Z. and Jura, D. 2003. Identification and measurement of mining subsidence with SAR interferometry: Potential and limitations. In *Proceedings, 11th FIG Symposium on Deformation Measurements*. Santorini, Greece, May 25–28.

Plattner, C., Wdowinski, S., Dixon, T.H., and Biggs, J. 2010. Surface subsidence induced by the Crandall Canyon Mine (Utah) collapse: InSAR observations and elasto-plastic modelling. *Geophys. J. Int.* 183(3):1089–1096. Accessed February 2013. doi: 10.1111/j.1365-246X.2010.04803.x.

Popiołek, E., and Krawczyk, A. 2006. Post mining deformation monitoring based on satellite radar interferometry (InSAR). In *The 3rd IAG / 12th FIG Symposium.* Baden, Austria, May 22–24.

Richards, J.A. 2009. *Remote Sensing with Imaging Radar.* New York: Springer.

Richardson, A., Agapito, J.F.T., and Gilbride, L., 1999. Rock mechanics issues in the trona patch. *Proceedings 18th International Conference on Ground Control in Mining*. Morgantown, WV: West Virginia University.

Roehler, H.W. 1992. *Introduction to Greater Green River Basin Geology, Physiography, and History of Investigations.* Geological Survey Professional Paper 1506–A. Washington, DC: U.S. Government Printing Office.

Rosen, P.A., Hensley, S., Joughin, I.R., Li, F.K., Madsen, S.N., Rodriquez, E., and Goldstein, R.M. 2000. Synthetic aperture radar interferometry. *Proc. IEEE* 88(3):333–382.

Rosen, P.A. 2014. UNAVCO Short course: Principles and theory of radar interferometry. Presented at InSAR: An introduction to processing and applications using ISCE and GIAnT, Boulder, CO, August 4–6.

Rosenqvist A., Shimada, M., and Watanabe, M. 2004. ALOS PALSAR: Technical outline and mission concept. 4th International Symposium on Retrieval of Bio- and Geophysical Parameters from SAR Data for Land Applications. Innsbruck, Austria, November 16–19.

Roth, A. 2004. *TerraSAR-X Science Plan.* TX-PGS-PL-4001, Issue 1.0. Cologne, Germany: DLR.

Roze, A., Zufferrey, J.C., Beyeler, A. and McClellan, A. 2015. *eBee RTK Accuracy.* White Paper. www.sensefly.com/drones/ebee-rtk.html. Accessed April 2015.

Santini, K., Faster, T., and Harris, R. 2006. Soda ash. In *Industrial Minerals and Rocks,* 7th ed. Edited by J.E. Kogel, N.C. Trivedi, J.M. Barker, and S.T. Krukowski. Littleton, CO: SME.

SARscape®. 2014. *User Guide.* Purasca, Switzerland: Sarmap.

Simons, M. and Rosen, P.A. 2007. Interferometric synthetic aperture radar geodesy. In *Treatise on Geophysics*. Vol. 3, Geodesy. Edited by G. Schubert. New York: Elsevier.

Singh, M.M. 1984. Review of coal mine subsidence control measures. *Trans. AIME* 276:1988–1992.

Singh, M.M. 1992. Mine subsidence. In *SME Mining Engineering Handbook,* 2nd ed. Edited by H.L. Hartman. Littleton, CO: SME.

Stein, J.R., Pankow, K.L., Koper, K.D., McCarter, M.K. 2015. Discriminating mining induced seismicity from natural tectonic earthquakes in the Wasatch Plateau region of central Utah. In *Proceedings 34th International Conference on Ground Control in Mining*. Morgantown, WV: West Virginia University.

Tien, J.C. 2011. Room-and-pillar mining in coal. In *SME Mining Engineering Handbook*, 3rd ed. Edited by P. Darling. Englewood, CO: SME.

U.S. Energy Information Administration. 2013. Annual Coal Report 2012. www.eia.gov/coal/annual/. Accessed June 2014.

Wegmuller, U., Spreckels, V., Werner, C., Strozzi, T., Wiesmann, A. 2005. Monitoring of mining induced surface deformation using L-band SAR interferometry. In *Geoscience and Remote Sensing Symposium, 2005, IGARSS '05, Proceedings. 2005 IEEE.* Accessed January 2015. doi: 10.1109/IGARSS.2005.1526447.

Whittaker, B.N. and Reddish, D.J. 1989. *Subsidence: Occurrence, Prediction and Control.* New York: Elsevier.

Wilson, D. and Rao, T.V. 1982. Longwall mining of trona by Allied Chemical Corp. In *Underground Mining Methods Handbook.* Edited by W.A. Hustrulid. Littleton, CO: SME.

Wright, P. and Stow, R. 1999. Detecting mining subsidence from space. *Int. J. Remote Sens.* 20(6):1183–1188.

Whyatt, J. and Varley, F. 2008. Catastrophic failures of underground evaporite mines. In *Proceedings 27th International Conference on Ground Control in Mining.* Morgantown, WV: West Virginia University.

Whyatt, J. 2015. Consequences of ground failure: Independent study with discussion. Presented at the University of Utah, Salt Lake City, UT, Fall 2015.

Xinglin, L., Donglie, L., Hongjun, S., Runpu, C. and Hongyu, L. 2014. Key technology of D-InSAR at X-Band for monitoring land subsidence in mining area and its application. *J. Electron. China* 31(5).

Zebker, H.A., Rosen, P.A., Goldstein R.M., Gabriel, A., and Werner, C.L. 1994. On the derivation of coseismic displacement fields using differential radar interferometry: The Landers earthquake. *J. Geophys. Res.* 99(B10):19617–19634.

Zhao, C., Lu, Z., Zhang, Q., Yang, C. and Zhu, W. 2014. Mining collapse monitoring with SAR imagery data: A case study of Datong mine, China. *J. Appl. Remote Sens.* 8(1).